Optimization of Muon Injection and Storage in the Fermilab $g-2$ Experiment: From Simulation to Reality

Nathan Seth Froemming

A dissertation
submitted in partial fulfillment of the
requirements for the degree of

Doctor of Philosophy

University of Washington

2018

Reading Committee:

David W. Hertzog, Chair

Peter Kammel

Alejandro Garcia

Program Authorized to Offer Degree:
Physics

University of Washington

Abstract

Optimization of Muon Injection and Storage in the
Fermilab $g-2$ Experiment: From Simulation to Reality

Nathan Seth Froemming

Chair of the Supervisory Committee:
Professor and Director of the Center for Experimental Nuclear Physics and Astrophysics
David W. Hertzog
Physics

The anomaly of the muon magnetic dipole moment, $a_\mu \equiv (g_\mu - 2)/2$, is a sensitive probe into the Standard Model (SM) of particle physics because it can be calculated with high precision and also measured with high precision. Comparison of the experimental and theoretical values of a_μ therefore provides a stringent test of the completeness of the Standard Model, with any deviation suggesting the existence of new physics as a possible explanation. The most recent experimental determination of a_μ was performed by the E821 collaboration at Brookhaven National Laboratory (BNL) from 1997–2001, where a final precision of $\delta a_\mu / a_\mu = \pm 540$ parts per billion (ppb) was achieved. The value of a_μ obtained by E821 presently differs from the SM prediction by 3.5–4.0 standard deviations, hinting strongly—albeit inconclusively—of the existence of new physics. The BNL experiment was limited by statistics. A next-generation experiment at Fermi National Accelerator Laboratory (Fermilab), which utilizes the same BNL storage-ring magnet with many significant upgrades, aims to measure a_μ to a final precision of 140 ppb, thus helping to resolve the discrepancy between experiment and theory once and for all. The new Fermilab measurement of a_μ requires approximately $\sim$20X the entire BNL dataset to be recorded and analyzed, a difficult task. Therefore, optimization of the muon injection efficiency, capture fraction, and stored-muon beam properties are critical requirements for completing the new measurement in a timely manner with the required precision. These topics are the subject of this thesis.

DEDICATION

Here's to the crazy ones. The misfits. The rebels. The troublemakers. The round pegs in the square holes. The ones who see things differently. They're not fond of rules. And they have no respect for the status quo. You can quote them, disagree with them, glorify or vilify them. About the only thing you can't do is ignore them. Because they change things. They push the human race forward. And while some may see them as the crazy ones, we see genius. Because the people who are crazy enough to think they can change the world, are the ones who do.

— Rob Siltanen, Craig Tanimoto, *et al.*

ACKNOWLEDGMENTS

Many people have contributed to the personal and professional development of the author of this thesis over the past several years in important and far-reaching ways. This thesis absolutely would not have been possible without the people acknowledged in this section, about whom the author writes with the deepest and most profound sense of gratitude and respect: David W. Hertzog, whose enthusiasm and love of physics has inspired the author on many occasions to think critically, creatively, and cleverly about solving pertinent real-world problems, and whose continued support and guidance through the years has enabled the author to grow into a unique and respected role as a physicist in the E989 collaboration at Fermilab; Peter Kammel, Alejandro Garcia, and the close-knit CENPA community at the UW for always offering meaningful perspective, good advice, and stimulating that playful type of curiosity which can only be found in a Monday Meeting; Catherine Provost and Marcel den Nijs of the UW Physics Department for their patience, persistence, and years of hard work in helping the author of this thesis and other graduate students succeed in physics at the UW and beyond; David Rubin (Cornell University) and Carol Johnstone (Fermilab) for providing a colorful-but-rigorous introduction to accelerator physics that has served (and will continue to serve) as a stepping stone into the author's future; Adam Lyon (Fermilab) and Kyle Knoepfel (Fermilab) for introducing the author to high-performance computing and instilling many good coding practices early on which continue to pay dividends, for example, in beam-tuning computer programs written by the author of this thesis and executed from Fermilab Main Control Room; Renée Fatemi (University of Kentucky, Lexington) for being an exemplary physicist, outstanding mentor, amazing friend and impeccable human being who helped the author successfully navigate through the darkest depths of his Ph.D. and emerge victorious; The E989 Run Coordinators, Brendan Kiburg (Fermilab) and Jarek Kaspar (UW/Fermilab), for their heroic efforts in making the experiment work at all, which in turn afforded the author many beam-tuning opportunities and adrenaline rushes; Chris Polly (Fermilab) for inspiring the author to be confidently curious in the exploration

of upstream beamlines, and for providing unspeakably delectable family-secret biscuits and gravy during the epic beam-tuning session of MLK Holiday Weekend 2018; Laura Kelton (University of Kentucky, Lexington) for being a superb comrade, friend, and beam-tuning buddy during Commissioning and Run 1, whose assistance enabled the author to perform many successful studies, including the author's favorite study of his entire graduate-student career (M5 Final-Focus MULTs); Diktys Stratakis (Fermilab), Jim Morgan (Fermilab), and Mike Syphers (Fermilab/NIU) for recognizing, cultivating, stimulating, and encouraging the author's growing interest in accelerator physics, as well as affording the author a promising future at NIU/Fermilab; Last but not least, to dear family members and friends (Texas, Seattle, Chicago, and New York) for their perpetual love, unwavering support, and eternal Sunshine that continues to brighten even the dreariest of days.

TABLE OF CONTENTS

LIST OF FIGURES

LIST OF TABLES

GLOSSARY

ACHROMAT: A section of beamline in which the initial and final dispersion are zero. More generally, a section of beamline in which the final dispersion is equal to the initial dispersion such that no new chromatic effects are introduced.

AFFINE TRANSFORMATION: A linear geometric mapping that preserves points, straight lines, planes, and the ratio of distances (for example, rotations and translations).

ACL: Accelerator Command Language. A custom computer language at Fermilab for interfacing with and controlling ACNET devices, e.g. magnetic quadrupoles, via software and/or computer terminals.

ACNET: Accelerator Controls NETwork (at Fermilab).

AD: Accelerator Division (at Fermilab).

ANOMALY, MAGNETIC: $a \equiv (g-2)/2$, where g is the Landé g-factor. The anomaly may also be interpreted as the fractional deviation from 2.

BEAM COOLING: A non-Hamiltonian process by which the density of particles in phase space is increased such that the beam emittance is decreased.

BETA FUNCTION: Relationship between the beam size and beam emittance, $\beta = \sigma^2/\epsilon$.

BETATRON OSCILLATION: Transverse oscillations of individual particles within the beam, usually generated by the restoring force of a field gradient (e.g. quadrupoles).

BOOSTER: Machine in the Fermilab Accelerator Complex that accelerates protons from 400 MeV to 8 GeV.

BOOSTER BATCH: The extraction of all beam contained within one circumference of the Booster machine ($C = 474\,\mathrm{m}$).

BOOSTER TURN: One Booster-circumference ($C = 474\,\mathrm{m}$) worth of protons from Linac. More Booster turns leads to higher-intensity proton beams.

BPM: Beam Position Monitor. BPMs are used to measure the beam's transverse position within the beam pipe.

CTAG: Calorimeter-TAGged event, i.e. a decay positron from $\mu^+ \to \bar{\nu}_\mu \nu_e e^+$ detected in a calorimeter that is above the nominal $\sim$1.85 GeV threshold. CTAGs are often used as a real-time proxy for muon storage.

CADMESH: A tool for importing blueprints from computer-aided design (CAD) programs directly into *Geant4*-based simulations. Here, the 3D volume of the solid is reduced to a 2D surface representation using many triangular and quadrangular facets ("mesh").

CBO: Coherent Betatron Oscillation, i.e. oscillation of the beam centroid about the nominal design trajectory. For example, horizontal CBO in the muon $g-2$ storage ring is generated by weak or improperly timed pulsed kicker magnets.

CRYOSTAT: A device used to maintain a very low temperatures, usually associated with superconducting magnets.

COURANT-SNYDER PARAMETERS: Also known as the "beam" or "Twiss" parameters, the Courant-Snyder parameters (β, α, γ) describe the shape and orientation of the beam ellipse in phase space, e.g. $\gamma x^2 + 2\alpha x x' + \beta x'^2 = \epsilon_x$, where ϵ_x is the beam emittance.

DR: Delivery Ring ($C = 505\,\mathrm{m}$). Formerly the anti-proton debuncher ring which has been repurposed for the Muon Campus. The DR connects the M2/M3 beamlines to the M4/M5 beamlines, allows for pions to completely decay to muons ($\beta\gamma c\tau_\pi = 173\,\mathrm{m}$), and allows for the time-of-flight separation of muons from protons.

DISPERSION: Linear correlation between transverse position and longitudinal momentum. The dispersion is often denoted using the symbols $D_{x,y}$ or $\eta_{x,y}$, for example, $\eta_x \delta = 45\,\mathrm{mm}$, where $\delta \equiv (p - p_0)/p_0$ and p_0 is the design momentum ($p_0 = 3.094\,35\,\mathrm{GeV}/c$ for E821/E989).

E821: The Brookhaven muon $g-2$ experiment (1997–2001), which measured a_μ to a fractional uncertainty of $\delta a_\mu / a_\mu = \pm 540$ parts per billion.

E989: The Fermilab muon $g-2$ experiment (2017–present), which aims to measure a_μ to a fractional uncertainty of $\delta a_\mu / a_\mu = \pm 140$ parts per billion.

EMITTANCE: A single number, usually denoted ϵ, that corresponds essentially to the area, volume, or "size" of the beam in phase space. The transverse emittance is a measure

of the beam spot size and divergence, while the longitudinal emittance is a measure of the bunch length and energy spread. Note, there are *two* phase-space variables per spatial dimension, e.g. $\epsilon = \gamma x^2 + 2\alpha x x' + \beta x'^2$, where ϵ is the emittance and (α, β, γ) are the Courant-Snyder parameters.

FAC: Fermilab Accelerator Complex.

FODO: A series of alternating focusing (F) and defocusing (D) quadrupoles, separated by open space (O) in between. FODOs are primarily used to transport beam downstream.

GYROMAGNETIC RATIO: The ratio of a particle or object's magnetic moment to its intrinsic "spin" angular momentum, $\boldsymbol{\mu}/\mathbf{S} = g(Qe/2m)$, where g is the Landé g-factor, Qe is the charge, and m is the mass. Note, $g = 1$ for a classical sphere, $g = 2$ for a point-like charged lepton according to the Dirac equation, and $g \gtrsim 2$ according to the Standard Model of particle physics, where quantum fluctuations shift $g > 2$.

INFLECTOR: A superconducting septum magnet designed to facilitate muon injection into the $g-2$ storage ring by creating a field-free channel through which the injected beam passes upon entering the storage ring.

LINAC: Linear accelerator, designed to accelerate charged particles in a single pass along a straight section of beamline.

M1: The first of the Muon-Campus beamlines ($\sim$180 m) that helps transport 8.9 GeV/c protons from the Recycler machine to the Target station, where 3.1 GeV/c π^+ are created. (The beam path is Recycler$\rightarrow$P1$\rightarrow$P2$\rightarrow$M1$\rightarrow$Target).

M2/M3: The intermediate $\sim$290 m section of Muon-Campus beamline leading from the Target to the muon Delivery Ring.

M4/M5: The final $\sim$130 m section of Muon-Campus beamline leading from the muon Delivery Ring to the $g-2$ experiment.

M5 FINAL FOCUS: The last six magnetic quadrupoles (Q020-Q025) approximately $\sim$20 m upstream of the muon $g-2$ storage ring.

MC: "Monte Carlo" or "Muon Campus," depending on the context.

MC-1: Muon Campus 1, i.e. the building at Fermilab in which the muon $g-2$ experiment (E989) is performed.

MCR: Main Control Room (at Fermilab).

MULT: "Multiknob," i.e. a collection of two or more ACNET devices, e.g. magnetic quadrupoles, adjusted in unison via one ACNET parameter, e.g. magnet current. MULTs are often used in more sophisticated beam-tuning efforts.

MUON EVENT: 16 pulses of 1×10^{12} protons occurring in a time period of 1.4 s. There are approximately 40 muon events per Super Cycle during normal operation.

MUON STORAGE REGION: The torus of major radius $\rho_0 = 7112\,\text{mm}$ and minor radius $r_0 = 45\,\text{mm}$ in the muon $g-2$ storage ring.

MUON CAPTURE EFFICIENCY: The number of muons stored in the $g-2$ ring divided by the number of muons injected. A typical muon capture efficiency is $f_{\text{store}} \simeq 2\,\%$.

OOP: Object-Oriented Programming, a paradigm of modern computing.

RF: Time-varying electromagnetic fields in the radio-frequency regime (MHz to GHz). RF plays a critical role in the acceleration of charged particle beams.

SCD: Scientific Computing Division (at Fermilab).

SCRAPING: The process by which the injected muon beam is intentionally shifted 2-3 mm transversally using asymmetrically charged quadrupoles such that the outer edge of the beam is "scraped" against the inner edge of the beam collimators ($r_0 = 45\,\text{mm}$). The scraping procedure occurs only during the first $\sim$25 µs of the fill and is used to help reduced the "lost muon" systematic error.

SUPER CYCLE: A time period of 60 s as measured by the Tevatron Clock (TCLK) at Fermilab.

TRANSFER OR TRANSPORT MATRIX: Linear map describing the evolution of the phase-space coordinates of a beam of charged particles through an array of beamline lattice elements, a.k.a. the Jacobian of the transformation of the vector of phase-space coordinates from an upstream location in the beamline to a downstream location.

TRIM: Small dipole corrector magnet used to adjust the horizontal or vertical beam position. Two TRIMs may be used together to adjust both the position and angle of the outgoing beam (see MULT above).

TUNE: The number of betatron oscillations per turn.

TURN: Shorthand for "circumference," "orbit," or "revolution." For example, the dilated muon lifetime in the $g-2$ storage ring is $\gamma\tau_\mu = 64.4\,\mu s \approx 430$ turns.

Chapter 1

INTRODUCTION

On July 4$^{\text{th}}$, 2012, the ATLAS and CMS collaborations at CERN's Large Hadron Collider (LHC) announced the independent observation of a new particle in the mass region near 126 GeV consistent with the Higgs boson, thus completing the Standard Model (SM) of particle physics. The discovery of the Higgs and overwhelming verification of the Standard Model itself—decades in the making—is a crowning achievement of modern science, the importance of which cannot be overstated. However, in the six years since the discovery of the Higgs, the LHC has revealed no hints of physics beyond the Standard Model (BSM) and egregious shortcomings in our knowledge and understanding of the physical universe persist. In order to address these shortcomings, high-intensity, high-precision searches for new physics beyond the Standard Model are becoming more important, albeit occurring at a lower energy than at the LHC. One such experiment is the Fermilab muon $g-2$ experiment (E989), which aims to measure the anomaly of the muon magnetic moment a_μ to an unprecedented precision of 140 parts-per-billion (ppb). The purpose of this chapter is to introduce the basic motivation and fundamental concepts underlying the new muon g–2 experiment at Fermilab, E989.

1.1 Spin Angular Momentum and Magnetic Dipole Moments

The Classical Picture

Charges in motion create magnetic fields. The magnetic field of the Earth, for example, is generated by the intrinsic angular momentum ("spin") of Earth and currents flowing in Earth's molten-iron outer core [1], as shown in Fig. 1.1(A). The shape of Earth's magnetic field is remarkably similar to that of a common bar magnet, with one north pole and one south pole, and is usually referred to as a *dipole* magnetic field.[1] Fundamental particles such

[1]Magnetic monopoles have never been observed in nature ($\boldsymbol{\nabla}\cdot\mathbf{B}=0$), in contrast to positive and negative electric charges being observed in nature ($\boldsymbol{\nabla}\cdot\mathbf{E}=\rho/\epsilon_0$). Higher-order fields such as quadrupole, sextupole,

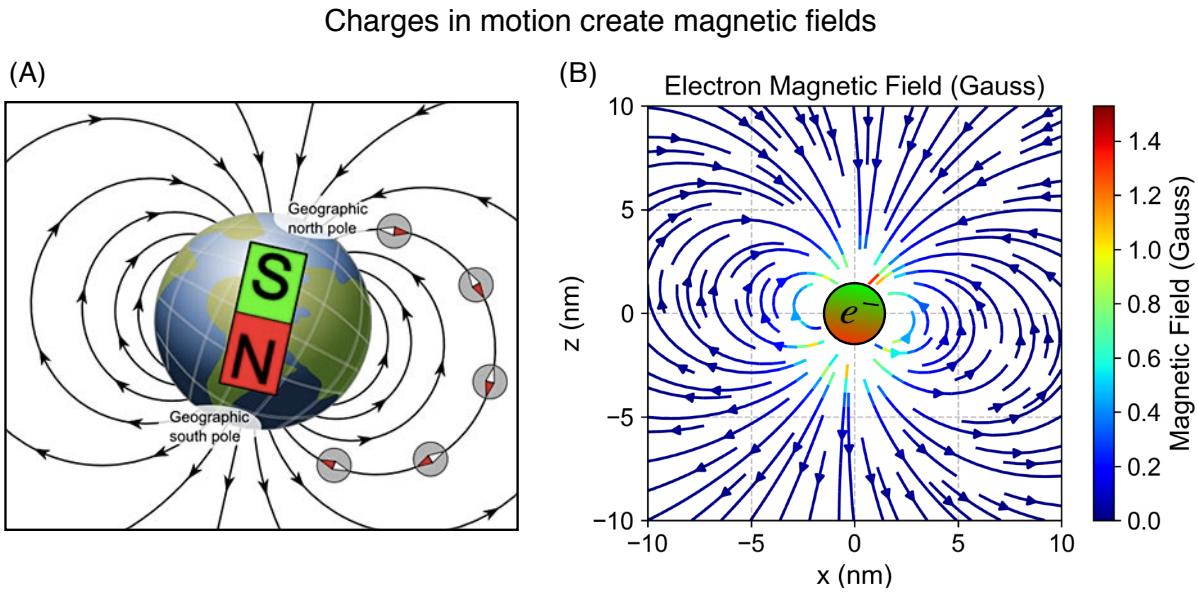

Figure 1.1: *Charges in motion create magnetic fields. (A) The magnetic field of the Earth is generated by Earth's intrinsic spin angular momentum and electric currents flowing in Earth's molten-iron outer core. The magnitude of the magnetic field is about 0.5 Gauss at the surface of the Earth. (B) Fundamental particles such as the electron, proton, and muon also possess charge and spin angular momentum, and therefore also exhibit a dipole magnetic field like that of the Earth. The magnitude of the electron magnetic field is about 1 Gauss at a radius* $r \simeq 1\,\mathrm{nm}$. *From Eq. (1.1), the magnetic field of the muon is* $m_e/m_\mu \simeq 1/207$ *times smaller in magnitude at the same distance due to the quantization of spin angular momentum.*

as the electron, proton, and muon also possess charge and intrinsic spin angular momentum, and therefore also exhibit dipole magnetic fields like that of the Earth [2, 3, 4],

$$\mathbf{B}^{(e)}_{\text{dip}}(\mathbf{r}) = \underbrace{\frac{\mu_0}{4\pi}\left(\frac{g_e e}{2m_e}\right)\frac{\hbar}{2}}_{-9.285\times10^{-31}\,\text{T}\,\text{m}^3}\left[\frac{3\,(\hat{\mathbf{m}}\cdot\hat{\mathbf{r}})\,\hat{\mathbf{r}}-\hat{\mathbf{m}}}{r^3}\right] \tag{1.1}$$

where Eq. (1.1) is shown for the electron in Fig. 1.1(B). The generic term *magnetic moment* is used to refer to an object's ability to generate and sustain a magnetic field of a particular strength, shape, and orientation. The terms "magnetic moment" and "magnetic dipole moment" are often used interchangeably, as will be discussed below.

The connection between a charged particle's intrinsic angular momentum and its magnetic moment played a crucial role in the development of quantum mechanics (QM) in the early 20$^{\text{th}}$ century, and later, in the development of quantum field theory (QFT) and the Standard Model (SM) of particle physics. Of the infinitude of moments possible in nature, the magnetic *dipole* moment is by far the most prevalent.[2] If the electron were a classical spinning sphere, the total spin angular momentum could be calculated by summing over infinitesimal bits of mass,

$$\mathbf{S} = \sum_i \mathbf{r}_i \times \mathbf{p}_i = \sum_i m_i\Big[(\mathbf{r}_i\cdot\mathbf{r}_i)\,\boldsymbol{\omega} - (\mathbf{r}_i\cdot\boldsymbol{\omega})\,\mathbf{r}_i\Big] \equiv I\boldsymbol{\omega} = \frac{2}{5}MR^2\,\boldsymbol{\omega}, \tag{1.3}$$

where $\mathbf{S}$ is the spin angular momentum, $\mathbf{r}_i$ is the position of the ith infinitesimal bit of

---

and so on are possible for both electric and magnetic fields.

[2]This statement can be made more precise in the following way: Maxwell's equation $\boldsymbol{\nabla}\cdot\mathbf{B} = 0$ implies the magnetic field $\mathbf{B}$ is derivable from a potential $\mathbf{B} = \boldsymbol{\nabla}\times\mathbf{A}$, where the magnetic vector potential $\mathbf{A}$ may be expanded in a power series,

$$\begin{aligned}\mathbf{A}(\mathbf{r}) &= \frac{\mu_0}{4\pi}\int\frac{\mathbf{j}(\mathbf{r}')}{|\mathbf{r}-\mathbf{r}'|}\,d^3\mathbf{r}' \\ &= \frac{\mu_0}{4\pi}\int\frac{\mathbf{j}(\mathbf{r}')}{r}\left[1+\left(\frac{r'}{r}\right)\cos\theta+\left(\frac{r'}{r}\right)^2\left(\frac{3\cos^2\theta-1}{2}\right)+\cdots\right]d^3\mathbf{r}', \\ &= \frac{\mu_0}{4\pi}\sum_{n=0}^{\infty}\frac{1}{r}\int\left(\frac{r'}{r}\right)^n P_n(\cos\theta)\;\mathbf{j}(\mathbf{r}')\,d^3\mathbf{r}',\end{aligned} \tag{1.2}$$

where $|\mathbf{r}-\mathbf{r}'| = \sqrt{r^2+r'^2-2rr'\cos\theta}$, $P_n(\cos\theta)$ are the Legendre polynomials of the first kind, and the integral over source currents $\mathbf{j}(\mathbf{r}')$ reduces to an integral over current loops $i\oint d\boldsymbol{\ell}'$ for the first term in the expansion. The important point is that $\oint d\boldsymbol{\ell}' = 0$ vanishes, corresponding to the non-existence of magnetic monopoles. Far away from the source, however, the second term in the expansion dominates, hence the importance of magnetic dipole moments in nature.

mass, $\mathbf{p}_i = m_i\mathbf{v}_i = m_i\boldsymbol{\omega} \times \mathbf{r}_i$ is the momentum, and the vector identity $\mathbf{A} \times (\mathbf{B} \times \mathbf{C}) = (\mathbf{A} \cdot \mathbf{C})\mathbf{B} - (\mathbf{A} \cdot \mathbf{B})\mathbf{C}$ has been used to rewrite $\mathbf{r}_i \times (\boldsymbol{\omega}_i \times \mathbf{r}_i)$. A similar calculation reveals that if the electron were a uniformly charged sphere, the magnetic moment would be given by

$$\boldsymbol{\mu} = \frac{1}{5} Q R^2 \, \boldsymbol{\omega}. \tag{1.4}$$

The ratio of the above two quantities is known as the *gyromagnetic ratio*, which is typically used to rewrite the magnetic moment in terms of the angular momentum,

$$\frac{\boldsymbol{\mu}}{\mathbf{S}} = \frac{Q}{2M} \quad \Rightarrow \quad \boldsymbol{\mu} = \frac{Q}{2M}\,\mathbf{S}. \tag{1.5}$$

A similar expression is used in physics literature to describe the magnetic moments of fundamental particles with a minor modification,

$$\boxed{\boldsymbol{\mu} \equiv g\left(\frac{q}{2m}\right)\,\mathbf{S}}\,, \tag{1.6}$$

where g is the Landé g-factor, originally written down to account for a missing multiplicative factor in the theoretical description of the anomalous Zeeman splitting [5]. Thus, the g-factor of a classical spinning sphere is $g = 1$, and as will be shown below, relativistic quantum mechanics and field theory predict $g \gtrsim 2$ for fundamental charged particles such as the electron and muon.

The Quantum Picture

The familiar experience of holding a compass in the presence of Earth's magnetic field and watching the needle "twist" in order to align itself with the field (Fig. 1.1) is synonymous with the statement that the potential energy U_B of the magnetic interaction is given by

$$U_B = -\boldsymbol{\mu} \cdot \mathbf{B} = -\mu B \cos\theta, \tag{1.7}$$

where $\boldsymbol{\mu}$ is the magnetic moment defined in Eq. (1.6), $\mathbf{B}$ is the external magnetic field, and θ is the angle between the two. The magnetic potential energy is minimized when the compass needle points in the direction of Earth's field. In 1922, O. Stern and W. Gerlach discovered

Eq. (1.7) may be used to separate a collimated beam of silver atoms[3] by introducing a magnetic-field gradient, $\partial B_z/\partial z > 0$, which gives rise to a force,

$$\mathbf{F}_B = -\boldsymbol{\nabla} U_B = \boldsymbol{\nabla}(\boldsymbol{\mu}\cdot\mathbf{B}) = \left(\mu_x \frac{\partial B_x}{\partial x}, \mu_y \frac{\partial B_y}{\partial y}, \mu_z \frac{\partial B_z}{\partial z}\right)^T . \tag{1.8}$$

The beam of silver atoms was observed to split into two distinct bands, which was interpreted at the time to be verification of "space quantization" (orbitals) in the Bohr-Sommerfeld theory.[4] This interpretation is now known to be incorrect. In 1925, R. Kronig, and separately G. Uhlenbeck and S. Goudsmit [6], proposed the theory that a "spinning electron" would produce a magnetic dipole moment responsible for the observed splitting, however, their calculations were too large by a factor of 2. Another problem with the "spinning-electron theory" was it predicted a speed much greater than the speed of light at the classical electron radius,

$$|\boldsymbol{\mu}_e| = \frac{1}{5} e r_e^2 \omega \approx \frac{e\hbar}{2m_e} \quad \Rightarrow \quad v = r_e\omega = \frac{5}{e r_e}\left(\frac{e\hbar}{2m_e}\right) = 342.6c, \tag{1.9}$$

where Eq. (1.4) has been used together with $r_e = 2.8179\times10^{-15}\,\mathrm{m}$ and $|\boldsymbol{\mu}_e| = 5.7884\times 10^{-5}\,\mathrm{eV/T}$. These shortcomings led W. Pauli to ridicule Kronig's theory so much that Kronig never published it [7]. Progress was made, however, in 1926 when L. Thomas explained the missing factor of 1/2 in Uhlenbeck and Goudsmit's results was the result of successive non-collinear Lorentz transformations required for centripetal acceleration in orbital motion [8]. Much to the chagrin of Kronig, Pauli is now generally credited for giving the first quantum-mechanical description of electron spin and magnetic moments interacting with external fields [9]. To achieve this, Pauli modified the Schrödinger equation *ad hoc* to include a two-component wavefunction, where each component represented the two possible spin orientations of the electron, with the magnetic interaction being given by

$$U_B = -\boldsymbol{\mu}\cdot\mathbf{B} = -\frac{gq}{2m}\mathbf{S}\cdot\mathbf{B} = -\frac{e\hbar}{2m}\boldsymbol{\sigma}\cdot\mathbf{B}. \tag{1.10}$$

Here, $\mathbf{S} = (\hbar/2)\boldsymbol{\sigma}$ is the electron spin, $\boldsymbol{\sigma} = (\sigma_x, \sigma_y, \sigma_z)$ is a vector of the now-famous 2×2 Pauli spin matrices, and $g = 2$ was imposed to match the data. Finally, in 1928, Dirac

[3] Silver (atomic number $Z = 47$) has one unpaired electron in its valence shell, i.e. $[\mathrm{Kr}]4d^{10}5s^1$.

[4] The Bohr-Sommerfeld theory is sometimes referred to as the "old quantum theory" in order to distinguish it from the "new quantum theory" of Heisenberg, Schrödinger, *et al.*, formulated in the mid 1920s.

showed in his seminal paper [10] that the electron spin and $g = 2$ are a natural consequence of the marriage of special relativity and quantum mechanics. In the non-relativistic limit, Dirac's relativistic theory of the electron reduces to [11]

$$i\hbar\frac{\partial\psi}{\partial t} = \left[\frac{\mathbf{p}^2}{2m} + qV - \frac{q}{2m}\left(\mathbf{L} + 2\mathbf{S}\right)\cdot\mathbf{B} + \frac{q^2}{2m}\mathbf{A}^2\right]\psi, \tag{1.11}$$

where the potential energy of the spin $\mathbf{S}$ interacting with the external magnetic field $\mathbf{B}$ is seen to be twice as large as the orbital magnetic moment $\mathbf{L}$ interacting with the external magnetic field. Thus, the Dirac theory predicts $g = 2$, consistent with experimental observations at the time, and in stark contrast to the classical value $g = 1$.

1.2 Standard-Model Expectation for a_μ

Dirac's 1928 result, $g = 2$ for the electron, is one of many remarkable features of the equation which bears his name.[5] The theory of quantum electrodynamics (QED) was also created by Dirac in 1927 when he showed how to quantize the electromagnetic field [13, 7]. Twenty years later, in 1947, J. Schwinger was investigating radiative corrections in electron phenomena and was able to predict a small shift to Dirac's value,

$$g \equiv 2(1 + a) = 2\left(1 + \frac{\alpha}{2\pi}\right) = 2.00232..., \tag{1.12}$$

where $a \equiv (g - 2)/2$ is generally referred to as the "magnetic anomaly." The value of the electron magnetic anomaly was under investigation by P. Kusch and H. Foley [14, 15] around the same time, who performed precision frequency measurements of the ratio of g-values in the $^3P_{3/2}$ and $^2P_{1/2}$ states of Gallium. Their experimental result, $\delta\mu_e/\mu_e = 0.00118 \pm 0.00003$, was in good agreement with Schwinger's prediction $\alpha/2\pi = 0.00116$ thus establishing QED and ushering in the modern era of quantum field theory (QFT). Since then, the weak and strong nuclear forces have been incorporated into QFT, leading to additional perturbations of the magnetic anomaly. The QFT describing QED, the weak nuclear force, and the strong nuclear force is generally referred to as the Standard Model (SM) of particle physics. The Standard-Model prediction for the muon magnetic anomaly a_μ is generally divided into three

[5] The existence of the anti-electron (and more generally anti-leptons), first observed by C. Anderson in 1933 [12], is another remarkable prediction of the Dirac equation.

parts,

$$a_\mu^{\rm SM} = a_\mu^{\rm QED} + a_\mu^{\rm EW} + a_\mu^{\rm Had}, \tag{1.13}$$

with several representative "Feynman diagrams" shown in Fig. 1.2.

The QED contribution to a_μ has been computed through 5 loops with the result [16]

$$\begin{aligned} a_\mu^{\rm QED} = \frac{\alpha}{2\pi} &+ 0.765857425(17)\left(\frac{\alpha}{2\pi}\right)^2 + 24.05050996(32)\left(\frac{\alpha}{2\pi}\right)^3 \\ &+ 130.8796(63)\left(\frac{\alpha}{2\pi}\right)^4 + 753.3(1.0)\left(\frac{\alpha}{2\pi}\right)^5 + \cdots, \end{aligned} \tag{1.14}$$

where the first term, $\alpha/2\pi = 0.00116$, is the seminal "Schwinger term" mentioned in Eq. (1.12). Loop contributions involving $W^\pm$, Z, or Higgs particles [Fig. 1.2(C, D)] are suppressed by at least a factor of $(\alpha/\pi)\, m_\mu^2/m_W^2 \simeq 4 \times 10^{-9}$, and therefore don't contribute much to a_μ. The final 2-loop electroweak result is [17]

$$a_\mu^{\rm EW}[\text{2-loop}] = (15.36 \pm 0.11) \times 10^{-11}. \tag{1.15}$$

Hadronic contributions to a_μ, in contrast, are relatively large and dominate the theoretical uncertainty. Here, the two most important contributions are the hadronic vacuum polarization (HVP) shown in Fig. 1.2(F) and the hadronic light-by-light (HLbL) shown in Fig. 1.2(G).

The HVP contribution can be evaluated with the aid of dispersion relations from the energy scan of the ratio $\sigma\left(e^+e^- \to \gamma^\star \to \text{hadrons}\right) / \frac{4\pi\alpha^2}{3s}$, which can be measured up to an energy cutoff above which perturbative quantum chromodynamics (pQCD) may be used (thanks to asymptotic freedom) [18],

$$a_\mu^{\rm HVP(LO)} = \left(\frac{\alpha m_\mu}{3\pi}\right)^2 \left(\int_{m_{\pi^0}^2}^{E_{\rm cut}^2} ds \frac{R_\gamma^{\rm data}(s)\hat{K}(s)}{s^2} + \int_{E_{\rm cut}^2}^{\infty} ds \frac{R_\gamma^{\rm pQCD}(s)\hat{K}(s)}{s^2} \right). \tag{1.16}$$

where $\hat{K}(s)$ is a known kernel function and the left-hand integral is dominated by the $\rho(770)$ resonance.[6] A recent summary of the various HLbL efforts is given in Ref. [19]. At present, there is a worldwide $g-2$ theory initiative that has been meeting regularly to develop an updated SM value for both HVP and HLbL. The above results are summarized in Table 1.1. Presently the difference between the experimental and theoretical values of a_μ is about $3.5\,\sigma$

[6] Note the mapping of experimental uncertainties to theoretical uncertainties.

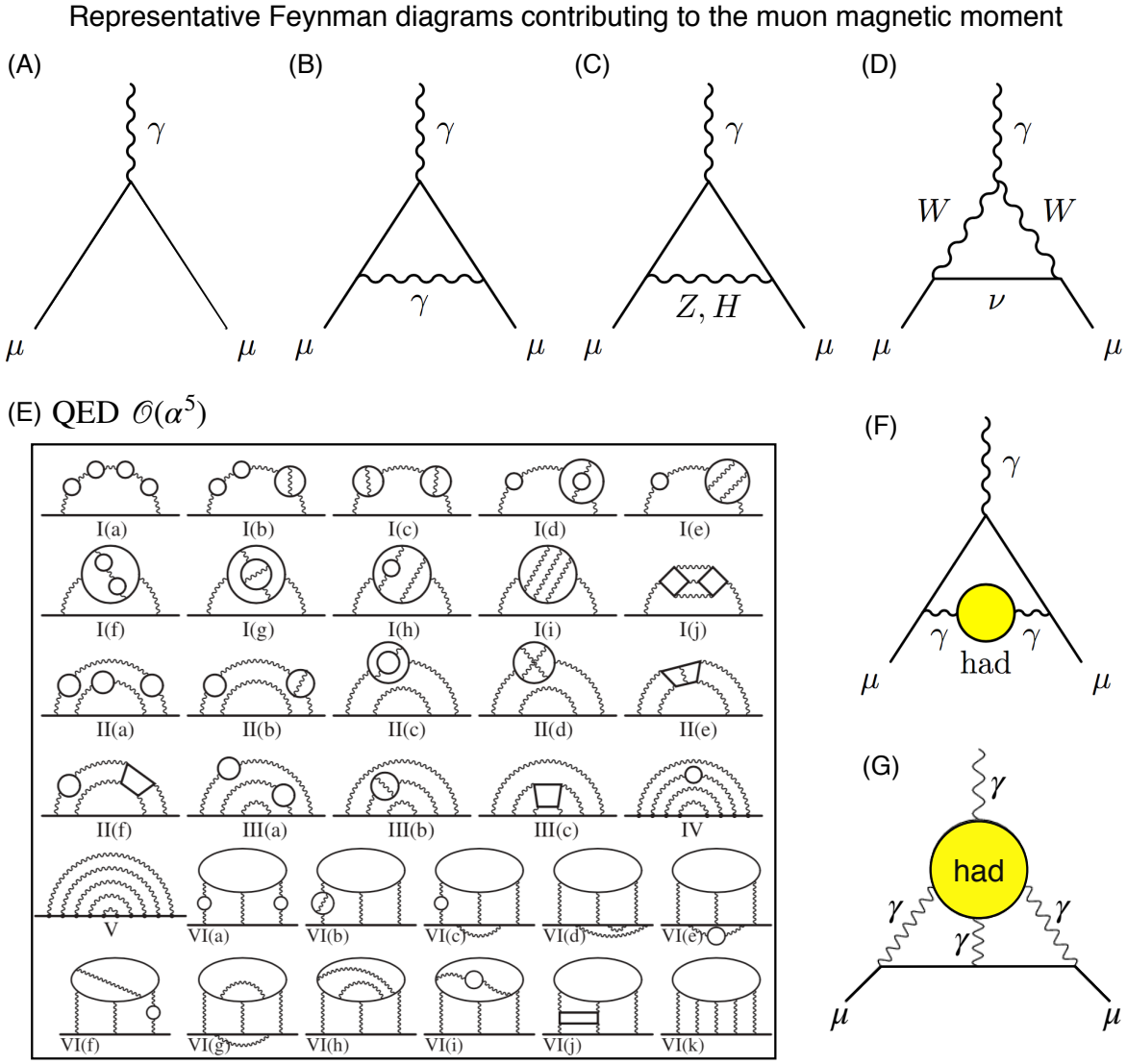

Figure 1.2: *Representative Feynman diagrams contributing to the muon magnetic moment. (A) Dirac term for a muon interacting with an external magnetic field, corresponding to* $g = 2$. *(B) Schwinger term,* $g = 2.002\,32\ldots$. *(C, D) The leading-order electroweak terms are quite small since the masses* $M_{\{W,Z,H\}}$ *are quite large. (E) Example 5th-order QED diagrams (12672 total). (F) Hadronic vacuum polarization (HVP). (G) Hadronic light-by-light (HLbL). The dominant errors in the theoretical value of* $g_\mu = 2(1 + a_\mu)$ *come from hadronic diagrams similar to (F) and (G).*

to $4.0\,\sigma$, with the experimental value larger than the theoretical value, $\Delta a_\mu = a_\mu^{\text{Exp}} - a_\mu^{\text{Thy}} = (30.6 \pm 7.6) \times 10^{-10}$. The goal of the new Fermilab muon $g-2$ experiment is to improve the BNL measurement by about a factor of four, which can be seen in Fig. 1.3.

Table 1.1: *Standard-Model Contributions to a_μ*

	Value ($\times 10^{10}$)	Uncertainty ($\times 10^{10}$)	Ref./Comment
QED (5 Loops)	**11 658 471.886**	**0.003**	[16]
Weak (2 Loops)	15.36	0.11	[17]
HVP (LO)	**689.46**	**3.25**	[20]
HVP (HO)	-8.70	0.06	[20]
HLbL	10.34	**2.88**	[20]
THEORY	11 659 178.3	4.3	See above
EXPERIMENT	11 659 209.1	6.3	[17]
$a_\mu^{\text{Exp}} - a_\mu^{\text{Thy}}$	30.6	7.6	$3.5\,\sigma$ – $4.0\,\sigma$

1.3 Beyond the Standard Model

The magnetic moment of the muon is particularly interesting to experimental and theoretical physicists because it can be both calculated and measure very precisely, and the sensitivity to new physics beyond the standard model generally goes as [23]

$$\delta a_\mu^{(\text{BSM})} \simeq C \frac{m_\mu^2}{M^2}, \qquad C \simeq \mathcal{O}(1), \tag{1.17}$$

where M is the mass scale of the new physics, i.e. the mass of the new particle. Thus the muon is $(m_\mu/m_e)^2 \simeq 42\,750$ more sensitive to new physics than the electron, while τ-lepton is simply too short lived to work with experimentally ($\tau_\tau = 2.9 \times 10^{-13}\,\text{s}$). One explanation for the possible difference between experiment and theory, $\Delta a_\mu = a_\mu^{\text{Exp}} - a_\mu^{\text{Thy}}$, might be a new physical process whereby supersymmetric particles enter into the quantum loop fluctuations similar to those shown in Fig. 1.2. The expected supersymmetric-induced shift to a_μ is given by [23, 17]

$$a_\mu^{\text{SUSY}} = \text{sgn}(\mu)\, 130 \times 10^{-11} \left(\frac{100\,\text{GeV}}{m_{\text{SUSY}}}\right)^2 \tan\beta, \tag{1.18}$$

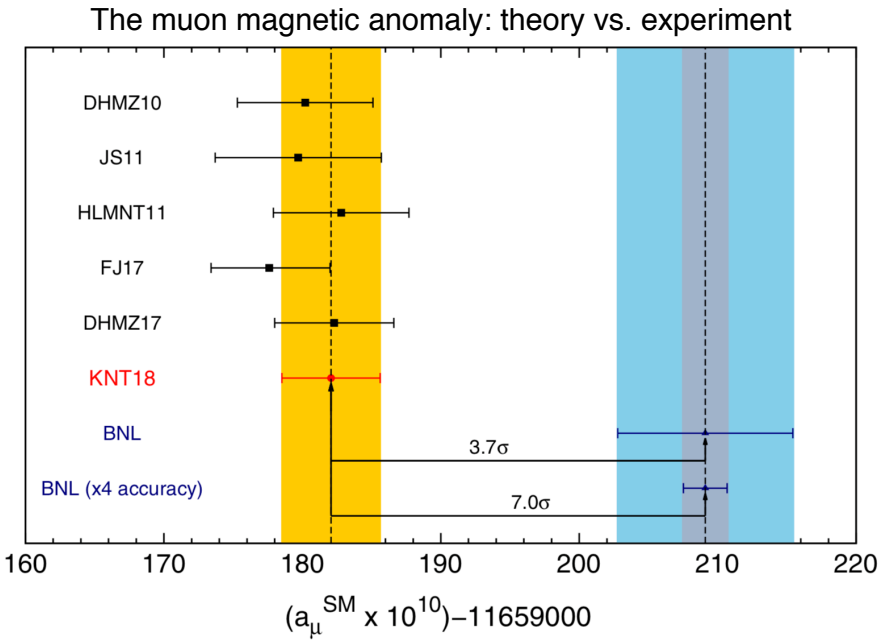

Figure 1.3: *The muon magnetic anomaly: theory vs. experiment. The solid yellow band at the left represents a collection of recent SM-calculated values of a_μ, where the mean value and uncertainty are those reported in KNT18 [21]. The solid blue band at the right represents the final experimental value of a_μ reported by the BNL E821 collaboration in 2006 [22]. The transparent red band at the right represents the increased sensitivity of the new Fermilab muon $g-2$ experiment (E989) over the BNL measurement, where the same mean value of a_μ obtained in the BNL measurement has been used for illustration purposes only.*

where $\mathrm{sgn}(\mu) = \pm 1$ corresponds to the sign of the μ term in the supersymmetric Lagrangian, $\tan\beta \simeq 3 - 40$ is a potential enhancement factor, and $m_{\mathrm{SUSY}} \sim$ 100-500 GeV is a representative mass scale. Such supersymmetric particles (or ramifications thereof) should be directly observable at the LHC. Unfortunately, there is no direct evidence yet supporting the supersymmetric interpretation. Another popular scenario that might lead to a shift $\Delta a_\mu = a_\mu^{\mathrm{Exp}} - a_\mu^{\mathrm{Thy}}$ was the "dark photon," i.e. a relatively light vector boson that couples to standard-model physics through mixing with the ordinary photon, however, the dark photon's contribution to a_μ seems to have been recently ruled out by the NA48/2 collaboration [24]. Therefore, the outlook for particle physics beyond the standard model is somewhat bleak at the time of writing. Nevertheless, E989 experimentalists are proceeding with the same fearlessness of failure as theoretician counterparts, because the final result of E989 will be interesting and important to the physics community regardless of the outcome.

1.4 Summary of the Experimental Technique

In order to perform a high-precision measurement of a_μ, the muon magnetic moment must be coupled to a magnetic field that is known with high precision. If the muons were at rest in the lab frame, the spin dynamics would be described by the Larmor precession,

$$\frac{\partial \mathbf{S}}{\partial \tau} = \boldsymbol{\mu} \times \mathbf{B} = \left(\frac{ge}{2m}\right) \mathbf{S} \times \mathbf{B}, \tag{1.19}$$

where $\mathbf{S}$ is the spin, $\boldsymbol{\mu}$ is the magnetic moment, and $\mathbf{B}$ is the external magnetic field, as shown in Fig. 1.4(A). The muons would then decay to positrons via $\mu^+ \to \bar{\nu}_\mu \nu_e e^+$, with the decay-positron intensity being correlated to the muon spin (due to parity violation in the weak decay, discussed below). In this way, the muon spin could be tracked as a function of time, and the coupling of the muon magnetic moment to the field could be extracted. Unfortunately, this technique measures g_μ, not a_μ, which differ by a factor of $g_\mu/a_\mu \approx 1700$, i.e. many more counts and a much higher-precision magnetic field would be required in order to measure the magnetic moment of the muon to the same precision. Thus the strategy is to measure a_μ directly.

The Fermilab muon $g-2$ experiment utilizes a 3.094 GeV/c polarized muon beam moving very nearly at the speed of light ($v_0 = 0.9994c$) to measure a_μ. Since relativistic muons are involved, it is worthwhile to discuss relativistic spin dynamics in some detail in order to

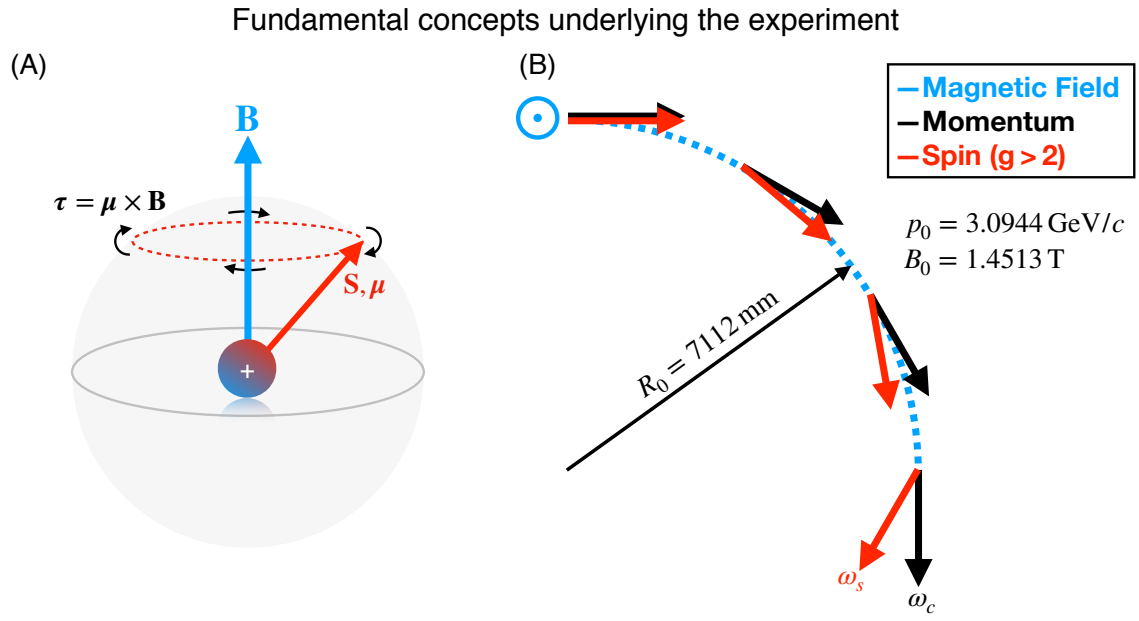

Figure 1.4: *Fundamental concepts underlying the experiment. (A) Larmor precession, in which an external magnetic field exerts a torque on the magnetic moment which causes the spin to precess around the direction of the field. (B) Spin dynamics of muons in a magnetic storage ring. Since $g_\mu > 2$, i.e. $a_\mu > 0$, the spin vector advances at a slightly faster rate than the momentum vector, with the difference being given by $\boldsymbol{\omega}_a \equiv \boldsymbol{\omega}_s - \boldsymbol{\omega}_c \approx (-e\mathbf{B}/m_\mu)\, a_\mu$.*

properly discuss the experiment. The constraint Eq. (1.19) in the co-moving frame leads one very naturally to guess

$$\frac{\partial \mathbf{S}}{\partial \tau} = \boldsymbol{\mu} \times \mathbf{B} \qquad \Rightarrow \qquad \frac{\partial S^\mu}{\partial \tau} \stackrel{?}{=} \left(\frac{ge}{2m}\right) F^{\mu\nu} S_\nu = \begin{pmatrix} \left(\frac{ge}{2m}\right) \mathbf{E} \cdot \mathbf{S} \\ \boldsymbol{\mu} \times \mathbf{B} \end{pmatrix}, \tag{1.20}$$

where $S^\mu = (0, \mathbf{S})$ is the muon spin 4-vector in the rest frame, τ is the proper time, and $F^{\mu\nu} = \partial^\mu A^\nu - \partial^\nu A^\mu$ is the field-strength tensor. Although the three spatial components of Eq. (1.20) are correct, $\partial \mathbf{S}/\partial \tau = \boldsymbol{\mu} \times \mathbf{B}$, the temporal component is incorrect since

$$0 = \partial_\tau \left(S \cdot U\right) = \partial_\tau \left(S^0 U^0 - \mathbf{S} \cdot \mathbf{U}\right) = \dot{S}^0 U^0 + S^0 \dot{U}^0 - \dot{\mathbf{S}} \cdot \mathbf{U} - \mathbf{S} \cdot \dot{\mathbf{U}}, \tag{1.21}$$

which, upon evaluation in the rest frame where $S^\mu = (0, \mathbf{S})$ and $U^\mu = (1, \mathbf{0})$, gives

$$0 = \dot{S}^0 - \mathbf{S} \cdot \dot{\mathbf{U}} \qquad \Rightarrow \qquad \dot{S}^0 = \mathbf{S} \cdot \dot{\mathbf{U}}. \tag{1.22}$$

The strategy is now very simple: subtract the incorrect value $\dot{S}^0 = \left(\frac{ge}{2m}\right) \mathbf{E} \cdot \mathbf{S}$ from Eq. (1.20) and add the correct value $\dot{S}^0 = \mathbf{S} \cdot \dot{\mathbf{U}}$ from Eq. (1.22), leading to

$$\frac{\partial S^\mu}{\partial \tau} = \begin{pmatrix} \mathbf{S} \cdot \dot{\mathbf{U}} \\ \boldsymbol{\mu} \times \mathbf{B} \end{pmatrix} = \begin{pmatrix} \left(\frac{ge}{2m}\right) \mathbf{E} \cdot \mathbf{S} \\ \boldsymbol{\mu} \times \mathbf{B} \end{pmatrix} - \begin{pmatrix} \left(\frac{ge}{2m}\right) \mathbf{E} \cdot \mathbf{S} \\ \mathbf{0} \end{pmatrix} + \begin{pmatrix} \mathbf{S} \cdot \dot{\mathbf{U}} \\ \mathbf{0} \end{pmatrix}. \tag{1.23}$$

This last expression, written term by term as Lorentz quantities, is

$$\frac{\partial S^\mu}{\partial \tau} = \left(\frac{ge}{2m}\right) F^{\mu\nu} S_\nu - \left(\frac{ge}{2m}\right) (U^\rho F_{\rho\sigma} S^\sigma) U^\mu + \left(\frac{e}{m}\right) (S^\rho F_{\rho\sigma} U^\sigma) U^\mu, \tag{1.24}$$

which is easy to verify in the co-moving frame, and where the Lorentz force $\dot{U}^\rho = \frac{e}{m} F^{\rho\sigma} U_\sigma$ has been used for the last term. Simplifying using the antisymmetry of $F^{\mu\nu} = \partial^\mu A^\nu - \partial^\nu A^\mu$ gives the celebrated Bargmann-Michel-Telegdi (BMT) equation [25, 4],

$$\boxed{\frac{\partial S^\mu}{\partial \tau} = \left(\frac{ge}{2m}\right) F^{\mu\nu} S_\nu + \frac{e}{m} \left(\frac{g-2}{2}\right) (S^\rho F_{\rho\sigma} U^\sigma) U^\mu}, \tag{1.25}$$

which is the backbone upon which the analysis of the spin precession of the muons in E821/E989 is based. It is interesting to note the magnetic anomaly $a = (g-2)/2$ has

emerged automatically in Eq. (1.25) from the proper covariant description of spin dynamics, and that the contribution of a_μ to $(\partial S^\mu/\partial\tau)$ enters as a Lorentz scalar times the four-velocity U^μ. This suggests muons circulating in a magnetic storage may be a plausible way to directly observe a_μ.

The BMT equation (1.25) is written in terms of the particle's rest frame instead of the lab frame where the $\{\mathbf{E}, \mathbf{B}\}$-fields are set. Transforming to the lab frame reveals the difference between the cyclotron and spin angular frequency is given by

$$\boldsymbol{\omega}_a \equiv \boldsymbol{\omega}_s - \boldsymbol{\omega}_c \approx -\frac{e}{m}\left[a_\mu \mathbf{B} - a_\mu \left(\frac{\gamma}{\gamma+1}\right)(\boldsymbol{\beta}\cdot\mathbf{B})\,\boldsymbol{\beta} - \left(a_\mu - \frac{1}{\gamma^2-1}\right)\frac{\boldsymbol{\beta}\times\mathbf{E}}{c}\right], \tag{1.26}$$

where the operational value $\gamma = 29.30$ ($p_0 = 3.094\,\mathrm{GeV}/c$) is chosen to eliminate the $\boldsymbol{\beta}\times\mathbf{E}$ term and $(\boldsymbol{\beta}\cdot\mathbf{B}) \approx 0$ by design (see Chapter 2 for a more complete discussion). Thus, in an ideal experiment, the anomalous precession angular frequency $\boldsymbol{\omega}_a$ is directly proportional to the well-known magnetic field,

$$\boxed{\boldsymbol{\omega}_a = -\frac{e}{m}a_\mu \mathbf{B}}, \qquad \text{(Ideal)} \tag{1.27}$$

and parity violation in the weak decay of the muon could be used to track muon spin vector as a function of time spent in the magnetic field as mentioned above. This is the basic approach taken in the Fermilab muon $g-2$ experiment. The experiment is discussed in more detail in the following chapter.

Chapter 2

EXPERIMENT OVERVIEW

This chapter begins with a discussion of the basic layout of the Fermilab Accelerator Complex and the machines used to generate and transport the required 3.1 GeV/c polarized muon beam to the $g-2$ experiment. Next, several subsystems in the muon storage ring are discussed, with an emphasis placed those subsystems playing a role in the injection of the muon beam into the storage ring. Lastly, this chapter concludes with a brief discussion of how data from the storage-ring magnetic field, decay-positron signal, and stored-muon-beam distribution are combined to extract the anomalous magnetic moment of the muon, a_μ, from the measured experimental data.

2.1 Fermilab Accelerator Complex

In order to perform the muon g–2 experiment at Fermilab, a beam of highly polarized muons is required. The muon beam is generated via a sequence in which primary protons are used to create secondary pions via a target, which in turn are used to create tertiary decay muons ($p \rightarrow \pi^+ \rightarrow \mu^+$). As a result, the upstream beamlines naturally separate into three distinct conceptual pieces:

1. Creation of an energetic proton beam

2. Creation of secondary pions using a target ($p \rightarrow \pi^+$)

3. Creation of muons from pion decay ($\pi^+ \rightarrow \mu^+$)

The purpose of this section is to review each of the relevant machines used to create the polarized muon beam required for the experiment. The discussion proceeds from upstream to downstream starting with a machine known as the "Source" or "Pre-Accelerator." An overview of the Accelerator Complex at Fermilab is shown in Fig. 2.1.

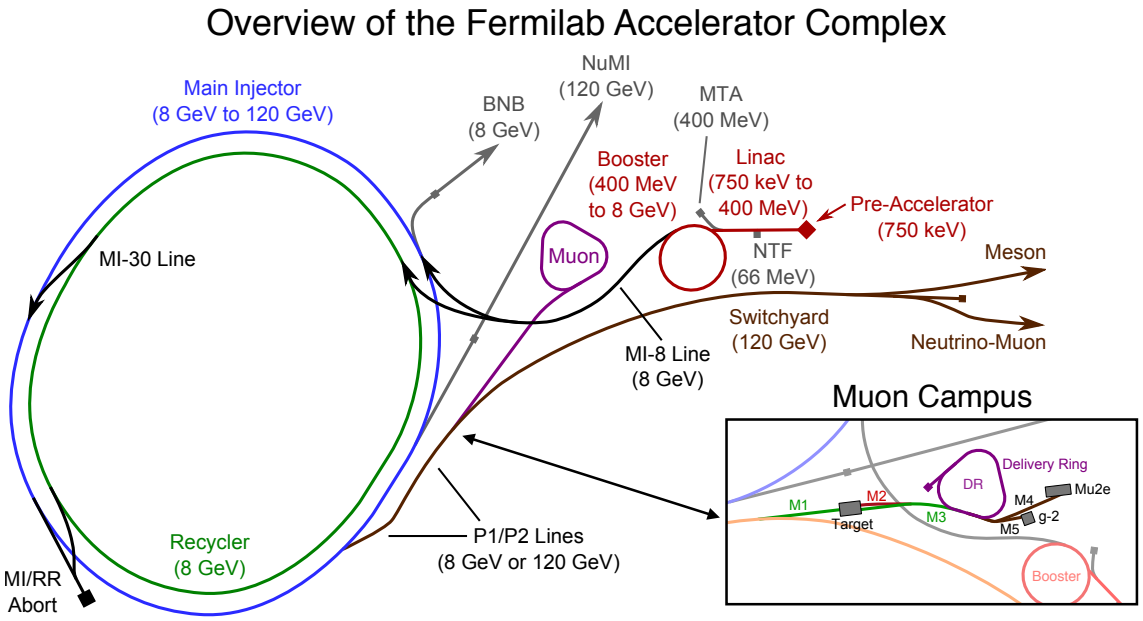

Figure 2.1: *Overview of the Fermilab Accelerator Complex. The creation of the* $8.9\,\mathrm{GeV}/c$ *proton beam required by the experiment is accomplished by the machines shown at the upper right in red: Pre-Accelerator (Source), Linac, and Booster. The Recycler machine (left, green) divides the* $\sim$*1600* ns*-long proton pulse from the Booster into four shorter* $\sim$*120* ns *pulses, each of which will fit inside the muon* g*–2 storage ring (*$T_{\mathrm{rev}} = 149\,\mathrm{ns}$*). The inset at the lower right shows the Muon Campus in greater detail, including the target station used to create pions and the downstream beamlines used to collect and transport muons to the experiment. The tiny building marked "*$g-2$*" is where the* $\rho_0 = 7112\,\mathrm{mm}$ *muon storage ring is housed and where the experiment (E989) takes place.*

2.1.1 Source, Linac, and Booster: Proton Beam

Fermilab built much of its reputation accelerating protons and antiprotons to nearly the speed of light, however, the acceleration process begins with anionic hydrogen (i.e. negative hydrogen ions, H^-). First, a beam of 35 keV H^- is generated in a machine known as the Pre-Accelerator (or Source) at a peak rate of about 15 Hz. Here, an einzel lens[1] is used to focus the H^- beam and to act as a beam chopper to precisely control the amount of beam entering the downstream machines. A typical beam pulse from the Source has ∼65 mA averaged over the bunch length of approximately ∼100 µs. Next, the H^- beam is focused transversally, bunched longitudinally, and accelerated to 750 keV using electric fields in a 4-ft section of radio-frequency quadrupoles (RFQs, $f = 201.24$ MHz). The ∼65 mA beam pulse then enters the Fermilab Linear Accelerator (Linac) where it is accelerated from 750 keV to 400 MeV in two stages.[2] The longitudinal length of Linac is 150 m and the beam current is ∼34 mA at the end of Linac.

As the 400 MeV beam from the Linac is injected into the Booster machine, the beam passes through a thin stripping foil to remove the excess electrons from H^-. Protons already circulating in the Booster are intentionally deflected from the closed orbit in order to overlap with the H^- in the injection region. Both ionic species pass through the stripping foil since the gains from intra-beam Coulomb attraction outweigh the losses due to multiple scattering in the thin stripping foil. This process, known as "charge-exchange injection," results in a pure proton beam that will ultimately be used to make muons through the $p \to \pi^+ \to \mu^+$ chain. The acceleration of the proton beam from 400 MeV to 8 GeV (kinetic energy) occurs by sweeping the RF from 37.8 MHz to 52.8 MHz, which decreases the revolution period from 2.2 µs to 1.6 µs in the 474-m-circumference Booster machine. The intensity of the final 8 GeV proton beam leaving the Booster is often quoted in units of "Booster turns," i.e. the number of times the Booster is filled with one circumference (474 m) of beam from the Linac. This concept is shown in Fig. 2.2. The complete extraction of all beam contained in one Booster circumference, i.e. 84 buckets of 52.8 MHz RF, is known as one "Booster batch." For the

[1] An einzel lens, or "uni-potential lens," focuses a beam of charged particles without changing the particle energy. A typical einzel lens consists of three cylindrical electrodes arranged longitudinally along the beam axis, where only the center electrode is charged so the integrated longitudinal electric field is zero.

[2] The Linac itself consists of two different types of linear accelerators, the low-energy and high-energy sections, whose details will not be discussed here. The split-off to the Neutron Therapy Facility (NTF) for cancer treatment is also contained in this segment of beamline.

muon $g-2$ experiment, the beam extracted from the Booster then proceeds downstream to the Target Station in order to create pions, and ultimately, muons. A summary of the multistep acceleration process discussed above is shown in Table 2.1.

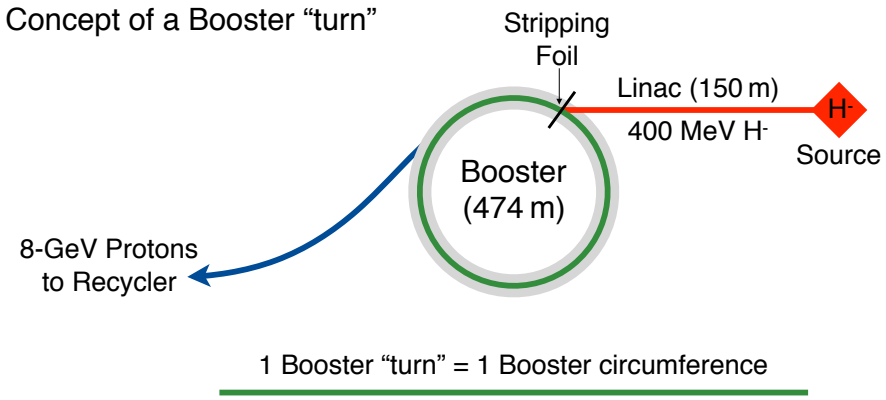

Figure 2.2: *One Booster "turn" is equivalent to one Booster-circumference worth of protons from Linac (after the injected H^- beam has been stripped of excess electrons). Booster may be filled with more than one turn, however, the maximum length of the extracted beam pulse may be at most one circumference-worth of protons ($C = 474\,\text{m}$, a.k.a. one Booster "batch"). Filling Booster with more turns leads to more-intense batches of extracted protons, ultimately leading to higher-intensity muon beams.*

Table 2.1: *Summary of Fermilab Machines Used to Create an* 8 GeV *Proton Beam*

Device/Machine	Beam Composition		Kinetic Energy (keV)	
	Initial	Final	Initial	Final
Source, Pre-Accelerator	—	H^-	0	35
Radio-Frequency Quadrupoles (RFQs)	H^-	H^-	35	750
Linac	H^-	H^-	750	400,000
Stripping Foil	H^-	p	400,000	400,000
Booster	p	p	400,000	8,000,000

2.1.2 Recycler: Bunch Formation

One logistical challenge faced by the experiment is the mismatch of the circumference of the Booster machine (474 m) and the circumference of the muon $g-2$ storage ring (45 m). A single beam pulse from the Booster is simply too long to fit within one turn of the muon storage ring.[3] This mismatch is unacceptable since the injected muon beam must be kicked onto the proper storage orbit within one turn of entering the ring, otherwise the beam will be kicked repeatedly on subsequent turns, which adversely affects muon capture efficiency and beam/data quality. The solution is to divide the single long beam pulse from the Booster ($T_{\text{batch}} \simeq 1600$ ns) into four shorter pulses, each of which will fit within one turn of the muon storage ring ($T_{\text{rev}} \simeq 150$ ns). This process, known as "rebunching," occurs via the application of 2.5 MHz RF over 90 ms in the Recycler machine, as shown in Fig. 2.3. The initial Booster batch is injected into the Recycler in temporally matched 52.8 MHz RF buckets at 80 kV. The 52.8 MHz voltage is then switched off and replaced by 2.5 MHz at 3 kV. The 2.5 MHz is then ramped adiabatically from 3 kV to 80 kV over $\Delta t = 90$ ms, leading to the formation of four distinct ∼120 ns pulses. Since each beam pulse from the Booster machine contains 4×10^{12} protons, each of the four rebunched pulses in the Recycler contains approximately 1×10^{12} protons per pulse. In this way, successive trains of 4 pulses may be concatenated to form the nominal group of 16 pulses per "Muon Event," which are sent to the target with the time structure shown in Fig. 2.3(C). Approximately 40 such Muon Events occur every Super Cycle (60 s).

2.1.3 Target Station: Pion Production

After the 8 GeV proton beam has been rebunched in the Recycler, each ∼120 ns pulse is extracted and sent to the Target Station via the P1/P2/M1 beamlines. Just before the proton beam impinges on the target, the beam is focused very hard to a transverse spot size of $\sigma_{x,y} \approx 0.15$ mm using a triplet of magnetic quadrupoles that comprise the target final focus. The target itself is essentially the same antiproton-production target used at the end of the Tevatron Collider Run II, consisting of a robust alloy of nickel, chromium, and iron called Inconel 600. Positively charged particles emanating from the Target are then focused by a

[3] The beam structure of the protons in the Booster is imprinted upon the π^+ distribution created at the Target Station, which in turn is imparted to the μ^+ ultimately delivered to the experiment.

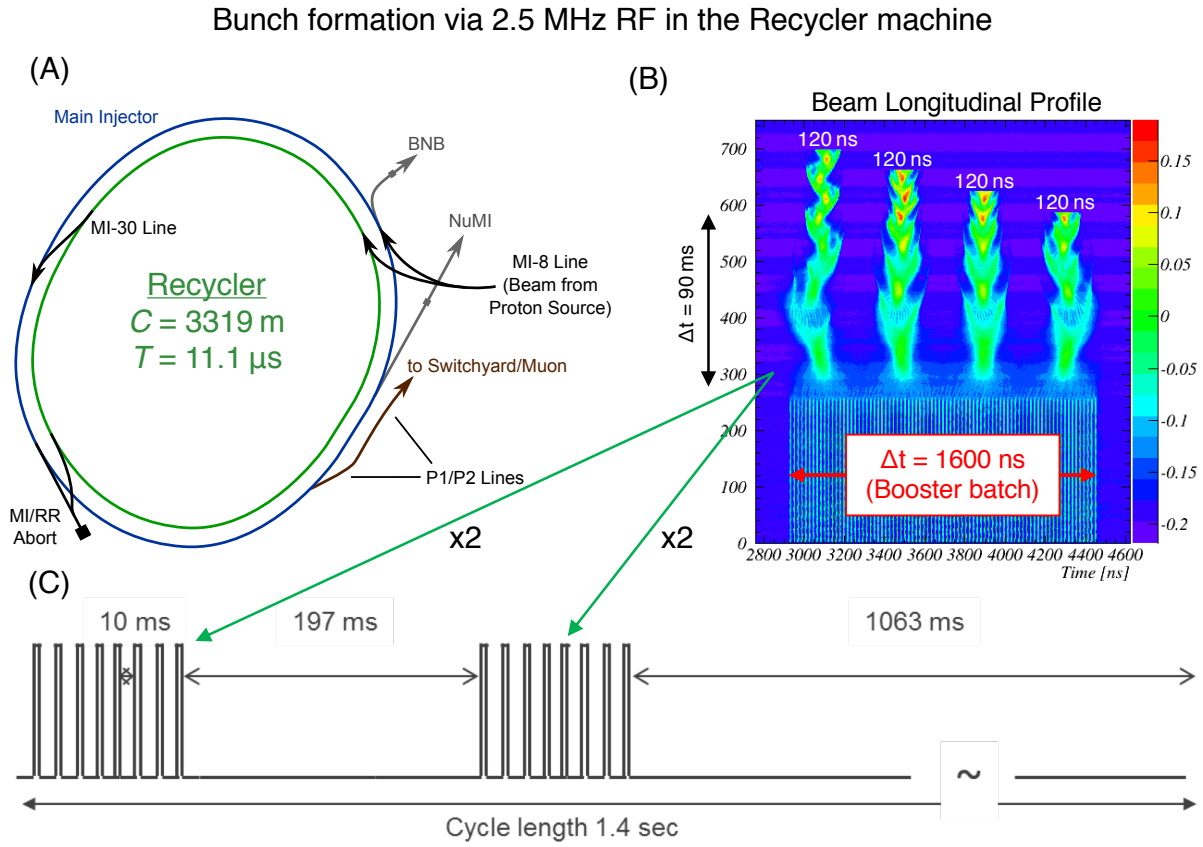

Figure 2.3: *The purpose of the Recycler machine (A) is to rebunch the single long* 4×10^{12} *proton pulse from the Booster (B) into four shorter* 1×10^{12} *pulses, each of which may fit within one turn of the muon storage ring. The rebunching process occurs via the application of* 2.5 MHz *RF over* 90 ms *in the Recycler. (C) While the Main Injector (another machine used for different experiments) is ramping, the Recycler is free for a period of seven Booster cycles. Two Booster batches are rebunched into eight bunches, and two such groups of eight bunches are concatenated to form one Muon Event. The beam pulses are extracted sequentially to E989 "from the caboose" every* $\Delta t = 10$ ms*, with a* 200 ms *gap between successive groups of eight bunches. The cycle length is* 1.4 s*, which repeats approximately 40 times every Super Cycle (*60 s*) during normal operations.*

lithium lens ($Z_{\mathrm{Li}} = 3$), i.e. a cylinder of Li whose transverse radius is 1 cm and whose 15 cm axis is oriented in the downstream direction of the beamline. A pulsed current of about 160 kA flows through the Li in the downstream direction, creating a strong axisymmetric magnetic field that provides the required transverse focusing for positive particles such as π^+. The layout of the target station is shown in the lower left of Fig. 2.4.

After being focused by the Li lens, the beam is then collimated and momentum-selected using a pulsed dipole bending magnet known as "PMAG." The main purpose of the collimator is to provide radiation shielding for PMAG in order to increase PMAG's lifetime. The collimator is a water-cooled copper cylinder whose longitudinal length is about 20 inches and whose outer transverse diameter is about 5 inches. The beam passes through a ∼1 inch hole bored along the axis of the cylindrical collimator, which is oriented in the downstream direction. Particles near the design momentum $p_0 = 3.1\,\mathrm{GeV}/c$ are bent 3° beam-left by PMAG into a channel that marks the formal beginning of the M2 beamline. Particles whose momenta deviate from the design momentum proceed directly downstream into the beam dump.

2.1.4 M2/M3 Beamlines: Pion Decay to Muons

Positively charged particles exiting the Target Station proceed immediately into the 2nd of the Muon-Campus beamlines, M2, and onward toward M3. The M2/M3 beamlines are designed to capture as many magic-momentum muons from pion decay as possible [26]. The geometry and lattice functions of the M2/M3 beamlines are shown in Fig. 2.4. The overall length of M2 is about 50 m, and much of it (including the Target Station) was built from the former antiproton AP2 line to reduce cost. At the M2/M3 merge, a large-aperture dipole bends the beam 3° beam-left, which cancels the horizontal dispersion introduced by the 3°-bend at PMAG (discussed in §2.1.3) since there is 540° betatron phase advance between the two locations.

The M3 beamline is essentially a ∼230 m FODO section that transports the beam from the M2 to the Delivery Ring, allowing for pions to decay to muons along the way. About halfway down M3 there is a 18.5° horizontal double-bend achromat [27] that bends the beam to the beam-right. The FODO section upstream of the horizontal-bend section has 90° phase advance per cell, while the downstream FODO section has 72° per cell, both of which reflect the need to keep $\beta_{x,y}$ small in order to maximize muon capture from pion decay (§A.4). The

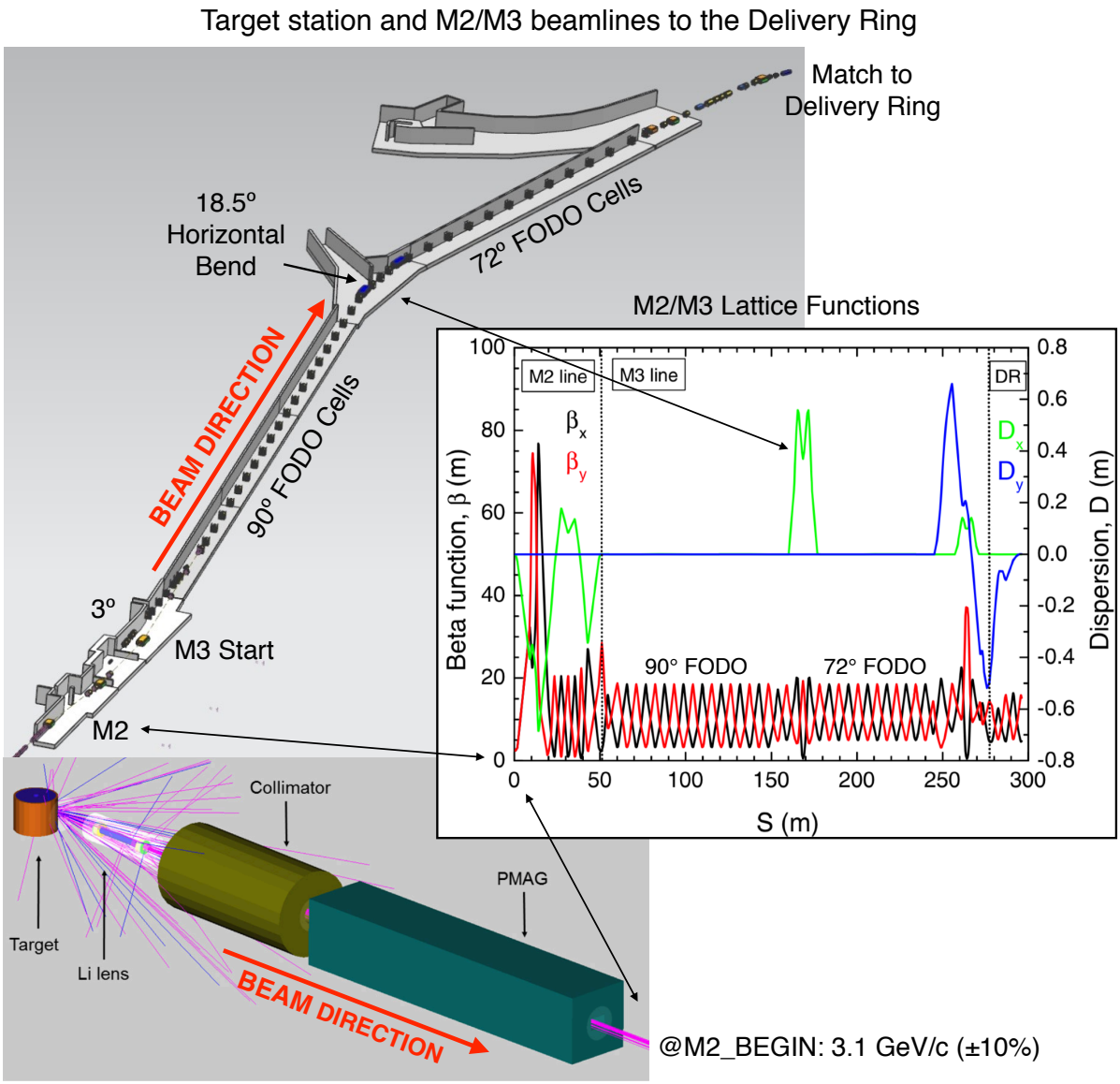

Figure 2.4: *Target station (lower left) and M2/M3 beamlines to the Delivery Ring. The relativistic kinematics of the* 3.1 GeV/c π^+ *imply one dilated lifetime in the lab frame corresponds to* $\beta\gamma c\tau_\pi = 173\,\mathrm{m}$ *of beamline, whereas the M2/M3 beamlines are about* 280 m. *Thus, approximately* $\exp(-280\,\mathrm{m}/173\,\mathrm{m}) = 20\%$ *of pions have not decayed to muons by the time the beam reaches the Delivery Ring.*

creation of the highly polarized muon beam required by the experiment is the direct result of (1) isotropic decay of the spin-0 pion in the rest frame and (2) the geometrical acceptance of the beam pipe in the lab frame, as shown in Fig. 2.5. Since the design momentum is 3.1 GeV/c, the Lorentz boost parameters are

$$\beta_0\gamma_0 = \frac{p_0}{m_\pi} = 22.17, \qquad \gamma_0 = \sqrt{1+(\beta_0\gamma_0)^2} = 22.19. \tag{2.1}$$

The Lorentz transformation that actively boosts the decay muon from the pion rest frame to the lab frame is

$$p^\mu_{(\text{Lab})} = \begin{pmatrix} \gamma_0 & 0 & 0 & \beta_0\gamma_0 \\ 0 & 1 & 0 & 0 \\ 0 & 0 & 1 & 0 \\ \beta_0\gamma_0 & 0 & 0 & \gamma_0 \end{pmatrix} \begin{pmatrix} E_\mu \\ |\mathbf{p}_\mu|\sin\theta^\star \\ 0 \\ |\mathbf{p}_\mu|\cos\theta^\star \end{pmatrix} = \begin{pmatrix} \gamma_0 E_\mu + \beta_0\gamma_0|\mathbf{p}_\mu|\cos\theta^\star \\ |\mathbf{p}_\mu|\sin\theta^\star \\ 0 \\ \beta_0\gamma_0 E_\mu + \gamma_0|\mathbf{p}_\mu|\sin\theta^\star \end{pmatrix}, \tag{2.2}$$

where the $+z$-direction is downstream, $\theta^\star$ is the decay angle in the pion rest frame with respect to the $+z$-direction (Fig. 2.5), and

$$E_\mu = \frac{m_\pi^2 + m_\mu^2}{2m_\pi} = 109.8\,\text{MeV} = (1.039)m_\mu, \qquad |\mathbf{p}_\mu| = \frac{m_\pi^2 - m_\mu^2}{2m_\pi} = 29.79\,\text{MeV}/c. \tag{2.3}$$

Since the Muon-Campus beamlines are designed to transport particles with momentum $|\delta| \lesssim 2\%$, only forward-decay muons are delivered to the experiment and the beam ensemble has a largely negative longitudinal polarization, $(\hat{\mathbf{s}}\cdot\hat{\mathbf{p}}) < 0$ for μ^+. More properties of the muon beam delivered to the experiment will be discussed the following subsections. The details of the match from the downstream end of M3 into the Delivery ring are complicated and the reader is encouraged to consult Ref. [28] for details.

2.1.5 Delivery Ring: Pion Decay and Muon Separation from Protons

The main purpose of the 505-m Delivery Ring (DR) is to allow pions to completely decay to muons, and to allow for the time-of-flight separation of muons from protons. The geometry, lattice, and time-of-flight separation of muons from protons in the DR are shown in Fig. 2.6 [26, 28]. The lattice of the DR has a 3-fold symmetry with additional mirror symmetry in each of the three periods. There are three zero-dispersion straight sections with injection from M3

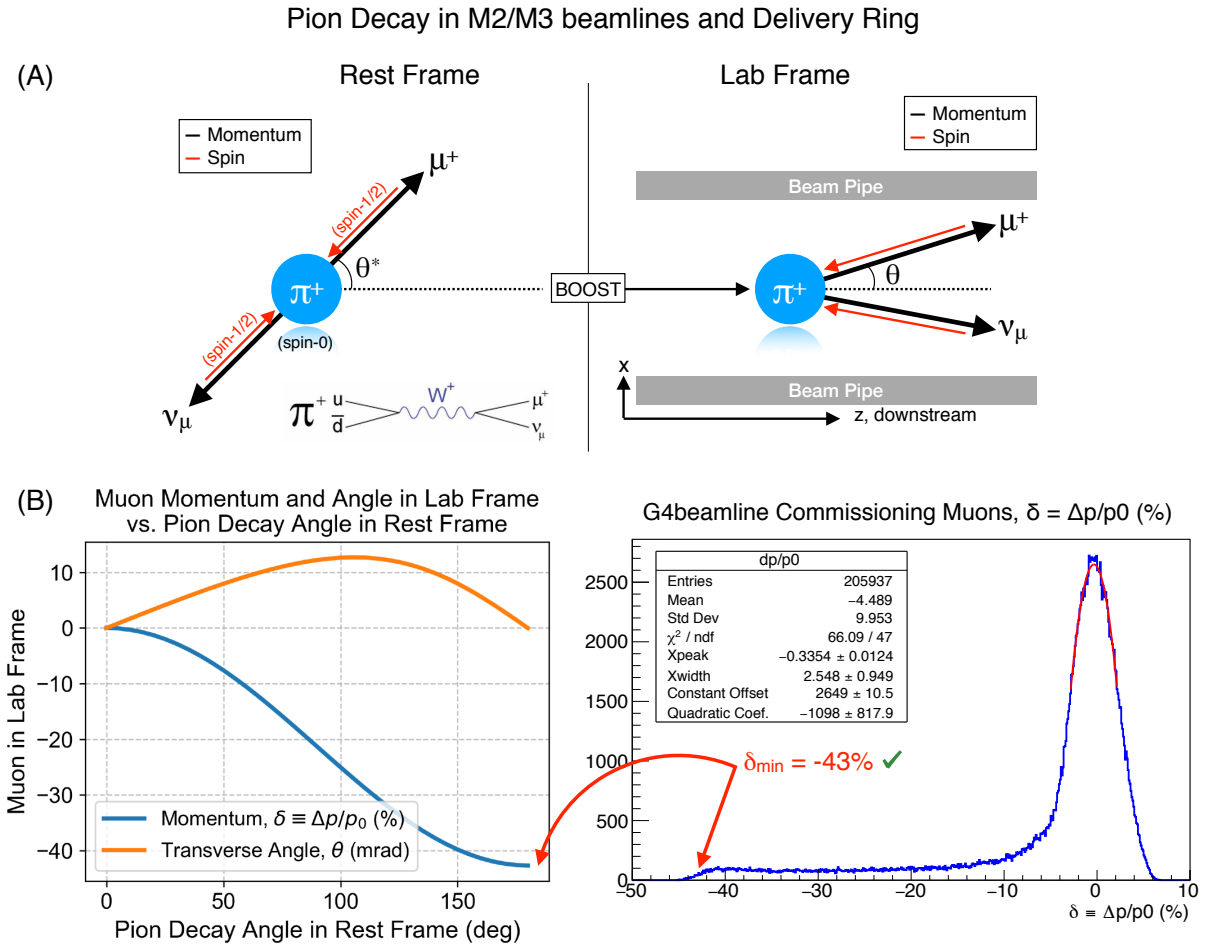

Figure 2.5: *Pion decay in M2/M3 beamlines and Delivery Ring. (A) Pion decay in rest frame (left) and lab frame (right). (B) Muon momentum and transverse angle in lab frame as a function of decay angle in pion rest frame, calculation (left) vs. simulation (right). The Muon-Campus beamlines are designed to transport* $|\delta \equiv (p - p_0)/p_0| \lesssim 2\%$ *downstream, where* $p_0 = 3.1\,\mathrm{GeV}/c$ *is the design momentum, i.e. backward-decay muons do not survive. The ensemble longitudinal polarization of the muon beam delivered to the experiment is therefore largely negative,* $(\hat{\mathbf{s}} \cdot \hat{\mathbf{p}}) < 0$*, as a result of parity violation in the weak decay of the spinless pion,* $\pi^+ \to \nu_\mu \mu^+$.

and extraction to M4/M5 both occurring in the same straight section (D30). After 4 turns around the DR, protons lag muons sufficiently and the protons may be cleanly removed via kickers in the Abort/Proton Removal line. Muons are then extracted and delivered to the experiment via the M4/M5 beamlines.

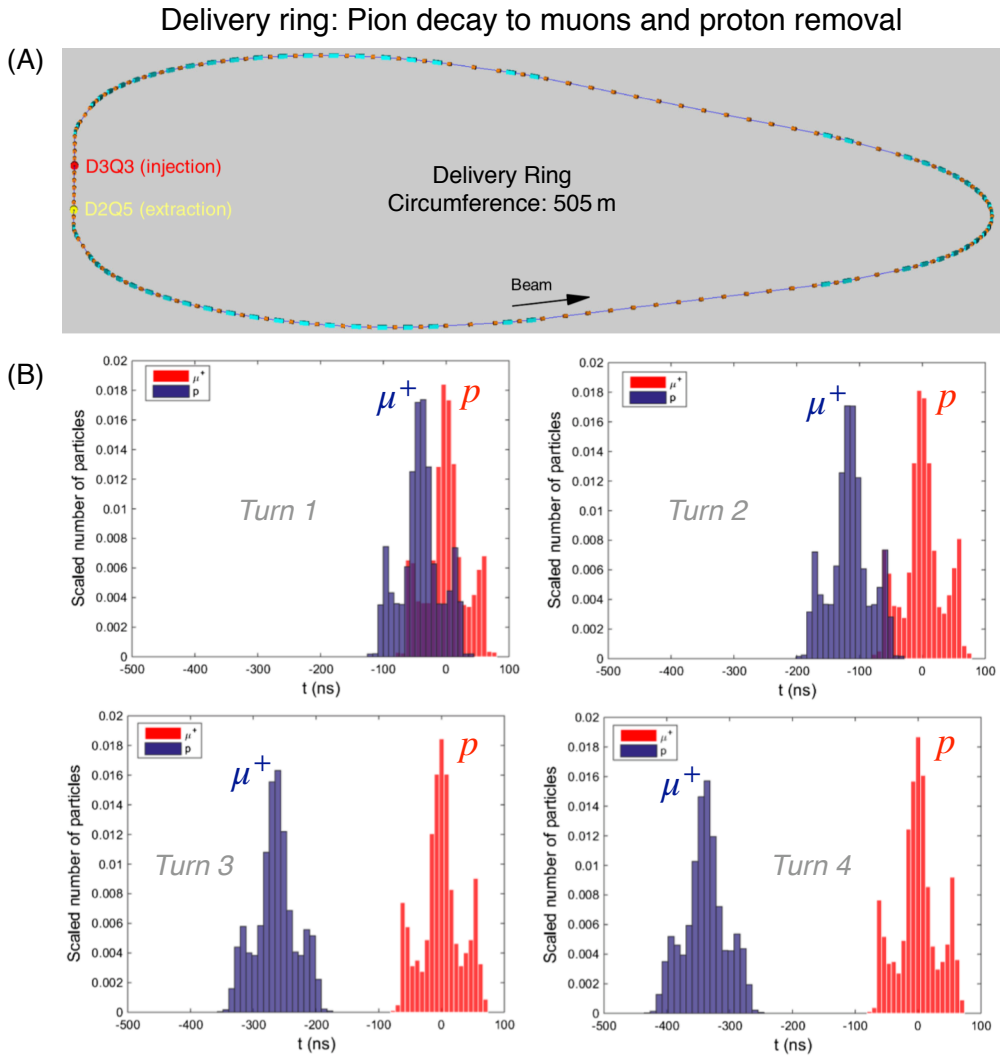

Figure 2.6: *(A) Delivery Ring geometry, and (B) time-of-flight separation of muons from protons [28]. The protons are kicked into a beam dump on the 4th turn, whereas the muons are kicked into a Lambertson magnet and extracted vertically to the muon g−2 experiment.*

2.1.6 M4/M5 Beamlines: Muon Transport to $g-2$ Experiment

The purpose of the M4/M5 line is to transport the muon beam from the DR to the muon $g-2$ experiment. The geometry and lattice functions of the M4/M5 beamline are shown in Fig. 2.7. Extraction from the DR begins with an inward horizontal kick into the field region of a special septum magnet (Lambertson), which marks the beginning of the 10.2 ft vertical climb from the DR to the plane of the muon $g-2$ storage ring. The vertical climb involves 7 magnets total: the DR extraction Lambertson mentioned above, quadrupole steering from a large-aperture quad (DQ25), a C-magnet (ECMAG), a downward leveling bend (EDWA), two upward bends (MDCs), and a final downward bend (CDC). The first stage of the vertical climb (up to and including the EDWA) is 4 ft in total elevation gain and carries the beam into the plane of the Mu2e experiment's M4 beamline. The M4 beamline is shared by the Mu2e and $g-2$ experiments for $\sim$30 m. The second stage of the vertical climb elevates the beam 6.2-ft from the plane of M4 to M5 and the $(g-2)_\mu$ experiment. Both vertical-bend sections are designed to be achromatic and can be independently tuned to meet the needs of the two experiments.

Immediately downstream of the vertial-achromat section is a strong horizontal triple-bend achromat (TBA) that produces a 27.1° bend to the beam-left. This large bending angle was required to meet the rigid constraint of the location of MC-1. The horizontal-bend section is $\sim$14 m in length, and consists of three MDC dipoles wired in series to produce 1/3 of the total 27° bend each. A short three-quad matching section then carries the beam into a FODO transport section with 90° phase advance per cell. At last the beam arrives at the M5 Final Focus immediately upstream of the $g-2$ storage ring. The M5 Final Focus is essentially half of a low-beta insertion [29, 27] and is discussed in more detail below along with the superconducting inflector magnet. The expected muon distribution at the end of the M5 beamline $\sim$30 cm upstream of the $g-2$ storage ring is shown in Fig. 2.8. Approximately 1×10^{-7} μ^+ per proton on target (POT) are delivered to the experiment within the momentum acceptance of the muon $g-2$ storage ring, $|\delta \equiv \Delta p/p_0| \lesssim 0.5\%$ [28]. The Courant-Snyder parameters $(\alpha, \beta)_{x,y}$ and dispersion $(\eta, \eta')_{x,y}$ of the transverse phase-space (x, x', y, y') shown in Fig. 2.8 are tunable using the magnetic quadrupoles in the M5 Final Focus. The eigenvectors and eigenvalues of the correlation matrix of the expected muon distribution at the end of the M5 beamline are shown in Fig. 2.9.

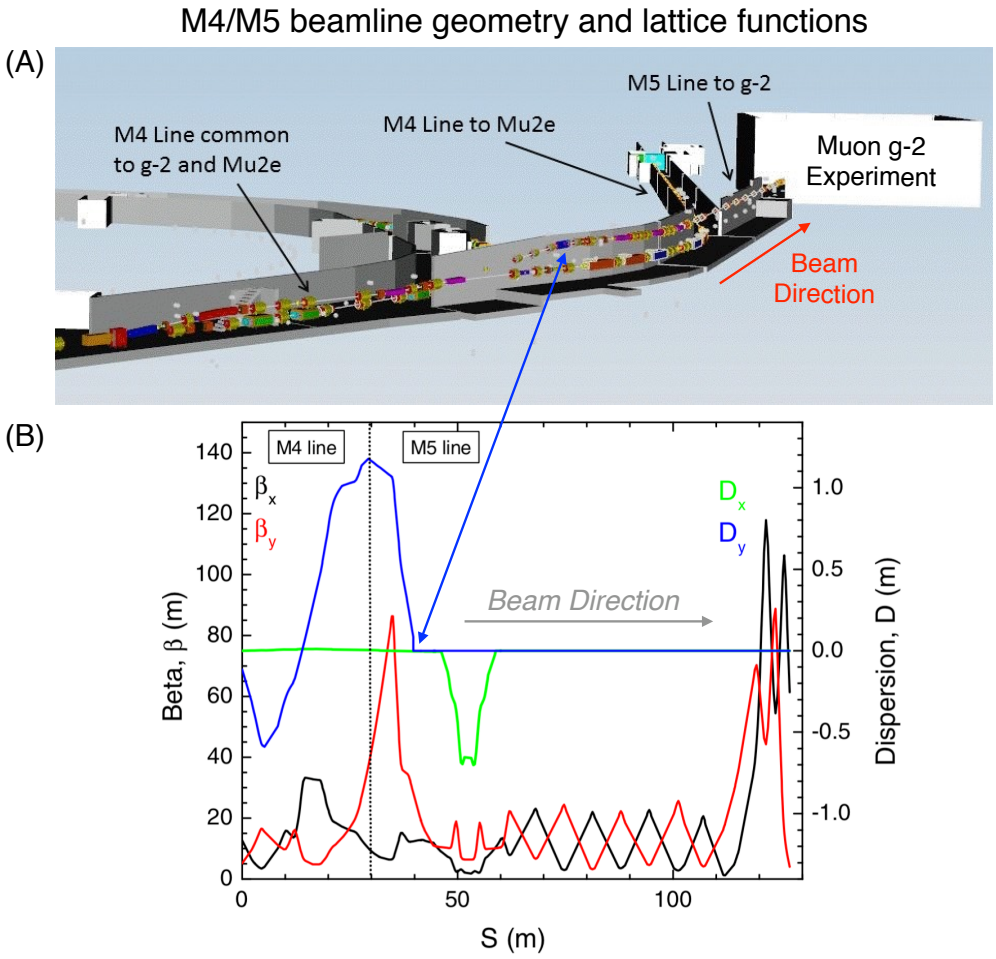

Figure 2.7: *M4/M5 beamline geometry and lattice functions. (A) The extraction of beam from the Delivery Ring (left) into the M5 line is vertical and occurs in two stages: The first vertical climb is about 4 ft into the M4/M5 beamline, which is common to both the muon $g-2$ and Mu2e experiments, while the second elevation gain is about 6.2 ft (10.2 ft total). The M5 beamline then continues 100 m downstream to the muon $g-2$ experimental hall, MC-1 (right). (B) Nominal lattice functions simulated with MAD-X.*

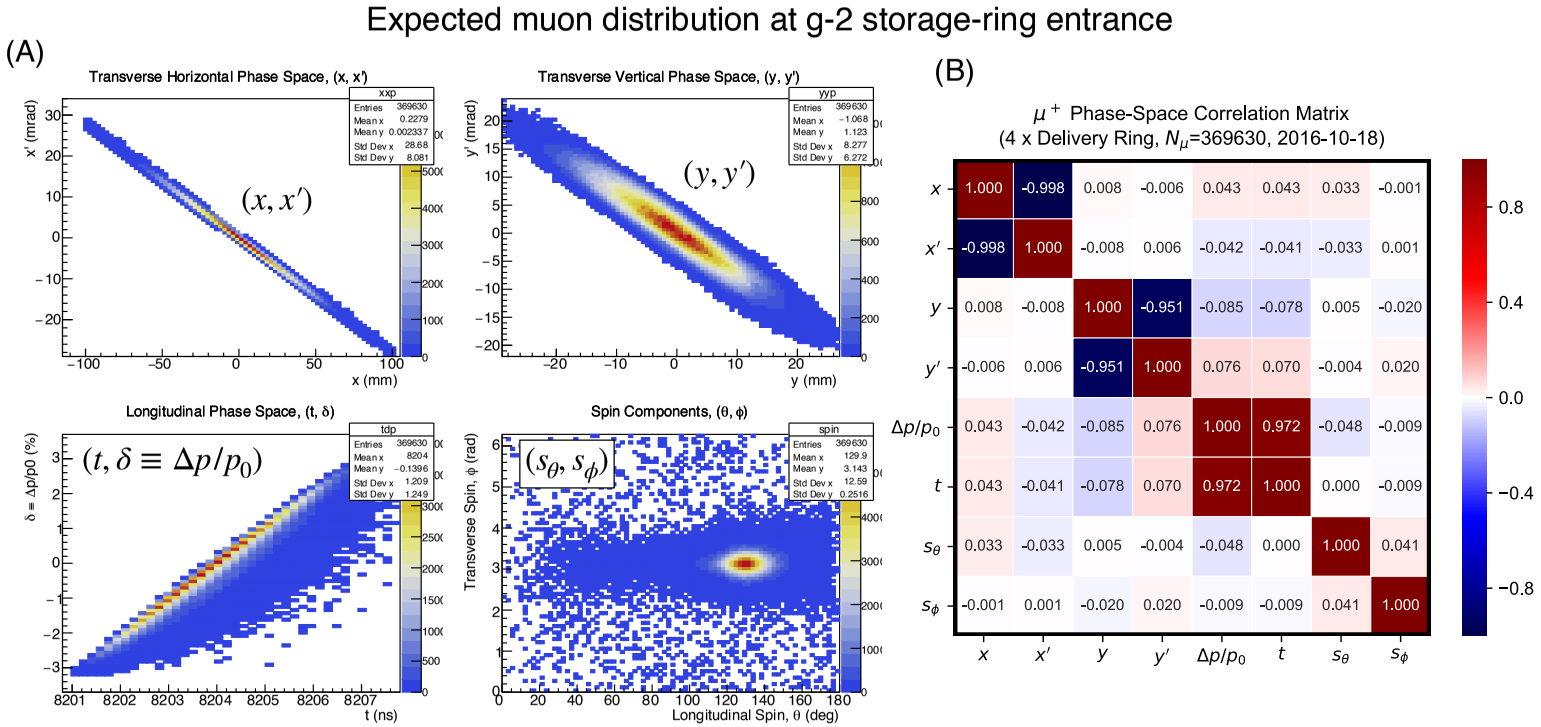

Figure 2.8: *Expected muon distribution at g–2 storage-ring entrance. (A) Phase-space distribution from a G4beamline simulation [30]. (B) Correlation matrix of G4beamline muons. The upper-left* 2×2 *sub-block* (x, x')*, for example, is clearly a sub-space of the eight-dimensional phase space* $\{\{x, x', y, y', t, \delta, s_\theta, s_\phi\}_i : i \in \text{particles}\}$*. Only weak correlations of* $(t, \delta \equiv \Delta p/p_0)$ *with other coordinates are observed. The eigenvalues and eigenvectors of the matrix (B) are shown in Fig. 2.9.*

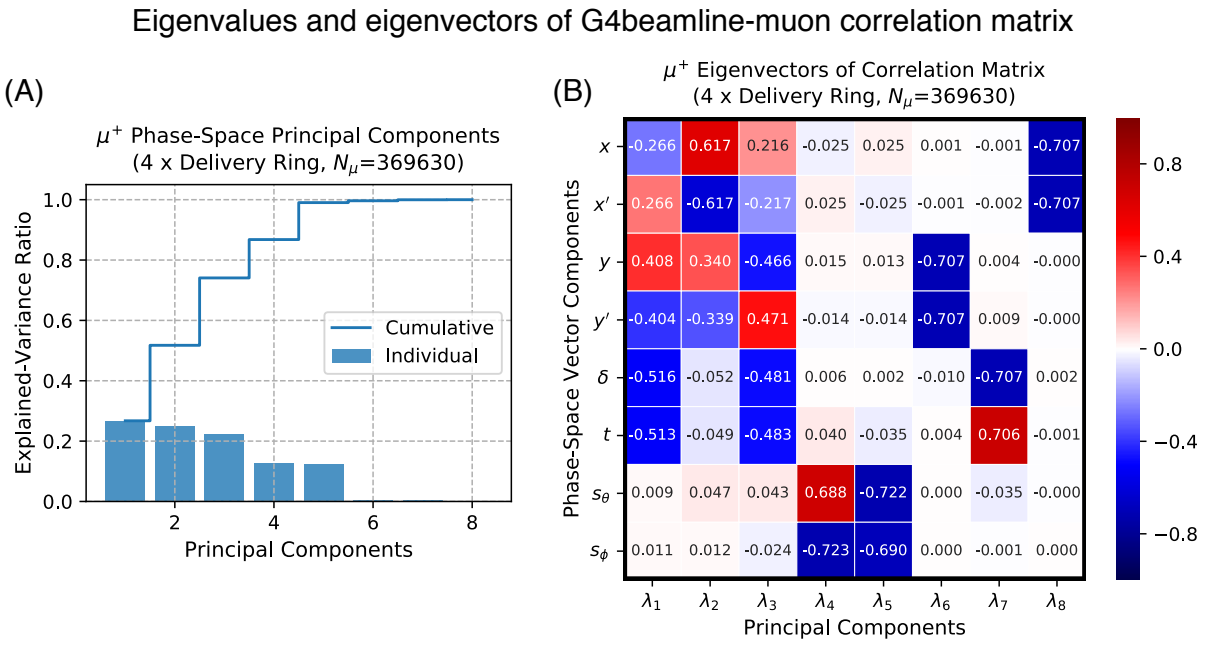

Figure 2.9: *Eigenvalues and eigenvectors of G4beamline-muon correlation matrix (Fig. 2.8). (A) Eigenvalues of G4beamline-muon correlation matrix, arranged in descending order and normalized so their sum totals unity. Larger eigenvalues contribute more to the spread of the data, $\lambda_i \sim \sigma_i^2$, hence the title "principal components" (horizontal axis) and "explained variance" (vertical axis). (B) Eigenvectors corresponding to the eigenvalues λ_i shown in (A). Here, the first three eigenvectors for $\lambda_{1,2,3}$ involve only the phase-space coordinates $(x, x', y, y', t, \delta)$ and not spin (s_θ, s_ϕ). Contrariwise, the eigenvectors corresponding to eigenvalues $\lambda_{4,5}$ involve spin, but not phase-space. The three remaining eigenvectors corresponding to $\lambda_{6,7,8}$ are essentially irrelevant, as evidenced by their very small eigenvalues shown in (A). The 5 meaningful eigenvectors could be used, for example, to construct a projection matrix that reduces the size of the phase space from $8 \times N_\mu$ to $5 \times N_\mu$, if memory/computational costs were an issue.*

2.2 The Muon $g-2$ Experiment

2.2.1 Storage Ring Magnet

As mentioned in Chapter 1, measuring a_μ to 140 ppb precision requires measuring the anomalous precession angular frequency $\boldsymbol{\omega}_a$ in a precisely-known magnetic field. In the limit of uniform circular motion in the horizontal midplane, the anomalous precession angular frequency is given by the difference of the cyclotron and spin precession angular frequencies,

$$\boldsymbol{\omega}_a \equiv \boldsymbol{\omega}_s - \boldsymbol{\omega}_c \approx -\frac{e}{m}\left[a_\mu \mathbf{B} - a_\mu \left(\frac{\gamma}{\gamma+1}\right)(\boldsymbol{\beta}\cdot\mathbf{B})\,\boldsymbol{\beta} - \left(a_\mu - \frac{1}{\gamma^2-1}\right)\frac{\boldsymbol{\beta}\times\mathbf{E}}{c}\right], \tag{2.4}$$

where $\boldsymbol{\omega}_c$ is the cyclotron angular frequency, $\boldsymbol{\omega}_s$ is the spin-precession angular frequency, a_μ is the muon anomalous magnetic moment, $\boldsymbol{\beta}$ is the velocity, and $\{\mathbf{E}, \mathbf{B}\}$ are the electric and magnetic fields in the lab frame. The experiment is designed around the "magic" momentum $p_0 = 3.094\,\mathrm{GeV}/c$, corresponding to a Lorentz $\gamma = 29.303$, which causes the coefficient of the $\boldsymbol{\beta}\times\mathbf{E}$ term in Eq. (2.4) to vanish. The physical object that provides the uniform vertical magnetic field experienced by the circulating muons is the storage ring shown in Fig. 2.10. Several parameters of the muon $g-2$ storage ring are shown in Table 2.2.

Table 2.2: *Physical Parameters of the E821/E989 Muon $g-2$ Storage Ring*

Parameter	Value
Iron Mass	682 metric tons
Muon equilibrium orbit radius	280.0 inches (7.112 m)
Design momentum	3.0944 GeV/c
Design magnetic field	1.4513 T
Design current	5200 A
Stored energy	6.1 MJ
Yoke width	139 cm
Pole Width	56 cm
Pole Gap	18 cm
Muon storage region diameter	9 cm

One noteworthy feature of the muon $g-2$ storage ring is it was originally built and used for the previous measurement at Brookhaven (E821), disassembled piece by piece, and

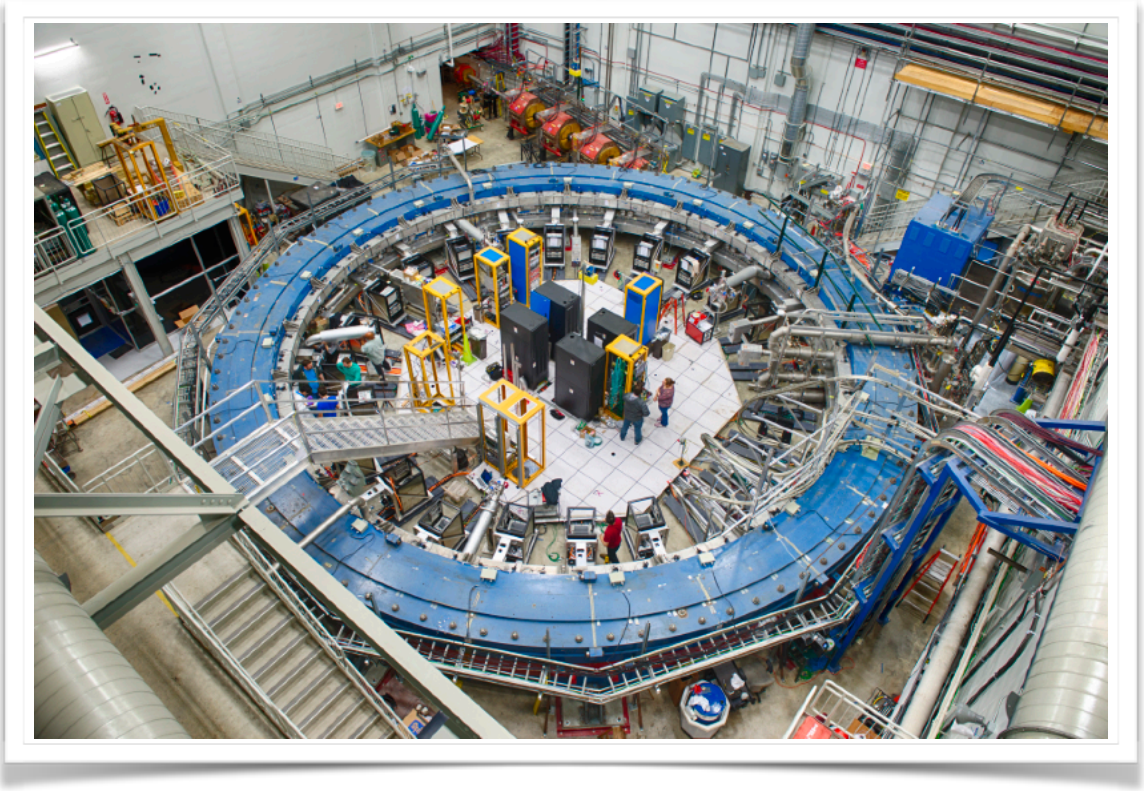

Figure 2.10: *The muon $g-2$ storage ring installed at Fermilab about two months before the experiment's first commissioning run in the summer of 2017. The muon beam enters the building (MC-1) via the beamline shown near the top of the page in red. The steel of the muon storage ring is painted blue. The superconducting C-magnet is open toward the center so positrons from muon decay ($\mu^+ \to \bar{\nu}_\mu \nu_e e^+$) can be observed by 24 calorimeters spread uniformly over ring azimuth. At the center of the ring are four large power supplies (black) to power the four electric quadrupoles that weakly focus the muon beam vertically in order to prevent the beam from diverging out of the ring. The design parameters of the muon $g-2$ storage ring are $p_0 = 3.094\,\mathrm{GeV}/c$ and $\rho_0 = 280.0\,\mathrm{inch} = 7112\,\mathrm{mm}$, from which it follows that $B_0 = 1.4513\,\mathrm{T}$. More parameters may be found in Table 2.2.*

shipped from New York to Chicago for the new experiment at Fermilab (E989).[4] Almost all components inside the storage ring have been upgraded, however, the main magnet itself is essentially unchanged. Aside from saving millions of dollars and years of development, one reason for re-using BNL's storage ring is any new magnet would have used exactly the same design momentum ($p_0 = 3.094\,\mathrm{GeV}/c$) at which the $\boldsymbol{\beta} \times \mathbf{E}$ term in Eq. (2.4) vanishes. Moreover, any new magnet almost certainly been made of iron, and Brookhaven already took great care to minimize the overall material cost of the magnet (driven by the iron yoke) while operating in a safe region of the $\mathbf{B} \simeq \mu\mathbf{H}$ curve. Finally, the Brookhaven muon $g-2$ storage ring boasts an extremely tunable "shim kit" which can be used to precisely manipulate the magnetic field experienced by the muons in the storage region, so the design is already highly optimized [31]. For the reasons listed above and others, the decision was made to re-use Brookhaven's muon storage ring for the new muon $g-2$ experiment at Fermilab.

A cross section of the muon storage ring is shown in Fig. 2.11. The geometry of the C-magnet iron causes the magnetic flux lines to circulate in such a way that gives rise to a very uniform dipole **B**-field between the pole tips where muons are stored. The magnet iron is excited by superconducting currents at four transverse locations in order to dramatically increase the field strength in the muon storage region to the nominal value of

$$B_0 \equiv \frac{p_0}{eR_0} = 1.4513\,\mathrm{T}, \tag{2.5}$$

where $p_0 = 3.0944\,\mathrm{GeV}/c$ is the design momentum and $\rho_0 = 280.0\,\mathrm{inch} = 7112\,\mathrm{mm}$ was Brookhaven's design choice inherited by Fermilab. Due to its size and weight (50-foot diameter, 680 metric tons), the C-magnet is built from many smaller pieces, some of which allow the magnetic field between the pole tips to be tuned or "shimmed" essentially multipole by multipole. The shape of the C-magnet is open toward the ring center in order to allow for decay positrons from $\mu^+ \to \bar{\nu}_\mu \nu_e e^+$ to be observed toward the ring center.

The magnetic field experienced by the orbiting muons in the storage region is extensively mapped using 17 pulsed-proton nuclear magnetic resonance (NMR) probes mounted on a "trolley" that drives around the storage ring and samples the ring **B**-field at a few thousand azimuthal locations.[5] The NMR trolley is shown in Fig. 2.12 as well as a representative

[4] The author of this thesis helped with this process (BNL, May 2012, removal of all wedge shims).

[5] This process requires the muon beam to be off.

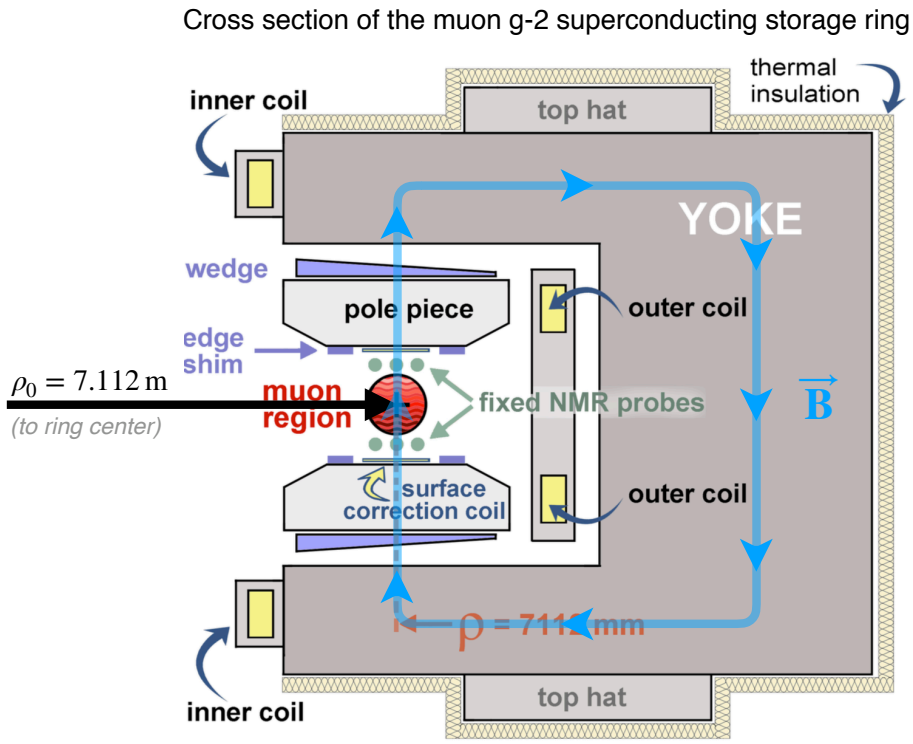

Figure 2.11: *Cross section of muon $g-2$ storage ring and magnetic field. The C-shaped magnet iron guides the magnetic flux (light blue) to a uniform dipole field in the muon storage region between the pole tips (red). The iron is excited by four superconducting coils (yellow). As shown, the current in the outer coils flow into the page, while the current in the inner coils flows out of the page, so the orientation of the* **B***-field points vertically upward for μ^+ storage. The muon momentum is out of the page and the ring center is toward the left. The "top hats," "wedge shims," "edge shims," and other components of the shim kit allow the field in the muon storage region to be fine-tuned essentially multipole by multipole.*

azimuthally-averaged multipole expansion of the ring magnetic field from E821. The contours of the average transverse magnetic field experienced by the muons are typically well below one part per million. Additionally, a set of 378 fixed NMR probes placed above and below the muon storage region (Fig. 2.11) continuously monitor the ring magnetic field during data taking in order to reconstruct **B**-field drift between trolley runs.[6] The various NMR probes are calibrated with respect to a *single* absolute probe that was also used to calibrate the field in a muonium microwave experiment performed at Los Alamos National Laboratory [32]. Finally, a "plunging probe" exists to transfer calibration data from the absolute probe to the trolley probes used to actually measure the **B**-field experienced by the circulating muons. The convolution of the muon beam with respect to the magnetic field is ultimately what is used to extract a_μ. This process will be discussed in more detail in §2.2.7.

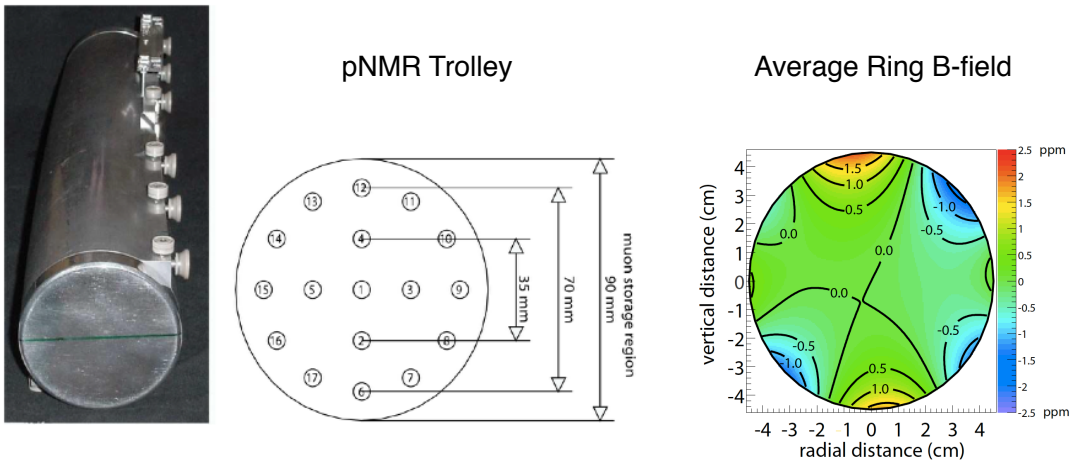

Figure 2.12: *The 50-cm long NMR Trolley (left) drives around the muon storage region and samples the magnetic field experienced by the muons, from which a multipole expansion is constructed (right). The azimuthal average of the magnetic field is then convolved with the muon beam distribution as one step in determining the anomalous magnetic moment of the muon, a_μ. The multipoles shown are an example from E821, where $|\delta B_0/B_0|_{\max} \lesssim 1\,\text{ppm}$ has already been achieved in E989 at the boundary of the muon storage region, $r_0 = 45\,\text{mm}$.*

[6] The trolley and fixed probes are identical, and the University of Washington played a prominent role in their fabrication.

2.2.2 Superconducting Inflector Magnet

Beam exits the M5 line and enters the muon storage ring via a 4-inch hole bored through the backleg yoke of the C-magnet iron, as shown in Fig. 2.13. A special superconducting septum magnet known as the "inflector" facilitates injection of the muon beam into the storage ring by canceling the main dipole field of the ring and providing a field-free channel through which the injected beam passes, as shown in Fig. 2.14. The novel truncated-double-cosine-theta geometry of the discrete superconducting currents largely traps the return magnetic flux, and a superconducting shield further prevents any remnant field from disturbing the high-precision dipole magnetic field in the muon storage region [33, 34, 35]. In this way, strict geometrical and field-uniformity constraints are satisfied, and the muon beam is injected as close as possible to the nominal storage-orbit radius, $\rho_0 = 7112\,\text{mm}$. Several other important physical parameters of the superconducting magnetic inflector system are shown in Table 2.3. The refurbished E821 inflector is the base design for E989. The author of this thesis played a significant role in the design of a new superconducting inflector, discussed in detail in (§3.4.5).

Table 2.3: *Physical Parameters of the E821/E989 Superconducting Inflector Magnet*

Parameter	**Value**
Magnetic length	1.7 m
Beam channel	$18(\text{W}) \times 56(\text{H})$ mm^2
Dipole field in beam channel	1.5 T (@2850 A)
Conductor transverse dimensions	2×3 mm^2
Number of turns	88
Conductor volume (NbTi : Cu : Al)	1 : 0.9 : 3.7
NbTi/Cu composite diameter	1.6 mm
Cold mass	60 kg
Stored energy	9 kJ

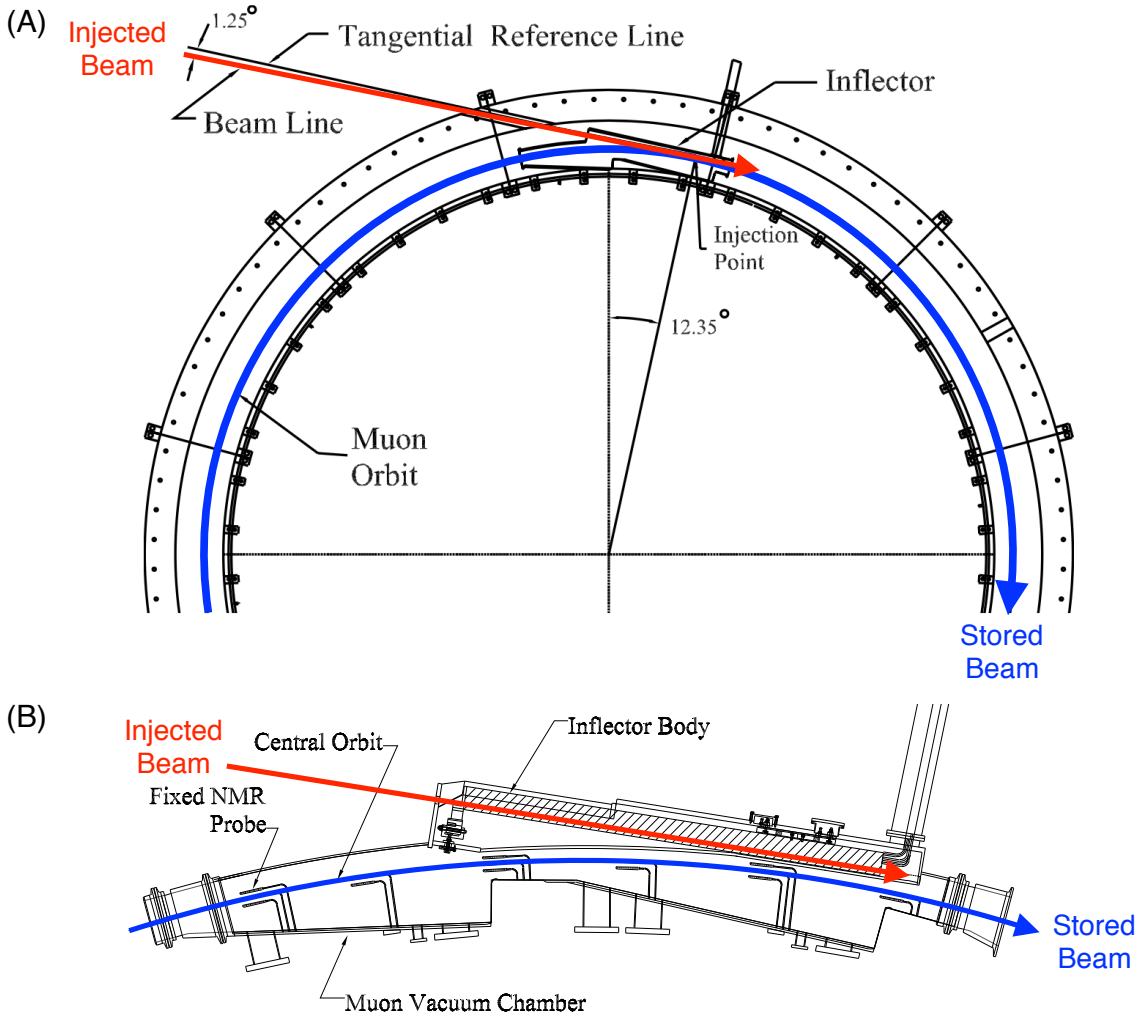

Figure 2.13: *(A) Beam enters the muon storage ring through a 4-inch hole in the backleg yoke of the C-magnet iron and proceeds to the 1.7-m long superconducting inflector magnet. The inflector magnet is designed to cancel the main ring field and provide a field-free corridor through which the injected beam enters the ring. The cancellation is not perfect, however, and the muon beam is injected at a* 1.25° *offset to compensate. (B) The injected beam is displaced* 77 mm *radially outward from the storage-orbit design radius* $\rho_0 = 7112$ mm*. The beam then proceeds* 90° *downstream which it is kicked onto the proper storage orbit (blue).*

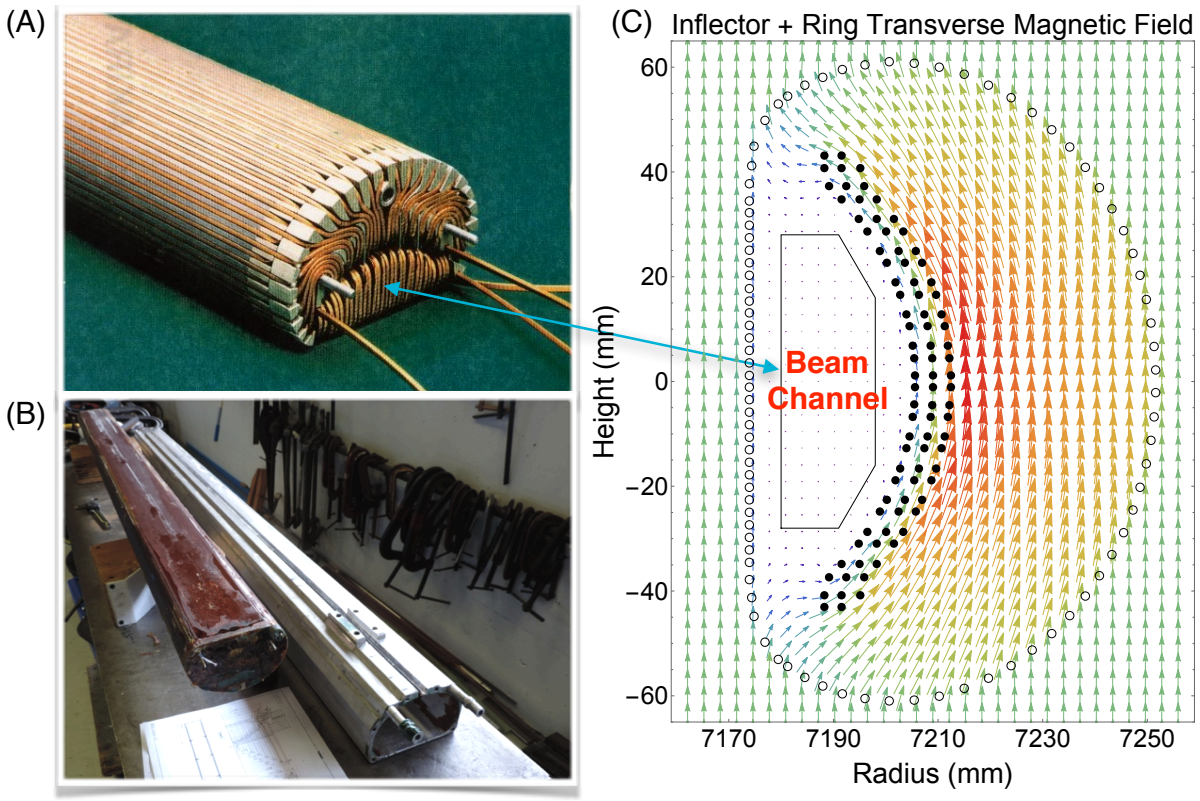

Figure 2.14: *(A) Superconducting coil geometry of the 1.7-meter long inflector magnet. (B) Inflector coils and superconducting shield being prepared for recommissioning at Fermilab. (C) Vector sum of inflector and storage-ring magnetic fields. The small, solid black circles are discrete superconducting currents flowing toward the reader, while the open circles are currents flowing away from the reader. The currents are arranged in a novel truncated-double-cosine-theta geometry giving rise to a dipole magnetic field that cancels the dipole magnetic field of the ring. The superposition creates a field-free region through which the injected beam enters the ring as close as possible to the design radius* $\rho_0 = 7112\,\mathrm{mm}$ *while not disturbing the dipole magnetic field in the muon storage region. The currents cover the beam channel at the upstream and downstream ends of the inflector.*

2.2.3 Fast Kicker Magnets

Beam exits the inflector and enters the high-precision magnetic field of the muon storage ring displaced 77 mm radially outward from the design radius, $\rho = \rho_0 + x = (7112 + 77)\,\text{mm}$, where $x \equiv \delta\rho$ is a convenient shorthand. Even at the larger injection radius, the uniform vertical magnetic field of the ring still causes the beam to orbit in a horizontal circle, however, the injection orbit is not concentric with the storage orbit, as shown in Fig. 2.15(A). Thus the beam must be "kicked" onto the proper storage orbit within the first turn, otherwise the beam will orbit back to the inflector, strike the body of the inflector/cryostat, and ultimately be lost. Although Fig. 2.15(A) suggest two kicker azimuthal locations are possible (90° and 270°), only the 90° location is realistic since significant beam losses would occur in the region near 180°.[7] The nominal outward radial kick of $\Delta x' \approx 77\,\text{mm}/7112\,\text{mm} = 10.8\,\text{mrad}$ is supplied by 3 pulsed electromagnets located at approximately 90° horizontal betatron phase advance downstream of the inflector exit. The ideal kicker magnetic field is a perfectly uniform vertical dipole field oriented in the opposite direction of the ring magnetic field. The ideal kicker waveform is a square pulse of full width exactly equal to the cyclotron period of the circulating muons, $T_c = 150\,\text{ns}$. The kicker cannot be made of any permanently magnetic material, otherwise the field uniformity of the main magnet would be affected in a negative way. Therefore, the kickers must be pulsed electromagnetic devices.

The magnetic-field profile generated by the curved kicker plates is shown in Fig. 2.15(B), while the temporal structure of a kicker pulse is shown in Fig. 2.15(C). The design of the electrodes and circuit will be discussed more completely in §3.4.2 and §4.4. The field strength of the kickers required to achieve the nominal $\Delta x' = 10.8\,\text{mrad}$ outward radial kick may be calculated from the Lorentz force,

$$\frac{dx'}{ds} \approx -\frac{1}{B\rho}\left(B_y + x\partial_x B_y + \tfrac{1}{2}x^2\partial_x^2 B_y + \cdots\right), \tag{2.6}$$

where $s \equiv \rho\theta$ is the longitudinal distance, $B\rho = 10.3216\,\text{T m}$ is the magnetic rigidity of the design trajectory, and the vertical component of the kicker field has been expanded in a Taylor series in the horizontal midplane about the center of the muon storage region, where

[7] The inner quadrupole electrodes are at $x = -50\,\text{mm}$, for example, whereas the beam exiting the inflector must pass through $x \approx -77\,\text{mm}$ near 180° if the kickers were located at ring azimuth 270°. Since $-77\,\text{mm} < -50\,\text{mm}$, a significant fraction of the beam would hit the inner quad electrodes and ultimately be lost.

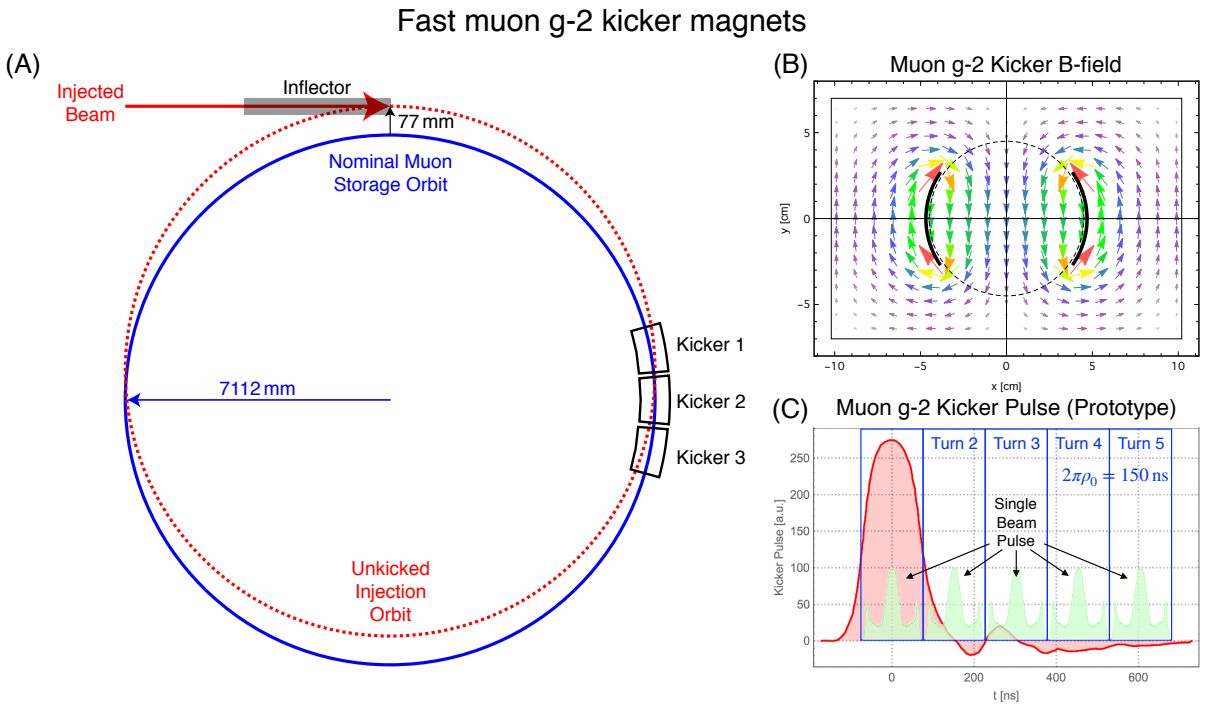

Figure 2.15: *(A) Cartoon demonstrating the need for pulsed kicker magnets in the muon g–2 storage ring. If no kickers were present, the injected beam would orbit back to the inflector after one turn (red circle), slam into the body of the inflector/cryostat, and ultimately be lost. The injected beam crosses the storage orbit (blue circle) at ∼90° downstream of the inflector exit, so the kickers must supply an outward radial kick of* $\Delta x' \approx 77\,\text{mm}/7112\,\text{mm} = 10.8\,\text{mrad}$ *to place the injected beam onto the proper storage orbit. (B) Kicker transverse magnetic field profile (§3.4.2). The circular kicker electrodes (solid black lines) are loosely based on a cosine-theta current distribution which produces a nearly uniform dipole magnetic field that momentarily opposes the field of the main magnet. (C) Prototype kicker pulse shape (red) measured at Cornell University circa 2015. The blue boxes are the revolution period,* $T_{rev} = 149\,\text{ns}$*. Ideally the kickers would supply the required kick on the first turn only, otherwise the single beam pulse (green) will be kicked repeatedly on subsequent turns leading to undesirable coherent oscillations of the mean radial position and ultimately beam losses and poor stored-beam quality (§4.4).*

again $x \equiv \delta\rho$ is a convenient shorthand.[8] Integrating Eq. (2.6) assuming a uniform dipole kicker pulse that exactly overlaps the injected beam pulse and using the fact that the three E989 kickers span $3 \times 1.27\,\mathrm{m}$ total gives

$$\int B_y \, d\ell \approx -(\Delta x')B\rho = -0.112\,\mathrm{T\,m} \quad \Rightarrow \quad \langle B_y \rangle_{\mathrm{kicker}} \approx -290\,\mathrm{G}. \tag{2.7}$$

In reality, the sextupole and higher multipoles lead to an increased magnetic field strength near the kicker electrodes relative to the center of the muon storage region, as shown in Fig. 2.15(B, green), so a better approximation is

$$\boxed{|B_{y0}|_{\mathrm{kicker}} \lesssim 290\,\mathrm{G}}, \tag{2.8}$$

where the subscript "0" emphasizes the kicker magnetic field value is taken at the center of the muon storage region. The optimal kicker strength for a realistic distribution of particles and the details of the kicker pulse generated by the tri-axial Blumlein circuit [26] will be discussed in more detail in Ch. 3 & 4. However, the above discussion provides the conceptual overview of the need for pulsed kicker electromagnets in the muon $g-2$ storage ring, which are required to place the injected beam onto the proper storage orbit.

2.2.4 Vertically Focusing Electric Quadrupoles

Once the muon beam has been kicked onto the proper orbit (§2.2.3), the circulating beam travels on a nearly perfect circle in the horizontal midplane as a result of the extremely uniform vertical magnetic field in the storage region ($B_{y0} = 1.4513\,\mathrm{T}, r_0 = 45\,\mathrm{mm}$). The beam is prevented from diverging out of the storage ring using vertically focusing quadrupoles, as shown in Fig. 2.16. The quadrupoles are electric so as not to spoil the high-precision dipole magnetic field of the storage ring. The four quadrupole electrodes are located at $\{\Delta x, \Delta y\} = \{\pm 50, \pm 50\}$mm relative to the design radius $\rho_0 = 7112\,\mathrm{mm}$ and are nominally charged to $\Delta V_{\{x,y\}} = \{-20.2, +20.2\}$kV relative to ground in order to achieve vertical focusing for positive muons. Since the circumference of the ring is $2\pi\rho_0 \simeq 45\,\mathrm{m}$, a particle with a vertical divergence of only $|y'| \approx 50\,\mathrm{mm}/45\,\mathrm{m} \simeq 1.1\,\mathrm{mrad}$ would strike a quad electrode and be lost

[8] In the horizontal midplane, the radial component of the kicker field vanishes by symmetry ($B_x = 0$), so the expansion Eq. (2.6) does not depend on the vertical coordinate (y).

after $\mathcal{O}(1)$ turns in the absence of vertical focusing. In the usual way [36, 29], the equations of motion for on-momentum muons can be derived from the Lorentz force, leading to the equations of motion for a simple harmonic oscillator,

$$\left[\frac{\partial^2}{\partial\theta^2} + Q_x^2\right] x = 0, \qquad \left[\frac{\partial^2}{\partial\theta^2} + Q_y^2\right] y = 0, \tag{2.9}$$

where $Q_x = \sqrt{1-n}$ and $Q_y = \sqrt{n}$ are the horizontal and vertical tunes, respectively, and

$$n \equiv \left(\frac{\rho_0}{v_0 B_0}\right) \frac{\partial E_x}{\partial x} \tag{2.10}$$

is the effective quadrupole field index (strength) for μ^+ storage. The solutions are sines and cosines. Here, the small gain in kinetic energy from the electric field, $\Delta E/E \simeq 20\,\text{kV}/3.1\,\text{GV} \sim 6.5 \times 10^{-6}$ has been ignored and the quads are assumed to uniformly span 360° of ring azimuth. In reality, space is required for the inflector (§2.2.2), kickers (§2.2.3), NMR trolley and garage (§2.2.1), and other components in the ring, so the quads only span 43.3% of ring azimuth as shown in Fig. 2.16(C). The four-fold symmetry helps minimize the beam "breathing," i.e. the variation of the beam width of the beam around the ring, and improves orbit stability. The quads are charged asymmetrically at injection in order to remove muons on the periphery of the storable phase space, as will be discussed in the next section (§2.2.5).

2.2.5 Beam Collimators

Knowledge of the magnetic field experienced by the circulating muons plays a critical role in the precise determination of a_μ. The purpose of the beam collimators is to define the spatial extent of the stored muon beam with respect to the high-precision magnetic field of the $g-2$ storage ring, as shown in Fig. 2.17. Since the collimators have an inner radius of $r_0 = 45\,\text{mm}$, the muon storage region is the interior region of a torus of major radius $\rho_0 = 7112\,\text{mm}$ and a minor radius $r_0 \leq 45\,\text{mm}$. Additionally, the collimators are used in conjunction with the vertically focusing electric quadrupoles (§2.2.4) to "clean up the beam" shortly after injection using a method called scraping. The scraping procedure involves charging the quad electrodes asymmetrically for ∼30 µs after injection in order to push the beam vertically down (on average) so muons near the periphery of the storable phase space

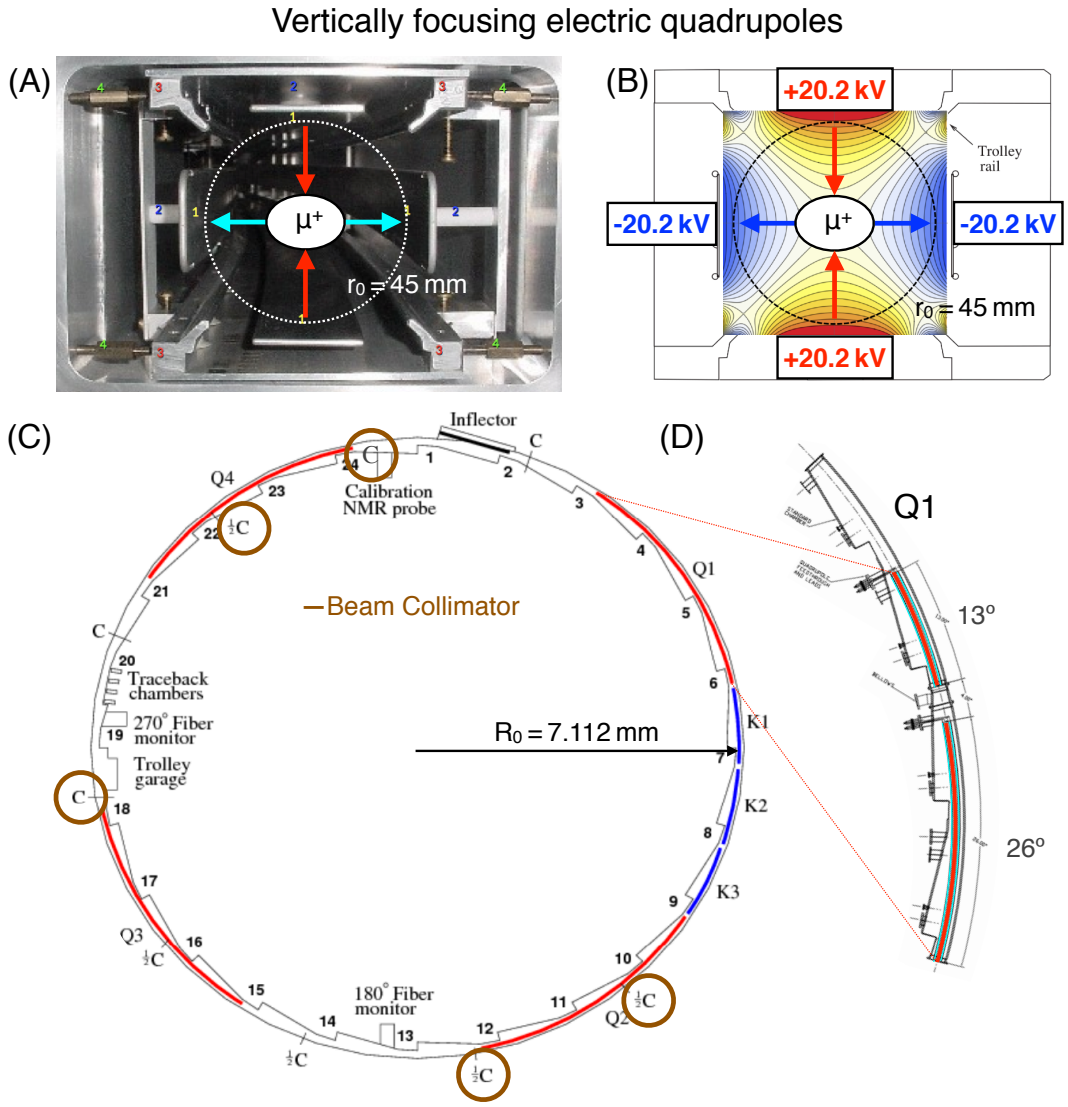

Figure 2.16: *Vertically focusing electric quadrupoles in the muon $g-2$ storage ring. (A) Transverse electrode geometry. The four quadrupole electrodes are separated by* 10 cm *and are* 47 mm *tall/wide. The rails on which the NMR trolley rides can be seen in the corners. (B) 28-pole multipole expansion of the electric potential used in simulations. The region exterior to the electrodes is handled by a field map. The nominal experimental run configuration has the top/bottom plates charged to* QHV = 20.2 kV*, while the inner/outer plates are charged to -QHV. (C) Azimuthal layout of the muon $g-2$ storage ring, where four quads (Q1-Q4) symmetrically span 43.3% of ring azimuth. (D) Each quad consists of a "short"* 13° *and a "long"* 26° *section in order to straddle the gap between vacuum chambers.*

strike a collimator and are ultimately lost. The motivation for scraping can be seen in the ideal decay-positron signal,

$$N_{\text{ideal}}(t) = N_0 \exp\left(-t/\gamma\tau_\mu\right)\left[1 + A\cos\left(\omega_a t - \phi_0\right)\right], \tag{2.11}$$

where N_0 is a normalization constant related to the number of injected muons at time $t = 0$. If the constant normalization term N_0 in Eq. (2.11) is actually changing throughout the fill, $N_0 \rightarrow N_0(t)$, the dominant effect is a phase shift in the argument of the cosine when fitting without taking this into consideration, which directly impacts the value of the anomalous precession frequency ω_a extracted from the measurement. This effect on the precision measurement of a_μ would be disastrous if unaccounted for, hence the motivation for scraping the beam against the collimators before the data-recording period. The author played a large role in the design of the new collimators, which are discussed more completely in §3.4.3.

2.2.6 $e^\pm$ Detectors

Finally, after the muon beam is injected into the $g-2$ storage ring (§2.2.2), kicked onto orbit (§2.2.3), and the vertically focusing electric quadrupoles (§2.2.4) scrape the beam against the collimators (§2.2.5), the formal data-recording period begins. Each data-recording period lasts ∼700 µs, which is also known as one "fill" of the ring.[9] Positrons emitted from the decay of stored muons ($\mu^+ \rightarrow \bar{\nu}_\mu \nu_e e^+$) curl inward toward the ring center where they are intercepted by 24 lead fluoride (PbF_2) Čerenkov detectors [37] spaced uniformly in ring azimuth, as shown in Fig. 2.19(A).

In the muon rest frame, the highest-energy decay positrons are emitted when the momenta of the neutrino pair are parallel, as shown in Fig. 2.19(B), leading to a maximum decay positron energy of $E_e^{\star(\max)} \simeq m_\mu/2 = 52.8\,\text{MeV}$. Additionally, the total angular momentum of the $\nu_e\bar{\nu}_\mu$ is zero when the neutrinos are emitted in the same direction (since massless leptons are left-handed in the weak interaction, while massless anti-leptons are right-handed), so the highest-energy decay positrons preferentially emerge in the direction of the muon spin in order to conserve angular momentum. The differential decay probability of the positrons

[9] The dilated muon lifetime in the lab frame is $\gamma\tau_\mu = 64.4\,\mu\text{s}$, so a data-recording period of ∼700 µs corresponds to about ten muon lifetimes, where $\exp(-700\,\mu\text{s}/64.4\,\mu\text{s}) = 1.9 \times 10^{-5}$.

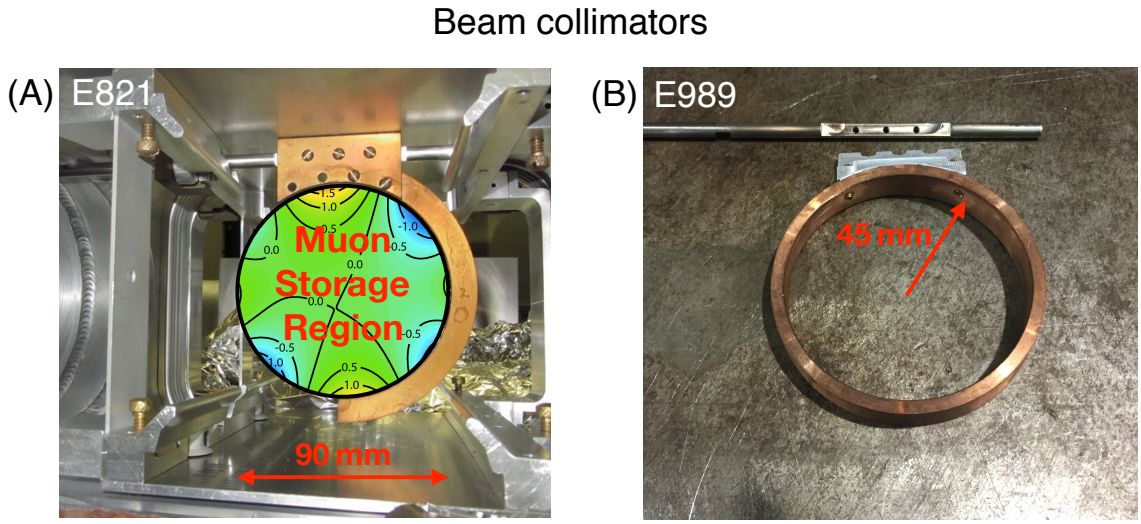

Figure 2.17: *(A) E821-style half collimator made of 3-mm thick copper. The missing material toward the left ($\rho < 7112\,\mathrm{mm}$) was the result of the E821 kickers being too weak to place the muon beam onto the proper storage orbit within the first turn after injection, Fig. 2.15(A). Several such collimators are placed around the ring in order to define the muon storage region, Fig. 2.16(C). The contours of the E821 azimuthally averaged magnetic field shown at the left are 0.5 ppm, and E989 will do about a factor of 2 better. (B) E989 collimator, designed by the author of this thesis in conjunction with Argonne and Brookhaven National Laboratories. The new collimators use a tapered "wedge" design in which the longitudinal thickness is proportional to the ring horizontal dispersion, which causes muons to be lost as rapidly as possible, as will be discussed more completely below in §3.4.3.*

emitted in the muon rest frame is given by [38, 22, 26]

$$dP^\star(y^\star,\theta^\star) \propto N^\star(y^\star)\Big(1 \pm A^\star(y^\star)\cos\theta^\star\Big)\,dy^\star\,d\Omega^\star, \tag{2.12}$$

where the starred quantities indicate the muon rest frame, $y^\star \equiv p_e^\star/p_e^{\star(\max)}$ is the momentum fraction of the electron, $d\Omega^\star \equiv d(\cos\theta^\star)\,d\phi^\star$ is the solid angle, $\theta^\star \equiv \cos^{-1}(\hat{\mathbf{p}}_e \cdot \hat{\mathbf{s}}_\mu)$ is the angle between the emitted positron and the muon spin, the "$\pm$" is for $\mu^\pm$ decay, and the number density $N^\star(y^\star)$ and asymmetry $A^\star(y^\star)$ are given by

$$N^\star(y^\star) = y^{\star 2}(3-2y^\star), \qquad A^\star(y^\star) = \frac{2y^\star-1}{3-2y^\star}, \tag{2.13}$$

which are shown in the muon rest frame and lab frame in Fig. 2.18. The important point is that since $g_\mu > 2$, i.e. $a_\mu > 0$, the muon spin vector rotates at a faster rate than the momentum vector (Eq. (2.4)), and implementing an energy threshold in the calorimeters allows the muon spin to be tracked as a function of time due to parity violation in the weak decay ultimately leading to the decay-positron spectrum shown in Fig. 2.19(C), also known as a "wiggle plot." The main purpose of the $e^\pm$ detectors is to extract the angular frequency of the muon anomalous spin precession, ω_a, which will be used in the next section to in combination with the magnetic field experienced by the circulating muons in order to extract the anomaly of the muon magnetic moment, a_μ.

2.2.7 Putting the Pieces Together: Precise Determination of a_μ

The experimental technique described above involves storing a highly polarized muon beam in a highly uniform magnetic field, for then the spin precession due to the muon anomalous magnetic moment is $\omega_a \simeq a_\mu(eB/m_\mu)$.[10] The lab-frame magnetic field is measured using proton nuclear magnetic resonance, as was discussed in §2.2.1, where $\omega_p = 2\mu_p B/\hbar$ is the precession angular frequency for a free proton (Larmor frequency),

$$\omega_a = a_\mu \frac{eB}{m_\mu} \qquad \Rightarrow \qquad a_\mu = \omega_a \frac{m_\mu}{eB} = \frac{\omega_a}{\omega_p}\frac{m_\mu}{e\hbar/2\mu_p}, \tag{2.14}$$

[10] In reality, corrections of order $\mathcal{O}(0.5\,\text{ppm})$ are applied to ω_a since the $(\boldsymbol{\beta}\times\mathbf{E})$ term in Eq. (2.4) is not strictly zero for all momenta stored in the muon $g-2$ ring.

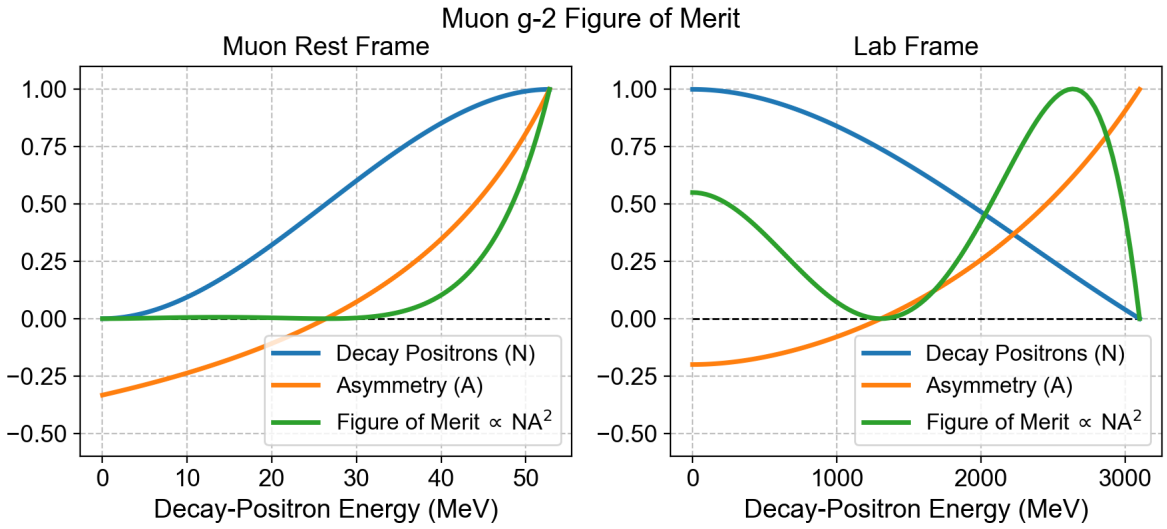

Figure 2.18: *Number of decay positrons per unit energy, N, value of the asymmetry, A, and relative figure of merit, NA^2 in the muon rest frame (left) and laboratory frame (right). The fractional statistical error on the anomalous angular precession frequency goes as $\delta\omega_a/\omega_a \sim 1/\sqrt{N}A$, so the uncertainty is minimized when $\sqrt{N}A \to NA^2$ is maximized. Integrating the lab curve (right) above a fixed threshold energy for all possible thresholds reveals an ideal energy threshold of $\sim$1.85 GeV maximizes the statistical power of the dataset [26].*

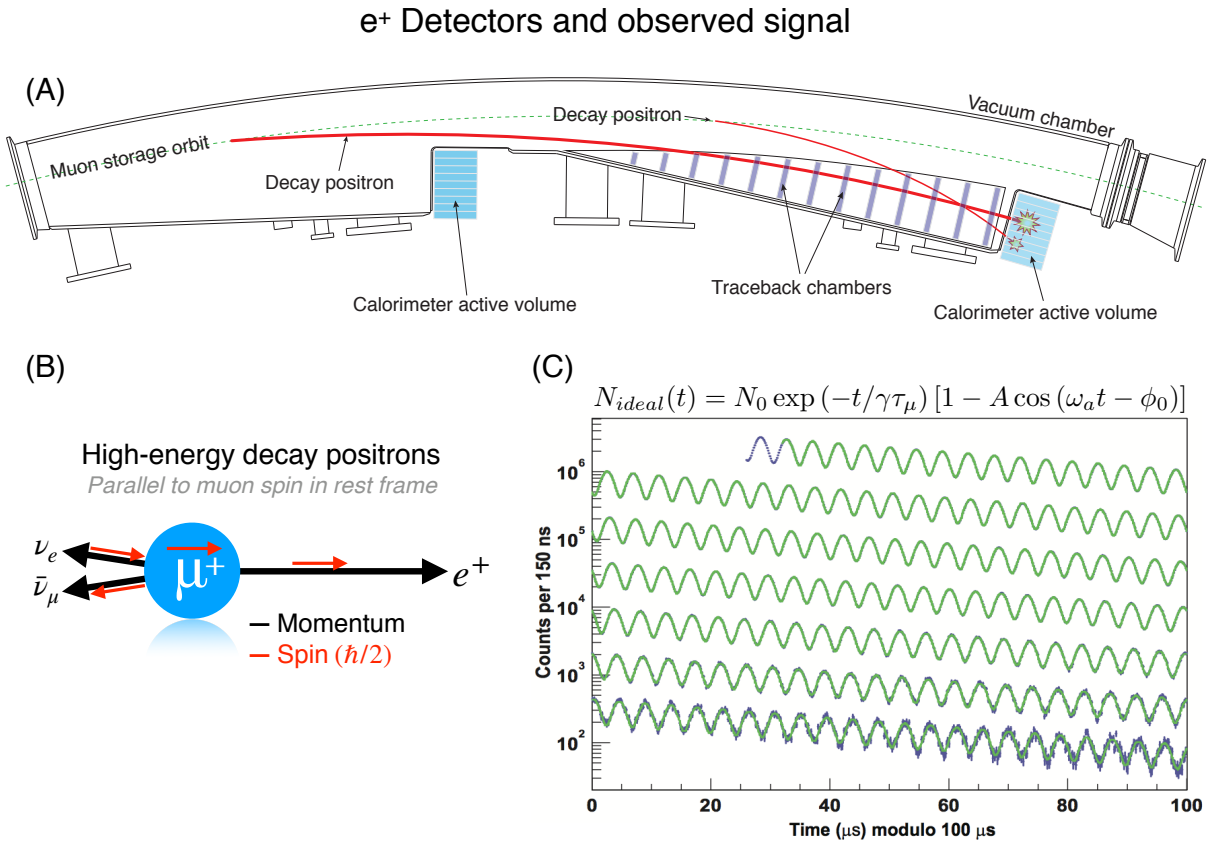

Figure 2.19: *e^+ Detectors and observed signal. (A) Stored muons decay to positrons via the weak interaction, $\mu^+ \to \bar{\nu}_\mu \nu_e e^+$. The decay positrons curl inward toward the ring center where they are intercepted by 24 segmented PbF_2 Čerenkov calorimeters spaced uniformly in ring azimuth (light blue). (B) The highest-energy positrons emerge parallel to the muon spin in the rest frame due to parity violation in the weak decay and conservation of angular momentum. (C) By implementing an energy threshold on decay positrons in the lab frame ($\sim$1.86 GeV), the pronounced rate at which the spin precesses due to the anomalous magnetic moment of the muon is observed in a so-called "wiggle plot".*

leading to

$$\boxed{a_\mu = \frac{\omega_a}{\tilde{\omega}_p}\left(\frac{m_\mu}{m_e}\,\frac{\mu_p}{\mu_e}\,\frac{g_e}{2}\right)}, \tag{2.15}$$

where $\mu_e = g_e e\hbar/4m_e$ has been used in going from Eq. (2.14) to Eq. (2.15), ω_a is discussed above, and

$$\tilde{\omega}_p \equiv \int M(r,\theta)\,\omega_p(r,\theta)\,r dr d\theta \tag{2.16}$$

is the azimuthally averaged magnetic field experienced by the muons circulating in the storage ring. The various other quantities in the parenthesis of Eq. (2.15) are known from other experiments [39], where $m_\mu/m_e = 206.7682826(46)$ (22 ppb), $\mu_e/\mu_p = -658.2106866(20)$ (3.0 ppb), and $g_e = -2.00231930436182(52)$ (0.00026 ppb). A summary of the procedure used to extract the muon anomaly from the data is shown in Fig. 2.20.

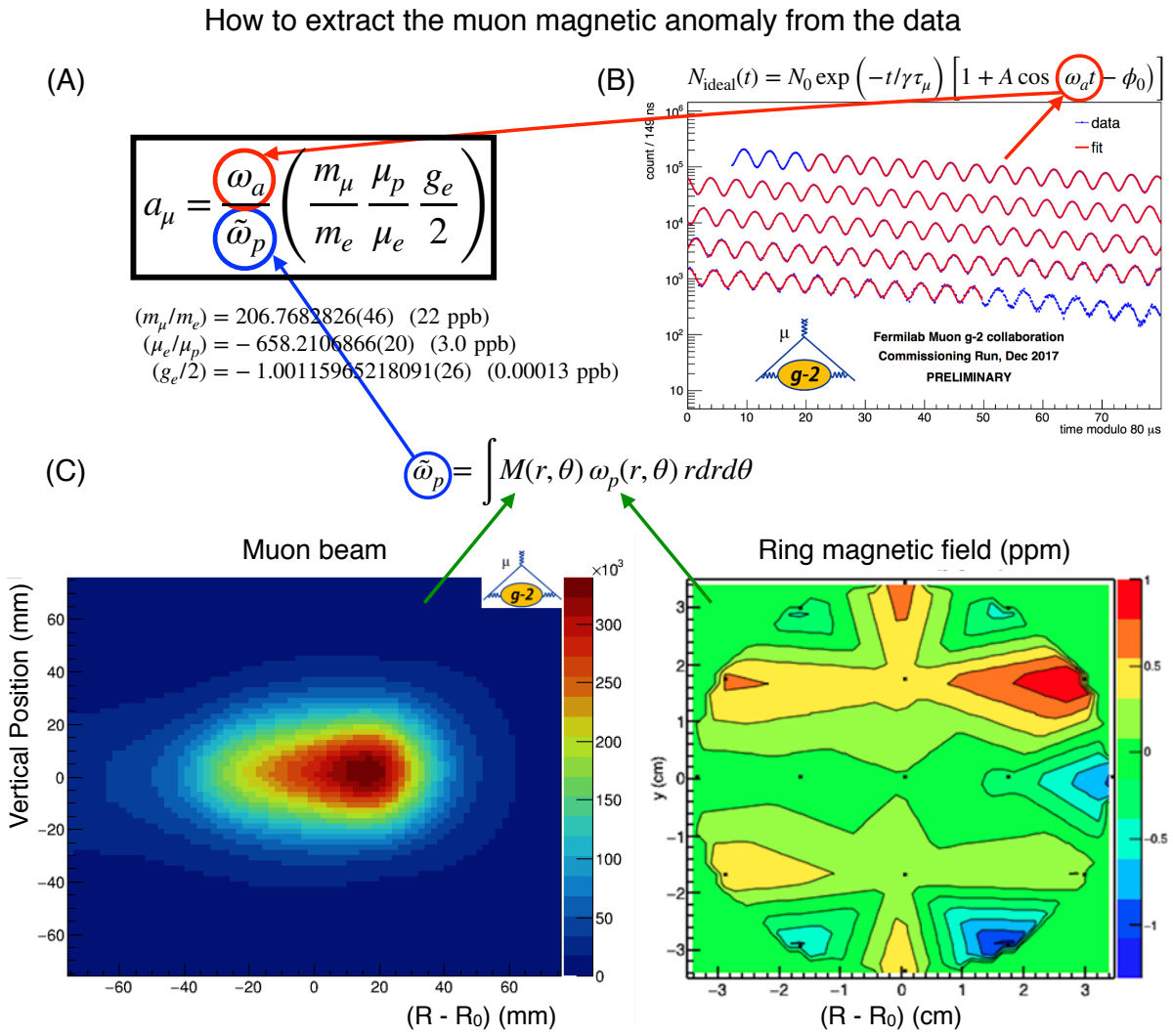

Figure 2.20: *How to extract the muon magnetic anomaly from the data. (A) Mathematical expression for extracting the muon anomaly from the data, where the quantities circled in red and blue are the data measured in the experiment. The terms in the parenthesis are physical constants known from other experiments. (B) Decay-positron spectrum, also known as a "wiggle plot," measured with the calorimeter system. (C) Convolution of the muon beam with the storage-ring magnetic field. The muon beam profile is reconstructed using decay-positron signals measured in the beam trackers, while the average magnetic field experienced by the circulating muons is measured with the proton-NMR trolley.*

Chapter 3

MODELING TOOLS AND DESIGN STUDIES

This chapter presents some of the modeling tools and design studies written and performed by the author of this thesis that have played a significant role in the design, optimization, and realization of the muon g–2 experiment at Fermilab (E989). First, a conceptual overview of muon $g-2$ simulations is presented, with emphasis given to E989's official Monte Carlo simulation, *gm2ringsim*, a significant fraction of which was written by the author of this thesis. Next, a few selected design studies are presented in a bit more detail, including the quads, kickers, collimators, inflector beam-monitoring system (IBMS), and new superconducting inflector magnet. The general format of this chapter is:

- Geometry
- Fields
- Particles
- Results

3.1 Brief Overview of Simulations

High-performance computing and sophisticated numerical techniques play an important role in the design, execution, and achievements of modern scientific experiments. At the LHC, for example, protons collide at a rate of hundreds of millions of times per second, generating colossal amounts of data that must be recorded, reconstructed, analyzed and understood by physicists. At Fermilab, for example, intense beams of energetic muons are used together with high-precision electromagnetic fields and sensitive detectors to probe the existence of rare physical processes that might contribute to the muon anomalous magnetic moment, also generating petabytes of data. Computers are associated with almost every aspect of modern physics experiments, from the low-level hardware interface to the highest-level simulations

and analyses [40]. At the heart of Fermilab's *gm2ringsim* are three codes written in the object-oriented C^{++} programming language:

1. *Geant4*: CERN framework for simulating the GEometry ANd Tracking (GEANT) of particles traversing matter and fields using Monte-Carlo methods [41, 42, 43]

2. *Art*: Fermilab event-processing framework, designed to meet the needs of smaller, local "Intensity-Frontier" experiments such as Mu2e and muon $g-2$ (as opposed to "Energy-Frontier" experiments at CERN such as ATLAS and CMS) [44]

3. *ArtG4/gm2ringsim*: custom application derived from the above two codes, written to model Fermilab the muon $g-2$ experiment from the injection of the muon beam into the storage ring to the end of the data-recording period, $\sim$700 µs after injection [45]

Each of the above three codes is sufficiently important to the physics community and to the muon $g-2$ experiment that a few more words are in order.

Geant4 has become the *de facto* industry standard for modeling high-energy, nuclear, accelerator, space and medical physics. The first release of *Geant4* was in December 1998, with $\sim$5 years of research and development prior to that point [41]. The code is formally hosted by CERN, with physicists, programmers, and software engineers contributing from many locations around the world. *Geant4* was the first toolkit of its kind to use C^{++} and the object-oriented programming (OOP) paradigm, which allows physicists to develop realistic, robust applications quickly by deriving from classes provided in the source-code distribution. The physics community is fortunate to have such a powerful, easy-to-use, *free* tool available as *Geant4*. An overview of the geometry-and-tracking (GEANT) simulation paradigm is shown in Fig. 3.1.

Fermilab's *Art* is an in-house event-processing framework developed and supported by Fermilab Scientific Computing Division (SCD), where the term "event processing" is left intentionally vague because the *Art* framework is sufficiently abstract, flexible, and powerful enough to handle events of arbitrary type as defined by the user. For example, an "event" might be a beam-beam crossing at a collider (e.g. Fermilab's DØ experiment), a fill of the $g-2$ storage ring with muons, or the simulation of a single muon in *gm2ringsim*. The intention of *Art*, as with *Geant4*, is to get physicists writing high-level physics code fast while

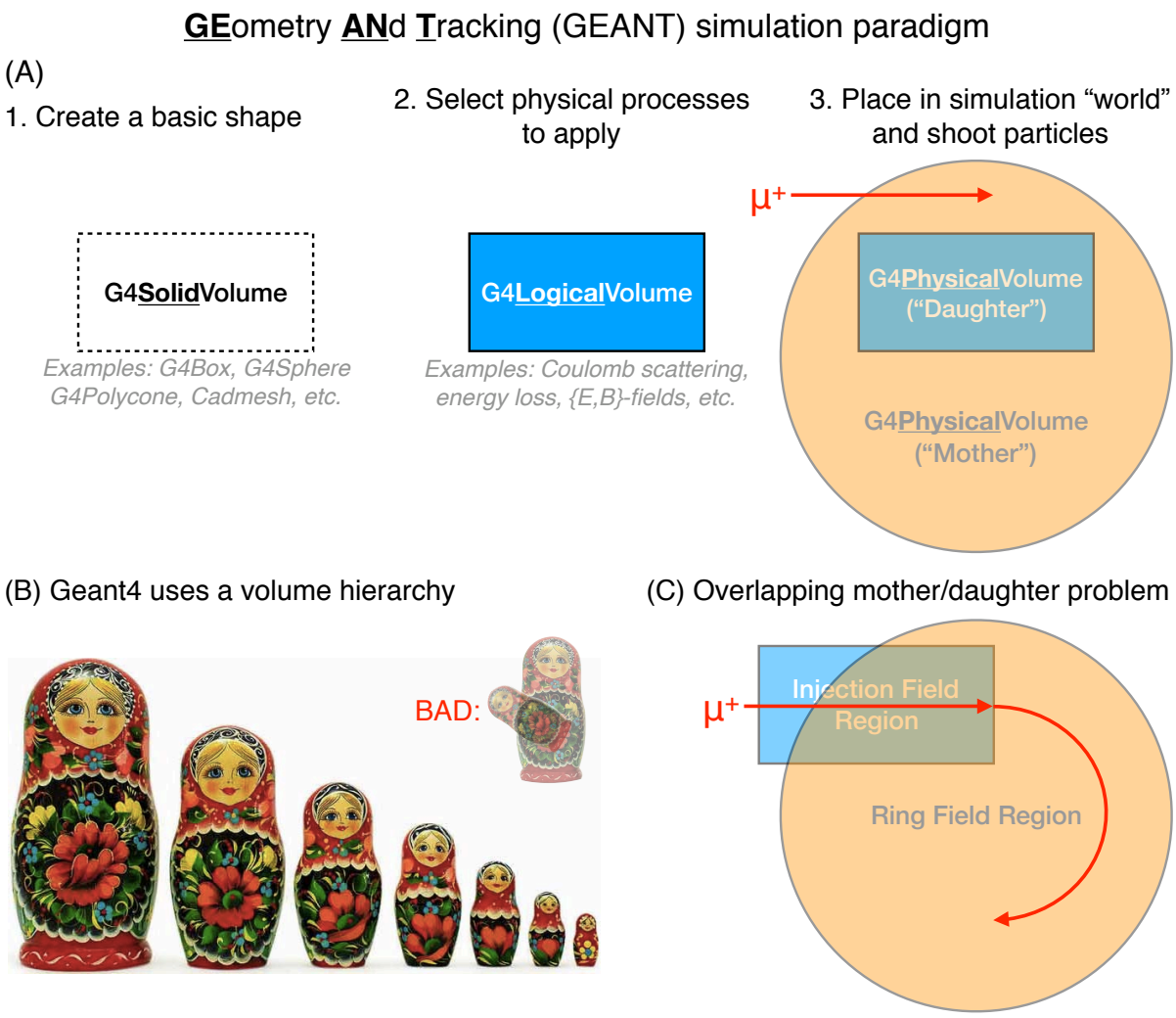

Figure 3.1: *GEometry ANd Tracking (GEANT) paradigm for the simulation of subatomic particles traversing matter and fields. (A) The essential steps are 1) create a basic shape, such as a* `G4Box`*; 2) apply physics to the shape, such as material interactions or electromagnetic fields; 3) place shapes in the simulation world, and "shoot particles" by specifying their initial position, momentum, and time. The Geant4 integrators then track the particles through the matter and fields. (B) Importantly, Geant4 uses a nested volume hierarchy in which all daughter volumes must be fully contained within their mother volumes. (C) Example overlapping mother-daughter problem, in which the daughter volume protrudes from its mother. This situation intended to represent the magnetic-field maps in the injection region of the muon $g-2$ storage ring (e.g. Fig. 3.4).*

minimizing the time spent developing low-level commonplace code. *Art* provides much of the infrastructure for tasks such as reading input, generating output, provenance tracking, message/error handling, database access, and so on [44]. One noteworthy byproduct of *Art* development is the Fermilab Hierarchical Configuration Language (FHiCL) [46], which allows users to trivially specify complicated, highly nested input parameters and run settings using simple input text files. This is particularly nice for C^{++} code since this approach largely circumvents the need to continually recompile.

The last of the three C^{++} codes mentioned above that play a critical role in muon $g-2$ simulations is *ArtG4*/*gm2ringsim*. Technically speaking, these are two different codes, however, they were developed at the same time for the same purpose (to simulate the muon $g-2$ experiment), so they will be regarded as one code for the sake of this document. *ArtG4* is described by its principal author, A. Lyon (Fermilab SCD), as "*Art* + *Geant4* = *ArtG4*" [45]. The basic idea is that *Geant4* is very adept at simulating a variety of physics processes, whereas *Art* offers tremendous flexibility for generating/analyzing data, so why not combine the two into one powerful simulation which can be maintained and supported locally at Fermilab for the muon g–2 experiment? The difficulty is that both *Art* and *Geant4* want to control the main event loop, so care must be taken to get *Art* to seize the *Geant4* event loop and to extract/produce the appropriate data at the appropriate time.[1] In this way, *ArtG4* is said to be the main *producer module* for *Geant4*, whereas *gm2ringsim* is a collection of *Art service modules* that build the *Geant4* detector geometries, fields, physics processes, sensitive detectors, hits, and other components of the simulation. All detectors and actions in *gm2ringsim* are plug-and-play using this approach, with the input FHiCL file defining the simulation configuration.

Another powerful feature in *gm2ringsim* is the implementation of a blueprint-based simulation geometry, as shown in Fig. 3.2. The blueprint-based approach is noteworthy since it removes all uncertainty as to whether or not the simulation faithfully represents the experiment: the blueprints being used to build actual objects in the experiment are the exact same blueprints being used to construct the simulation geometry. It is hard to imagine a more direct approach. The tool that enables *gm2ringsim* to work with blueprints is called *Cadmesh* [47], which allows users to import common file formats from computer-aided design

[1] For this purpose, A. Lyon borrowed code from Mu2e's R. Kutschke (Fermilab SCD) in order to break up the `G4RunManager::BeamOn()` method.

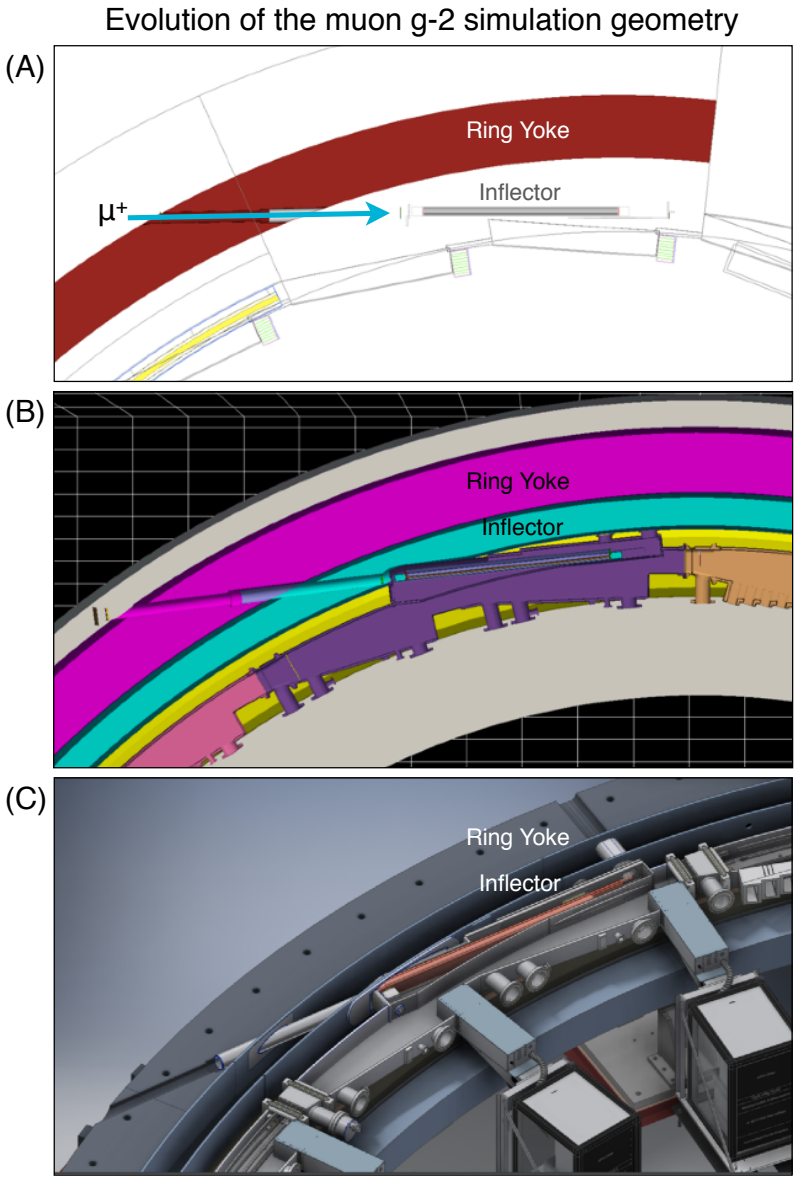

Figure 3.2: *Evolution of muon $g-2$ simulation geometry, gm2ringsim. (A) Early simulations used native Geant4 shapes to help guide the design of subsystems. (B) As designs were created, simulated, optimized and finalized, blueprints were also created and imported directly into the simulation using a tool called Cadmesh. The example shown above is the vacuum chambers with modifications for the straw-tracker "staircase" toward the far right. (C) Current and future g–2 simulations are trending toward an all-blueprint-based geometry.*

(CAD) programs directly into *Geant4* without the use of external software from third-party vendors, which might be prohibitively expensive for some users. *Cadmesh* uses components of the open-source Visualization and Computer Graphics Library (*VCGLIB*) [48] to construct *Geant4* "tesselated solids" (`G4TesselatedSolid`), where three-dimensional solid volumes are represented by their two-dimensional surfaces using many triangular and quadrangular facets connected with vertices ("cad" + "mesh" = *Cadmesh*), as shown in Fig. 3.3.

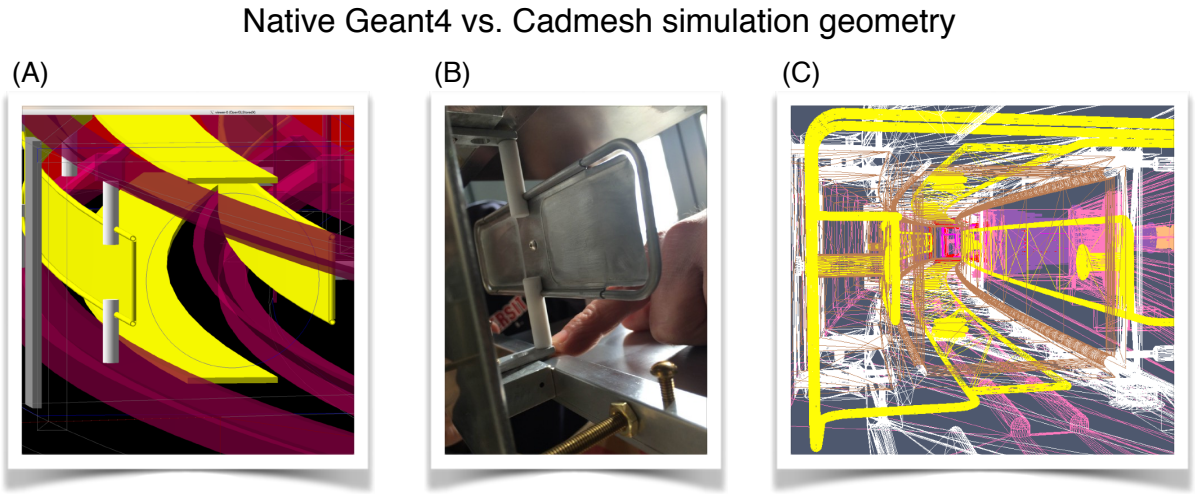

Figure 3.3: *Native Geant4 vs. Cadmesh simulation geometry. (A) Example Geant4 simulation geometry of Q1-outer electrode and redesigned supports through which the beam passes during injection (§3.4.1). The quad electrodes are shown in yellow, while the supports, also known as "standoffs," are shown in white. (B) Actual geometry of Q1-outer and new standoffs. (C) Cadmesh geometry of Q1-outer and standoffs (yellow), which approximates the three-dimensional solid volumes using many triangular and quadrangular facets to represent its surface. More highly curved surfaces require more facets, which impacts simulation startup time, particle-tracking fidelity, and visualization burden.*

3.2 A New Approach to Electromagnetic Fields in gm2ringsim: Unified Fields

One difficulty with simulating electromagnetic fields within the GEANT paradigm (Fig. 3.1) is, often times, available field maps do not encompass the full spatial extent of the material geometry. Smaller field maps are usually the result of computer-memory or output-file-size constraints, and the implementation of smaller field maps in *Geant4* can make preserving the volume hierarchy required in the GEANT paradigm difficult if not impossible to maintain. Complicated *Cadmesh* geometries introduce further difficulties with preserving the volume hierarchy. Avoiding these difficulties is the principal motivation for a new approach to fields in *gm2ringsim* ("Unified Fields"), which does away with the need to use *Geant4* solid, logical, and physical volumes within the storage ring in *gm2ringsim*, thereby circumventing all difficulties associated with overlapping mother-daughter volumes in the *Geant4* hierarchy.

Figure 3.4 shows how several different subset magnetic fields are used to build the total magnetic field of the muon storage ring in *gm2ringsim*.[2] A blueprint of the ring cross-section (Fig. 3.4(A)) reveals the ring is well described by cylindrical coordinates, however, the 4-inch hole in the backleg yoke of the C-magnet iron (which the beam passes through during injection) breaks the azimuthal symmetry (Fig. 3.4(C)). In order to save computational resources and reduce output-file size, the 2D transverse geometrical and material properties in the blueprint are entered into a two-dimensional *Opera* simulation[3] [49], which produces a tabulated magnetic field (ρ, z, B_ρ, B_z) as shown in Fig. 3.4(B), where the grid spacing is $\{\Delta\rho, \Delta z\} = 1\,\text{cm}$. All tabulated electromagnetic fields in *gm2ringsim* are implemented using custom interpolation classes written by the author (discussed below); regardless, the available tabulated magnetic field of the ring is simply too coarse for the muon storage region (Fig. 3.4(B), $r_0 = 45\,\text{mm}$), where the azimuthally averaged magnetic field varies by $\mathcal{O}(1\,\text{ppm})$, so a multipole expansion is used instead. As mentioned above, this approach may seem reasonable, however, it fails to take into account the magnetic field in the muon injection region (Fig. 3.4(C)). As shown in Fig. 3.4(D), the available field-map table[4] covers a small rectangular region of the ring (with a finer grid spacing, $\{\Delta x, \Delta y, \Delta z\} = 5\,\text{mm}$),

[2] This example was the original motivation for a new approach to fields. It was implemented using a singleton class in the injection code that ultimately became a part of *gm2ringsim*.

[3] *Opera Simulation Software,* Opera-2d Magnetization and Hysteresis Module.

[4] W. Meng, personal communication. The field in the muon injection region was originally simulated for BNL Experiment E969, i.e. the follow-up to E821, which never happened because E969 lost funding.

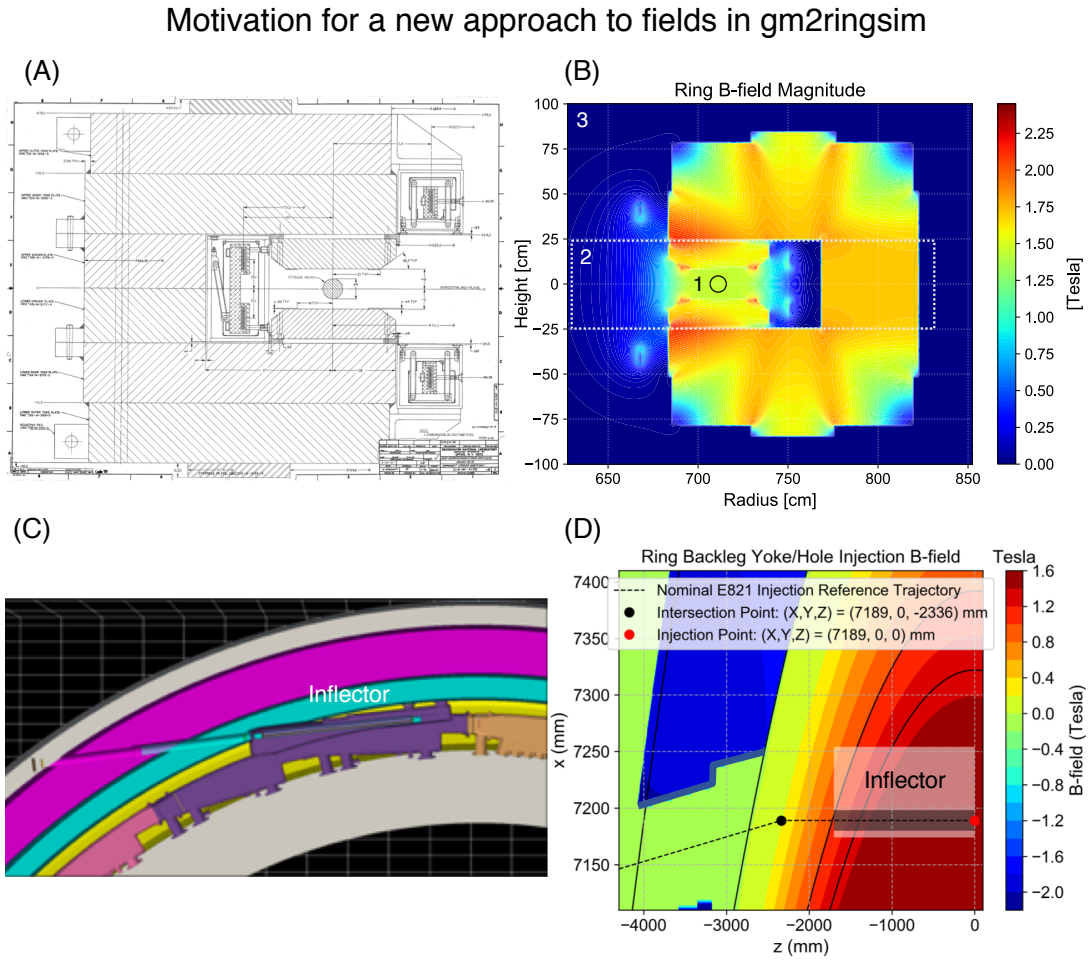

Figure 3.4: *Example fields in gm2ringsim and motivation for a new approach to fields. (A, B) Transverse geometry and magnetic field of the muon $g-2$ storage ring, excluding the 4-inch hole bored through the backleg yoke. The ring field outside the injection region is implemented in three parts: 1) the detailed multipole-expansion region, 2) the fringe-field region, and 3) the rest of the simulation "world." (C, D) Geometry and field in the injection region of the muon storage ring. The Cartesian grid and short vertical extent of the available field map ($y \in \{0, 5, ..., 30\}$ mm) are not amenable to the natural cylindrical coordinate system of the vacuum chambers and ring (A, B), which ultimately makes implementing this field in Geant4 very challenging due to the unavoidable overlapping mother-daughter issues shown in Fig. 3.1.*

and the vertical magnetic field is only defined for the upper-half plane, $y \in \{0, 5, ..., 30\}$ mm. The spatial extent of *this* field map is incompatible with the geometry of the magnet iron, cryostat, vacuum chambers and inflector. Another field to be implemented is the inflector magnetic field; see §3.4.5. The take-home message of the above discussion is that preserving the logical hierarchy required by the GEANT paradigm (Fig. 3.1) is difficult if not impossible given existing field maps, material geometry and physics requirements, all of which motivated the author to create a new solution by thinking outside the proverbial `G4Box`.[5]

The new approach to electromagnetic fields in *gm2ringsim* circumvents the need to use `G4SolidVolume`s, `G4LogicalVolume`s, and `G4PhysicsVolume`s to describe the electromagnetic fields of the various ring subsystems contained within the volume shown in Fig. 3.4(B.2).[6] All electromagnetic fields in *gm2ringsim* are now constructed, managed, and implemented using a new `gm2FieldManager_service`, which is both an object derived from `G4Field` (so that field data, equations of motion, etc., can be communicated to *Geant4* at the right time in the event loop) as well as an *Art* service (so it is globally accessible in the simulation like a singleton that can add data to the *Art* run/event). The consolidation of all *gm2ringsim* fields into one has been given the nickname "Unified Fields."[7] The Unified-Field approach is novel in that it completely decouples the fields from the geometry by breaking with the GEANT paradigm, therefore circumventing any/all problems arising from overlapping mother/daughter issues shown in Fig. 3.1.

In the Unified-Field approach, the various GEANT volumes of the field regions are replaced with mathematical "fiducial functions," an overview of which is shown in Fig. 3.5. The original shape for the "soft edge" of the fiducial functions (Fig. 3.5(A)) was inspired by $f(x) = \tanh(x)$, which the author used for modeling early kicker pulses in the BMAD simulation ($\Delta t_{\text{rise}} \simeq 20\,\text{ns}, \Delta t_{\text{flat}} \simeq 120\,\text{ns}, \Delta t_{\text{fall}} \simeq 20\,\text{ns}$). The hyperbolic tangent is related to the "sigmoid" or "activation" function commonly used in machine learning, $\sigma(x) = 1/(1 + e^{-x}) = (1 + \tanh(x/2))/2$, which is the form implemented in *gm2ringsim*. As shown in Fig. 3.5(B), two sigmoids are pieced together, shifted, and rescaled in order to construct a fiducial function, where the user enters the position, width, and edge sharpness as parameters

[5] Other examples of the motivation for a new approach to fields in *gm2ringsim* include the inflector magnetic field, trolley rails, quad-field regions, and kicker-field regions (not discussed).

[6] This volume has become known as "the Arc" in *gm2ringsim*.

[7] The term "Unified Fields" was coined by Professor Renée Fatemi (University of Kentucky, Lexington).

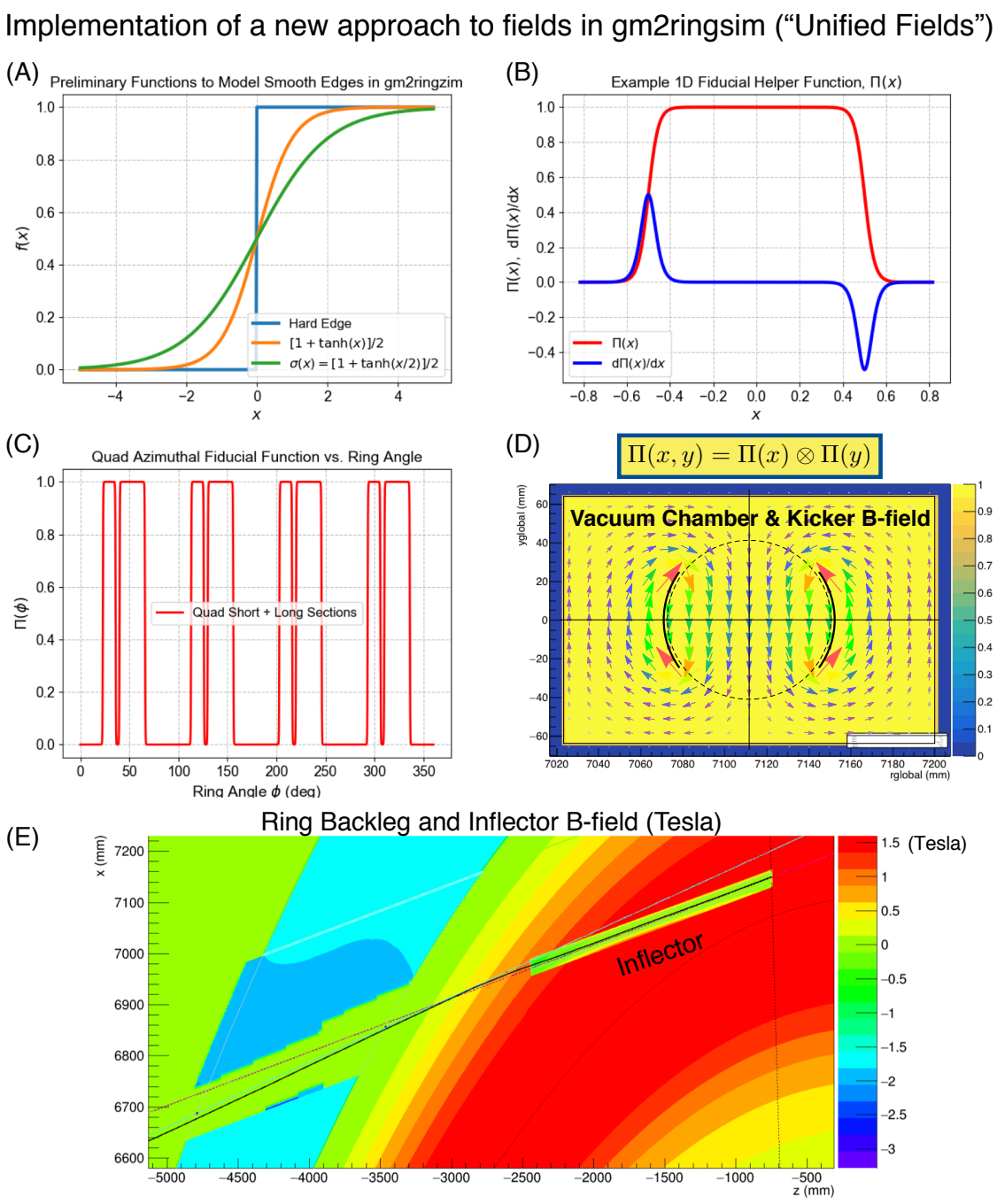

Figure 3.5: *Implementation of a new approach to fields in gm2ringsim (“Unified Fields”). Simple mathematical functions (“Fiducial Functions”) take the place of* `G4SolidVolumes`*,* `G4LogicalVolumes`*, and* `G4PhysicalVolumes`*. See text for details.*

to the C^{++} constructor. The value of the fiducial function is $f(x) \in [0,1]$ after renormalization, where $f(x) = 0$ corresponds to being "outside" the volume, $f(x) = 1$ corresponds to being "inside" the volume, and $0 < f(x) < 1$ corresponds to being in the fringe field. An entire ecosystem of base and derived fiducial-function classes was developed to simulate the various field regions in the $g-2$ experiment, the details of which are beyond the present scope. An example one-dimensional fiducial function is shown in Fig. 3.5(C), which is used to model the azimuthal extent of the vertically focusing electric quadrupoles. Here, only the longitudinal fiducial function Q1 is needed since the quads are four-fold symmetric. An example two-dimensional fiducial function is shown in Fig. 3.5(D), which is used to model the transverse cross section of the vacuum chamber. The magnetic fields in the injection region are shown in Fig. 3.5(E). The global locations of the fields in *gm2ringsim* are handled via generalized linear transformations known as *affine transforms*, where

$$y = mx + b \quad \Rightarrow \quad \mathbf{y} = M\mathbf{x} + \mathbf{b} \quad \Rightarrow \quad \begin{pmatrix} \mathbf{y} \\ 1 \end{pmatrix} = \underbrace{\begin{pmatrix} M & \mathbf{b} \\ 0 & 1 \end{pmatrix}}_{\text{Affine Transform}} \begin{pmatrix} \mathbf{x} \\ 1 \end{pmatrix}. \tag{3.1}$$

For the placement of the fields in *gm2ringsim*, the matrix M in Eq. (3.1) is always a rotation matrix and the vector $\mathbf{b}$ is always a translation vector. One noteworthy feature of affine transforms as written in Eq. (3.1) is they are "closed under multiplication," for example,

$$\begin{pmatrix} M & \mathbf{b} \\ 0 & 1 \end{pmatrix}_{\text{Total}} = \begin{pmatrix} R_2 & \mathbf{x}_2 \\ 0 & 1 \end{pmatrix} \begin{pmatrix} R_1 & \mathbf{x}_1 \\ 0 & 1 \end{pmatrix} = \begin{pmatrix} R_2 R_1 & R_2\mathbf{x}_1 + \mathbf{x}_2 \\ 0 & 1 \end{pmatrix}, \tag{3.2}$$

or

$$\begin{pmatrix} M & \mathbf{b} \\ 0 & 1 \end{pmatrix}_{\text{Total}} = \begin{pmatrix} R_3 & \mathbf{x}_3 \\ 0 & 1 \end{pmatrix} \begin{pmatrix} R_2 & \mathbf{x}_2 \\ 0 & 1 \end{pmatrix} \begin{pmatrix} R_1 & \mathbf{x}_1 \\ 0 & 1 \end{pmatrix} = \begin{pmatrix} R_3 R_2 R_1 & R_3(R_2\mathbf{x}_1 + \mathbf{x}_2) + \mathbf{x_3} \\ 0 & 1 \end{pmatrix}. \tag{3.3}$$

are also affine transforms. This feature is very nice because it means the complicated, nested positioning and rotation of all objects in *gm2ringsim* can be reduced to a single total affine transform with respect to the simulation "world" no matter how many substituent affine transforms are involved along the way. A realistic example of Eq. (3.2) is the coordinate transformation of the IBMS{1,2} or TØ detectors into the downstream end of the

M5 beamline, which includes the 1.25° offset and the "intersection point" (E821 blueprint D19-M-4101-4 for the interested reader). As another example, a realistic implementation of Eq. (3.3) is the correct global positioning and rotation of the inflector magnetic field about the inflector pivot point shown in E821 blueprint D19-M-4619-5. Thus, given any point in *gm2ringsim*, the transformation to the local frame of the object or field in question is the inverse of the object's total affine transformation Eq. (3.1),

$$\mathbf{x} = M^{-1}(\mathbf{y} - \mathbf{b}), \tag{3.4}$$

where both the affine transform and its inverse are cached at the construction of C^{++} object in *gm2ringsim* for computational speedup. In summary, given a global simulation point (x, y, z, t), the cached inverse affine transform Eq. (3.4) is used to transform the global point to local coordinates; the field is retrieved from the new custom field classes; and finally, the cached affine transform Eq. (3.1) is used to convert the local field back to global *Geant4* coordinates.

3.3 Particle Distributions and Phase-Space

In order to create realistic HEP simulations program developers must specify, among other things, realistic representations of simulation (1) geometry, (2) fields, and (3) particles. Generating particle distributions in phase space is the topic of this section, which briefly reviews three "particle guns" that have played an important role in the $g-2$ collaboration's simulations to date. Here, using "particle guns" to "shoot particles" in the simulation is a colorful way of saying the initial conditions of the equations of motion have been fully specified so the numerical integration may commence. From the accelerator-physics viewpoint, it is convenient to regard the initial conditions as corresponding to the input phase-space coordinates $(x, x', y, y', t, \delta, s_\theta, s_\phi)$, which fully specify the initial position, time, momentum, energy, and spin polarization of the particle being investigated in the simulation. The particle guns discussed below have had a significant impact on the muon $g-2$ experiment, for example, in the redesign of the quads, kickers, inflector, IBMS and collimators. Additionally, the particle guns discussed below have enabled all E989 simulation "Mock Data Challenges."

3.3.1 JacobianGun: Transport Matrices from Tracking Simulations

The concept of a reference trajectory is extremely important in accelerator physics: the entire beamline and accelerator are designed and built around the reference trajectory. The *JacobianGun* is a simple simulation tool that enables the user to quickly investigate arbitrary candidate reference trajectories and construct the Courant-Snyder parameters and dispersion as a function of downstream distance in the beamline. An example is shown in Fig. 3.6. A FORTRAN version of the *JacobianGun* was first created to resolve an internal dispute between two collaborators regarding the focusing strength of the fringe fields in the injection region of the muon storage ring shortly before the Optics Review, in which the design of the M4/M5 beamline was finalized (Oct 2014). A C^{++} version of the *JacobianGun* was used extensively in the design of the new superconducting inflector magnet discussed later in this chapter (§3.4.5).

The purpose of this section is to establish the basic principles upon which the *JacobianGun* is based, and to make the connection to accelerator physics and magnet currents dialed in from Fermilab Main Control Room. The underlying principle of the *JacobianGun* is simply a Taylor expansion of a vector-valued function,

$$\mathbf{f}(\mathbf{x}_0 + \delta\mathbf{x}) = \mathbf{f}(\mathbf{x}_0) + \delta\mathbf{x} \cdot \boldsymbol{\nabla}\mathbf{f}(\mathbf{x}_0) + \frac{1}{2}\delta\mathbf{x} \cdot \boldsymbol{\nabla}^2\mathbf{f}(\mathbf{x}_0) \cdot \delta\mathbf{x} + \mathcal{O}(\|\delta\mathbf{x}\|^3), \tag{3.5}$$

where $\mathbf{f}(\cdots)$ means "propagate the beam downstream," $\mathbf{x}_0 \equiv (x_0, x_0', y_0, y_0', \delta_0)^T$ is the user's reference trajectory about which the Taylor expansion Eq. (3.5) will be performed,[8] $\delta\mathbf{x}$ is a perturbation, and $\mathbf{f}(\mathbf{x}_0 + \delta\mathbf{x})$ are the coordinates of the perturbed reference at a downstream location. Each of the initial degrees of freedom x_0^j is perturbed, one at a time, in order to numerically construct the Jacobian of the transformation from upstream to downstream. In this case $\mathbf{f}(\cdots)$ describes the effects of the beamline elements and electromagnetic fields experienced by the charged particles as the beam is propagated down the line. Physically, the quantity of interest is

$$\delta\mathbf{f} \equiv \mathbf{f}(\mathbf{x}_0 + \delta\mathbf{x}) - \mathbf{f}(\mathbf{x}_0) \approx \boldsymbol{\nabla}\mathbf{f}(\mathbf{x}_0) \cdot \delta\mathbf{x}, \tag{3.6}$$

which represents the deviation of the beam from the design trajectory at the downstream

[8] The time coordinate and spin have been ignored for notational clarity.

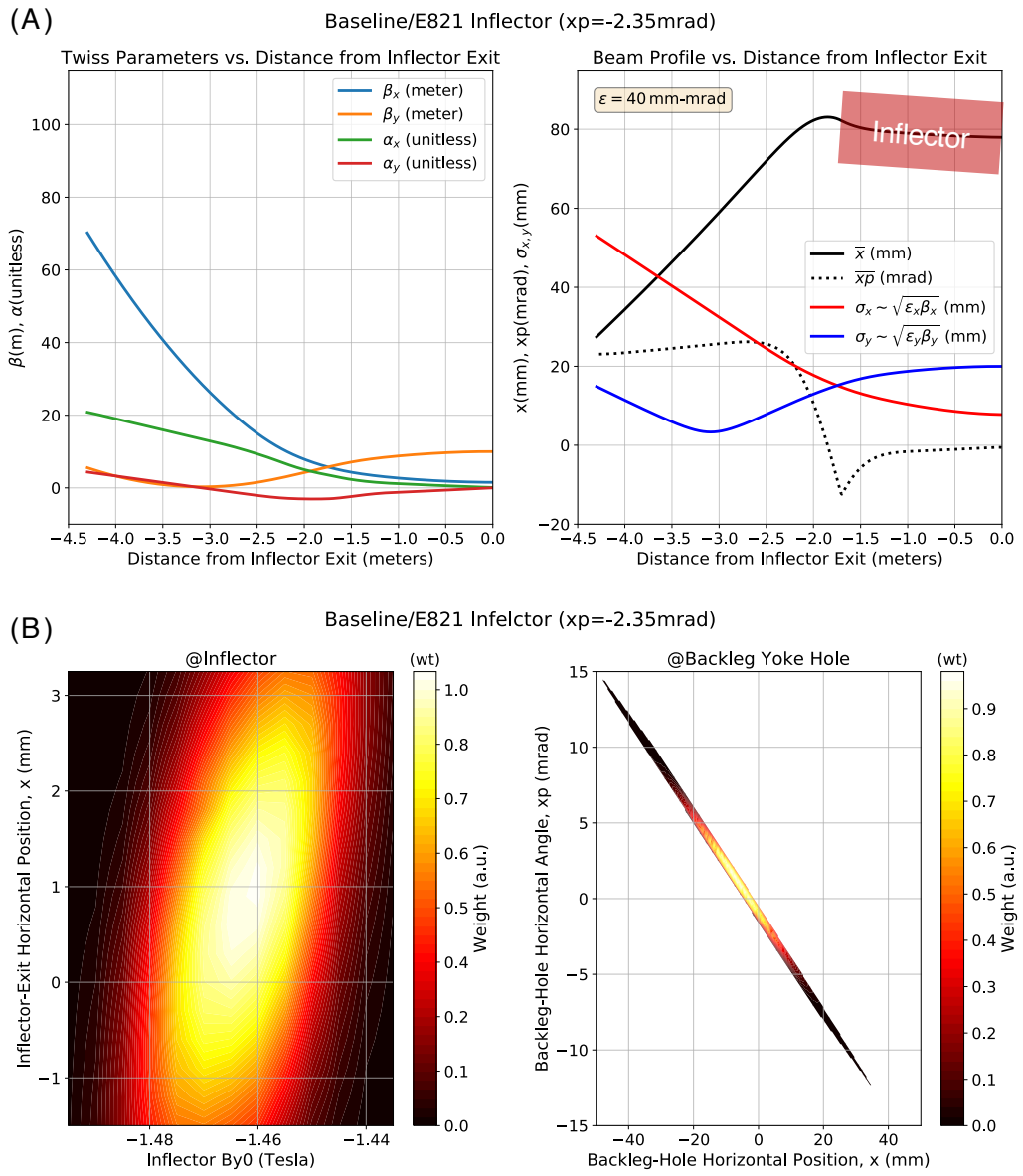

Figure 3.6: *(A) Example JacobianGun simulation to investigate the beam centroid and width through the backleg yoke hole of the storage ring and through inflector. The left plot shows the downstream evolution of the beam parameters extracted from the JacobianGun as a function of distance from the inflector exit, while the right plot shows the beam centroid and width evolution (assuming $\epsilon = 40\,\mu\text{m}$). The fringe field of the ring is strongly vertically focusing. (B) Example rapid optimization of the inflector magnetic field and injection offsets at the storage-ring entrance calculated using the JacobianGun. See text for discussion.*

location. Since $\boldsymbol{\nabla}$ is a linear operator, the various input and output vectors may be "stacked up" into one master equation,

$$\underbrace{\delta\begin{pmatrix}\mathbf{f}_1 & \mathbf{f}_2 & \cdots & \mathbf{f}_N\end{pmatrix}}_{\equiv\delta\mathbf{F}} \approx \underbrace{\boldsymbol{\nabla}\mathbf{f}(\mathbf{x}_0)}_{\equiv\mathbf{J}} \cdot \underbrace{\delta\begin{pmatrix}\mathbf{x}_1 & \mathbf{x}_2 & \cdots & \mathbf{x}_N\end{pmatrix}}_{\equiv\delta\mathbf{X}}, \tag{3.7}$$

where $\delta\mathbf{X}$ are the perturbed trajectories at the upstream location and $\delta\mathbf{F}$ are the perturbed trajectories at the downstream location. The above matrix equation $\delta\mathbf{F} = \mathbf{J}\cdot\delta\mathbf{X}$ is then inverted by multiplying on the right by $\delta\mathbf{X}^{-1}$, leading to a concise expression for the Jacobian of the transformation from upstream to downstream,

$$\boxed{\mathbf{J} \equiv \boldsymbol{\nabla}\mathbf{f}(\mathbf{x}_0) \approx \delta\mathbf{F}\cdot\delta\mathbf{X}^{-1}}\,. \tag{3.8}$$

Note the similarity to the ordinary derivative, $df/dx \leftrightarrow \delta\mathbf{F}\cdot\delta\mathbf{X}^{-1}$. As written, the above result is only correct to order $\mathcal{O}(\|\delta\mathbf{x}\|^1)$, however, better results $\mathcal{O}(\|\delta\mathbf{x}\|^{n\geq 2})$ are obtained by adding and subtracting combinations of

$$\mathbf{f}(\mathbf{x}_0+\delta\mathbf{x}) = \mathbf{f}(\mathbf{x}_0) + \delta\mathbf{x}\cdot\boldsymbol{\nabla}\mathbf{f}(\mathbf{x}_0) + \frac{1}{2}\delta\mathbf{x}\cdot\boldsymbol{\nabla}^2\mathbf{f}(\mathbf{x}_0)\cdot\delta\mathbf{x} + \cdots, \tag{3.9a}$$

$$\mathbf{f}(\mathbf{x}_0-\delta\mathbf{x}) = \mathbf{f}(\mathbf{x}_0) - \delta\mathbf{x}\cdot\boldsymbol{\nabla}\mathbf{f}(\mathbf{x}_0) + \frac{1}{2}\delta\mathbf{x}\cdot\boldsymbol{\nabla}^2\mathbf{f}(\mathbf{x}_0)\cdot\delta\mathbf{x} - \cdots. \tag{3.9b}$$

Equation (3.9a) is known as the "forward-difference equation" (due to the plus sign) while Eq. (3.9b) is known as the "backward-difference equation" (due to the minus sign). Together these equations may be used to construct the "central-difference Jacobian,"

$$\boldsymbol{\nabla}\mathbf{f}(\mathbf{x}_0) = \frac{\mathbf{f}(\mathbf{x}_0+\delta\mathbf{x}) - \mathbf{f}(\mathbf{x}_0-\delta\mathbf{x})}{2\delta\mathbf{x}} + \mathcal{O}(||\delta\mathbf{x}||^2), \tag{3.10}$$

which requires twice the number of perturbations as Eq. (3.8) (forward and backward) but is more precise by one power of $\mathcal{O}(\|\delta\mathbf{x}\|)$. For example, using Eq. (3.10) over Eq. (3.8) for a spatial perturbation $\delta x^i = 0.1\,\text{mm}$ gives a result whose error is smaller by a factor of $\sim$10. Equation (3.10) is the form used in the *JacobianGun*. Additionally, the perturbations used to construct the Jacobian Eq. (3.10) may be used to calculate the diagonal components of the Hessian matrices (2^{nd} derivatives, i.e. curvature) using a central-sum formula, i.e. Eq. (3.9a)

plus (3.9b), leading to

$$\boldsymbol{\nabla}^2\mathbf{f}(\mathbf{x}_0) = \frac{\mathbf{f}(\mathbf{x}_0+\delta\mathbf{x}) - 2\mathbf{f}(\mathbf{x}_0) + \mathbf{f}(\mathbf{x}_0-\delta\mathbf{x})}{\delta\mathbf{x}^2} + \mathcal{O}(||\delta\mathbf{x}^1||). \tag{3.11}$$

The Hessian matrices have been used, for example, to verify linear optics in the injection region of the muon $g-2$ storage ring.

Finally, when implementing the above expressions on a computer, one must take care to get the indices right. The perturbations used to construct all components of the central-difference Jacobian matrix and the diagonal components of the Hessian matrices are

$$J^i{}_j \equiv [\boldsymbol{\nabla}\mathbf{f}(\mathbf{x}_0)]^i{}_j = \frac{f^i(...,x_0^j+\delta x^j,...) - f^i(...,x_0^j-\delta x^j,...)}{2\delta x^j}, \tag{3.12a}$$

$$H^i{}_{jj} \equiv \left[\boldsymbol{\nabla}^2\mathbf{f}(\mathbf{x}_0)\right]^i{}_{jj} = \frac{f^i(...,x_0^j+\delta x^j,...) - 2f^i(...,x_0^j,...) + f^i(...,x_0^j-\delta x^j,...)}{(\delta x^j)^2}, \tag{3.12b}$$

while the off-diagonal components of the Hessians are

$$\begin{aligned} H^i{}_{jk} \equiv \left[\boldsymbol{\nabla}^2\mathbf{f}(\mathbf{x}_0)\right]^i{}_{jk} = \frac{1}{4\,\delta x^j\,\delta x^k}\Bigg\{ \\ + \Big[f^i(...,x_0^j+\delta x^j,...,x_0^k+\delta x^k,...) + f^i(...,x_0^j-\delta x^j,...,x_0^k-\delta x^k,...)\Big] \\ - \Big[f^i(...,x_0^j-\delta x^j,...,x_0^k+\delta x^k,...) + f^i(...,x_0^j+\delta x^j,...,x_0^k-\delta x^k,...)\Big]\Bigg\}, \end{aligned} \tag{3.13}$$

where $k > j$ and each Hessian matrix (one per degree of freedom) is symmetric, $\mathbf{H}_{jk} = \mathbf{H}_{kj}$. As an example, phase-space coordinates in *gm2ringsim* are typically written as $\mathbf{x} = (x, x', y, y', \delta)^T$, so calculation of the Jacobian Eq. (3.12a) involves $1 + 2N = 11$ perturbations, which may also be used to construct the diagonal components of the Hessian matrices Eq. (3.12b). Calculation of all components of the Hessians involves $1 + 2N^2 = 51$ perturbations. One could continue in this way to higher-order perturbations, however, the number of simulations grows as $\mathcal{O}(N^2)$ and returns are diminishing since the vast majority of fields encountered by the particles are either constant or linear, i.e. dipole or quadrupole.

Having numerically constructed the Jacobian matrix (also known as a "transport matrix") and verified linear optics using the Hessian matrices, the connection to accelerator physics may now be established. Using the results derived in §A.3, if the transport matrix that

propagates $(x, x', \delta)^T$ is

$$J = \begin{pmatrix} M_{11} & M_{12} & M_{13} \\ M_{21} & M_{22} & M_{23} \\ M_{31} & M_{32} & M_{33} \end{pmatrix}, \tag{3.14}$$

the beam parameters evolve downstream according to

$$\begin{pmatrix} \beta_x \\ \alpha_x \\ \gamma_x \end{pmatrix} = \begin{pmatrix} M_{11}^2 & -2M_{11}M_{12} & M_{12}^2 \\ -M_{11}M_{21} & M_{11}M_{22} + M_{12}M_{21} & -M_{12}M_{22} \\ M_{21}^2 & -2M_{21}M_{22} & M_{22}^2 \end{pmatrix} \begin{pmatrix} \beta_x \\ \alpha_x \\ \gamma_x \end{pmatrix}, \tag{3.15}$$

and

$$\begin{pmatrix} D_x \\ D'_x \\ 1 \end{pmatrix} = \begin{pmatrix} M_{11} & M_{12} & M_{13} \\ M_{21} & M_{22} & M_{23} \\ 0 & 0 & 1 \end{pmatrix} \begin{pmatrix} D_x \\ D'_x \\ 1 \end{pmatrix} \tag{3.16}$$

where only the 3×3 horizontal sub-block has been written for notational clarity. The width of the beam then evolves downstream according to

$$\sigma_x^2 = \epsilon_x \beta_x + (D_x \sigma_\delta)^2, \qquad \sigma_y^2 = \epsilon_y \beta_y + (D_y \sigma_\delta)^2. \tag{3.17}$$

Example beam centroid and width evolution calculated using the *JacobianGun* is shown in Fig. 3.6, which played a role in the design of the new inflector (§3.4.5).

3.3.2 MuonGasGun: Circumventing Tracking with Accelerator Physics

In the early days of Fermilab muon $g-2$ injection simulations (c. 2012), the beam phase space arriving at the ring entrance was not precisely known, a realistic model of the injection fields did not exist, the kickers had not been designed yet, and so on. To make matters worse, simple simulations of stored muons (which circumvented the above issues) required large amounts of computer time since the stored muons had to be tracked many hundreds if not thousands of turns before decaying.[9] These difficulties were circumvented by a tool that has become known as the *MuonGasGun*, which has found great utility in the collaboration. Original simulations performed with the *MuonGasGun* allowed calorimeter design decisions

[9] The average muon decay time is $\langle \gamma \tau_\mu \rangle = 64\,\mu\text{s} \sim 430$ turns.

to be made, e.g. the number and size of the PbF_2 crystals (§2.2.6), however, the *MuonGasGun* has since evolved into a sophisticated simulation tool that features a full model of injection and allows the user to specify the stored-muon beam dynamics, e.g. the horizontal coherent betatron oscillation (CBO) amplitude. The *MuonGasGun* has also enabled E989 Mock Data Challenges MDC1 and MDC2, more calorimeter studies, tracker studies, fast-rotation analyses, etc., and this tool is used regularly in favor of full-fledged (computationally expensive) tracking simulations. The purpose of this section is to give a brief overview of the *MuonGasGun*.

The basic concepts underlying the *MuonGasGun* are shown in Fig. 3.7. The original idea of the *MuonGasGun* [50] was that, long after injection, the beam fills the ring azimuth approximately uniformly, and therefore the stored muon beam may be modeled as a "gas of muons" at equilibrium.[10] The time-consuming step of tracking muons many turns may then be bypassed since the beam and spin dynamics are extremely well known *a priori*. In the continuous-quadrupole approximation, for example, the matrices that transport the phase-space vectors $(x, x', \delta \equiv \Delta p/p_0)^T$. and $(y, y')^T$ downstream through ring angle θ as measured from the inflector exit are given by [29, 27]

$$\mathcal{M}_x = \begin{pmatrix} \cos(Q_x\theta) & \frac{\rho_0}{Q_x}\sin(Q_x\theta) & \frac{\rho_0}{Q_x^2}(1-\cos(Q_x\theta)) \\ -\frac{Q_x}{\rho_0}\sin(Q_x\theta) & \cos(Q_x\theta) & \frac{1}{Q_x}\sin(Q_x\theta) \\ 0 & 0 & 1 \end{pmatrix} \equiv \begin{pmatrix} C_x & S_x & D_x \\ C_x' & S_x' & D_x' \\ 0 & 0 & 1 \end{pmatrix} \tag{3.18}$$

for the horizontal and

$$\mathcal{M}_y = \begin{pmatrix} \cos(Q_y\theta) & \frac{\rho_0}{Q_y}\sin(Q_y\theta) \\ -\frac{Q_y}{\rho_0}\sin(Q_y\theta) & \cos(Q_y\theta) \end{pmatrix} \equiv \begin{pmatrix} C_y & S_y \\ C_y' & S_y' \end{pmatrix} \tag{3.19}$$

for the vertical, where [27, 51]

$$\begin{aligned} Q_x &= \sqrt{(1-n) + \left(\frac{2n+n^2}{1-n}\right)\delta} \quad \approx \sqrt{1-n} - \left(\frac{2n+n^2}{2(1-n)^{3/2}}\right)\delta, \\ Q_y &= \sqrt{n\left(1 + \left(\frac{1+n}{1-n}\right)\delta\right)} \qquad \approx \sqrt{n} + \sqrt{n}\left(\frac{1+n}{2-2n}\right)\delta, \end{aligned} \tag{3.20}$$

[10] The transverse distributions in [50] were the measured distributions from E821 Final Report [22].

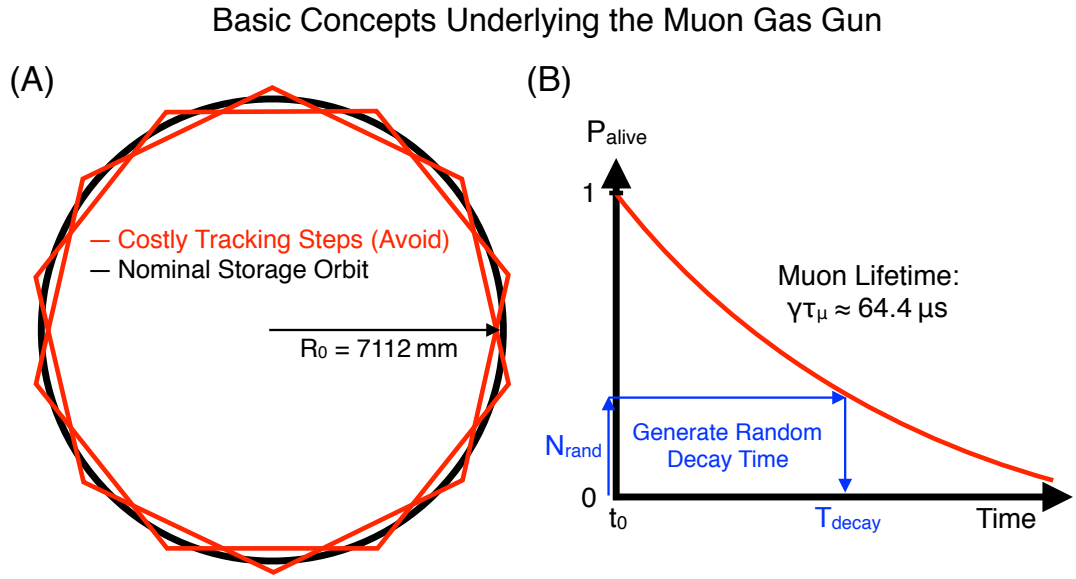

Figure 3.7: *Basic concepts underlying the MuonGasGun. (A) The ideal trajectory of muons orbiting in the storage ring is a perfect circle (black) due to the highly uniform magnetic field in the storage region. In Geant4, however, the simulated trajectory is approximated using many straight-line segments known as "chords" (red lines), where high-field regions require more chords. Only in the limit in which the number of simulation steps tends to infinity does the simulated trajectory approach the true dynamical trajectory. (B) Costly tracking steps are avoided by first randomly generating a muon decay time (based on the muon's energy) and mapping the decay time to a ring azimuthal position. The muon {position, momentum, spin} are then set at the decay point as if the muon had been tracked the full distance. The connection between a muon's initial longitudinal {position, momentum, spin} in the injected bunch and the muon's final {position, momentum, spin} at the decay vertex is made using equations from accelerator physics and spin dynamics. The muon is then forced to decay immediately, thus having avoided all costly tracking steps. In this way, simulating many muons automatically generates the correct decay-positron spectrum ("wiggle plot"), injected-muon-bunch-structure evolution (fast rotation), coherent betatron oscillation (CBO), and so on.*

are the momentum-dependent horizontal and vertical tunes and [52]

$$n \equiv \left(\frac{\rho_0}{v_0 B_0}\right)\frac{\partial E_x}{\partial x} \tag{3.21}$$

is the dimensionless quadrupole field index (strength) for electrostatic focusing discussed in §2.2.4. Note that since the quadrupole electric fields are linear with respect to the displacement from the storage-region center, $\mathbf{E} = (E_x, E_y) \propto (x, -y)$, the forces do not mix the horizontal and vertical coordinates, which is why Eqs. (3.18) and (3.19) are written separately instead of as one large matrix. Note also there is no vertical dispersion since the bend plane of the muon storage ring is in the horizontal midplane, which is why Eq. (3.19) is only two-dimensional whereas (3.18) involves the three coordinates $(x, x', \delta \equiv \Delta p/p_0)^T$. Once a random muon decay time has been generated, as shown in Fig. 3.7(B), Eqs. (3.18) and (3.19) are used to propagate the muon position and momentum to the decay vertex: the decay radius is $\rho = \rho_0 + x$, the momentum-magnitude is $p = (1+\delta)p_0$, and so on. The spin is then rotated using [22]

$$\boldsymbol{\omega} = \boldsymbol{\omega}_a + \boldsymbol{\omega}_{\mathrm{EDM}} = \boldsymbol{\omega}_a - \frac{q\eta}{2m}(\boldsymbol{\beta} \times \mathbf{B}) \tag{3.22}$$

where $\boldsymbol{\omega}_a = \boldsymbol{\omega}_s - \boldsymbol{\omega}_c$ is the spin precession angular frequency arising from the muon anomalous magnetic moment and η is a unitless constant proportional to the electric dipole moment (EDM) of the muon, $\mathbf{d}_\mu \equiv (\eta q/2mc)\mathbf{S}$. In this way, the time-consuming step of tracking the muons many hundreds if not thousands of turns is avoided.

When the injected muon beam is not kicked onto the storage orbit properly, the beam "wobbles" back and forth coherently about the design radius ($\rho_0 = 7112\,\mathrm{mm}$) in a sinusoid-like manner known as coherent betatron oscillation (CBO). The fundamental concept underlying horizontal CBO in the muon $g-2$ experiment, which arises from an under-kicked beam, is shown in Fig. 3.8. In the *MuonGasGun*, the user specifies FHiCL parameters $\{..., x_{\mathrm{inf}}, x_{\mathrm{eq}}, A_{\mathrm{CBO}x}, ...\}$, which are used to calculate the required kick in order to achieve the

desired beam CBO by evaluating Eq. (3.18) at 90° betatron phase advance,

$$\underbrace{\begin{pmatrix} x \\ x' \\ \delta \end{pmatrix}}_{\substack{\text{Beam at} \\ \text{kickers}}} = \underbrace{\begin{pmatrix} 0 & \frac{\rho_0}{Q_x} & \frac{\rho_0}{Q_x^2} \\ -\frac{Q_x}{\rho_0} & 0 & \frac{1}{Q_x} \\ 0 & 0 & 1 \end{pmatrix}}_{\substack{\text{Eq. (3.18) at 90°} \\ \text{betatron phase} \\ \text{advance}}} \underbrace{\begin{pmatrix} x_{\text{inf}} \pm A_{\text{CBO}x} \\ 0 \\ \delta = x_{\text{eq}}/[\rho_0/(1-n)] \end{pmatrix}}_{\substack{\text{User's FHiCL} \\ \text{parameters}}}, \tag{3.23}$$

where the $\{^{+}_{-}\}$ in the top row of the rightmost vector is for an $\{^{\text{over}}_{\text{under}}\}$-kicked beam, $\delta \equiv \Delta p/p_0$ is the fractional momentum offset from the design momentum $p_0 = 3.094\,35\,\text{GeV}/c$, $x_{\text{eq}} = \eta_x \delta$ is the beam equilibrium horizontal position, $\eta_x = \rho_0/(1-n)$ is the ring average horizontal dispersion, $n = (\rho_0/v_0 B_0)\,\partial_x E_x$ is the dimensionless quadrupole field index ("quad strength"), and $\rho_0 = 7112\,\text{mm}$ is the design radius. The kick required to achieve the user's desired horizontal CBO amplitude is then just the negative of the second row of Eq. (3.23). In the *MuonGasGun*, the user also specifies the Courant-Snyder parameters of the injected beam at the inflector as well as the emittance, dispersion and dispersion-derivative, which will be discussed in more detail in §3.3.3 when the creation of arbitrary phase-space distributions is discussed. Figure 3.7(B) shows how random muon decay times are generated by inverting the characteristic decaying-exponential lifetime of the muon,

$$P_{\text{alive}}(t) = \exp\left(-(t-t_0)/\gamma\tau\right) \qquad \Leftrightarrow \qquad t_{\text{decay}} = t_0 - \gamma\tau \log\left(n_{\text{rand}}\right), \tag{3.24}$$

where $n_{\text{rand}} \in [0,1)$ is a flat (uniform) random number, t_0 corresponds to the asymmetric or non-uniform time structure of the injected bunch, and $\gamma\tau$ is the dilated lifetime of the particular muon being simulated. The random decay time generated using Eq. (3.24) is then converted to a ring azimuthal angle using $\theta = \omega_c t_{\text{decay}}$, which is then inserted into Eqs. (3.18) and (3.19) to evolve the muon position and momentum while modeling the appropriate single-particle betatron oscillations along the way. The spin vector is rotated in a similar manner using Eq. (3.22). When many muons are simulated in this manner, the time-evolution of the injected bunch (including fast rotation), beam dynamics (including CBO), and "wiggle plot" all emerge automatically. A concrete example is shown in Fig. 3.9.

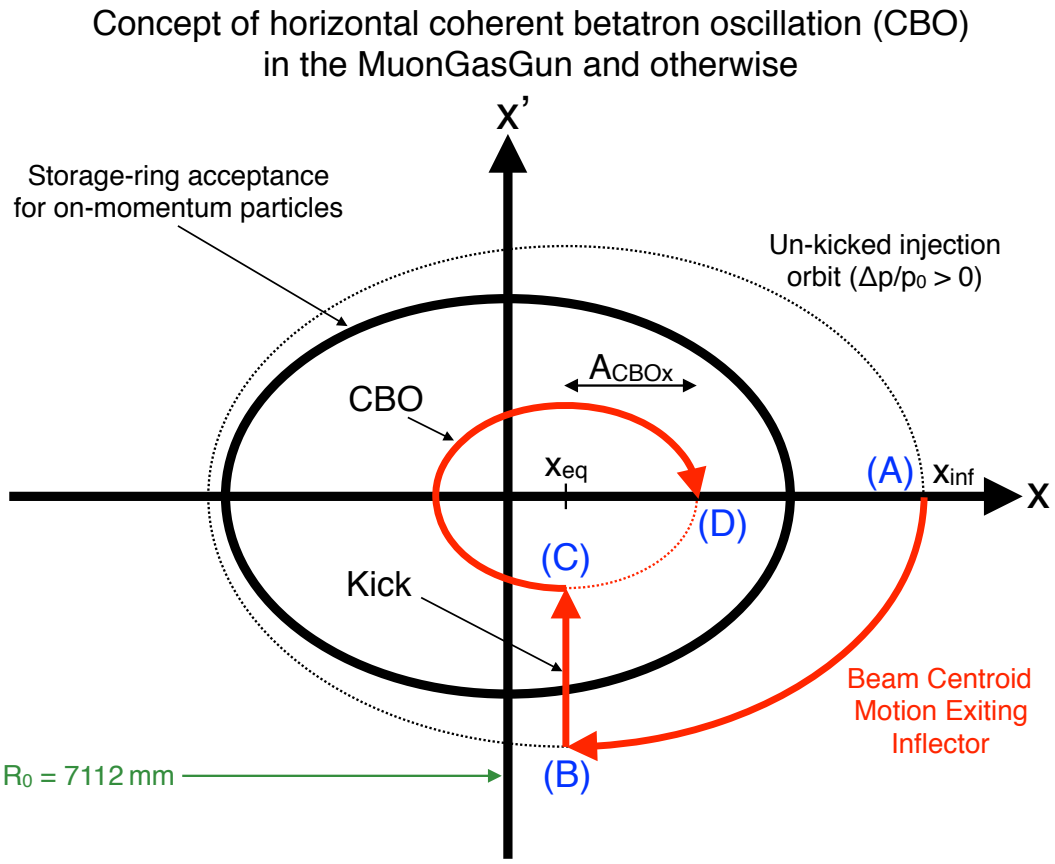

Figure 3.8: *Concept of horizontal coherent betatron oscillation (CBO) arising from an improperly kicked beam in the MuonGasGun and otherwise. The case of an underkicked beam is shown above. (A) In the MuonGasGun, the user specifies the beam centroid position at the inflector exit,* $x_{\rm inf}$*. (B) The beam is then orbited* 90° *betatron phase advance downstream to the kickers, where the beam receives an outward radial kick* $\Delta x' < x_{\rm inf}/7112\,{\rm mm} \lesssim 10.8\,{\rm mrad}$*, which is less than the kick required to place the beam on the proper storage orbit. (C) The underkicked beam then oscillates coherently around the equilibrium horizontal position,* $x_{\rm eq} = \delta\bar{\eta}_x$*, where* $\delta \equiv \Delta p/p_0$ *is the fractional deviation from the design momentum* $p_0 = 3.094\,35\,{\rm GeV}/c$ *and* $\bar{\eta}_x \equiv \rho_0/(1-n)$ *is the average horizontal ring dispersion that depends on the quadrupole field index* $n \equiv (\rho_0/v_0 B_0)\,\partial_x E_x$*. (D) The amplitude of the horizontal CBO is* $A_{{\rm CBO}x} \equiv \max(x - x_{\rm eq})$*. In the MuonGasGun, the user's* $\{x_{\rm inf}, x_{\rm eq}, A_{{\rm CBO}x}\}$ *specified by* FHiCL *parameters are used to calculate the required kick that will give rise to the desired horizontal CBO. The vertical CBO arising from injection offsets is also correctly modeled.*

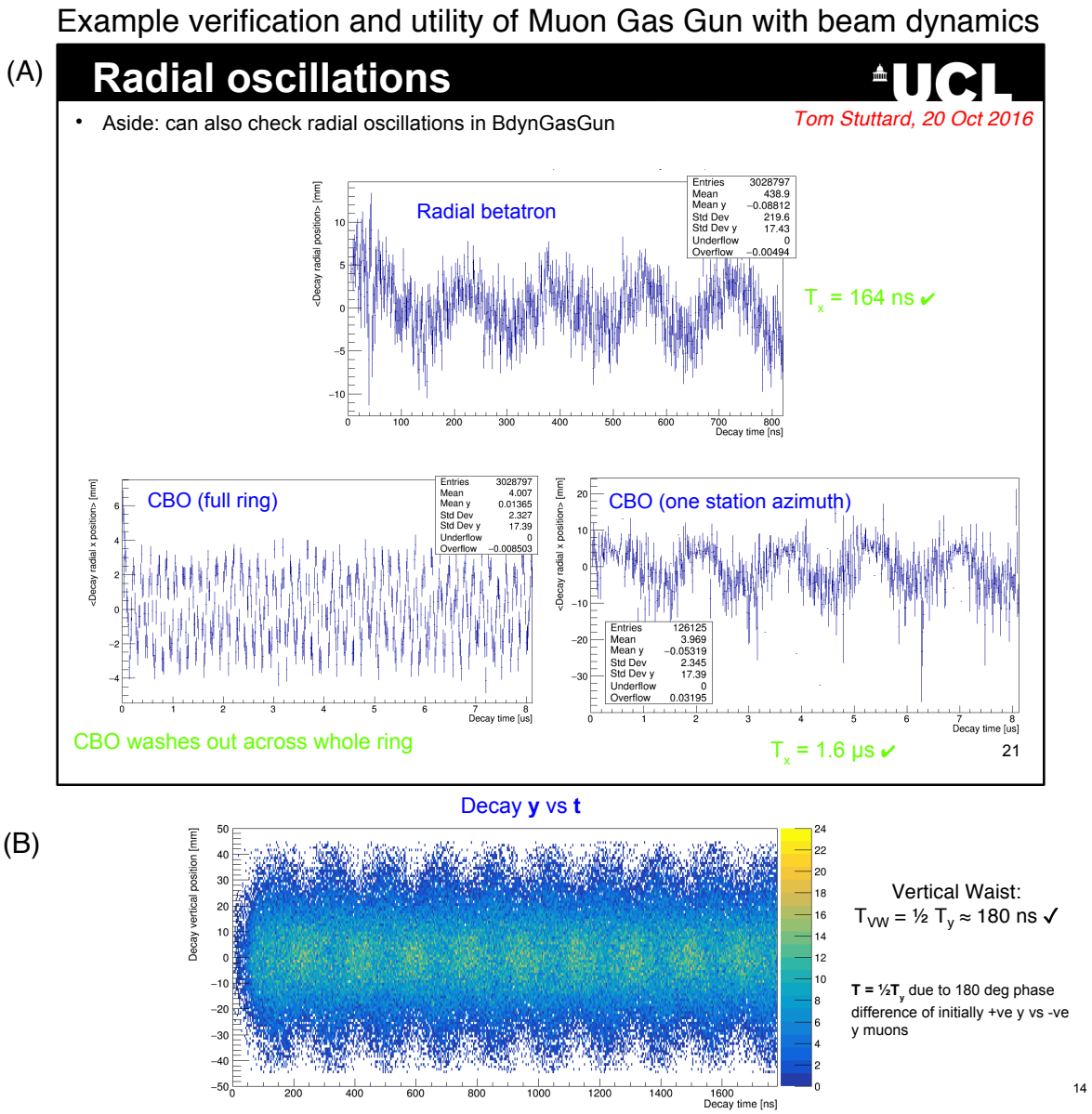

Figure 3.9: *Example verification and utility of Muon Gas Gun with beam dynamics, courtesy of the tracker team at the University College London [53]. (A) Radial oscillations. (B) Vertical oscillations. The above results were used for a review in late 2016.*

3.3.3 TheBeamGun: Realistic Particle Distributions at Injection

In order to optimize injection into the muon $g-2$ storage ring, the position offset and angle of the injected beam must be investigated in addition to the Courant-Snyder parameters and dispersion. Optimizing the beam position and angle corresponds to optimizing the beam centroid motion through the inflector, while optimizing the Courant-Snyder parameters and dispersion corresponds to optimizing the beam focusing through the inflector and matching to the lattice functions of the $g-2$ storage ring. The main purpose of this section is to discuss how such manipulations are performed in *gm2ringsim* and to make the connection with accelerator physics and Fermilab Accelerator Division. Additionally, for readers less familiar with accelerator physics, an alternative version of phase-space creation is discussed, in which the eigenvalues and eigenvectors of the covariance and/or correlation matrices are used to generalize the input distribution to an arbitrary number of particles.

The input phase-space distribution of muons for realistic injection simulations using *gm2ringsim* is shown in Fig. 2.8. This distribution was generated with a G4beamline tracking simulation from Fermilab Accelerator Division [30] in which positively charged primary, secondary, and tertiary particles ($p \rightarrow \pi^+ \rightarrow e^+$) are propagated from the Target through all beamlines to the end of M5, about 30 cm upstream of the storage ring. The beam parameters inherent in this distribution were established as baseline values for the Optics Review of Oct 2014 [54] using straightforward theoretical arguments and preliminary tracking results; it remains to be seen whether these beam parameters actually optimize injection into the storage ring, both in simulation and in reality. The ability to manipulate the Courant-Snyder parameters and dispersion of arbitrary input phase-space distributions is one of many features of a *gm2ringsim* tool that has become known as *TheBeamGun*.[11] *TheBeamGun* has enabled the E989 "Mock Data Challenges" for simulating realistic run conditions and developing sophisticated analyses, and it has emerged as an invaluable tool for understanding stored-beam profiles, momentum distributions, coherent betatron oscillations, etc. that are now central to the collaboration. Physically, manipulating the Courant-Snyder parameters and dispersion corresponds to adjusting beamline magnet currents. Since it is possible to measure the beam parameters in the M5 beamline (§4.2), results like the ones presented in this section allow for a direct connection to be established between simulation and Accelerator-Division magnets

[11] A. Chapelain, a post-doc at Cornell University in Ithaca, NY, coined this nickname.

and power supplies (§4.3), which play a critical part in getting beam to the experiment and optimizing injection into the muon $g-2$ storage ring.

The first step toward properly manipulating an input phase-space distribution like Fig. 2.8 is to calculate the covariance matrix, $\mathbf{\Sigma}_{ij} \equiv \langle (x_i - \bar{x}_i)(x_j - \bar{x}_j) \rangle$, which is related to the beam parameters in the following way [29]:

$$\mathbf{\Sigma} = \begin{pmatrix} \epsilon_x \beta_x + \eta_x^2 \sigma_\delta^2 & -\epsilon_x \alpha_x + \eta_x \eta_x' \sigma_\delta^2 & \eta_x \sigma_\delta^2 \\ -\epsilon_x \alpha_x + \eta_x \eta_x' \sigma_\delta^2 & \epsilon_x \gamma_x + \eta_x'^2 \sigma_\delta^2 & \eta_x' \sigma_\delta^2 \\ \eta_x \sigma_\delta^2 & \eta_x' \sigma_\delta^2 & \sigma_\delta^2 \end{pmatrix}. \tag{3.25}$$

Here, only the 3×3 subspace $(x, x', \delta \equiv \Delta p/p_0)$ of the 8-dimensional phase-space has been written for notational clarity.[12] Next, looking at the rightmost column of the above matrix, the dispersion and derivative (η_x, η_x') may be calculated by dividing by $\mathbf{\Sigma}_{\delta\delta} = \sigma_\delta^2$. More generally, *all* momentum dependence may be subtracted from the covariance matrix Eq. (3.25) using the clever formula

$$\boxed{\Sigma_{ij} - \frac{\Sigma_{i\delta}\Sigma_{j\delta}}{\Sigma_{\delta\delta}}} = \begin{pmatrix} \epsilon_x \beta_x & -\epsilon_x \alpha_x & 0 \\ -\epsilon_x \alpha_x & \epsilon_x \gamma_x & 0 \\ 0 & 0 & 0 \end{pmatrix} \quad \Rightarrow \quad \tilde{\mathbf{\Sigma}} \equiv \begin{pmatrix} \epsilon_x \beta_x & -\epsilon_x \alpha_x \\ -\epsilon_x \alpha_x & \epsilon_x \gamma_x \end{pmatrix}, \tag{3.26}$$

which reduces the full covariance matrix $\mathbf{\Sigma}$ in Eq. (3.25) to the simpler 2×2 matrix $\tilde{\mathbf{\Sigma}}$ on the right-hand side of Eq. (3.26). The beam emittance is then just

$$|\tilde{\mathbf{\Sigma}}| = \underbrace{(\beta_x \gamma_x - \alpha_x^2)}_{=1} \epsilon_x^2 = \epsilon_x^2, \tag{3.27}$$

where the Courant-Snyder invariant $\beta_x \gamma_x - \alpha_x^2 = 1$ has been used. Thus, the beam parameters of an arbitrary input phase-space distribution of particles may be calculated using

$$\boxed{\begin{array}{lll} \epsilon_x = |\tilde{\mathbf{\Sigma}}_{xx}|^{1/2}, & \beta_x = \tilde{\mathbf{\Sigma}}_{xx}/\epsilon_x, & \alpha_x = -\tilde{\mathbf{\Sigma}}_{xx'}/\epsilon_x, \\ \gamma_x = \tilde{\mathbf{\Sigma}}_{x'x'}/\epsilon_x, & \eta_x = \mathbf{\Sigma}_{x\delta}/\mathbf{\Sigma}_{\delta\delta}, & \eta_x' = \mathbf{\Sigma}_{x'\delta}/\mathbf{\Sigma}_{\delta\delta}, \end{array}} \tag{3.28}$$

[12] The relevant phase-space coordinates including spin are $(x, x', y, y', t, \delta, s_\theta, s_\phi)$, where $(s_x, s_y, s_z) \equiv (\sin\theta\cos\phi, \sin\theta\sin\phi, \cos\theta)$. Some authors write $\mathbf{s} = (s_x, s_y, s_z)$, however, the constraint $s_x^2 + s_y^2 + s_z^2 = 1$ implies there are only two degrees of freedom.

where $\mathbf{\Sigma}$ is the full covariance matrix, Eq. (3.25), and $\tilde{\mathbf{\Sigma}}$ is the betatron-only part of the covariance matrix, Eq. (3.26).

Once the beam parameters Eq. (3.28) have been calculated, the next step is to actually manipulate the distribution of particles. First, the momentum dependence must be subtracted from all particles' transverse phase-space coordinates. Remembering the phase-space coordinates are the sum of betatron and dispersion components,

$$\mathbf{x} = \mathbf{x}_\beta + \mathbf{x}_\delta = \begin{pmatrix} x \\ x' \end{pmatrix}_\beta + \delta \begin{pmatrix} \eta_x \\ \eta_x' \end{pmatrix}, \tag{3.29}$$

the calculated results for (η_x, η_x') from Eq. (3.28) may be used to write $\mathbf{x}_\beta = \mathbf{x} - \mathbf{x}_\delta$ for all particles in the distribution. The resulting phase-space vector $\mathbf{x}_\beta$ then transforms as

$$M_\beta \mathbf{x}_\beta = M_\beta \left(\mathbf{x} - \mathbf{x}_\delta \right), \tag{3.30}$$

where

$$\mathcal{M}_\beta = \begin{pmatrix} \sqrt{\frac{\beta_f}{\beta_i}} \left(\cos\phi_{fi} + \alpha_i \sin\phi_{fi} \right) & \sqrt{\beta_f \beta_i} \sin\phi_{fi} \\ \frac{-1}{\sqrt{\beta_f \beta_i}} \left[(\alpha_f - \alpha_i) \cos\phi_{fi} + (1 + \alpha_f \alpha_i) \sin\phi_{fi} \right] & \sqrt{\frac{\beta_i}{\beta_f}} \left(\cos\phi_{fi} - \alpha_f \sin\phi_{fi} \right) \end{pmatrix}. \tag{3.31}$$

is a standard result found in any accelerator-physics textbook. Here, the subscripts denote the initial and final parameters, and $\phi_{fi} \equiv \phi_f - \phi_i$ is the betatron phase advance. The author much prefers to write Eq. (3.31) as

$$\mathcal{M}_\beta = \underbrace{\begin{pmatrix} \sqrt{\beta_f} & 0 \\ -\alpha_f/\sqrt{\beta_f} & 1/\sqrt{\beta_f} \end{pmatrix}}_{=\mathcal{F}^{-1}} \underbrace{\begin{pmatrix} \cos\phi_{fi} & \sin\phi_{fi} \\ -\sin\phi_{fi} & \cos\phi_{fi} \end{pmatrix}}_{=R(\phi)} \underbrace{\begin{pmatrix} 1/\sqrt{\beta_i} & 0 \\ \alpha_i/\sqrt{\beta_i} & \sqrt{\beta_i} \end{pmatrix}}_{=\mathcal{F}} \tag{3.32}$$

which has the following clear conceptual meaning:

1. The right-most matrix $\mathcal{F}$ in Eq. (3.32) is known as a "Floquet transform" that reduces the beam to a circle of radius $r_{xx'} = \sqrt{\epsilon_x}$ in phase space. Note the area of the phase-space ellipse is preserved, $A = \pi r_{xx'}^2 = \pi \epsilon_x$, since the determinant is $\|\mathcal{F}\| = 1$.

2. The middle matrix $R(\phi)$ in Eq. (3.32) is the betatron phase advance, which is nothing

more than a clockwise rotation. For symmetric particle distributions, the rotation is trivial since circles are invariant under rotation. (This was the purpose of performing Step 1 above.)

3. The left-most matrix $\mathcal{F}^{-1}$ in Eq. (3.32) is the inverse Floquet transform that converts the circular phase space from Step 2 to the user's arbitrary desired Courant-Snyder parameters. The determinant of the matrix is $\|\mathcal{F}^{-1}\| = 1 = \|\mathcal{F}\| = \|R\|$, so the area of the phase space ellipse is preserved by the total transformation Eq. (3.31). Stated differently, magnetic fields do no work, and energy is conserved.

The very last step is to add the user's desired dispersion and derivative $(\eta, \eta')_{x,y}$ to the phase space using Eq. (3.29). In this way, the phase-space coordinates of an arbitrary input distribution of particles may be properly transformed to any desired Courant-Snyder parameters, dispersion (plus derivative), and phase advance. The open-source, super-fast C^{++} template library for linear algebra EIGEN [55] was introduced into *gm2ringsim* to perform the phase-space manipulations described above.

TheBeamGun is the default particle source for the E989 collaboration's official *Art*-based simulation, *gm2ringsim*. *TheBeamGun* has been used on many occasions to provide insight on optimizing injection into the muon $g-2$ storage ring as well as the resulting stored-muon beam distribution. Figure 3.10 is one such example showing that, although the muon $g-2$ storage ring has $\bar{\eta}_x = \rho_0/(1-n) \approx 8.1\,\text{m}$ average horizontal dispersion (at QHV = 20.2 kV), the beam prefers $\eta_x = 0\,\text{m}$ at injection. This constitutes a rather large injection mismatch in the eyes of most accelerator physicists since it leads to a large dispersion wave propagating around the ring,

$$\begin{pmatrix} \eta_x(\theta) \\ \eta'_x(\theta) \\ 1 \end{pmatrix} = \begin{pmatrix} \cos(Q_x\theta) & \frac{\rho_0}{Q_x}\sin(Q_x\theta) & \frac{\rho_0}{Q_x^2}(1-\cos(Q_x\theta)) \\ -\frac{Q_x}{\rho_0}\sin(Q_x\theta) & \cos(Q_x\theta) & \frac{1}{Q_x}\sin(Q_x\theta) \\ 0 & 0 & 1 \end{pmatrix} \begin{pmatrix} \eta_x(0) \\ \eta'_x(0) \\ 1 \end{pmatrix}, \tag{3.33}$$

where $Q_x = \sqrt{1-n}$ is the horizontal tune. If injection really prefers $(\eta_x, \eta'_x) = (0,0)$ as claimed by Fig. 3.10(A), then the maximum dispersion in the ring is $\max(\eta_x) = 2\bar{\eta}_x = 2\rho_0/Q_x^2$, as can be seen from the upper-right entry of the matrix in Eq. (3.33). Physically, the cause of the large dispersion mismatch is the narrow $18(\text{W})\times56(\text{H})\,\text{mm}^2$ aperture of the

1.7-m inflector. For example, if the fractional momentum offset is $\delta \equiv \Delta p/p_0 = +0.1\,\%$, the displacement would be $\Delta x = \bar{\eta}_x \delta = 8\,\text{mm}$ in the inflector beam channel if the beam were dispersion-matched to the muon storage ring at injection. This is a serious problem since the inflector aperture is only $\pm 9\,\text{mm}$ horizontally, leading to significant losses due to scraping in the inflector beam channel.[13] Thus, in the competition between scraping in the inflector beam channel vs. scraping in the ring due to horizontal dispersion, the scraping in the inflector is more costly, so injection prefers $\eta_x = 0\,\text{m}$ in order to maximize stored particles in the ring, as shown in Fig. 3.10. Here, the terms "muon capture efficiency" and/or "muon storage fraction" (f_{store}) refer to the number of particles remaining within the muon storage region (i.e. a torus of major radius $R_0 = 7112\,\text{mm}$ and minor radius $r_0 = 45\,\text{mm}$) after a prescribed number of turns (typically 20), without quad scraping, divided by the number of particles injected into the ring,

$$f_{\text{store}} \equiv \left.\frac{N_{\text{store}}(t)}{N_{\text{inject}}}\right|_{t=20\,\text{Turns}}. \tag{3.34}$$

Another interesting result obtained using *TheBeamGun* and *gm2ringsim* is shown in Fig. 3.11. The optimal focusing of the muon beam into the $g-2$ storage ring prefers a long, narrow, highly correlated ridge of Courant-Snyder parameters (β, α) for both transverse planes. Similar arguments made for dispersion vs. inflector (i.e. one paragraph above and Fig. 3.10) apply here as well: In the competition between matching the beam to the lattice functions of the ring $(\bar{\beta}_x, \bar{\beta}_y) = \rho_0(Q_x^{-1}, Q_y^{-1}) = (7.6\,\text{m}, 20.6\,\text{m})$ at QHV $= 20.2\,\text{kV}$ and fitting the beam through the narrow inflector transverse aperture $(\Delta x, \Delta y)_{\text{inf}} = (18\,\text{mm}, 56\,\text{mm})$, more muons are captured when the beam is focused to a horizontal waist near the longitudinal midpoint of the 1.7-m inflector ($\beta_x \approx (9\,\text{mm})^2/\epsilon_x = 2.0\,\text{m}$) rather than matched to the ring ($\beta_x = 7.6\,\text{m}$).[14] For the vertical focusing, other factors such as the geometrical admittance of the ring (which also involves the (β_x, η_x) waves mentioned above) lead to smaller optimal values of β_y compared to the matched case.

A final example of the utility of *TheBeamGun* is shown in Fig. 3.12, which also estab-

[13] Note, this result does not include any betatron amplitude, which makes matters worse. Additionally, the magnetic-field gradient in the inflector beam channel is horizontally defocusing, which also makes matters worse.

[14] For large injection β_x, one must also be mindful of the 4-inch hole in the backleg yoke of the muon storage-ring magnet iron.

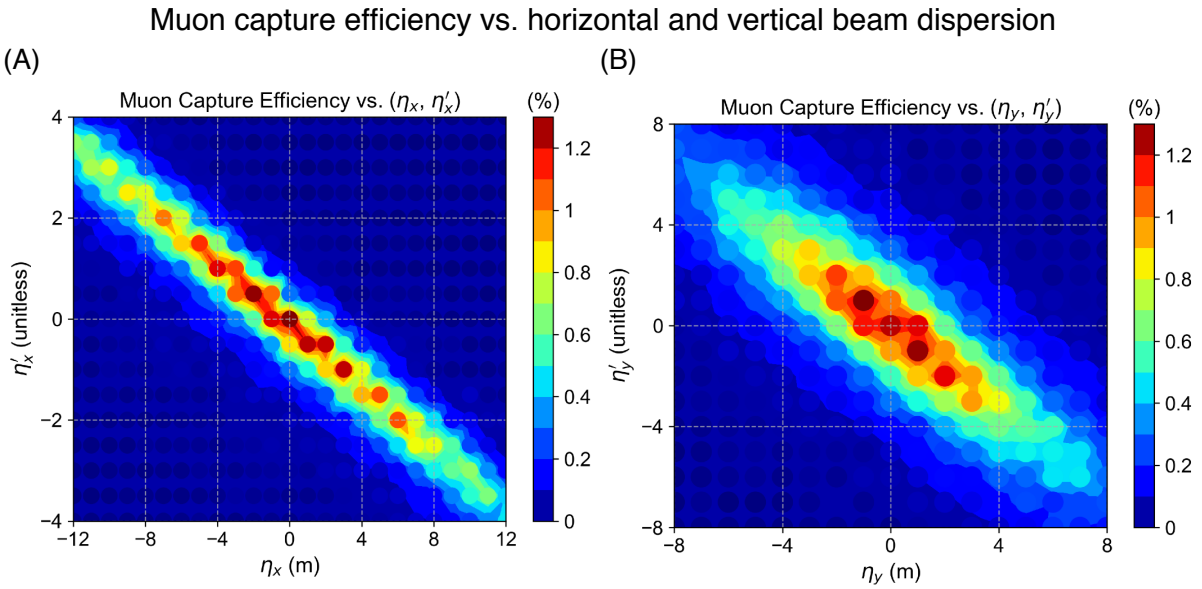

Figure 3.10: *Muon capture efficiency vs. horizontal and vertical beam dispersion at the entrance of the $g-2$ storage ring. Each data point is a simulation of $\mathcal{O}(10^5)$ injected muons run on Fermigrid, a supercomputer. The simulation starts at $\Delta s = -4.3\,\mathrm{m}$ upstream of the inflector exit, i.e. about $30\,\mathrm{cm}$ upstream of the storage-ring magnet iron. TheBeamGun is used to investigate arbitrary Courant-Snyder parameters and dispersion. (A) Muon capture efficiency vs. horizontal beam dispersion (η_x, η'_x). Injection prefers zero dispersion and derivative even though the average horizontal dispersion of the muon storage ring is nominally $\eta_x = \rho_0/(1-n) = 8.1\,\mathrm{m}$. Although this mismatch leads to a large dispersion wave propagating in the muon $g-2$ storage ring, Eq. (3.33), it minimizes beam scraping in the narrow $18(W)\times 56(H)\,\mathrm{mm}^2$ inflector channel, ultimately leading to more muons being captured in the ring. (B) Muon capture efficiency vs. vertical beam dispersion (η_y, η'_y). Injection prefers zero vertical dispersion, as expected, since the muon storage ring does not bend the particles vertically. The prominent anti-correlation of $(\eta, \eta')_{x,y}$ is present in both plots above since more muons are stored if the dispersion is being focused into the ring.*

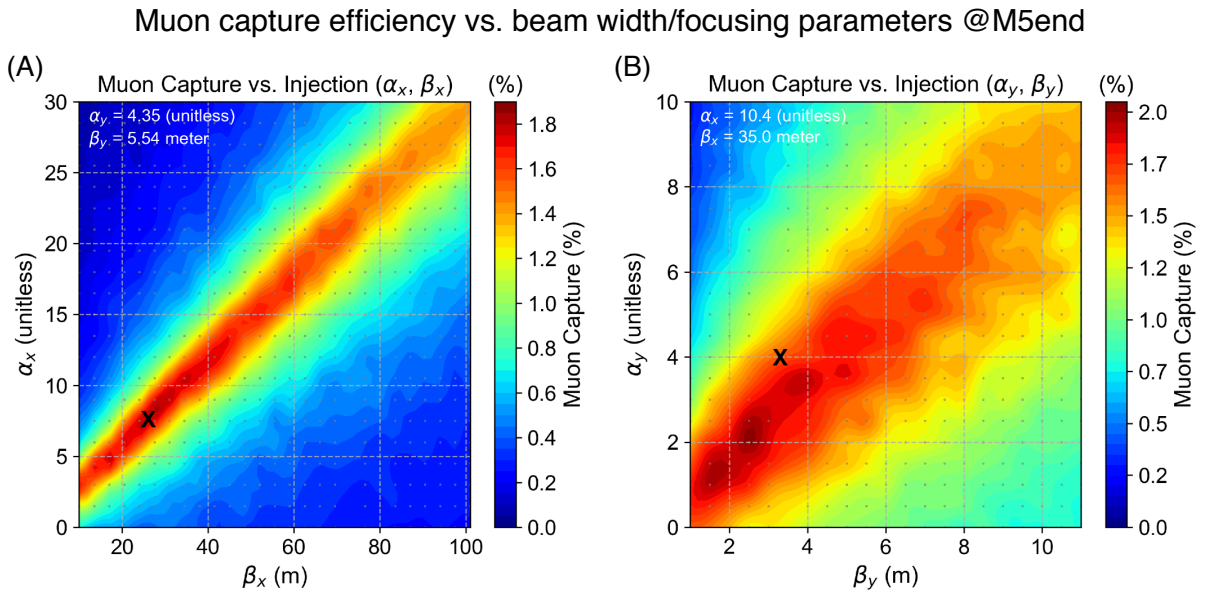

Figure 3.11: *(A) Muon capture efficiency vs. Courant-Snyder parameters* (β_x, α_x) *at the entrance of the storage ring. (B) Muon capture efficiency vs. Courant-Snyder parameters* (β_y, α_y) *at the entrance of the storage ring. The strong linear correlation arises in both plots because the beam must be made physically small in order to mitigate losses due to scraping in the narrow inflector beam channel* $(18(W)\times 56(H)\,\mathrm{mm}^2)$*. The black "X" marks are the measured beam parameters at the entrance of the muon storage ring, which served as the starting point of a more sophisticated tuning study discussed in* §4.3.

lishes the connection to the real experiment. Simulations indicates a long, narrow band of acceptable (x, x'), which reflects the narrow 18 mm aperture of the 1.7-m inflector, as shown in Fig. 3.12(A). Simulations also predict the beam prefers to be displaced horizontally by $\Delta x \simeq 10$ mm to 15 mm toward the "beam right" (i.e. smaller ring radius), which is consistent with observations, as shown in Fig. 3.12(B). Simulation also predicts the beam prefers to be injected with a slightly positive angle $\Delta x \simeq 2$ mrad to 3 mrad, which is also consistent with observations, as shown in Fig. 3.12(C). Thus, *TheBeamGun* and *gm2ringsim* seem to be doing a good job at faithfully representing trends in optimizing muon injection into the $g-2$ storage ring.

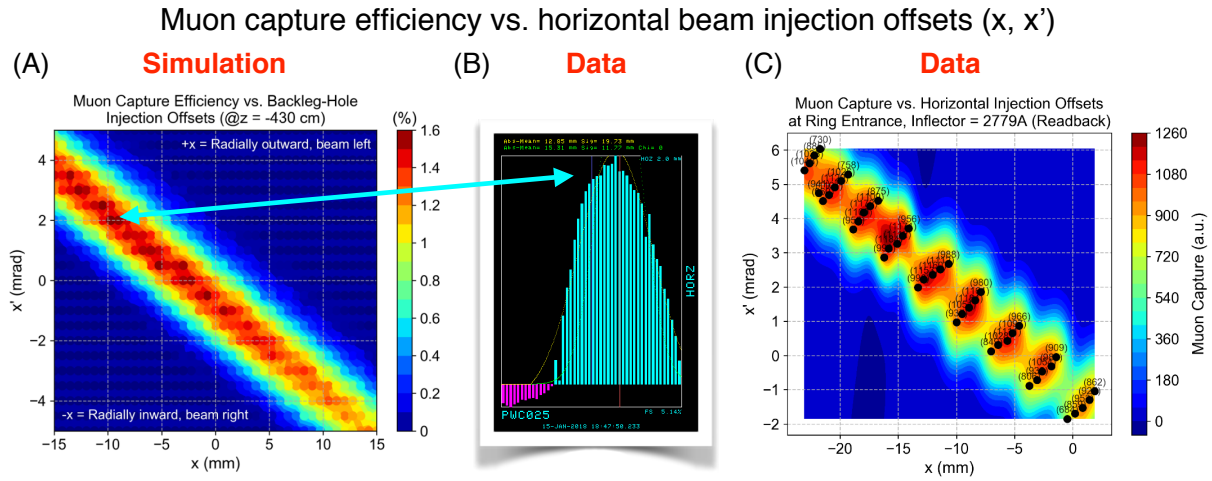

Figure 3.12: *Muon capture efficiency vs. horizontal beam injection offsets* (x, x'). *(A) Results from gm2ringsim. (B) Example profile from PWC025 immediately upstream of the muon storage ring. (C) Reconstructed* (x, x') *using the IBMS{1,2} detectors. Simulation and observation agree the beam prefers to be injected toward the "beam right" (smaller ring radius) with a slightly radially outward angle.*

3.4 Selected Design Studies

Many of the simulation tools written by the author of this thesis have been used by the collaboration to perform realistic studies that have led to real design decisions and improvements in the experiment. An example was shown in Fig. 3.9 for the straw trackers. The

purpose of this section is to give a more in-depth overview of the author's own personal studies that have impacted the experiment in an appreciable way. Here, the emphasis will be on muon injection and storage optimization, since performing the Fermilab muon $g-2$ experiment will require a 21-fold increase in recorded muon-decay events over the previous BNL experiment.

3.4.1 Quadrupole Electrodes and Supports

As was discussed in §2.2.4, the purpose of the electric quadrupoles is to provide weak vertical focusing that prevents the muon beam from diverging out of the ring and being lost. The 28-pole expansions of the quadrupole electric potentials employed in the *gm2ringsim* unified-field approach are shown in Fig. 3.13. A tabulated field map calculated using the open-source finite-element code *FEMM* [56] is used for the region outside the electrodes. The fields are controllable via input parameter to arbitrary order (in both upright and skew multipoles), arbitrary field index $n \equiv (\rho_0/v_0 B_0)\,\partial_x E_x$, arbitrary RC scraping time constants τ_{RC} per quad, etc.

When the beam is injected into the muon storage ring, the beam must physically pass through the Q1-outer electrode and supports, as shown in Fig. 3.14. The E821 Q1-outer electrode was 0.10-0.13 mm aluminum, while the supports were cylinders of Macor ceramic (an insulator) with $d = 1$ cm and with the axis of the cylinder oriented in the radial direction in the horizontal midplane of the storage ring [52]. Muons at 3.1 GeV/c are minimum-ionizing particles (MIPs), so the harmful effect of the Q1-outer electrode and supports on the muon capture efficiency was thought to be small. The author of this thesis was the first to realize the effect was much larger than the $\sim$10 % previously thought [57, 58, 59, 60]. The Q1-outer electrode and supports were redesigned as a direct result of this discovery. The effect of the quad supports on muon storage and the gains from the redesigned supports are summarized in Fig. 3.15. The effect of the Q1-outer electrodes on muon storage and the gains from the redesigned electrode are summarize in Fig. 3.16. The final design of the Q1-outer electrode is 0.001-inch thick aluminized mylar, and the support material has been entirely removed from the beam path, as shown in Fig. 3.17 [61]. The redesigned standoffs should increase muon storage by 20-25%, while the redesigned electrodes should increase muons by another 20-25%, making for a combined increase of 40-50% more stored muons.

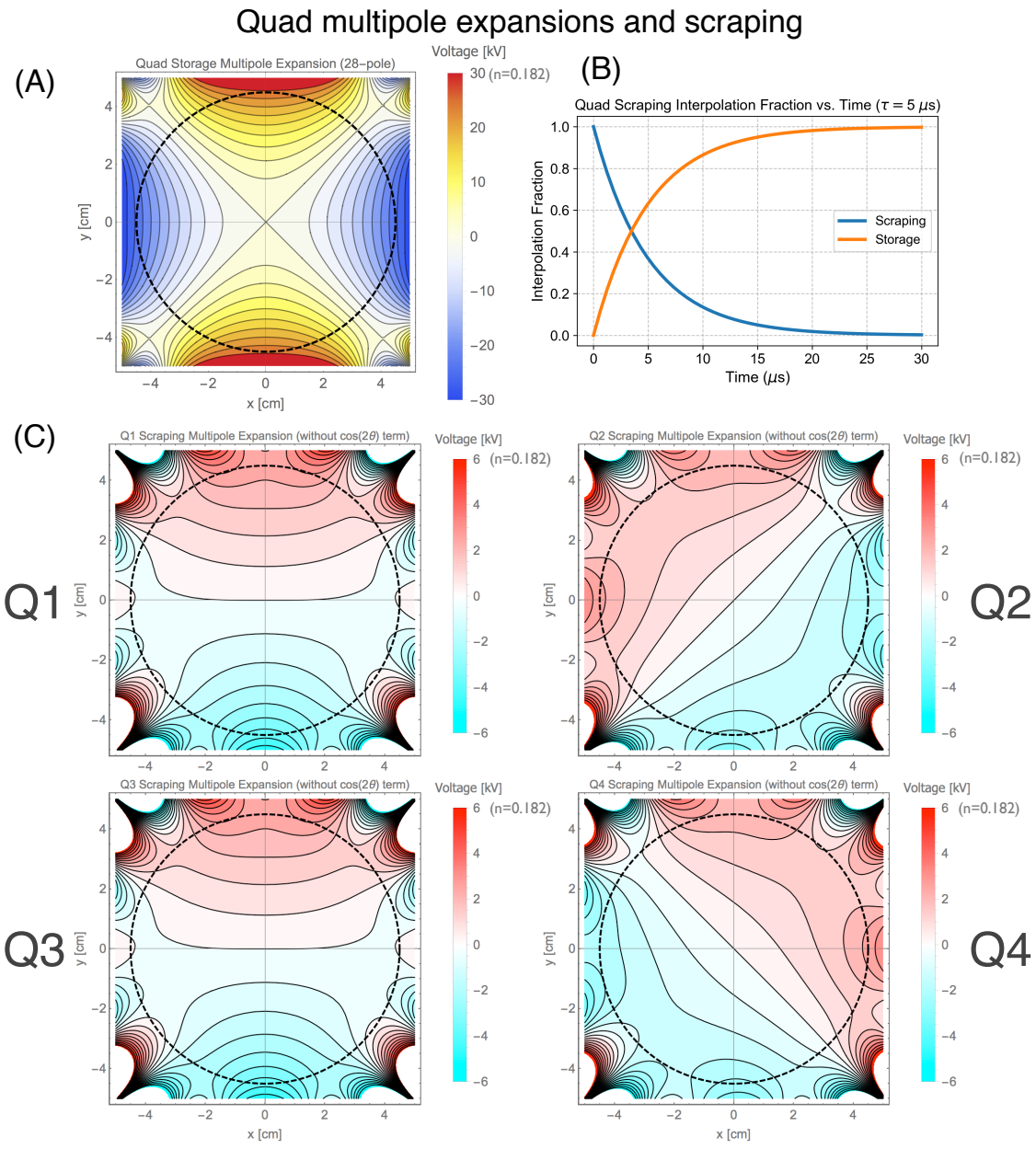

Figure 3.13: *(A) Quad multipole expansion for μ^+ storage. The region outside the electrodes is handled with a field map. The nominal E989 voltage is $\pm 20.2\,\mathrm{kV}$. (B) Example scraping time structure and interpolation fractions. The model is a simple RC circuit with a default time constant of $\tau_{RC} \sim 5\,\mu\mathrm{s}$. (C) Scraping multipoles, excluding $\cos(2\theta)$ term [52, 62]. The beam is pushed down by 2-3 mm on average, and the radial E-field oscillates once per turn since the horizontal tune is $Q_x = \sqrt{1-n} \sim 1$.*

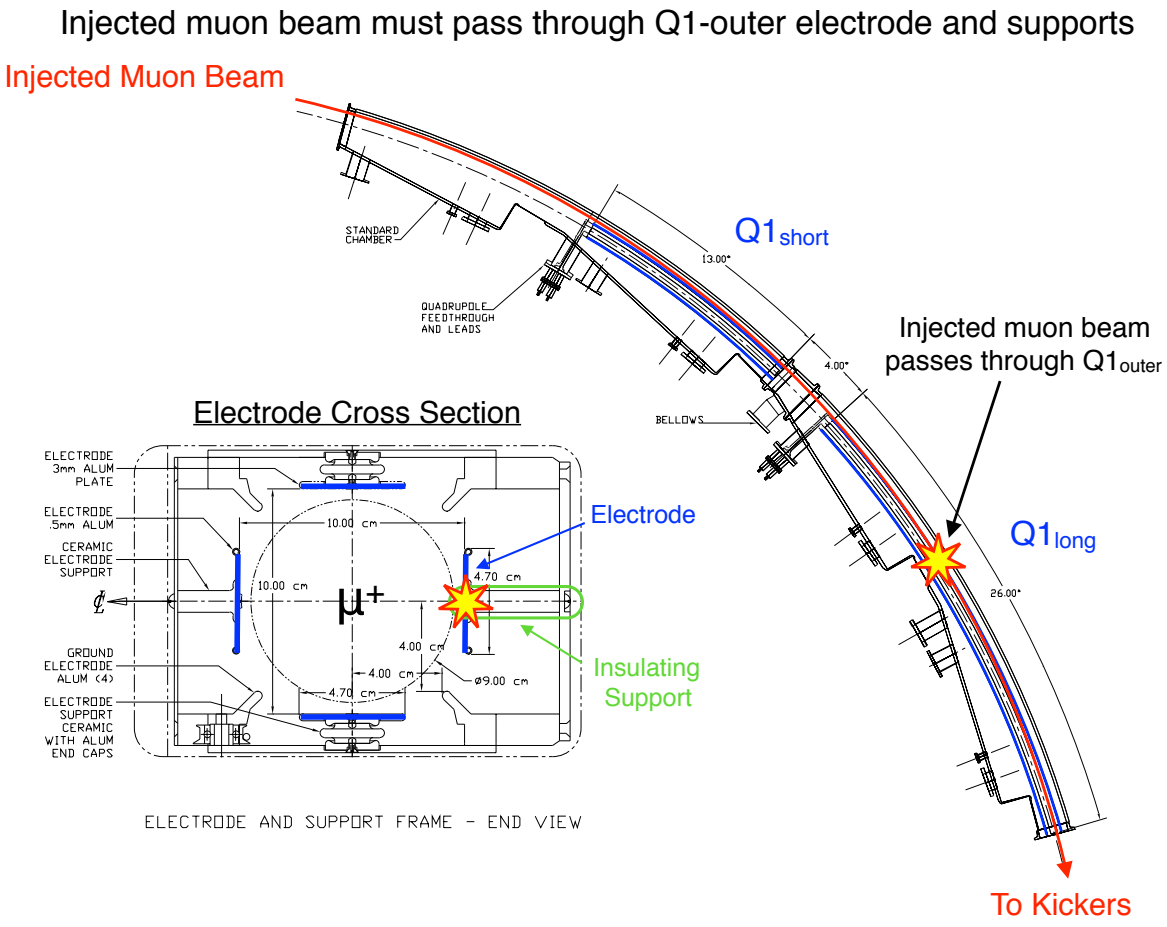

Figure 3.14: *The injected muon beam must physically pass through the outer electrode of Q1. In E821, the Q1-outer electrode was 0.115 mm aluminum, however, since the beam penetrates at such a shallow angle, the actual amount of material experienced by the beam is considerably larger (∼1 cm). The beam must also penetrate through the Macor insulating supports (d=1 cm) to which the electrode is fastened.*

(A)

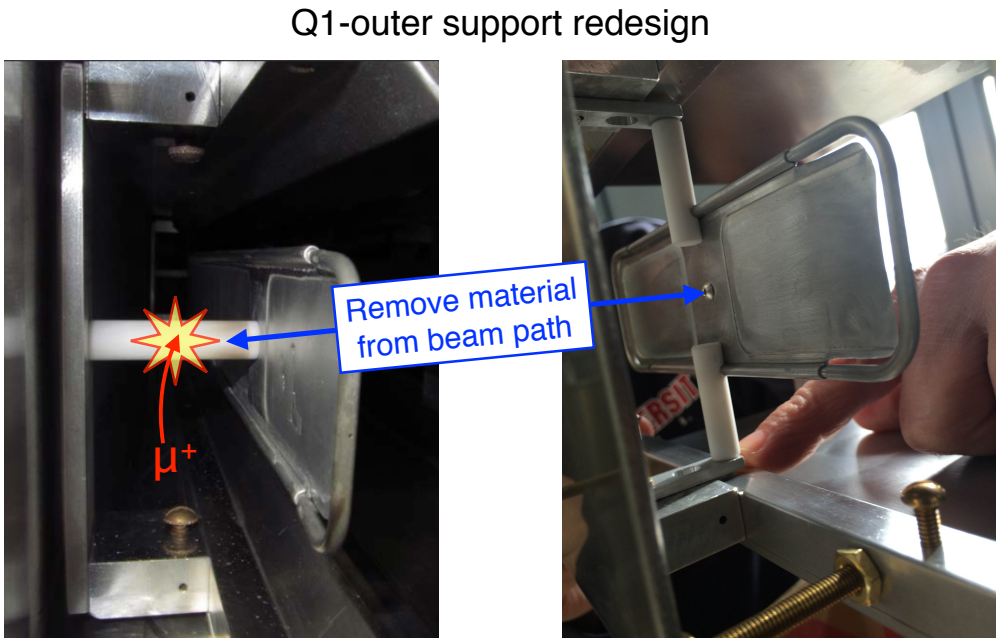

(B)

Config	Q1SO	x(cm)	Standoff	Q1LO	x(cm)	Standoff	Ninject	Nstore	fstore (%)	δstore (%)	Change (%)
0	Al	5.0	E821	Al	5.0	E821	200,000	4613	**2.31**	0.03	–
1	Al	5.0	E989	Al	5.0	E821	200,000	5154	**2.58**	0.04	12
2	Al	5.0	E821	Al	5.0	E989	200,000	4941	**2.47**	0.04	7
3	Al	5.0	E989	Al	5.0	E989	200,000	5674	**2.84**	0.04	23

Figure 3.15: *Q1-outer support redesign. (A) Nominal E821 design (left) and prototype new design (right). The new design effectively removes all material from the injection beam path, preventing losses due to emittance blowup. (B) Using the new design for both the Q1-short-outer (Q1SO) electrode and Q1-long-outer (Q1LO) results in a gain of 20-25% more stored beam over the nominal design according to simulation.*

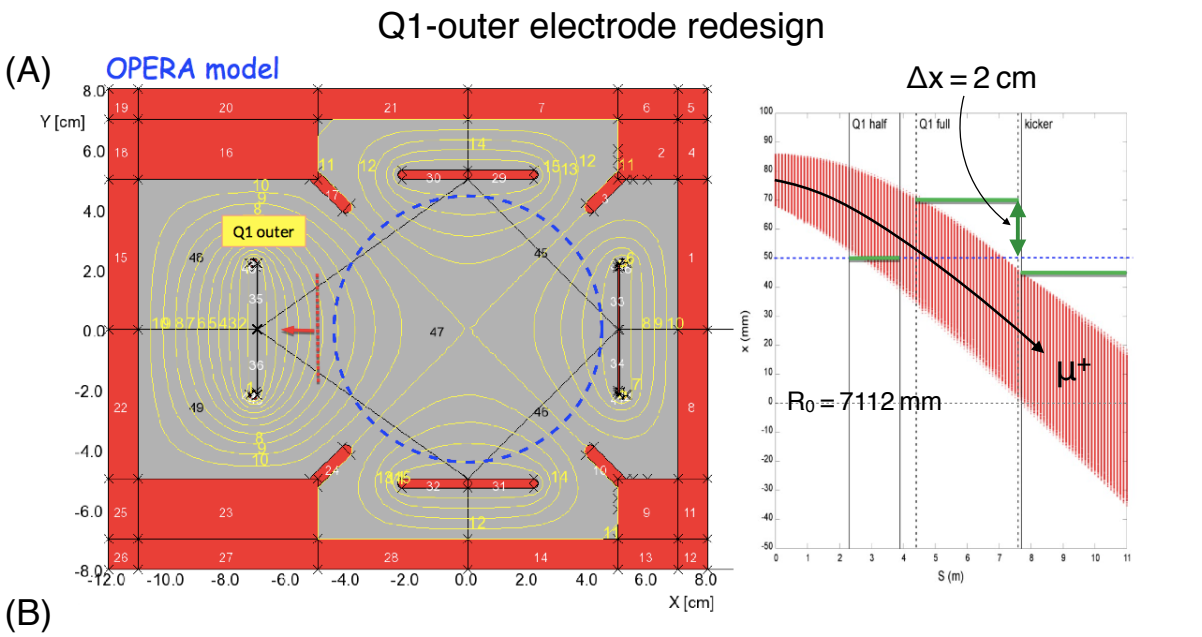

(B)

Config	Q1SO	x(cm)	Standoff	Q1LO	x(cm)	Standoff	Ninject	Nstore	fstore (%)	δstore (%)	Change (%)
3	Al	5.0	E989	Al	5.0	E989	200,000	5674	**2.84**	0.04	23
10	Al	5.0	E989	Al/Be	5.0	E989	200,000	6266	**3.13**	0.04	36
11	Al	5.0	E989	Be	5.0	E989	200,000	6586	**3.29**	0.04	43
12	Al/Be	5.0	E989	Al	5.0	E989	200,000	5630	**2.82**	0.04	22
13	Al/Be	5.0	E989	Al/Be	5.0	E989	200,000	6391	**3.20**	0.04	39
14	Al/Be	5.0	E989	Be	5.0	E989	200,000	6722	**3.36**	0.04	46
15	Be	5.0	E989	Al	5.0	E989	200,000	5652	**2.83**	0.04	23
16	Be	5.0	E989	Al/Be	5.0	E989	200,000	6402	**3.20**	0.04	39
17	Be	5.0	E989	Be	5.0	E989	200,000	6674	**3.34**	0.04	45

Final Design: New E989 standoffs, 0.001" aluminized-mylar electrode, gain >45%

Figure 3.16: *Q1-outer electrode redesign. The nominal electrode configuration is 0.10-0.13 mm aluminum. (A) Early designs called for radially displacing Q1-long-outer from $x = 5$ cm to a final location of $x = 7$ cm, however, this change would have doubled the quad voltage, $(7\,\text{cm}/5\,\text{cm})^2 = 2$, which was not achievable. (B) The next iteration of designs called for changing the material of both Q1-long- and Q1-short-outer.*

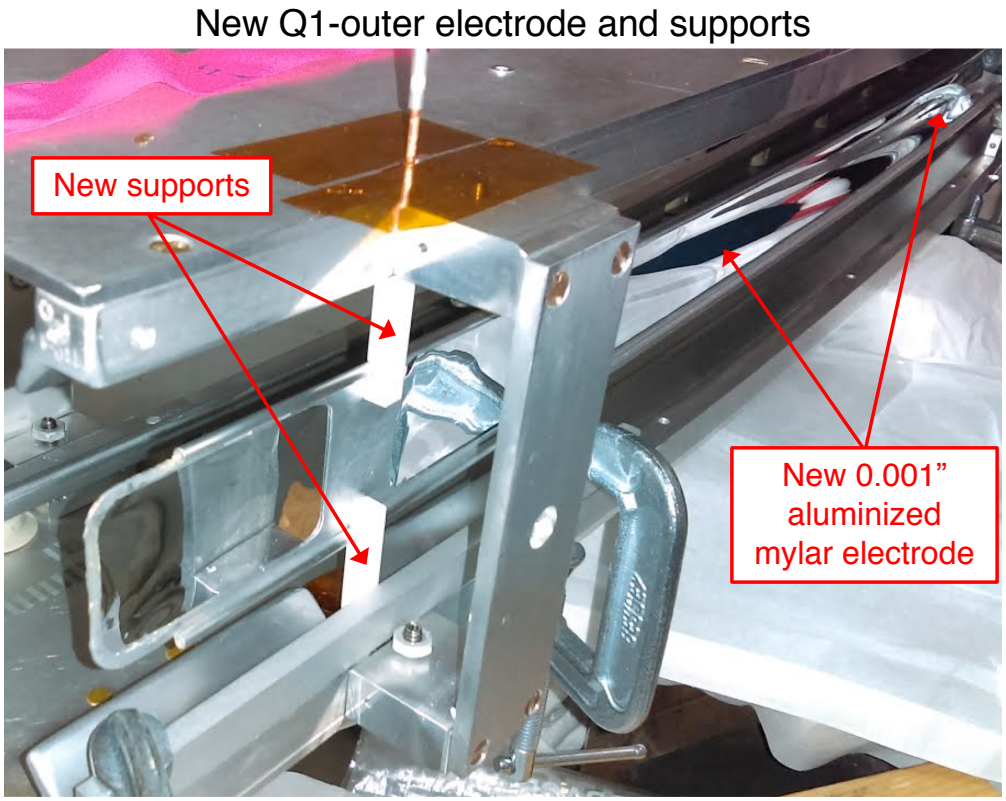

Figure 3.17: *New Q1-outer electrode and supports as built [61]. The electrode is 0.001-inch aluminized mylar, and the support material is entirely removed from the beam path.*

3.4.2 Pulsed Kicker Magnets

The pulsed kicker magnets located 90° downstream from the inflector exit deflect the momentum of the beam $\Delta x' \simeq 10.8\,\text{mrad}$ radially outward in order to place the injected beam on the storage orbit for the data-recording period, as discussed in §2.2.3. The kicker fields essentially consist of two parts: (1) the Blumlein circuit, which generates the time structure of the kicker pulse, and (2) the electrode geometry, which generates the "shape" of the **B**-field as current flows longitudinally on the skin of the aluminum electrodes. The conceptual design for the new kicker electrodes and circuit had already been proposed by Cornell University [63] when the author went to visit in late 2013 to help optimize the kicker-electrode geometry similar to §3.4.1 and help write the BMAD tracking simulation.[15] The design improvements to the electrode geometry will be discussed in this section, whereas the design improvements to the Blumlein circuits will be postponed to §4.4 (Commissioning) since the author's only direct involvement with the kicker Blumlein circuits was in the Spring of 2018 during commissioning.

Figure 3.18 shows a comparison between the {E821, E989} kicker electrodes and the resulting transverse **B**-field profiles calculated by the author using *FEMM* [56]. Three features stand out: (1) the E989 electrodes have a much smaller cross-sectional area than the E821 electrodes; (2) the E989 electrodes are as close as possible to the muon storage region ($r_0 = 45\,\text{mm}$); and (3) the E989 electrodes are curved, whereas the E821 electrodes are flat. The reasons for these differences are nicely codified in the expression

$$A^\mu(\mathbf{r}, t) = \frac{\mu_0}{4\pi} \int \frac{j^\mu(\mathbf{r}', t_r)}{|\mathbf{r} - \mathbf{r}'|}\, d^3\mathbf{x}', \tag{3.35}$$

where $A^\mu = (V/c, \mathbf{A})$ is the 4-potential, $j^\mu = (\rho c, \mathbf{j})$ is the 4-current density,[16] and $t_r = t - |\mathbf{r} - \mathbf{r}'|/c$ is the retarded time [4]. In E821, it was realized the kickers were not giving the required $\int B_y d\ell \simeq 0.112\,\text{T m}$ to achieve the nominal outward radial kick of $\Delta x' \simeq 10.8\,\text{mrad}$, so one way of increasing the magnetic field $\mathbf{B} = \boldsymbol{\nabla} \times \mathbf{A}$ is to increase the current *density*, i.e. increasing j^μ in the numerator of Eq. (3.35), which has everything to do with the physical smallness of the E989 plates compared to the E821 plates. For example, looking

[15] The quad-electrode studies in §3.4.1 required a realistic input phase-space distribution, which the author learned about remotely from Prof. D. Rubin at Cornell [64].

[16] A stationary electric charge is a current purely polarized in time.

at Fig. 3.18(A), the E821 electrodes are ∼10 cm tall, whereas the E989 electrodes span an arc length of $r\theta \sim 5$ cm, so the E989 electrodes will have roughly a factor of $10/5 = 2$ higher current *density* for the same unit current compared to the E821 electrodes. This simple calculation agrees well with the gauss-per-kiloamp results shown in Fig. 3.18(B, right). Another way to increase the magnetic field strength is to place the electrodes as close as possible to the muon storage region, i.e. decrease the denominator of Eq. (3.35). This is why the E989 electrodes are as close as possible to the muon storage region. Lastly, it is trivial to show a cosine-theta current distribution gives rise to a pure dipole magnetic field,[17] which is why the E989 kickers are based on a simple cosine-theta design in which the dipole kicker field opposes the dipole ring field over the duration of the kicker pulse.

In simulations the kicker field is approximated as $\mathbf{B}(t, x, y, z) \approx T(t) \otimes (B_x(x, y), B_y(x, y))$, where the pulse time structure $T(t)$ is the measured kicker pulse like shown in Fig. 2.15 and the transverse **B**-field is the tabulated field like shown in Fig. 2.15 or Fig. 3.18. Here, the longitudinal dependence of the field is ignored for simplicity ("hard edge" model) since BMAD is a lattice-oriented code. The effect of the curved kicker plates on the injected muon phase space is shown in Fig. 3.19. In order to mitigate the effects of the sextupole and higher-order multipoles shown in Fig. 3.19(C), the author tried (1) shifting the outer electrode to larger radii similar to Fig. 3.16(A), and (2) decreasing the radius of curvature of the outer E989 kicker plate to make it flatter like the E821 electrode. Ultimately these design modifications spoiled the field strength and/or uniformity, so the decision was made to build the cosine-theta-based kicker plates shown in Fig. 2.15 in order to achieve the $\int B_y d\ell \simeq 0.112\,\mathrm{T\,m} \rightarrow \Delta x' \simeq 10.8$ mrad nominal outward radial kick required in the Fermilab muon $g-2$ experiment.

[17] The region between the kicker electrodes is free of sources, so $\boldsymbol{\nabla} \times \mathbf{B} = \mathbf{0}$ implies $\mathbf{B} = -\boldsymbol{\nabla}\psi$, and $\boldsymbol{\nabla} \cdot \mathbf{B} = 0$ implies $-\nabla^2\psi = 0$, in which case potential theory may be used to express the transverse multipoles. Additionally, the relation $\boldsymbol{\nabla} \times \mathbf{B} = \boldsymbol{\nabla} \times (\boldsymbol{\nabla} \times \mathbf{A}) = \boldsymbol{\nabla}(\boldsymbol{\nabla} \cdot \mathbf{A}) - \boldsymbol{\nabla}^2\mathbf{A} = \mathbf{0}$ may be used to write $-\nabla^2\mathbf{A} = \mathbf{0}$ in the Coulomb gauge, which is *three* copies of the Laplacian, one per each component of **A**, whereas $-\nabla^2\psi = 0$ is just one Laplacian for the magnetic scalar potential ψ. Regardless of working with ψ or **A**, it is trivial to show a cosine-theta current distribution gives rise to a uniform dipole field since the potential for a dipole goes as $z = x + iy = \cos\theta + i\sin\theta$ and the field is the derivative of the potential (i.e. constant).

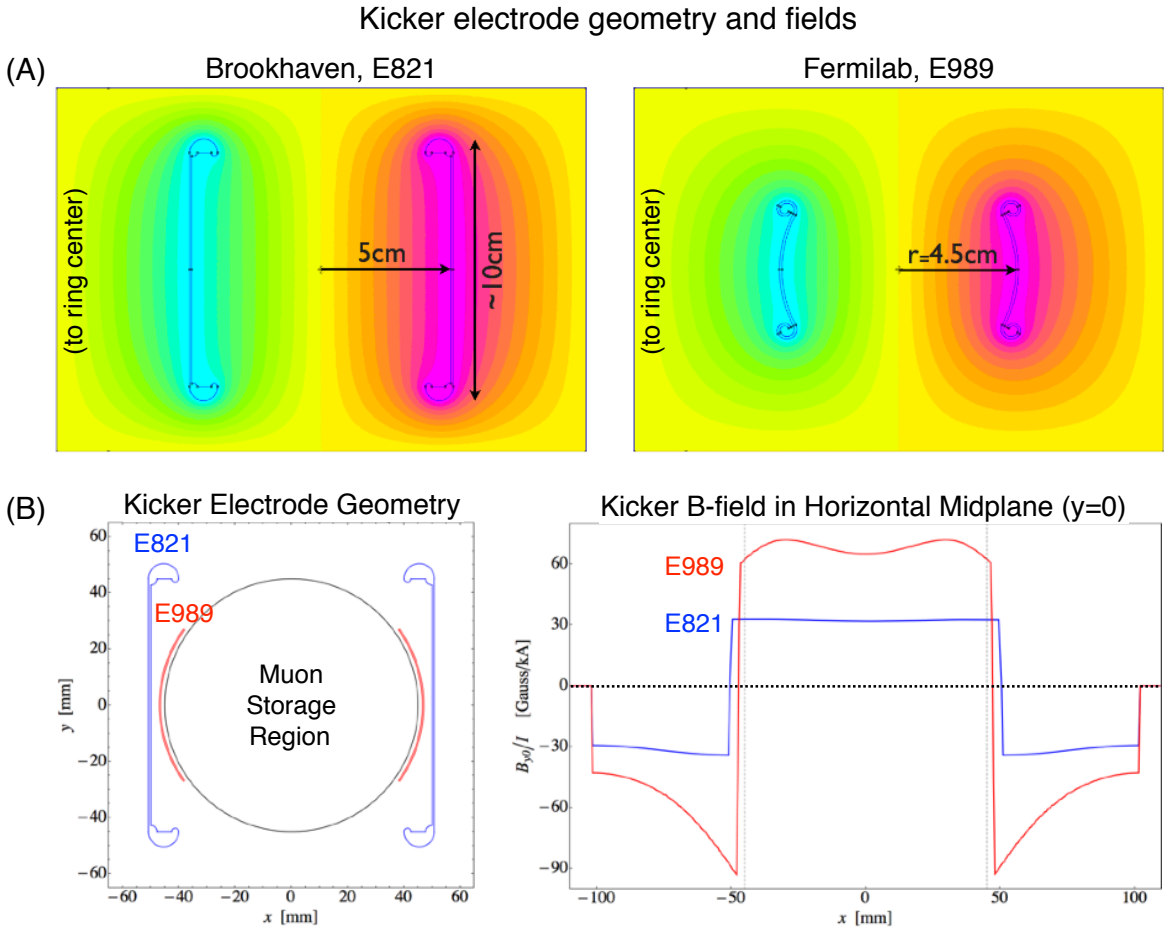

Figure 3.18: *Kicker electrode geometries and fields. (A) Cross section of the E821 (left) and E989 (right) electrodes and transverse magnetic vector potentials calculated using the open-source finite-element code FEMM [56]. The current in the right-hand plate (magenta) is out of the page for μ^+ storage, so the magnetic field $\mathbf{B} = \nabla \times \mathbf{A}$ points downward to the ground. The kicker magnetic field opposes the ring magnetic field, which in turn deflects the momentum of the beam radially outward by $\Delta x' \approx 77\,\mathrm{mm}/7112\,\mathrm{mm} = 10.8\,\mathrm{mrad}$. (B) Comparison of kicker electrode geometries (left) and magnetic fields in the horizontal midplane (right). The E989 electrode geometry gives a larger-magnitude magnetic field per unit current than the E821 plates by about a factor of two.*

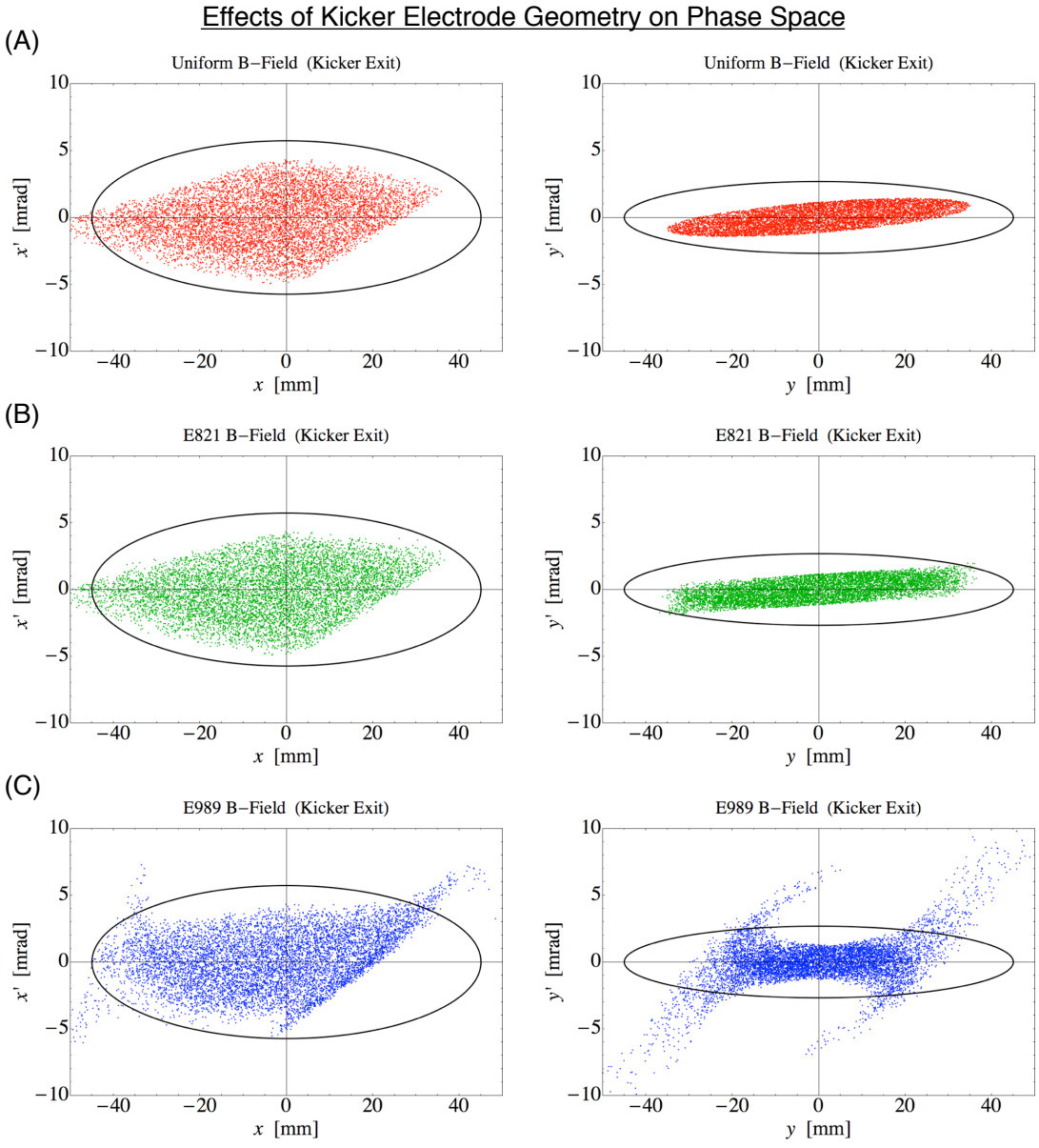

Figure 3.19: *Effects of kicker magnetic fields on horizontal (left) and vertical phase space (right) at the exit of the kicker region calculated with BMAD. (A) Uniform magnetic field. (B) E821 magnetic field. (C) Candidate E989 magnetic field. The sextupole moment and higher terms in the potential ($n = 3, 5, 7, \ldots$) cause more particles to be kicked out of the transverse acceptance of the muon $g-2$ storage ring, which is drawn for $n = 0.182$ above.*

3.4.3 Beam Collimators

The collimators define the spatial extent of the stored muon beam with respect to the high-precision magnetic field of the $g-2$ storage ring, as was discussed in §2.2.5. Additionally, the stored muon beam is "scraped" against the collimators shortly after injection in order to reduce muon losses during the data-collection period, which in turn improves data quality by reducing a systematic error in the anomalous precession angular frequency ω_a. Much progress had been made on the new collimator design by W. Morse *et al.* (BNL) [65] when the author of this thesis was asked to perform realistic simulations to help optimize the final design. It had already been decided the new collimators would have a circular aperture of $r_0 = 45\,\text{mm}$ like the E821 collimators, however the material and transverse/longitudinal thicknesses had not been decided. Three non-magnetic materials were being considered: graphite, aluminum and copper. A few basic properties of these materials are gathered in Table 3.1 [17].

Table 3.1: *Basic Properties of Candidate Collimator Materials*

	Material		
Property	C (Graphite)	Al	Cu
Nuclear Charge, Z	6	13	29
Magnetic susceptibility, $\chi_m^{(\text{vol})}$	-8.3×10^{-4}	2.2×10^{-5}	-9.6×10^{-6}
Density (g/cm^3)	2.21	2.70	8.96
Radiation Length (cm)	19.3	8.90	1.44
Scattering Angle, 1 cm (mrad)	0.89	1.35	3.62
$\langle dE/dx \rangle$, 3.1 GeV/c μ^+ (MeV/cm)	-4.46	-5.20	-15.4
Critical Energy, μ^+ (GeV)	1060	612	317
Critical Energy, e^+ (MeV)	79.5	41.5	18.8

The muon $g-2$ beam collimators eject particles from the storage region by shifting the particle's phase-space coordinates (x, x', y, y', δ) outside the acceptance of the storage ring, as derived in §**??**. The physical processes that cause 3.1 GeV/c muons to be lost are (1) multiple Coulomb scattering, which arises predominantly from "hard" interactions with the nuclei in the material,[18] and (2) energy loss, which arises predominantly from energy being transferred

[18] The radiation length of the material goes as $X_0 \sim Z^{-2}$, so $\theta_{\text{rms}} \sim Z\sqrt{x}$, c.f. Eq. (3.36).

to the electrons of the material. The ideal collimator will (1) cause muons to be ejected from the storage region as rapidly as possible during the scraping procedure while (2) not affecting the decay-positron signal as $\mu^+ \to e^+$ make their way from the storage region to the 24 detectors spread uniformly over ring azimuth. From the critical energies in Table 3.1,[19] one can see the energy loss of 3.1 GeV/c muons is predominately through ionization, while the energy loss of decay-positrons is predominately through Bremsstrahlung (which then leads to e^+e^- pair-production cascades, commonly referred to as "showers").

In order to investigate the effects of multiple Coulomb scattering on the muon loss rate, Eq. (33.15) of [17],

$$\theta_{\text{rms}} = \frac{13.6\,\text{MeV}}{\beta c p}\, z \sqrt{\frac{x}{X_0}} \left[1 + 0.038 \log\left(\frac{z^2 x}{\beta^2 X_0}\right)\right], \tag{3.36}$$

was used to choose a set of candidate collimator materials and thicknesses that give rise to the same RMS scattering angle, as shown in Fig. 3.20(A). Similarly, in order to investigate the effects of energy loss on muon loss rate, Eq. (33.11) of [17],

$$\Delta_p = \xi \left[\log\left(\frac{2mc^2\beta^2\gamma^2}{I}\right) + \log\left(\frac{\xi}{I}\right) + j - \beta^2 - \delta(\beta\gamma)\right], \tag{3.37}$$

was used to choose a set of material thicknesses that give rise to the same most-probable energy loss, as shown in Fig. 3.20(B). Note, the PDG advises *not* to used the Bethe equation,

$$\left\langle -\frac{dE}{dx} \right\rangle = K z^2 \frac{Z}{A} \frac{1}{\beta^2} \left[\frac{1}{2} \log\left(\frac{2m_e c^2 \beta^2 \gamma^2 W_{\text{max}}}{I^2}\right) - \beta^2 - \frac{\delta(\beta\gamma)}{2}\right], \tag{3.38}$$

since rare events with large ΔE drive the mean of the distribution into the tail [17]. The candidate materials and thicknesses mentioned above were input into *gm2ringsim* and the muon loss rate was investigated by launching muons directly into the upstream facets of the various candidate collimator designs at $t = 0$ and tracking the time at which the minor toroidal radius of the muons exceeded $r > r_0 + 10\,\text{mm} = 55\,\text{mm}$. Both Coulomb scattering and energy loss contribute to the muon loss rate, as shown in Fig. 3.21. Notice energy loss is

[19] The critical energy is the energy at which energy losses due to ionization equal energy losses due to radiation (Bremsstrahlung). Below the critical energy, energy is primarily lost through ionization as described by the Bethe equation (3.38) for $\beta\gamma \gtrsim 0.1$ [17].

the preferred mechanism by which muons are lost since $\langle \Delta E \rangle < 0$ always, whereas scattering angles are both positive and negative ($\langle \Delta\theta \rangle = 0$).

The absolute momentum acceptance of the ring is determined by the bending field (which generates horizontal dispersion) and the inner edge of the collimator $r_0 = 45\,\text{mm}$,

$$|\delta \equiv \Delta p/p_0| \lesssim \frac{r_0}{\bar{\eta}_x} = \frac{45\,\text{mm}}{7112\,\text{mm}/(1-n)} \approx 0.5\%. \tag{3.39}$$

High-momentum muons arriving that just barely touch the inner edge of the collimator at $x = 45\,\text{mm} = r_0$ will therefore need to lose $\Delta\delta \approx 2(-0.5\%) = -1.0\%$ to be carried outside of the momentum acceptance of the storage ring, Eq. (3.39).[20] Similarly, on-momentum muons with betatron-oscillation amplitudes of $A_x = 45\,\text{mm} = r_0$ will only just barely touch the inner edge of the collimator at $x = -45\,\text{mm} = -r_0$, and must therefore have their momentum shifted by $\Delta\delta \approx -0.5\%$ in order to be carried outside of the momentum acceptance of the storage ring. This "one-strike-you're-out" philosophy together with the need to mitigate deleterious effects on decay positrons led to the author to propose the conceptual design shown in Fig. 3.22, which features a unique variable-thickness or "wedge" shape.[21] The final design is shown in Fig. 3.23, while the installation and retraction are shown in Fig. 3.24.

[20] At the time the new collimators were being designed, the quadrupole high voltage for E989 was supposed to be 32 kV ($n = 0.189$), leading to an average horizontal dispersion of $\eta_x = 8.77\,\text{m}$, and hence, an absolute momentum acceptance of $|\delta \equiv \Delta p/p_0| \leq 0.51\%$.

[21] A similar design is being used in the M5 beamline to downshift high-momentum muons into the momentum acceptance of the storage ring [66].

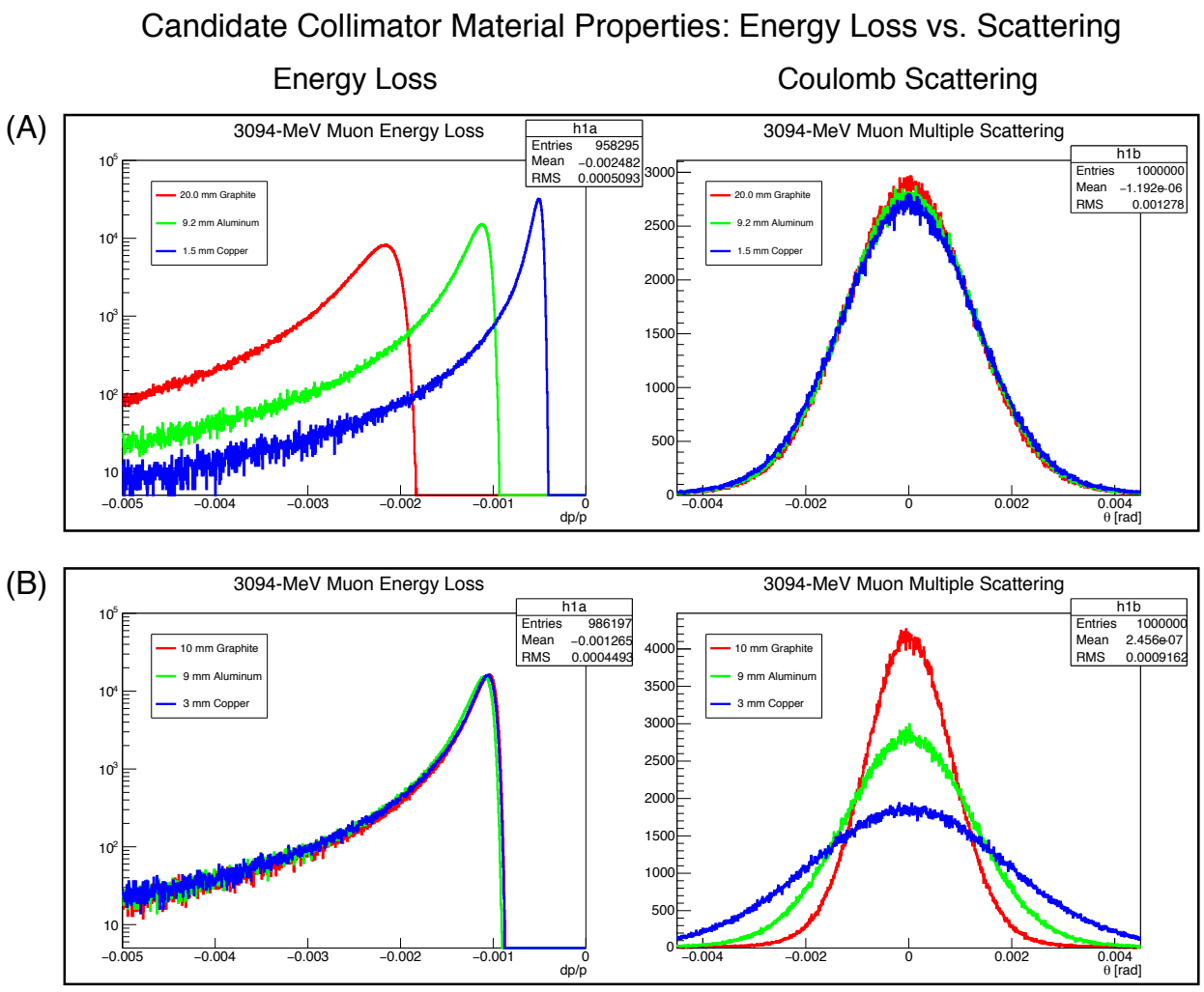

Figure 3.20: *Candidate collimator materials chosen to isolate the effects of multiple Coulomb scattering and energy loss for* $3.1\,\mathrm{GeV}/c$ *anti-muons. These distributions are calculated using a simple Geant4 program. (A) The materials* $\{\mathrm{Gr}, \mathrm{Al}, \mathrm{Cu}\} = \{20, 9.2, 1.5\}\,\mathrm{mm}$ *have the same RMS scattering angles (right) but different energy-loss distributions (left). (B) The materials* $\{\mathrm{Gr}, \mathrm{Al}, \mathrm{Cu}\} = \{10, 9, 3\}\,\mathrm{mm}$ *have the same energy-loss distributions (left) but different RMS scattering angles (right).*

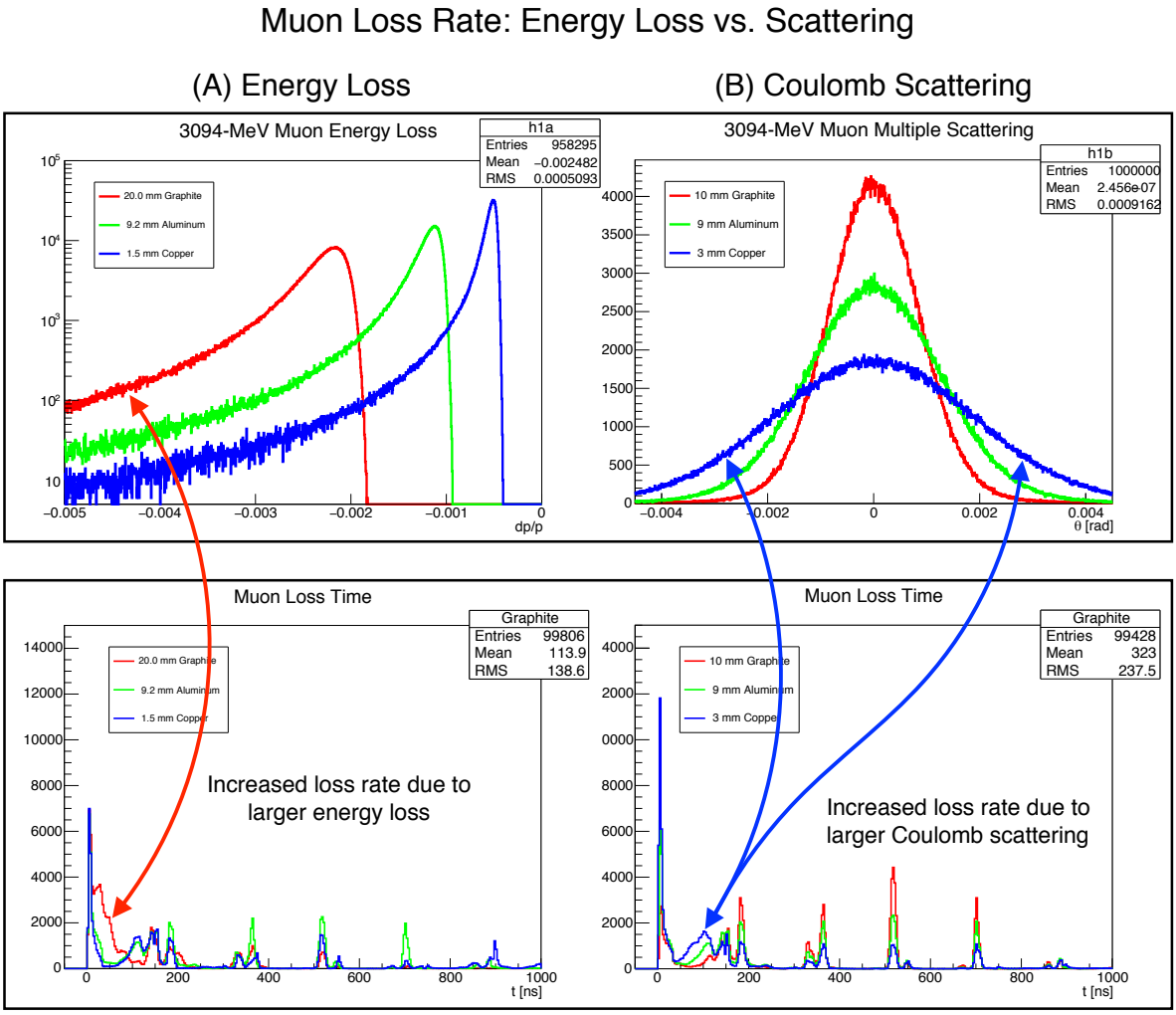

Figure 3.21: *Demonstration that both energy loss and multiple Coulomb scattering contribute to the muon loss rate. The muon loss time is defined to be the time at which the muon exits the torus of major radius* $R_0 = 7112\,\text{mm}$ *and minor radius* $r_0 = (45 + 10)\,\text{mm}$ *after striking a collimator. (A) Larger energy loss causes muons to be lost more rapidly for the same RMS scattering angle, c.f. Fig. 3.20(A). (B) Larger Coulomb scattering causes muons to be lost more rapidly for the same energy loss, c.f. Fig. 3.20(B). Ideally striking a collimator causes the muon momentum (transverse or longitudinal) to be shifted outside of the acceptance of the muon storage ring.*

(A) E989 Collimator Conceptual Design

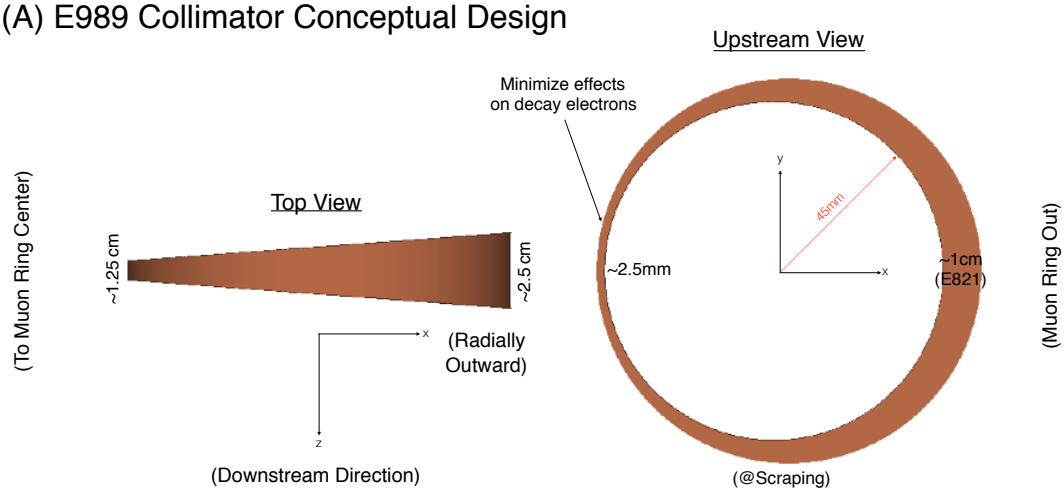

(B) Energy Loss and RMS Scattering Angle vs. Copper Thickness

#	dx(cm)	<dE/dx>(MeV/cm)	<dE>(MeV)	dE_MostProb(MeV)	dpp_Avg(%)	dpp_MostProb(%)	ScatRMS(mrad)
	0.1	-15.746	-1.575	-1.066	-0.051	-0.034	1.043
	0.2	-15.746	-3.149	-2.219	-0.102	-0.072	1.519
	0.3	-15.746	-4.724	-3.405	-0.153	-0.110	1.891
	0.4	-15.746	-6.298	-4.612	-0.204	-0.149	2.209
	0.5	-15.746	-7.873	-5.835	-0.255	-0.189	2.492
	0.6	-15.746	-9.448	-7.071	-0.305	-0.229	2.749
	0.7	-15.746	-11.022	-8.317	-0.356	-0.269	2.987
	0.8	-15.746	-12.597	-9.572	-0.407	-0.310	3.210
	0.9	-15.746	-14.171	-10.835	-0.458	-0.350	3.421
	1.0	-15.746	-15.746	-12.105	-0.509	-0.391	3.620
	1.1	-15.746	-17.321	-13.382	-0.560	-0.433	3.811
	1.2	-15.746	-18.895	-14.664	-0.611	-0.474	3.994
Inner Edge	1.3	-15.746	-20.470	-15.952	-0.662	-0.516	4.170
	1.4	-15.746	-22.044	-17.244	-0.713	-0.558	4.339
	1.5	-15.746	-23.619	-18.540	-0.764	-0.600	4.503
	1.6	-15.746	-25.194	-19.841	-0.815	-0.642	4.662
	1.7	-15.746	-26.768	-21.146	-0.866	-0.684	4.817
	1.8	-15.746	-28.343	-22.455	-0.916	-0.726	4.967
	1.9	-15.746	-29.917	-23.767	-0.967	-0.769	5.114
	2.0	-15.746	-31.492	-25.082	-1.018	-0.811	5.257
	2.1	-15.746	-33.067	-26.401	-1.069	-0.854	5.396
	2.2	-15.746	-34.641	-27.722	-1.120	-0.896	5.533
	2.3	-15.746	-36.216	-29.047	-1.171	-0.939	5.667
	2.4	-15.746	-37.790	-30.374	-1.222	-0.982	5.798
Outer Edge	2.5	-15.746	-39.365	-31.704	-1.273	-1.025	5.926

(Calculated from PDG formulas)

Figure 3.22: *E989 collimator conceptual design. (A) The collimator geometry is tapered toward the storage-ring center (left) in order to mitigate deleterious effects on decay positrons and utilize the horizontal ring dispersion to cause muons to be lost after striking the collimator once. (B) Calculated energy loss and multiple-scattering angles for copper [17]. Copper was chosen over graphite and aluminum as the material for the new collimators in E989.*

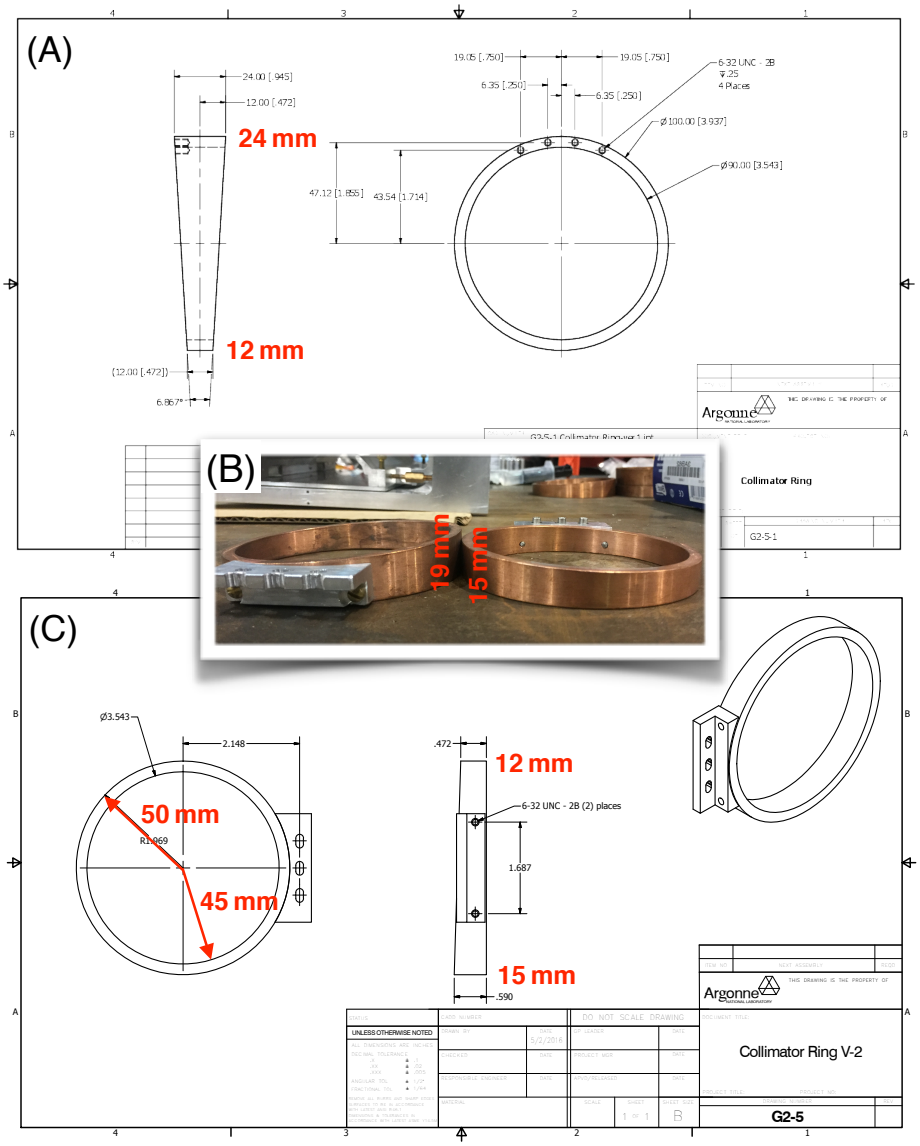

Figure 3.23: *Collimators designed and fabricated. (A) Preliminary design. (B) Intermediate design. (C) Final design. The longitudinal thickness of the collimator copper at largest ring radius was decreased from* 24 mm *to* 15 mm *overall to avoid trolley snags during field measurements.*

Figure 3.24: *Collimator installation and retraction test.*

3.4.4 Inflector Beam-Monitoring System (IBMS)

The Inflector Beam-Monitoring System (IBMS) is an arrangement of three detectors located in the injection-region of the muon $g-2$ storage ring that measure the longitudinal and transverse properties of the injected beam as it enters the storage ring [67]. These detectors provide invaluable real-time feedback of the beam centroid and widths, and hence play a critical role in beam-tuning and injection-optimization efforts through the narrow aperture of the superconducting inflector. Recognition of the need for these detectors and their physical realization is due largely to P. Kammel at the University of Washington (UW), with D. Hertzog (UW) providing valuable support, feedback, and insight along the way. The author of this thesis was lucky to play a part in the development of the IBMS detectors as well, e.g. using *gm2ringsim* to assess expected beam profiles and rates, upon which real design decisions were based. An example simulation is shown in Fig. 3.25 [67].

The basic mechanism by which the IBMS detectors operate is twofold: First, minimum-ionizing particles (MIPs) such as 3.1 GeV/c muons traverse a grid of thin plastic scintillating fibers (0.5 mm diameter, Fig. 3.25(B)), giving rise to optical photons (blue/green light) that travels down the length of the fiber due to total internal reflection. Next, the scintillation light is detected by small 1 mm^2 silicon-based photomultipliers (SiPMs) on then end of each fiber, each of which consists of 10^4 tiny avalanche photodiodes (pixels) operating in Geiger mode that allow for the detection of single photons [68, 69]. The energy loss of the particles traversing the scintillating fibers is primarily through ionization, which is well described by the Bethe Eq. (A.50), and it is expected the light output should be proportional to the amount of energy deposited in the material, i.e. $d\mathcal{L} \propto \langle dE/dx \rangle \, dx$. Here, the π-bonding orbitals of the aromatic rings of the plastic (e.g. polystyrene, like the IBMS fibers) and dopants therein play a key role in the scintillation process [70]. An improved model has been proposed by Birks [71],

$$\frac{d\mathcal{L}}{dx} = \mathcal{L}_0 \frac{\langle dE/dx \rangle}{1 + k_B \langle dE/dx \rangle}, \tag{3.40}$$

where $\mathcal{L}$ is the luminescence, $\mathcal{L}_0$ is an overall normalization factor, x is the longitudinal thickness of the scintillator, $\langle dE/dx \rangle$ is the average energy loss described by the Bethe Eq. (A.50), and k_B is "Birks' constant," which is a property of the scintillation material that must be determined experimentally [17]. The sharp leading edge of the SiPM output pulse (1-5 ns) generated by the scintillation light primarily arises from the rate at which

the avalanche develops, whereas the longer tail of the output signal is an RC time constant ($\tau_{RC} \approx$ 10-30 ns) that depends on quantities such as the pixel capacitance and the value of the quench resistor which effectively halts the avalanche.

The expected IBMS detector response for a variety of tune-up settings is shown in Fig. 3.26. Results from these simulations and others were used to make key design decisions regarding the detector dimensions, fiber spacing, expected rates, detector electronics and other key performance parameters, as shown in Fig. 3.27. Figure 3.27 also shows the fabrication of the IBMS detectors at the UW and the installation of the detectors at Fermilab. Lastly, Fig. 3.28 shows example beam profiles measured by the IBMS{1,2} detectors during normal physics data taking. Profiles like these are used regularly by the Accelerator Division and the Experiment to monitor the overall health and quality of the beam being injected into the storage ring. Simulation agrees well with reality, e.g. Fig. 3.12.

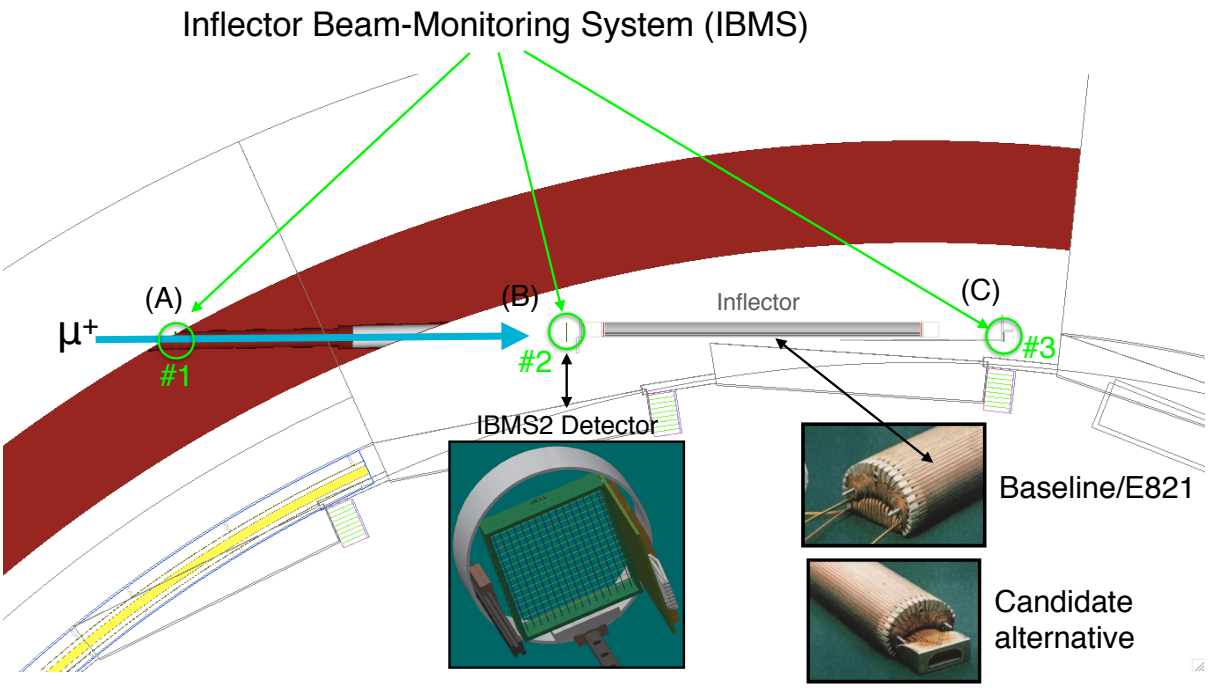

Figure 3.25: *Overview of the Inflector Beam-Monitoring System (IBMS). The IBMS consists of three detectors that measure the position and width of the injected beam as it enters the muon $g-2$ storage ring.*

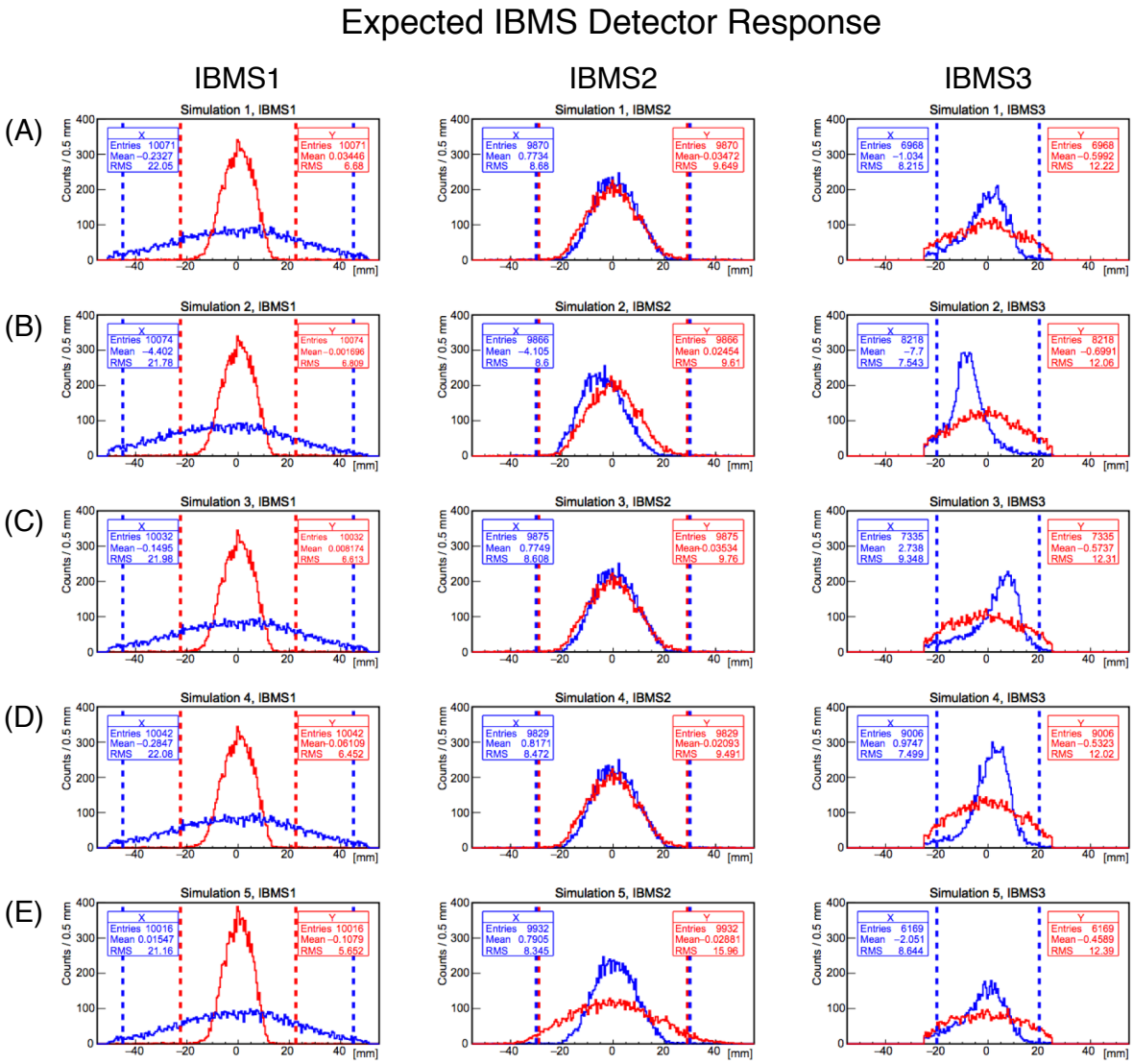

Figure 3.26: *Expected IBMS detector response at candidate fiber locations [67]. (A) Reference simulation, where the beam is injected exactly down the centerline of the beam pipe and the magnetic field of the unrotated inflector is exactly opposite the magnetic field of the ring ($|B_{y0}| = 1.4513\,\mathrm{T}$). (B) Perturbation by $\Delta x = -5\,\mathrm{mm}$ at the ring entrance. The change is registered on all three detectors. (C) Perturbation of the inflector field by $\Delta B_{y0} = -300\,\mathrm{G}$. (D) Perturbation of the inflector rotation by $\Delta x'_{\mathrm{inf}} = -4\,\mathrm{mrad}$. (E) Perturbation of the injection Courant-Snyder parameters by $\Delta\{\beta_x, \alpha_x, \beta_y, \alpha_y\} = \{-, +, -, +\}\,10\,\%$.*

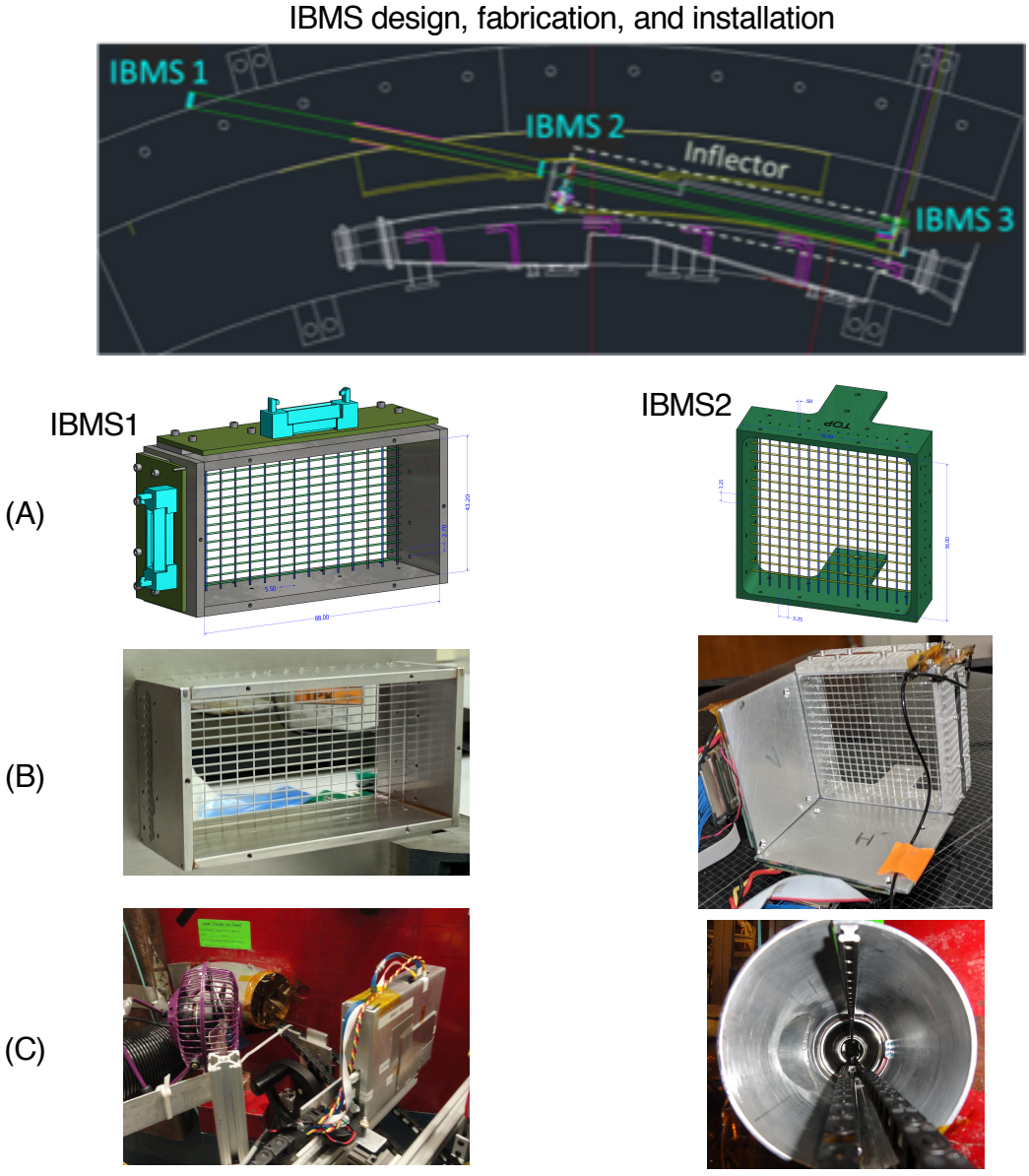

Figure 3.27: *IBMS design, fabrication, and installation. (A) IBMS design at the University of Washington (UW). (B) IBMS fabrication at UW. (C) IBMS installation at Fermilab.*

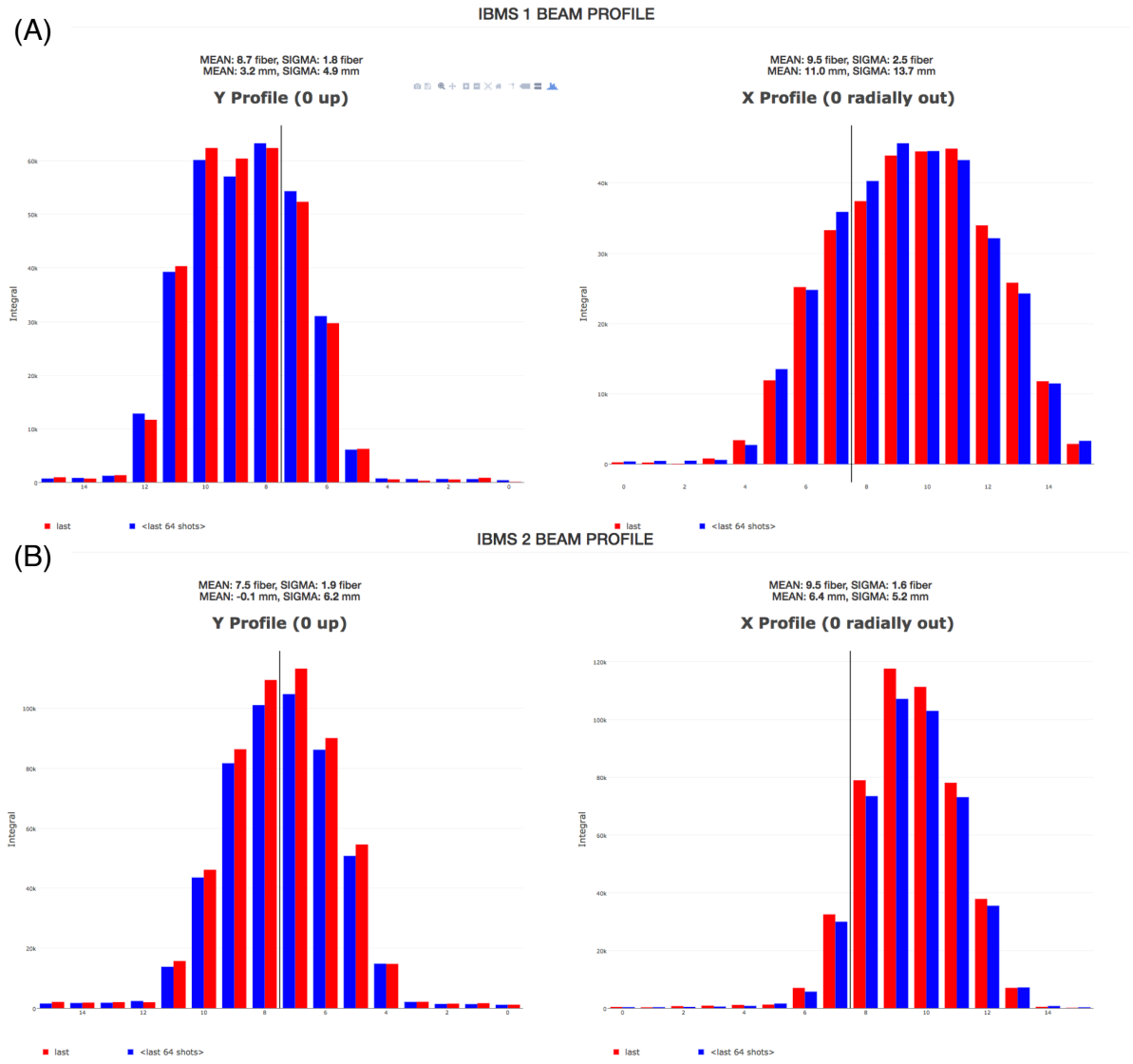

Figure 3.28: *Example IBMS beam profiles used regularly by Accelerator Division and the Experiment. (A) IBMS1 profiles, immediately upstream of the muon $g-2$ storage-ring magnet iron. (B) IBMS2 profiles, $\sim$25 cm upstream of the inflector entrance. In both plots, the vertical beam profile is shown at the left, while the horizontal beam profile is shown at the right.*

3.4.5 New Superconducting Inflector Magnet

The main role of the superconducting inflector magnet is to provide a field-free channel through which the injected beam passes as it enters the muon $g-2$ storage ring, as was discussed in §2.2.2. The truncated-double-cosine-theta geometry of the superconducting coils shown in Fig. 3.29 creates two major difficulties that reduce injection efficiency considerably:

1. A large injection mismatch is caused by the narrow 18 mm horizontal inflector aperture

2. Emittance blowup is caused by multiple Coulomb scattering in the superconducting coils that cover the upstream and downstream ends of the inflector beam channel

The above difficulties may be regarded as ways to improve a redesigned superconducting inflector. The first issue is solved by widening the horizontal beam channel, while the second issue is solved by removing material from the beam path at the upstream and downstream ends of the inflector. Unfortunately, it is not possible to widen the inflector beam channel due to existing geometry constraints, field-uniformity constraints, and the fact that displacing the centerline of the inflector beam channel radially outward by Δx increases the required kick to $\Delta x' = (77\,\text{mm} + \Delta x)/7112\,\text{mm} \gtrsim 10.8\,\text{mrad}$, which is difficult to achieve experimentally. Therefore, the main strategy in the redesign of the new superconducting inflector magnet is to remove the material covering the beam channel at the upstream and downstream ends, as shown in Fig. 3.30.

The material properties of the superconducting coils are discussed in Refs. [34, 35]. The superconducting coils are physically wrapped around an aluminum body called a "mandrel" with two 1.5 mm-thick windows, one on each end. The cold mass has an additional two 1.5 mm-thick windows that are being removed in the new inflector (Fig. 3.30). Thus, the total longitudinal thickness of material being removed from the beam path in the new inflector is ∼9.1 mm Al, ∼0.8 mm Cu, and ∼0.8 mm NbTi (1:1 mass ratio). This is important since the transverse acceptance of the ring is only (§**??**)

$$\begin{aligned} x'_{\text{max}} &\simeq \left(\frac{45\,\text{mm}}{7112\,\text{mm}}\right)\sqrt{1-n} \quad \approx 5.9\,\text{mrad} \\ y'_{\text{max}} &\simeq \left(\frac{45\,\text{mm}}{7112\,\text{mm}}\right)\sqrt{n} \qquad \approx 2.2\,\text{mrad} \end{aligned} \tag{3.41}$$

for a quadrupole high voltage of QHV $\pm$ 20.2 kV (n = 0.119), which is comparable to the amount of material the injected beam must penetrate in terms of RMS scattering angle (Fig. A.4). Preliminary simulations showed removing all material in the upstream and downstream ends of the inflector resulted in a ~50% gain in capture efficiency, however, these simulations did not take into account the difference in field uniformity (since the new inflector inner coil had not been designed yet). The evolution of the design of the new inflector inner-coil end pieces is shown in Fig. 3.31. The corresponding magnetic fields simulated in *gm2ringsim* are shown in Fig. 3.32. The expected gains from the new inflector are shown in Fig. 3.33. The winding of the superconducting coils of the new inflector are shown in Fig. 3.34. The new inflector will be installed in the Fall of 2018.

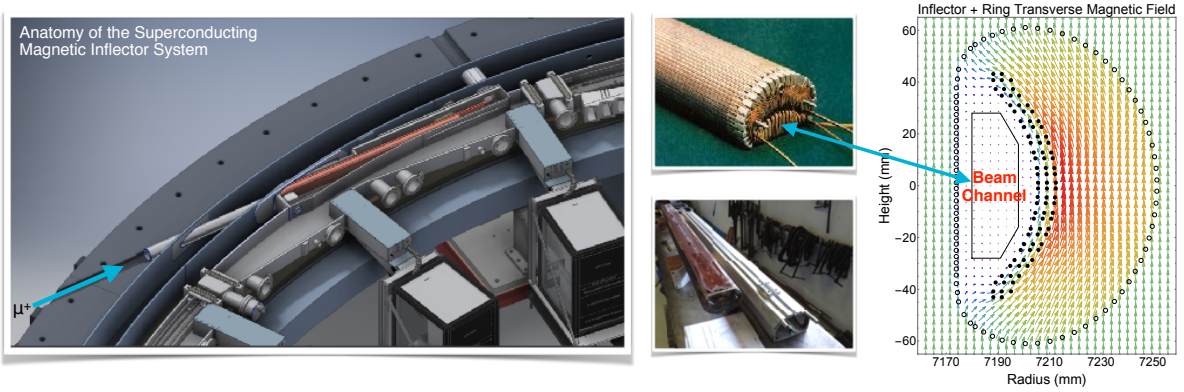

Figure 3.29: *Anatomy of the superconducting magnetic inflector system. The* 3.1 GeV/c *muon beam enters the storage ring through a 4-inch hole bored horizontally through the backleg yoke of the C-magnet iron shown at the far left, where it then proceeds* ~2.5 m *downstream into the body of the 1.7-m inflector. Both the upstream and downstream ends of the inflector beam channel are covered with superconducting NbTi:Cu/Al wires wrapped in a truncated-double-cosine-theta pattern in order to construct a uniform dipole magnetic field that largely cancels the magnetic field of the storage ring (right).*

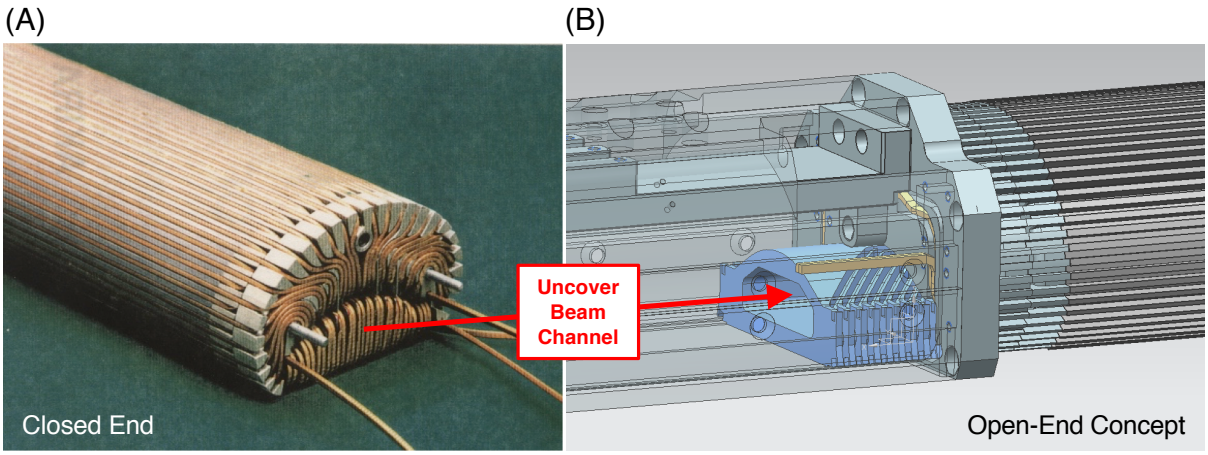

Figure 3.30: *Basic idea of the new inflector: remove the material covering beam channel to avoid emittance blowup. (A) Superconducting coil geometry for the closed-ended inflector, where the NbTi:Cu/Al wires cover the beam channel. (B) CAD drawing of a prototype open-inflector end, where the material covering the beam channel has been completely removed in order to prevent emittance blowup due to multiple Coulomb scattering.*

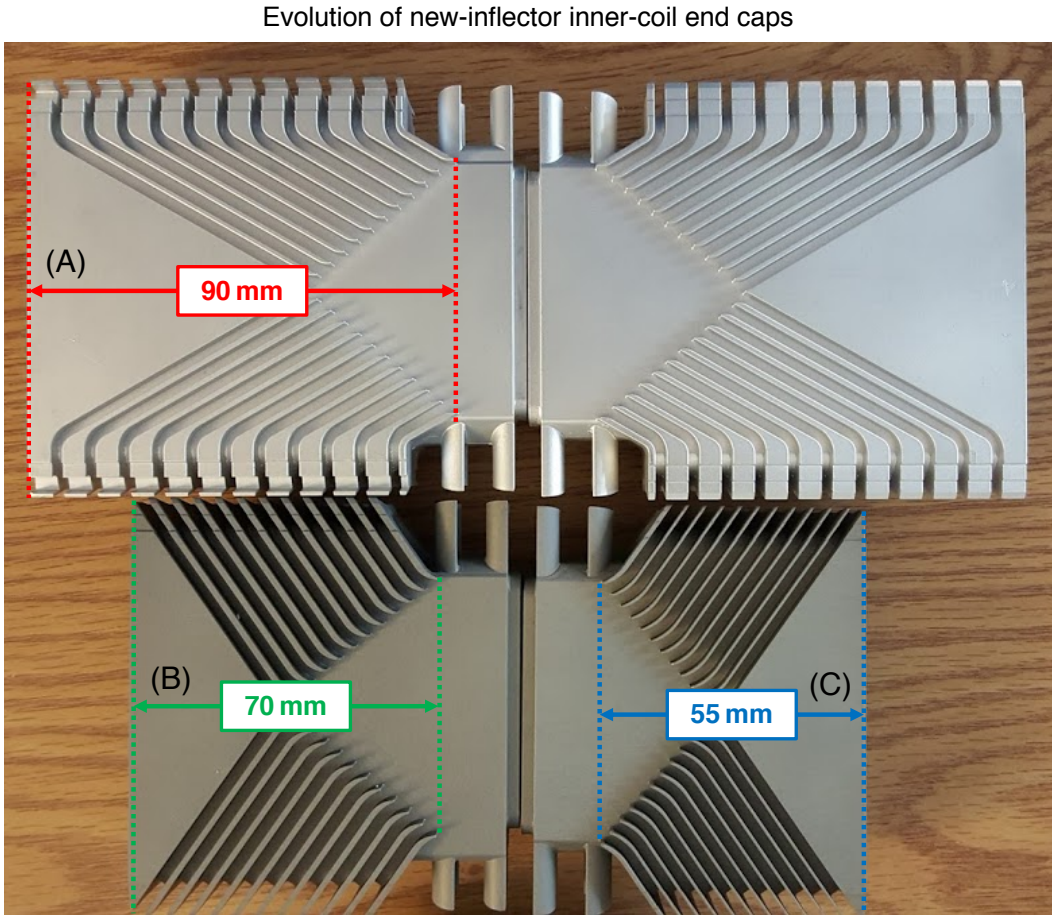

Figure 3.31: *Optimization of new superconducting inflector inner-coil mandrel ends. (A) First design iteration for both upstream and downstream ends, made out of aluminum. This design was too magnetically short ($L_{\mathrm{mag}}^{(\mathrm{inf})} = 156\,\mathrm{cm} < 170\,\mathrm{cm}$), and caused too much curvature in the beam channel. (B) Downstream inner-coil end-cap of the final design iteration, made out of "Ultem," a polymer that has a similar thermal-contraction coefficient as aluminum but is insulating, thereby preventing shorts during winding. This downstream end piece is slightly longer than the upstream end shown in (C) in order to reduce the load on the superconducting shield. The overall length of the new inflector is* 1754 mm, *as measured from the upstream and downstream edges of the inner-coil end caps shown above, with the extra* $\sim$5 cm *protruding into the lead box at the downstream end in order to maximize the magnetic length.*

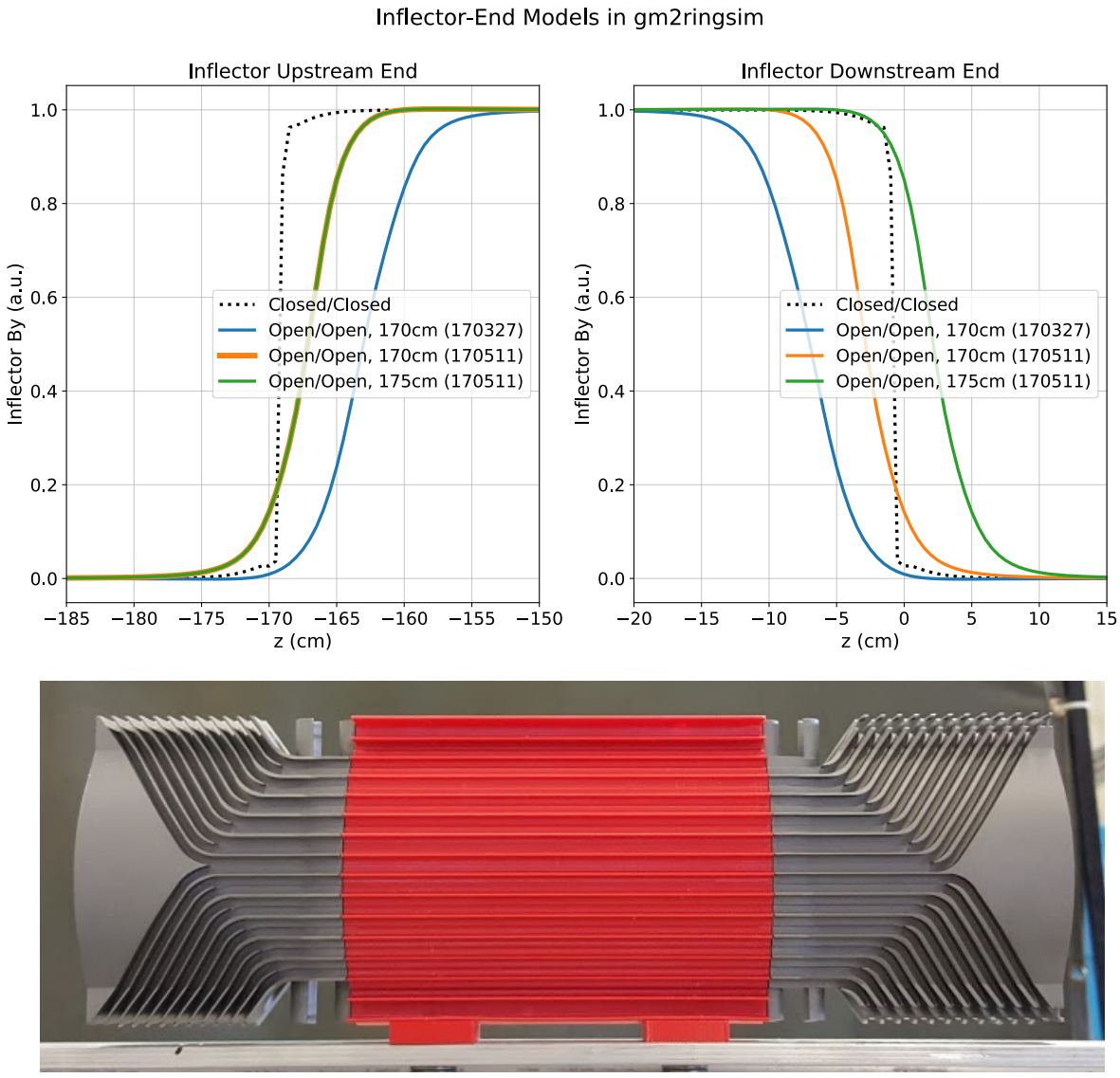

Figure 3.32: *Example candidate new-inflector magnetic fields investigated with gm2ringsim. Here, the vertical component of the magnetic field is plotted as a function of longitudinal distance down the centerline of the inflector beam channel.*

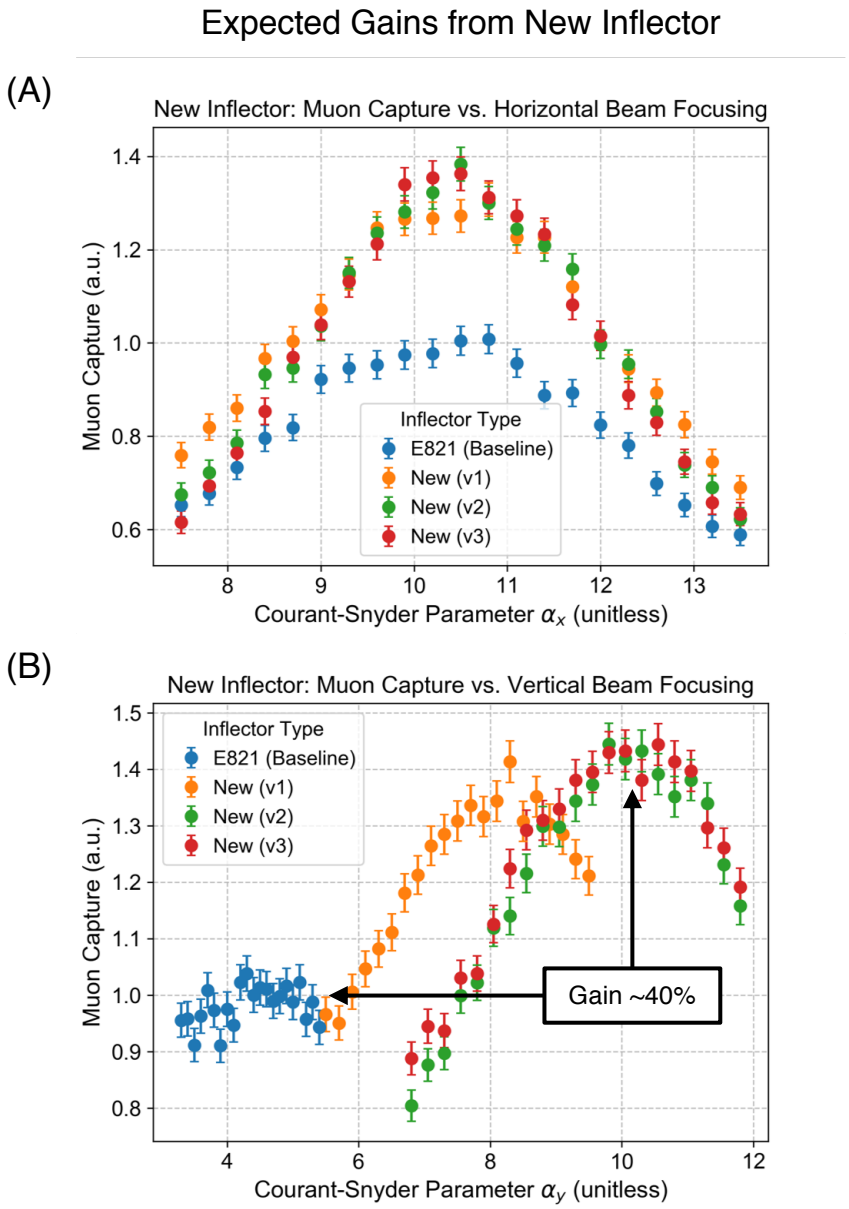

Figure 3.33: *Muon capture efficiency vs. Courant-Snyder $\alpha_{x,y}$ at the entrance of the $g-2$ storage ring. (A) Horizontal focusing: the location of the peak α_x is the same for all inflector designs due to the narrow horizontal inflector aperture ($\Delta x = 18\,\mathrm{mm}$). The quadrupole gradient in the inflector ends is horizontally focusing, so the peak is more pronounced for the open-ended designs. (B) Vertical focusing: the location of the peak α_y is different for the different designs since the gradients are more vertically defocusing for more closely spaced coil wrappings.*

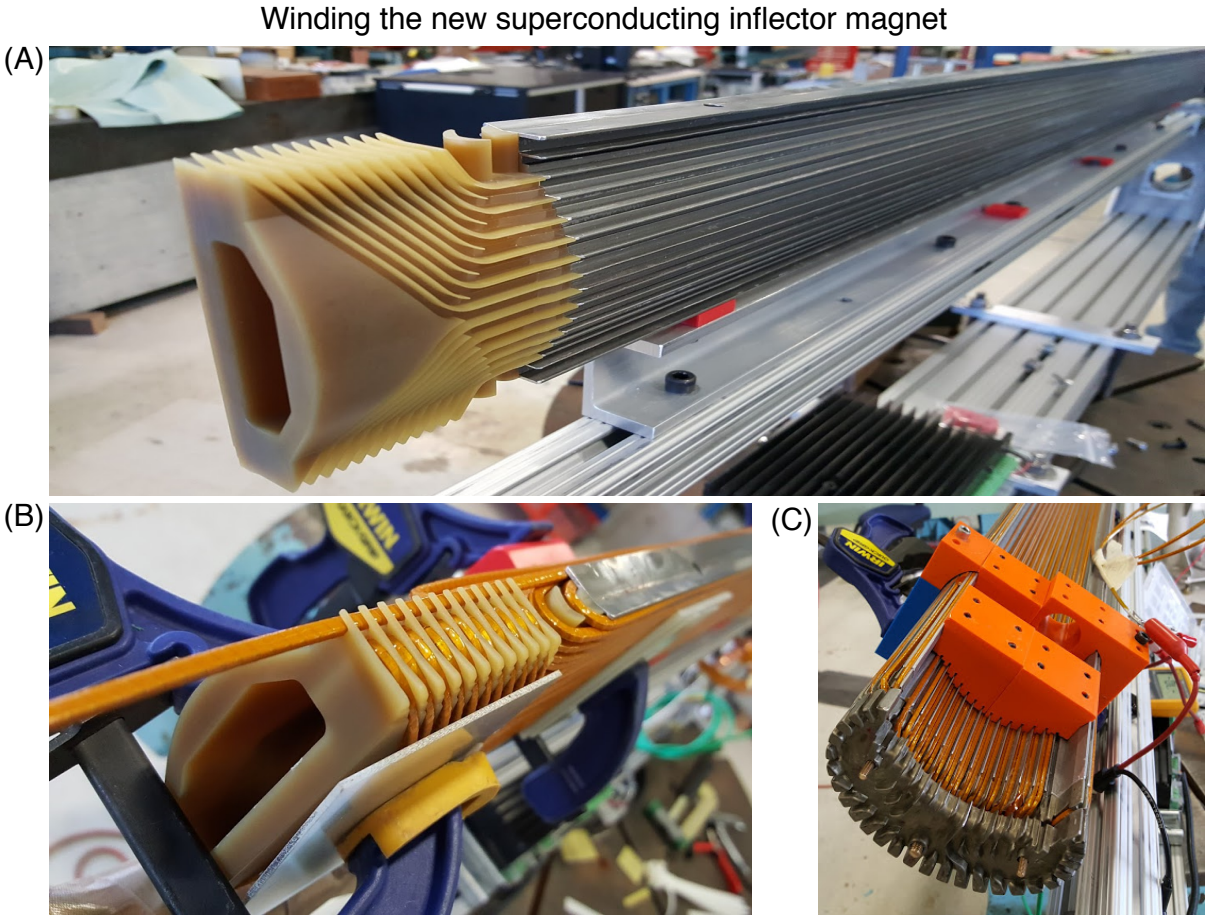

Figure 3.34: *(A) Upstream end of inner coil mandrel with redesigned end. (B) Wrapped inner coil, downstream end. (C) First layer of wrapping of the outer coil, with jig for testing electrical shorts to the body of the aluminum mandrel.*

Chapter 4

COMMISSIONING AND RUN 1

This chapter highlights some of the recent studies performed over the past six months related to the commissioning of the Muon $g-2$ Experiment for physics-quality data and the optimization of the injected muon beam through the superconducting inflector magnet into the storage ring. The first section of this chapter discusses new tools developed by the author that allow for the rapid optimization of the steering and focusing of the injected beam into the ring using automated beam-tuning scripts written in the Accelerator Control Language (ACL). Next, a measurement of the beam parameters in the M5 Final Focus is performed, and the results are used as the starting point for more sophisticated studies using "multiknobs" (MULTs) in which several beamline devices are adjusted simultaneously. Having optimized injection into the $g-2$ storage ring, this chapter concludes with a discussion of a major problem encountered by the experiment that the author played a key role in helping to resolve.

4.1 Accelerator-Division Liaison, New ACNET *Parameters, and Automated Beam-Tuning Scripts*

Beam was established to the Fermilab muon $g-2$ experiment for the first physics run (Run 1) on the evening of Fri 17 Nov 2017, as shown in Fig. 4.1. One challenge faced that evening was the lack of real-time feedback from the experiment for reporting the rate at which beam was being captured in the muon $g-2$ storage ring. Telephone, text message, and social media were all used that night to understand why MC-1 was unable to detect the beam even though it was arriving at the entrance of the storage ring.[1] Injection-tuning efforts in the coming days also brought to light a more general problem in the mind of the author: the fate of the experiment depends critically on the M5 Final Focus (M5FF), yet the experiment is not allowed to adjust the M5FF magnets since the magnets are owned

[1] MC-1's trigger timing was off, as was learned later that night.

and operated by AD. On the other hand, AD is more than capable of adjusting the M5FF magnets, yet AD is not so familiar with the nuances of optimizing injection into the muon storage ring. Therefore, injection tuning would likely proceed at a slow rate, and it would be beneficial for both AD and the experiment if this shortcoming were to be fixed. Here, the author's understanding of how to optimize injection into the $g-2$ storage ring, knowledge of computers, and burgeoning understanding of accelerator physics could be put to good use. By actively identifying problems like the ones mentioned above and attempting to fix them, the author emerged as a liaison between AD and the experiment. Many productive hours were spent in the coming months attempting to identify shortcomings and bridging gaps in communication/understanding as well as assisting with beam-tuning efforts directly from Fermilab Main Control Room (MCR). One example of a final product delivered by the author in his new role as liaison is shown in Fig. 4.2, in which the communication loop mentioned above was completed by creating a new set of custom $g-2$ beam-tuning variables directly in the Fermilab Accelerator Controls Network (ACNET). Several of these new ACNET variables are now used regularly by Accelerator Division and the experiment for creating canonical diagnostic plots and assessing global historical progress since the data is part of the permanent record at Fermilab and since these variables are generally useful outside the realm of instantaneous beam tuning (as was foreseen by the author).

Armed with the new set of custom beam-tuning variables in ACNET mentioned above, an interesting new possibility arrises: beam tuning can be automated via computer scripts written in the Accelerator Control Language (ACL) to control magnet settings and extract meaningful injection-related data from the experiment in real time. This means injection into the muon $g-2$ storage ring may now be rapidly optimized, which is the topic of the remainder of this chapter. Optimizing injection into the storage ring essentially involves two classes of studies in the M5 Final Focus: (1) beam steering and (2) beam focusing through the inflector, as shown in Fig. 4.3. The beam-steering studies involve small dipole corrector magnets known as "TRIMs," whereas the beam-focusing studies involve large magnetic quadrupoles immediately upstream of the ring. Several beam-tuning scripts have been developed by the author, for example, to scan over TRIMs currents and record the capture efficiency observed at MC-1 in real time. An example set of beam-steering optimizations is shown in Fig. 4.4, in which the currents of the last two horizontal TRIMs nearest the ring (HT020, HT024) are scanned in order to determine the optimal horizontal injection position and angle of

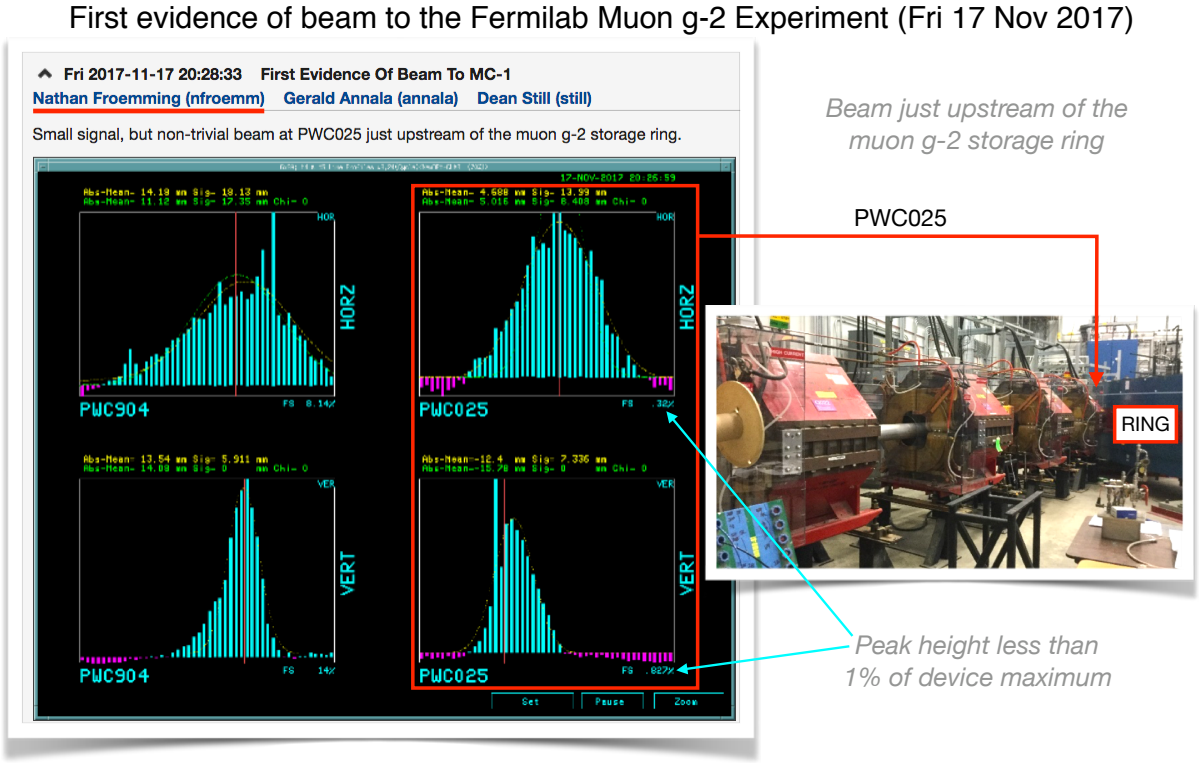

Figure 4.1: *Fermilab Accelerator-Division elog documenting the first evidence of beam to MC-1 for the first physics run of the Muon g−2 Experiment. The PWC904 detector (beam profiles, left column) is* ∼112 m *upstream of the storage ring in the M4 beamline, while PWC025 detector (right column) is* ∼1.0 m *upstream of the ring in the M5 Final Focus. Horizontal beam profile are shown in the top row, while vertical profiles are shown in the bottom row. The picture at the right shows the physical location of the PWC025 detector immediately upstream of the storage ring. The vertical scale of the PWC025 profiles is less than 1% of the full saturation value of the device, indicating the small amount of beam arriving at the ring was barely registering in the detector.*

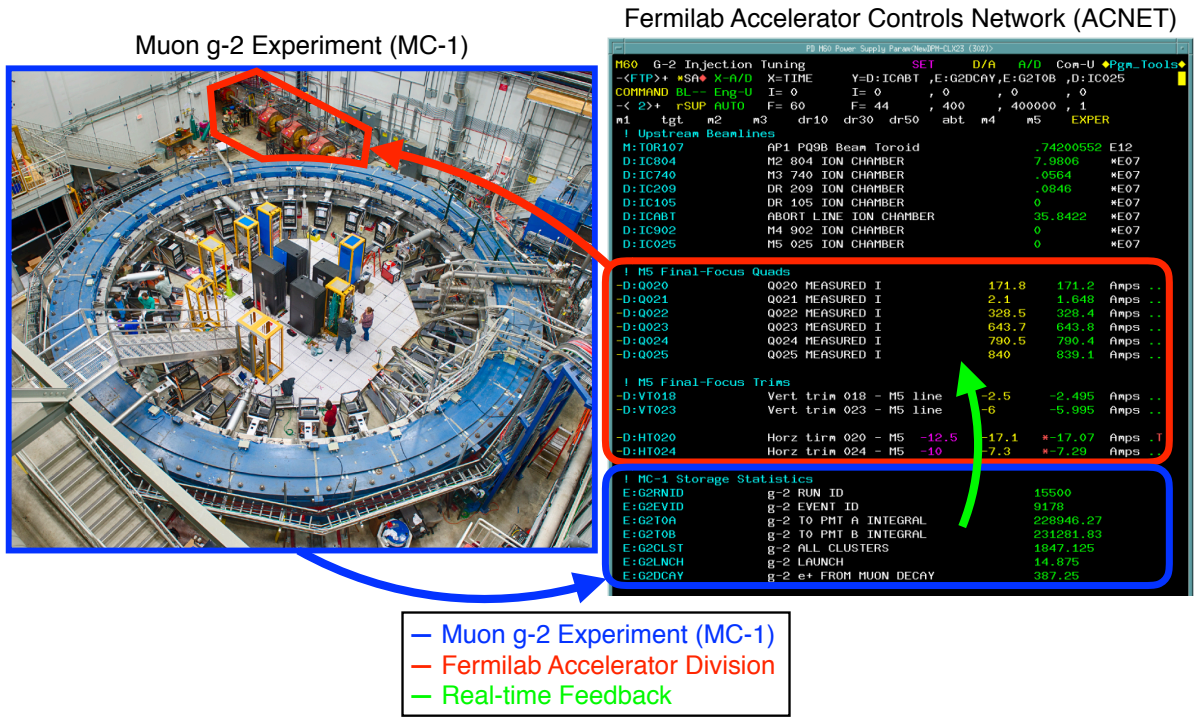

Figure 4.2: *Completing the communication loop: New ACNET parameters from MC-1 for beam tuning. Fermilab Accelerator Division (AD) owns and operates all beamline devices, for example, in the M5 Final Focus (M5FF) shown in red. The amount and quality of the stored muon beam depends critically on the settings of the M5FF magnets, yet the experiment is not allowed to adjust these devices. To make matters worse, the real-time effects of AD's tuning efforts on capture efficiency of the injected beam were not being communicated to AD, so injection tuning was proceeding at an unacceptably slow rate. The author identified this shortcoming and closed the communication loop as follows: First, custom variables were created in the Accelerator Controls Network (*ACNET*) to facilitate* $g-2$ *beam tuning. Next, the experiment writes to the new* ACNET *variables using the wireless internet (blue). Finally, AD is made aware of the effects of its tuning efforts on muon capture efficiency, and uses this information to rapidly optimize injection into the storage ring.*

the beam entering the ring for three different inflector settings. Here, "capture efficiency" is defined as $\sum$G2CLST (number of reconstructed $g-2$ calorimeter clusters) divided by $\sum$TOR107 (protons on target, as measured by AD's beam toroid 107 far upstream of the ring), where the summation symbols indicate the quantities have been accumulated over a number of beam cycles[2] defined by the user in the script. These results indicate an inflector current of ∼2780 A optimizes muon capture efficiency for this particular setting of MC-1's quads, kickers, etc. Since each data point took only ∼15 s to record, these results were established much faster than recording all values by hand, as had been done in the past. Similar results for the vertical position and angle of the injected beam were obtained rapidly and conclusively as well. An example of the other class of injection study mentioned above, i.e. beam-focusing studies using quadrupoles, is shown in Fig. 4.5. Here, the currents of the two quadrupoles nearest the ring (Q024, Q025) are scanned in order to optimize the combined focal length of the quad doublet. All quads and TRIMs in the M4/M5 beamline were explored in a similar manner and with a similar efficacy since the scan script was written generally enough to accept two arbitrary ACNET devices as input parameters.

[2]More specifically, TCLK $93s and/or TCLK $94s.

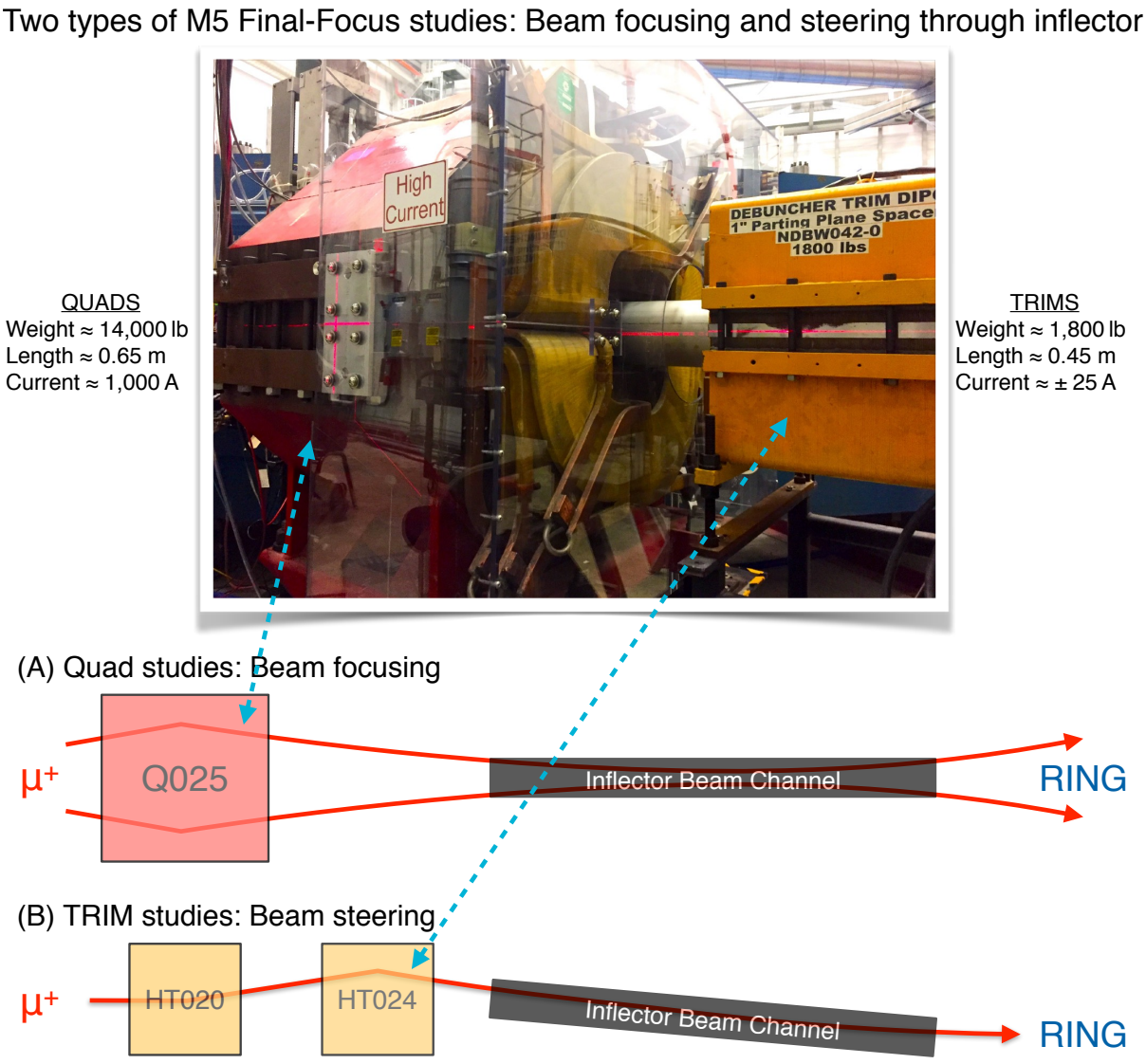

Figure 4.3: *For optimizing injection into the muon $g-2$ storage ring, there are essentially two types of studies involving the M5 Final Focus: beam focusing and beam steering through the inflector. (A) Large magnetic quadrupoles are used to control the beam focusing through the inflector into the ring. (B) Small dipole corrector magnets known as "TRIMs" are used to steer the beam through the inflector into the ring.*

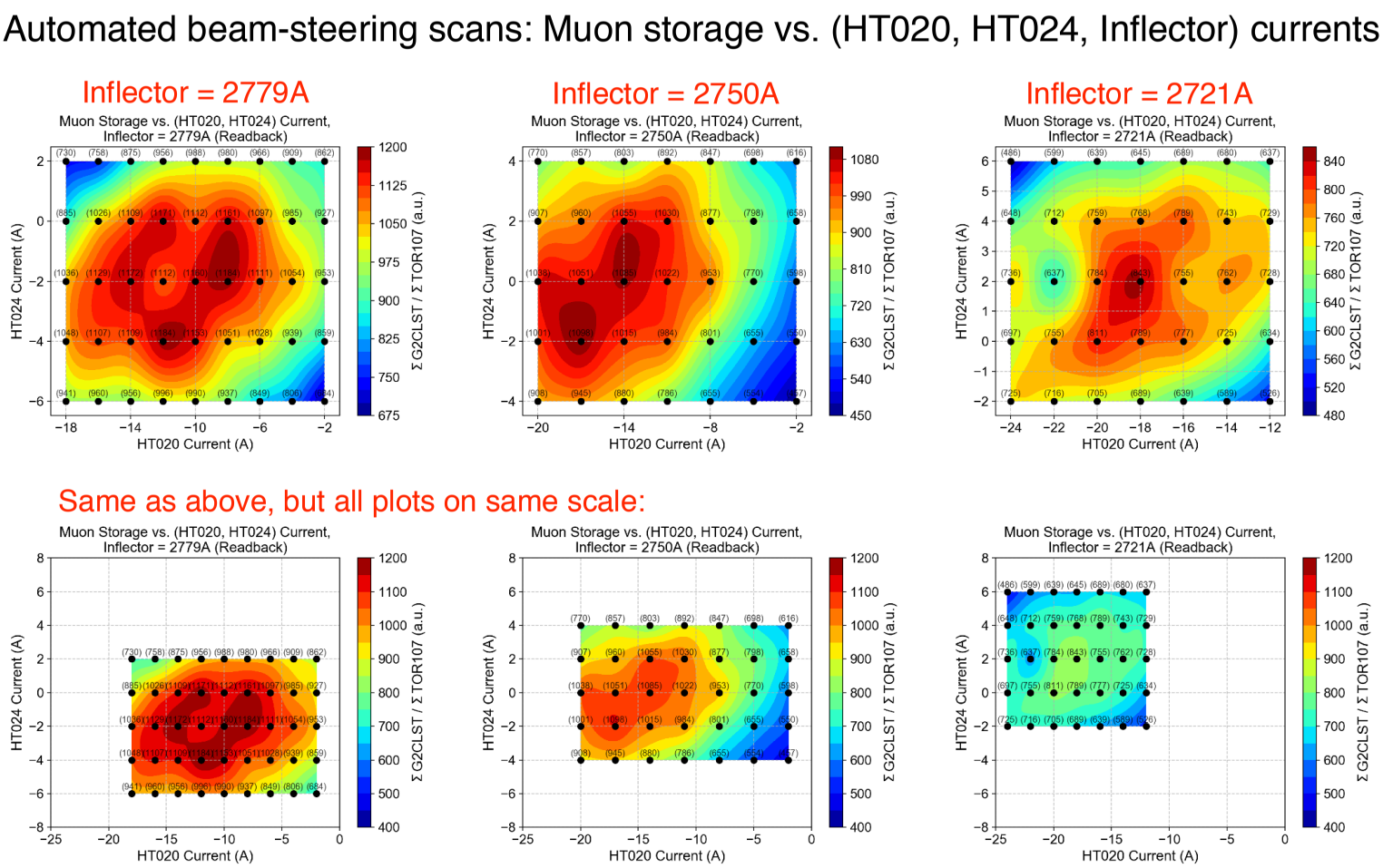

Figure 4.4: *Example automated beam-steering scans: Muon capture vs. (HT020, HT024, Inflector) currents. The top row of plots corresponds to three different inflector currents* $\{2780, 2750, 2720\}$ A *for which muon capture is monitored as a function of the currents of the last two horizontal TRIMs in the beamline (HT020, HT024). The contours correspond to the capture efficiency in the ring using new* ACNET *parameters to facilitate beam tuning (see text for discussion). The bottom row of plots is the same as the top row with all plots on the same scale, indicating an inflector current of* 2780 A *works best for this set of MC-1 quad voltages, kicker settings, etc.*

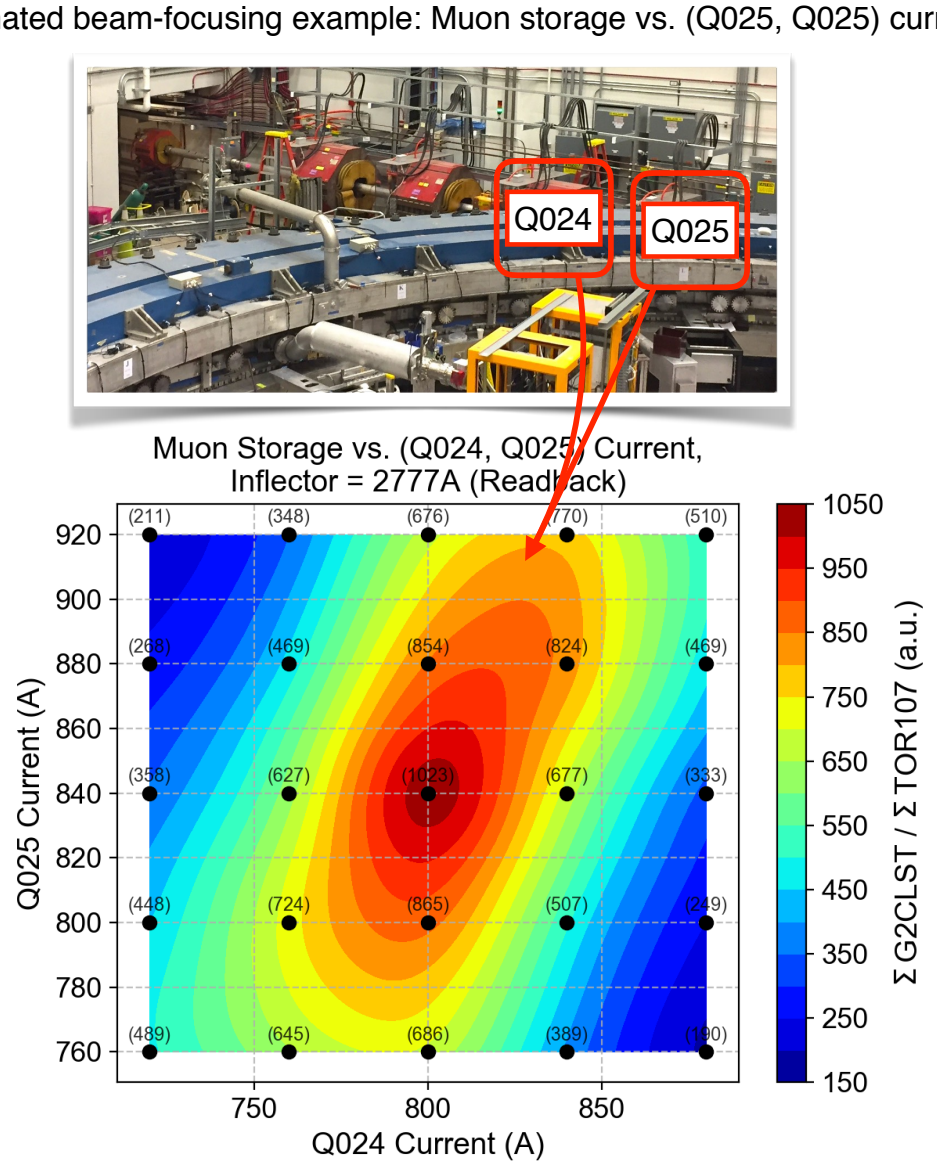

Figure 4.5: *Example automated beam-focusing scan utilizing the new ACNET parameters shown in Fig. 4.2 and one of several custom ACL scripts written by the author. Here, the currents of the last two magnetic quadrupoles in the M5 Final Focus (Q024, Q025) are being scanned in order to maximize the muon capture efficiency in the storage ring as measured by the number of reconstructed calorimeter clusters* ($\sum$ G2CLST) *normalized by the number of protons on target* ($\sum$ TOR107) *accumulated over one super cycle* (∼60 s).

4.2 Beam-Parameter Measurements in the M5 Final Focus

The new tools discussed in the previous section allow the beam steering and focusing in the M5 Final Focus (Fig. 4.5, top) to be rapidly optimized using computer scripts written in the Accelerator Control Language (ACL) to adjust two devices, such as (Q024, Q025), while monitoring muon injection efficiency as a function of magnet current, for example. The beam-steering studies are relatively simple and involve position and angle, which implies the use of two dipole magnets, however, the beam-focusing studies involve four Courant-Snyder parameters in principle, $(\alpha_x, \beta_x, \alpha_y, \beta_y)$, which implies the use of at least four quadrupoles. The original ACL scripts mentioned above were written for beam-steering optimizations, i.e. the scripts are limited to two magnets at most (HT020 and HT024, for example). Moreover, performing a brute-force multidimensional scan of the M5-Final-Focus quadrupoles is not an option since it is too costly in terms of time, resources, and presupposed operational stability of the experiment. Something more clever must be done, and measuring the beam parameters $(\alpha_x, \beta_x, \alpha_y, \beta_y)$ in the M5 Final Focus (M5FF) is the first step toward formulating a better plan of attack. This section describes the measurement of the beam parameters in the M5FF. The results obtained in this section will be used as the starting point of a more sophisticated study in which several M5FF quadrupoles are adjusted simultaneously in order to fine-tune the injection Courant-Snyder parameters $(\alpha_x, \beta_x, \alpha_y, \beta_y)$.

Magnetic quadrupoles are the accelerator physicist's tool of choice for manipulating beam widths and controlling the focusing properties of the beamline. As is discussed in Appendix A, changing a quadrupole current amounts to changing the shape and orientation of the phase-space ellipse,

$$\epsilon_x = \gamma_x x^2 + 2\alpha_x x x' + \beta_x x'^2, \tag{4.1}$$

where the emittance ϵ_x specifies a particular contour in phase space, $\beta_x = \sigma_x^2/\epsilon_x$ is related to the beam size, α_x describes the orientation ("tilt") of the phase-space ellipse, and $\beta_x\gamma_x - {\alpha_x}^2 = 1$ is the Courant-Snyder invariant. One way of experimentally determining the transverse beam parameters $\{\epsilon, \beta, \alpha\}_{x,y}$ is using the so-called "quadrupole-scan technique."[3] An overview of the experimental technique is shown in Fig. 4.6. First, a quadrupole in the

[3]The "quad scan" being discussed here is different than the quad scan performed in §4.1. The quad scan in this section is generally used by accelerator-based institutions worldwide to measure the beam parameters (not optimize beam focusing into the muon $g-2$ storage ring).

beamline is scanned over a range of focusing strengths (i.e. magnet currents) and the beam width is observed to change at a downstream detector. Next, a quadratic polynomial of the form $\sigma^2(x) = c_0 + c_1 x + c_2 x^2$ is fit to the observed beam sizes $\{\sigma_n^2 : n \in \text{measurements}\}$, where the independent variable x is related to the quadrupole focusing strength. Finally, the three polynomial fit coefficients $\{c_0, c_1, c_2\}$ are mapped to the space of beam parameters $\{\epsilon, \beta, \alpha\}$ using accelerator physics.

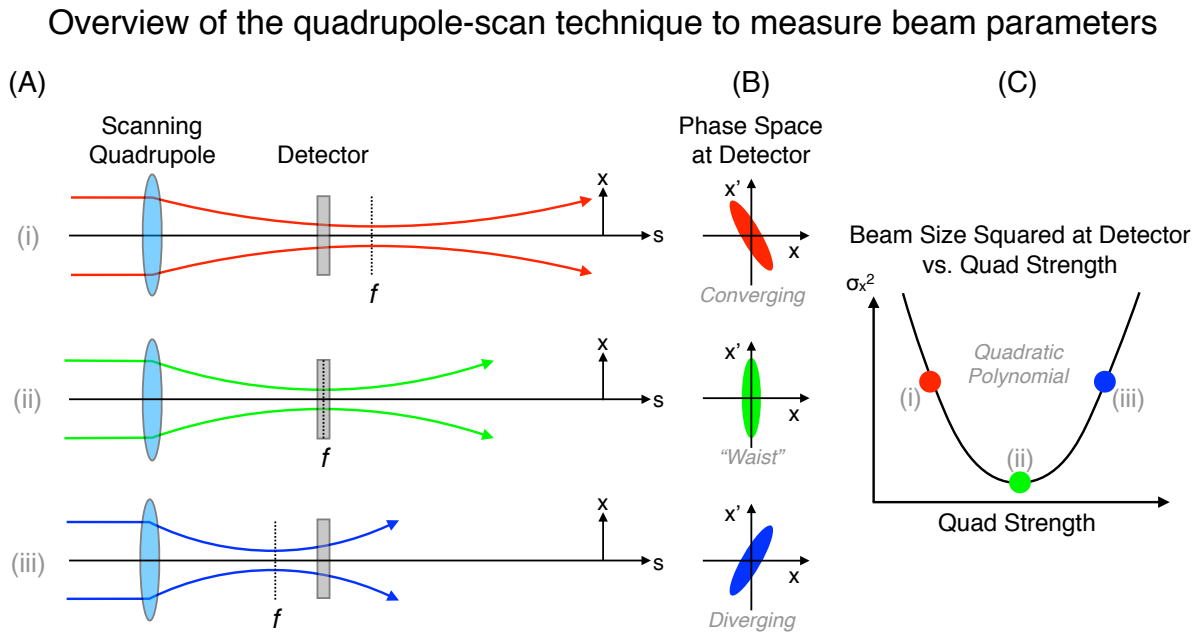

Figure 4.6: *Overview of the quadrupole-scan technique for measuring beam parameters. (A) As the quadrupole current is scanned, the focal length "f" changes, as does the beam width observed at the downstream detector. (B) Phase-space representation of the detected beam as the quadrupole current is scanned. The beam width passes through a minimum ("waist") when the ellipse is upright in phase-space (green) and the quad focal length f is exactly at the detector. (C) When the observed beam widths are plotted as a function of quad strength, the data follow a parabola of the form* $\sigma^2(x) = c_0 + c_1 x + c_2 x^2$. *The three polynomial fit coefficients* $\{c_0, c_1, c_2\}$ *are then mapped to the space of beam parameters* $\{\epsilon, \beta, \alpha\}$ *using accelerator physics.*

The quad-scan technique provides a simple and robust way to extract the beam param-

eters at a particular location in the beamline. This technique has been used on several occasions to measure the horizontal and vertical beam parameters $\{\epsilon, \beta, \alpha\}_{x,y}$ in the M5 beamline, especially at Q020. This location is very important since it marks the formal beginning of the M5 Final Focus. To measure the beam parameters, Q020 is scanned over a range of currents (0 A to 180 A) and the beam profiles at detector PWC021 are recorded.[4] In terms of the beamline layout, PWC021 can be seen in Fig. 4.5 near the ladder in the picture, which was being used to adjust PWC021 from above at the time. PWC021 is 11.6 m downstream from the centerline of Q020 and 0.4 m upstream from the edge of Q022. Example PWC021 beam profiles and fits are shown in Fig. 4.7. The most commonly used fit function is a 4-parameter Gaussian with baseline offset,

$$f(\{A, B, \bar{x}, \sigma_x\}; x) = A \exp\left[-\frac{1}{2}\left(\frac{x-\bar{x}}{\sigma_x}\right)^2\right] + B. \tag{4.2}$$

Other fit functions such as Lorentzians were investigated, however, the analysis presented below uses Eq. (4.2).

Once several beam profiles like Fig. 4.7(B) have been collected and fit, the connection to the beam parameters $\{\epsilon, \beta, \alpha\}$ may be established using accelerator physics. Since PWC021 is 11.6 m downstream from the centerline of Q020, yet the overall length Q020 is only 0.7 m, the analysis will first be discussed in the context of the thin-lens approximation to simplify the mathematics and establish the conceptual framework of extracting the beam parameters from the profile measurements. In the thin-lens approximation, the total transformation matrix that transports the beam from just upstream of the quadrupole (Q020) to the downstream detector (PWC021) is given by

$$M = \underbrace{\begin{pmatrix} 1 & L \\ 0 & 1 \end{pmatrix}}_{\substack{\text{Propagate} \\ \text{Q020 to} \\ \text{PWC021}}} \underbrace{\begin{pmatrix} 1 & 0 \\ \mp\frac{1}{f} & 1 \end{pmatrix}}_{\text{Q020}} = \begin{pmatrix} 1 \mp \frac{L}{f} & L \\ \mp\frac{1}{f} & 1 \end{pmatrix} \equiv \begin{pmatrix} C & S \\ C' & S' \end{pmatrix}, \tag{4.3}$$

where the $\{{}^{-}_{+}\}$ signs are for the $\{{}^{\text{horizontal}}_{\text{vertical}}\}$ planes given the polarity of Q020. Here, f is the quad focal length (which depends on the quad current; calculated using data from

[4] Q021 is off for this measurement.

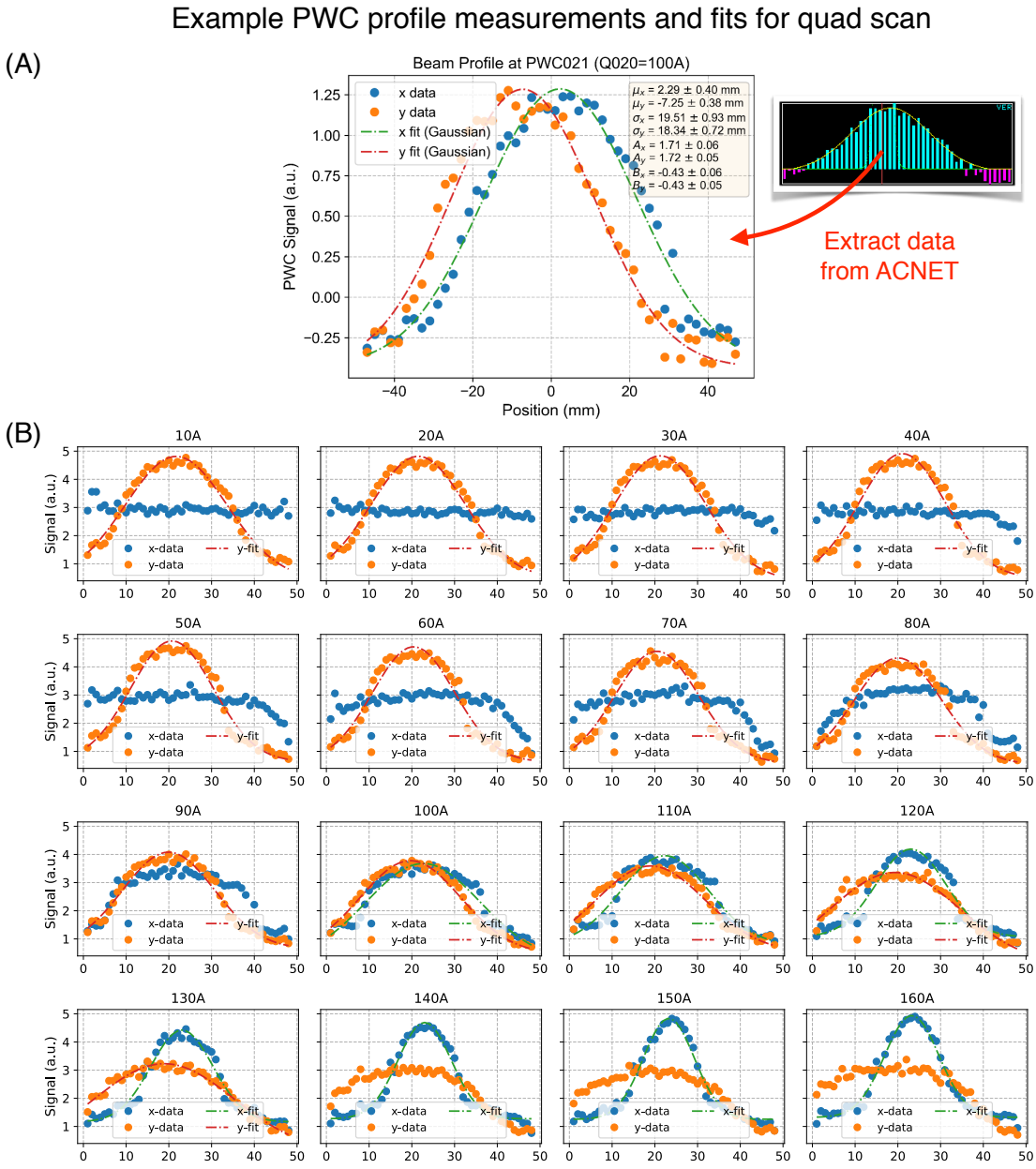

Figure 4.7: *(A) Example PWC021 profiles and fits for* Q020 = 100 A. *The horizontal data is in blue, while the horizontal fit is in green. The vertical data is in orange, while the vertical fit is in red. The fit function is a Gaussian with a baseline offset, Eq. (4.2). (B) PWC021 profiles and fits over a range of currents* Q020 = $\{10, 20, \ldots, 160\}$A. *The main purpose of this step is to collect a set of beam widths* $\{\sigma_n^2 : n \in \text{measurements}\}$ *that may be fit using a parabola, as shown in Fig. 4.6(C).*

Accelerator-Division), and $L = 11.6\,\mathrm{m}$ is the distance from the center of Q020 to the downstream observation point at PWC021. Armed with the transformation matrix Eq. (4.3), the theory of Appendix A may now be applied to determine the evolution of the beam parameters downstream,

$$\underbrace{\begin{pmatrix}\beta\\ \alpha\\ \gamma\end{pmatrix}}_{\text{PWC021}} = \underbrace{\begin{pmatrix} C^2 & -2CS & S^2 \\ -CC' & (C'S+CS') & -SS' \\ C'^2 & -2C'S' & -S'^2 \end{pmatrix}}_{\text{Propagate Q020 to PWC021}} \underbrace{\begin{pmatrix}\beta_0\\ \alpha_0\\ \gamma_0\end{pmatrix}}_{\text{Q020}}, \tag{4.4}$$

where the shorthands $C \equiv \left(1 \mp \frac{L}{f}\right)$, etc., are defined on the righthand side of Eq. (4.3). Multiplying the top row of Eq. (4.4) by the conserved beam emittance ϵ and remembering the spatial variance goes as $\sigma^2 = \epsilon\beta$ for dispersionless beams, the measured beam width at PWC021 as a function of Q020 beam parameters and Q020 focusing strength is given by

$$\sigma^2 = \epsilon\beta_0 \left(1 \mp \tfrac{L}{f}\right)^2 - 2L\epsilon\alpha_0 \left(1 \mp \tfrac{L}{f}\right) + L^2\epsilon\gamma_0. \tag{4.5}$$

For simplicity, the author tends to write the above expression as the quadratic polynomial

$$\sigma^2(x) = Bx^2 - 2ALx + CL^2, \tag{4.6a}$$

$$A \equiv \epsilon\alpha_0, \qquad B \equiv \epsilon\beta_0, \qquad C \equiv \epsilon\gamma_0, \qquad x \equiv \left(1 \mp \tfrac{L}{f}\right), \tag{4.6b}$$

which has the added benefit that the calculation of the beam emittance is a mnemonic that closely resembles the Courant-Snyder invariant $\beta\gamma - \alpha^2 = 1$,

$$\epsilon^2 = \epsilon^2(\beta\gamma - \alpha^2) = BC - A^2. \tag{4.7}$$

To summarize, the measured beam parameters expressed in terms of the polynomial Eq. (4.6a) are

$$\boxed{\epsilon = +\sqrt{BC - A^2}, \qquad \alpha_0 = A/\epsilon, \qquad \beta_0 = B/\epsilon, \qquad \gamma_0 = C/\epsilon}. \tag{4.8}$$

The beam parameters at Q020 obtained using the quad-scan technique and the thin-lens approximation are shown in Fig. 4.8(A).

One shortcoming of the above analysis is the assumption that the quadrupole in the

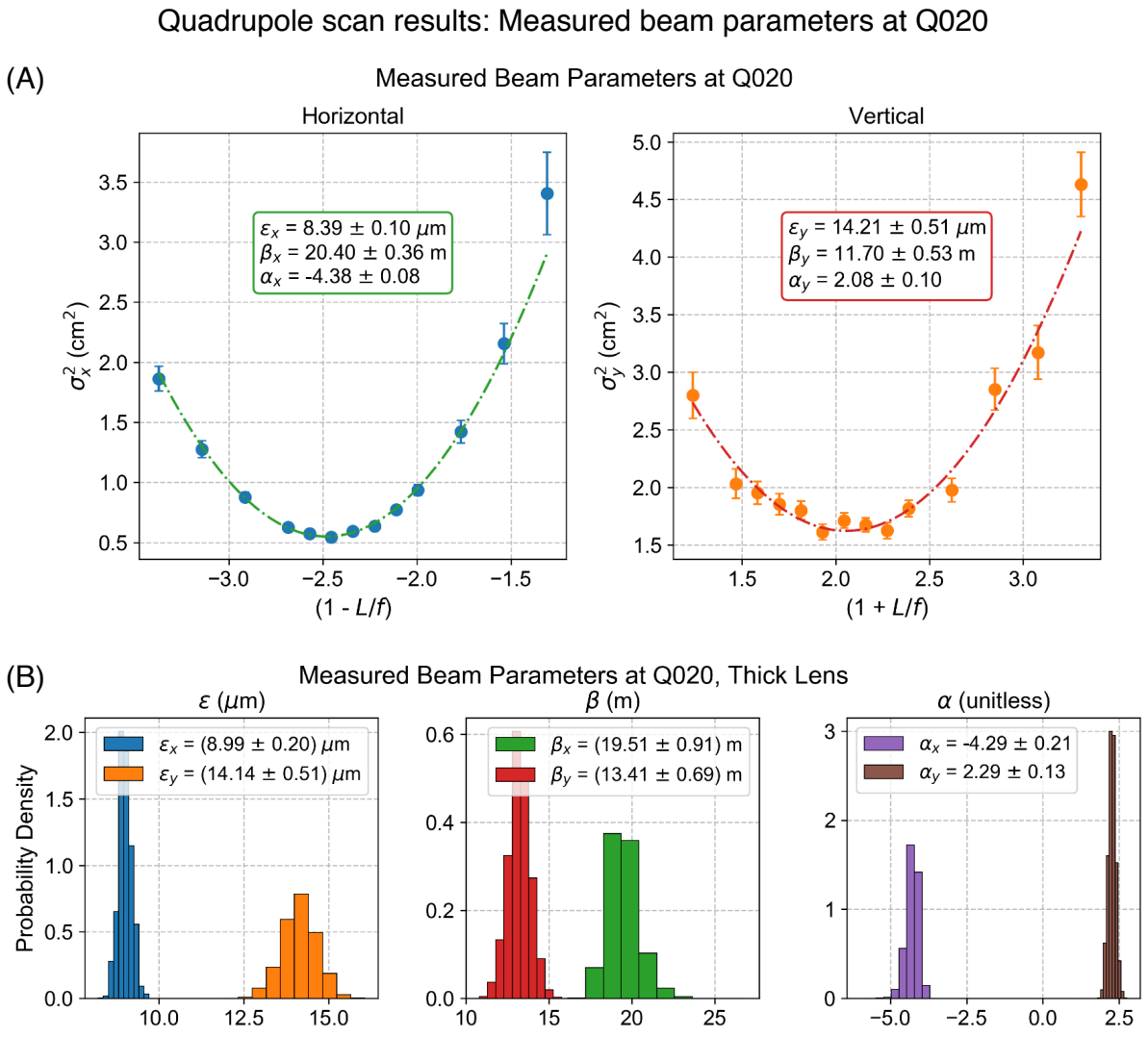

Figure 4.8: *Quadrupole scan results: Measured beam parameters at the entrance of Q020 obtained using (A) thin-lens and (B) thick-lens quad models. The thin-lens results agree well with the thick-lens results since distance between the center of the quad (Q020) and the detector (PWC021) is* 11.6 m *whereas the quad length is only* 0.7 m.

beamline (Q020) is infinitely thin. The above analysis may be made more realistic using a thick-lens quad model, however, this change to the analysis means the mathematics becomes more abstruse/obtuse and parabolas like Fig. 4.8 may no longer be drawn. The reason is the simple thin-lens quad matrix in Eq. (4.3) now becomes

$$M_Q = \begin{pmatrix} 1 & 0 \\ \mp\frac{1}{f} & 1 \end{pmatrix} \quad \Rightarrow \quad \begin{cases} \begin{pmatrix} \cos(\sqrt{k}\ell) & \frac{1}{\sqrt{k}}\sin(\sqrt{k}\ell) \\ -\sqrt{k}\sin(\sqrt{k}\ell) & \cos(\sqrt{k}\ell) \end{pmatrix}, & (k>0, \text{ focusing}) \\ \\ \begin{pmatrix} \cosh(\sqrt{|k|}\ell) & \frac{1}{\sqrt{|k|}}\sinh(\sqrt{|k|}\ell) \\ \sqrt{|k|}\sinh(\sqrt{|k|}\ell) & \cosh(\sqrt{|k|}\ell) \end{pmatrix}, & (k<0, \text{ defocusing}) \end{cases}, \tag{4.9}$$

which, when inserted into Eq. (4.4), no longer gives a simple quadratic polynomial in the variable $|k|\ell \sim 1/f$ for the beam width $\sigma^2 = \epsilon\beta$. Nevertheless, the derivation leading to Eq. (A.26) shows that for any 2×2 transport matrix

$$M = \begin{pmatrix} C & S \\ C' & S' \end{pmatrix},$$

the beam width evolves downstream according to

$$\sigma^2 = \epsilon\beta = \epsilon\beta_0 C^2 - 2\epsilon\alpha_0 CS + \epsilon\gamma_0 S^2 = \begin{pmatrix} C^2 & -2CS & S^2 \end{pmatrix} \begin{pmatrix} \epsilon\beta_0 \\ \epsilon\alpha_0 \\ \epsilon\gamma_0 \end{pmatrix}, \tag{4.10}$$

where the more complicated components of the thick-lens quad matrices Eq. (4.9) must now be used compared to the thin-lens case. The form of Eq. (4.10) suggests the collection of

measured beam widths at PWC021 may be gathered up into a matrix equation,

$$\mathbf{y} \equiv \underbrace{\begin{pmatrix} \sigma_1^2 \\ \sigma_2^2 \\ \vdots \\ \sigma_N^2 \end{pmatrix}}_{\substack{\text{PWC021} \\ \text{Measurements}}} = \underbrace{\begin{pmatrix} C_1^2 & -2C_1S_1 & S_1^2 \\ C_2^2 & -2C_2S_2 & S_2^2 \\ \vdots & \vdots & \vdots \\ C_N^2 & -2C_NS_N & S_N^2 \end{pmatrix}}_{\substack{\text{Beamline Settings,} \\ \text{“Coefficient Matrix”}}} \underbrace{\begin{pmatrix} \epsilon\beta_0 \\ \epsilon\alpha_0 \\ \epsilon\gamma_0 \end{pmatrix}}_{\substack{\text{Q020} \\ \text{Desired}}} \equiv \mathbf{M}\mathbf{x}, \tag{4.11}$$

where $\mathbf{y} \equiv (\sigma_1^2, \sigma_2^2, \ldots, \sigma_N^2)^T$ is the vector of N beam widths measured at PWC021, $\mathbf{M}$ is the coefficient matrix of shape $N \times 3$ that depends on the beamline settings, and $\mathbf{x} \equiv \epsilon(\beta_0, \alpha_0, \gamma_0)^T$ is the 3-vector of desired beam parameters at Q020.[5] Since the coefficient matrix $\mathbf{M}$ has shape $N \times 3$, it might not posses an inverse (since it is not necessarily square), and care must be taken in extracting the beam-parameter vector $\mathbf{x} = \epsilon(\beta_0, \alpha_0, \gamma_0)^T$. One solution is to first multiply on the left by $\mathbf{M}^T$ in order to form the 3×3 matrix $\mathbf{M}^T\mathbf{M}$, which does possess an inverse (since it is square), followed by multiplication on the left by $(\mathbf{M}^T\mathbf{M})^{-1}$. Doing so gives the gives the measured beam parameters [27, 72],

$$\mathbf{x} \equiv \begin{pmatrix} \epsilon\beta_0 \\ \epsilon\alpha_0 \\ \epsilon\gamma_0 \end{pmatrix} = \left[\left(\mathbf{M}^T\mathbf{M}\right)^{-1} \mathbf{M}^T \right] \mathbf{y}, \tag{4.12}$$

where $\mathbf{y} = (\sigma_1^2, \sigma_2^2, \ldots, \sigma_N^2)^T$ is again the vector of beam widths observed at PWC021 and $\mathbf{M}$ is the coefficient matrix defined in Eq. (4.11). The components of the vector $\mathbf{x}$ are then used to solve for the emittance $\epsilon^2 = \epsilon^2 (\beta_0\gamma_0 - \alpha_0^2) = x_1x_3 - x_2^2$, which in turn are used to solve for $(\beta_0, \alpha_0, \gamma_0) = (x_1, x_2, x_3)/\epsilon$. It is worth briefly mentioning the collection of measurements $\mathbf{y} = (\sigma_1^2, \sigma_2^2, \ldots, \sigma_N^2)^T$ do not have to come from the same detector so long as the profiles are measured downstream of the location of interest and the coefficient matrix $\mathbf{M}$ in Eq. (4.11) is known from the beamline model. This is a good way to obtain a more holistic view of the beamline and to constrain results, however, this approach is not immune to discontinuous changes to the beam parameters from scraping, for example. This approach was pursued by

[5] Note: An equation of the form Eq. (4.11) exists for both the horizontal and vertical transverse dimensions since quads focus in one plane and defocus in the other.

the author, however, it was not trusted since there was evidence of vertical beam scraping in the M5 Final Focus at the time the beam profiles were collected. It is also worth briefly mentioning the above matrix-inversion approach to determining the beam parameters does not allow for experimental uncertainties. One approach explored by the author is to write Eq. (4.11) instead as

$$\mathbf{y} \pm \delta\mathbf{y} \equiv \underbrace{\begin{pmatrix} \sigma_1^2 \pm \delta\sigma_1^2 \\ \sigma_2^2 \pm \delta\sigma_2^2 \\ \vdots \\ \sigma_N^2 \pm \delta\sigma_N^2 \end{pmatrix}}_{\substack{\text{Measurements and} \\ \text{Uncertainties}}} = \underbrace{\begin{pmatrix} C_1^2 & -2C_1S_1 & S_1^2 \\ C_2^2 & -2C_2S_2 & S_2^2 \\ \vdots & \vdots & \vdots \\ C_N^2 & -2C_NS_N & S_N^2 \end{pmatrix}}_{\text{Beamline Magnet Settings}} \underbrace{\begin{pmatrix} \epsilon\beta_0 \pm \delta(\epsilon\beta_0) \\ \epsilon\alpha_0 \pm \delta(\epsilon\alpha_0) \\ \epsilon\gamma_0 \pm \delta(\epsilon\gamma_0) \end{pmatrix}}_{\substack{\text{Desired and} \\ \text{Uncertainties}}} = \mathbf{M}\left(\mathbf{x} + \delta\mathbf{x}\right), \quad (4.13)$$

which does include experimental uncertainties. The measurement vector $\mathbf{y}$ may then be randomly perturbed thousands of times by Gaussian-distributed noise $\delta\mathbf{y}$ (which is known from the fit results) in order to determine the range of beam parameters $\mathbf{x} \pm \delta\mathbf{x}$ encountered in Eq. (4.12). These results are shown in Fig. 4.8(B) and agree quite well with the thin-lens results. The final summary of measured beam parameters at Q020 in the M5 beamline obtained using the quad-scan technique is shown in Table 4.1 as well as a comparison to the expected values. Other techniques such as Simulated Annealing (SA) were also investigated with similar results. The measured beam parameters obtained in this section will be used as the starting point for a more sophisticated optimization of the muon beam focusing into the $g-2$ storage ring discussed in the next section.

Measured Beam Parameters at Q020 in the M5 Final Focus

	Horizontal			Vertical		
	ϵ_x(µm)	β_x(m)	α_x(unitless)	ϵ_y(µm)	β_y(m)	α_y(unitless)
Thin Lens	8.4(1)	20.4(4)	−4.4(1)	14.2(5)	11.7(5)	2.1(1)
Thick Lens	9.0(2)	19.5(10)	−4.3(2)	14.2(5)	13.5(6)	2.3(1)
Expected [73, 30]	14.8	19.0	−2.5	16.0	4.6	0.8

Table 4.1: *Summary of beam-parameter measurements at Q020 in the M5 Final Focus obtained using the quadrupole-scan technique. Uncertainties are shown in parenthesis. The reported emittance is the geometric RMS emittance. The measured horizontal emittance is low compared to the G4beamline simulation [30], perhaps due to scraping in the Delivery-Ring injection and/or extraction, however the Courant-Snyder parameters agree well with the M4/M5 design lattice [73]. The measured vertical emittance agrees well [30] yet the Courant-Snyder parameters do not [73], perhaps due to a Delivery-Ring extraction mismatch that has propagated down M4/M5.*

4.3 M5 Final-Focus "Multiknob" (MULT) Studies

Any rigorous study aiming to optimize the focusing of the injected beam into the muon $g-2$ storage ring will use the magnetic quadrupoles nearest the ring to target the Courant-Snyder parameters $\{\alpha_x, \beta_x, \alpha_y, \beta_y\}$. This section of beamline, known as the M5 Final Focus (M5FF), is shown in red in Fig. 4.2. The M5FF is dispersion-free by design $(\eta_x, \eta'_x, \eta_y, \eta'_y)^T = \vec{0}$ due to the narrow inflector aperture through which the beam must pass during injection. As mentioned above, one difficulty with performing beam-focusing studies is that quadrupoles focus in one plane but *defocus* in the other plane: horizontal focusing causes the beam to blow up vertically, and vice versa. However, it is possible to separate the horizontal focusing from the vertical focusing using a construction known as a "multiknob" (MULT), in which several beamline devices such as quadrupoles are adjusted simultaneously.[6] One procedure for constructing MULTs developed independently by the author is outlined below,

[6]Fermilab ACNET device names were originally limited to four characters, hence "multiknob" → MULT.

and results are given that demonstrate the focusing of the beam into the muon storage ring can be optimized using MULTs in the M5 Final Focus.

As first step toward designing a beam-focusing study, the measured Courant-Snyder parameters $\{\alpha_x, \beta_x, \alpha_y, \beta_y\}$ obtained in §4.2 are propagated to the end of the M5 beamline as shown in Fig. 4.9. Here, quadrupole excitation data from Fermilab Accelerator Division is used to convert simulation quadrupole strengths in units of $[k] = \mathrm{m}^{-2}$ to ACNET quadrupole currents in units of $[I] = \mathrm{A}$, and a simple *MAD-X* simulation of the M5 Final Focus is used to transport the beam parameters downstream to the entrance of the storage ring (Fig. 4.9, right). Next, the resulting beam parameters at the end of the M5 beamline are overlayed on contour plots of muon capture efficiency vs. injection $(\alpha, \beta)_{x,y}$ from *gm2ringsim*, as shown in Fig. 4.10. The main purpose of this step is to assess where in the landscape of optimal focusing the measured beam parameters lie and to guide future MULT-construction efforts in subsequent steps. The results shown in Fig. 4.10 suggest the measured beam parameters are close to the optimal values, however, there is room for improvement.

One salient feature in each of the subplots in Fig. 4.10 is the strong linear correlation between Courant-Snyder parameters (β, α) that maximize capture efficiency of the beam injected into the ring. This is expected since the muon beam must pass through the narrow transverse aperture (18(W)×56(H) mm^2) of the 1.7-m long inflector, and that, by definition $\alpha \equiv -\frac{1}{2}(d\beta/ds)$. Stated differently, the muon beam can be made larger at the ring entrance if the focusing strength is increased such that the beam remains focused to a waist near the middle of the inflector beam channel. Similarly, the muon beam can be made smaller as long as the focusing is decreased to preserve the waist in the inflector, leading to the correlations observed in Fig. 4.10. The structure of Fig. 4.10 also suggests a novel way to optimize beam focusing into the storage ring: instead of tuning along the canonical $\{\hat{\beta}, \hat{\alpha}\}$-directions, the M5FF quadrupoles could be adjusted to move the beam parameters "parallel to" and "perpendicular to" the red ridges of optimal focusing shown in Fig. 4.10. Although these new directions are just linear combinations of the canonical $\{\hat{\beta}, \hat{\alpha}\}$-directions commonly used accelerator physics, they are tailor-made for optimizing injection into the muon $g-2$ storage ring. Thus, an effective tuning strategy is to (1) "climb up the ridge" as rapidly as possible using the MULT moves $\{\beta, \alpha\}_{x,y}$ perpendicular to the ridge, then (2) "walk along the ridge" using the MULT that moves $\{\beta, \alpha\}_{x,y}$ parallel to the ridge, and (3) repeat until the muon capture efficiency is maximized. As will be demonstrated below, a few iterations of this

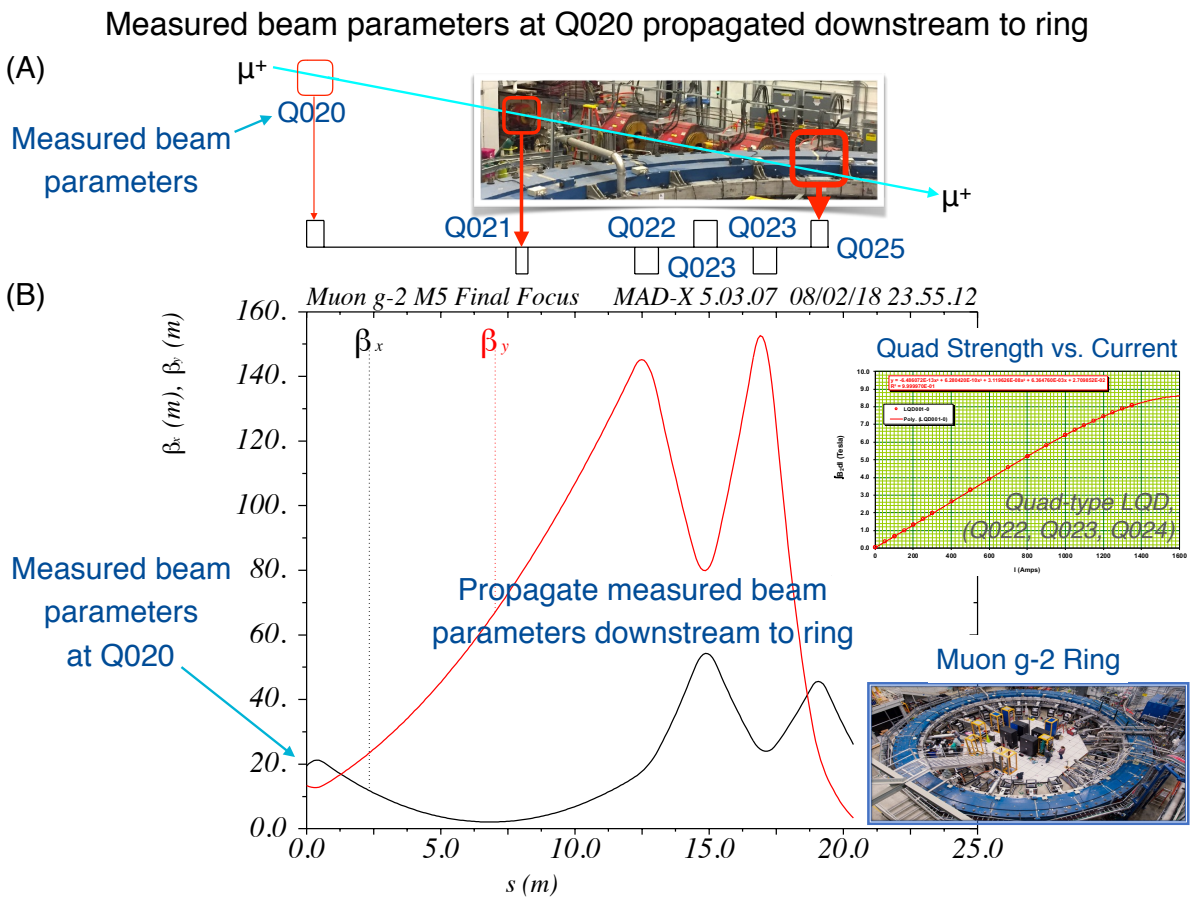

Figure 4.9: *The measured beam parameters at Q020 are propagated to the entrance of the muon $g-2$ storage ring using a simple MAD-X model. (A) Physical layout of the M5 Final Focus. The muon storage ring is at the right in blue. (B) Example simulation results from MAD-X. The measured beam parameters at Q020 are the simulation input at the left. The output of the simulation is the beam parameters at the entrance to the muon storage ring. The inset at the right is an example of a "quad excitation curve" from Fermilab Accelerator Division, in which the quad focusing strength increases linearly with the applied current until the saturation of the magnet steel becomes important (red line toward right). Four different excitation curves are used since the M5 Final Focus is comprised of four different types of quadrupoles, (Q020=4Q24, Q021=SQA, {Q022, Q023, Q024}=LQD, Q025=LQB).*

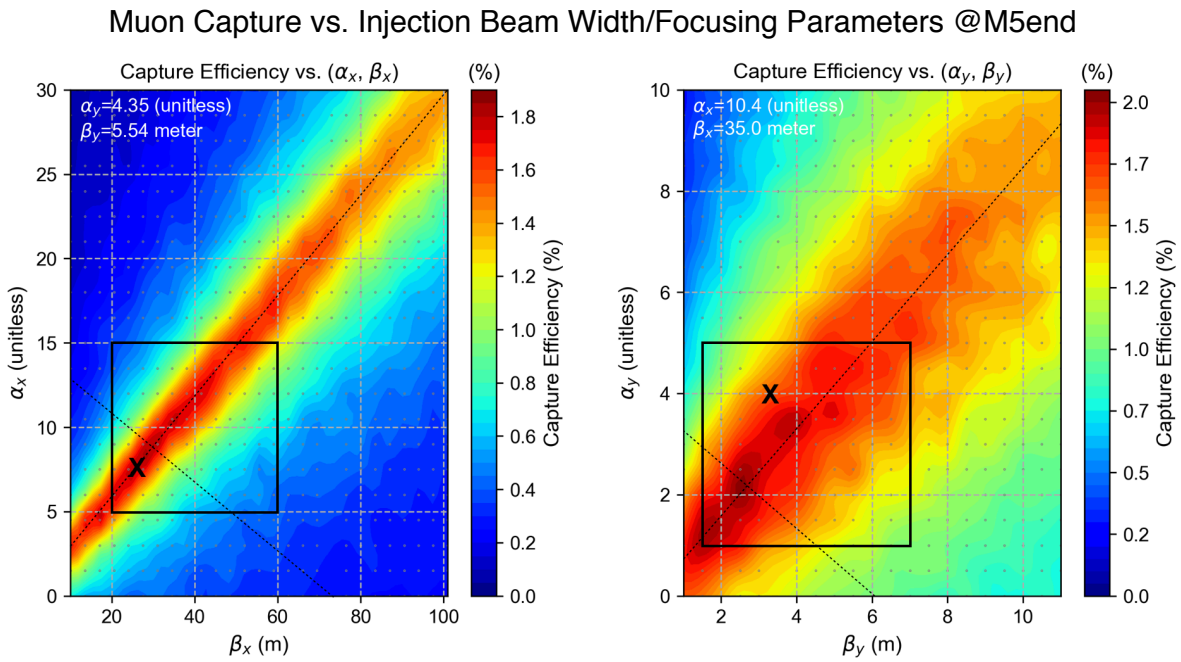

Figure 4.10: *Muon storage vs. beam width/focusing parameters* $(\beta, \alpha)_{x,y}$ *at the end of the M5 beamline about* 30 cm *upstream of the ring. The left subplot is muon capture efficiency vs. horizontal* (β_x, α_x)*, while the right subplot is muon capture efficiency vs. vertical* (β_y, α_y)*. The underlying contour plot is from gm2ringsim, where each tiny grey dot is a simulation of* $\mathcal{O}(10^5)$ *injected muons executed on Fermigrid (a supercomputer). The black "X" marks are the measured beam parameters at Q020 propagated downstream to the end of the M5 beamline before any further optimization (Fig. 4.9). The black boxes represent a desirable range of* $(\beta, \alpha)_{x,y}$ *that will be explored using MULTs below. In addition to the canonical* $(\hat{\beta}, \hat{\alpha})$*-directions, the thin black lines represent a different set of orthogonal basis vectors that allow the beam parameters to be varied in a direction "parallel to" or "perpendicular to" the red ridge of optimal beam focusing parameters shown above.*

procedure leads to the rapid optimization of the focusing of the beam into the muon storage ring.

The four beam parameters of interest $\{\beta_x, \alpha_x, \beta_y, \alpha_y\}$ imply at least four quadrupoles will be involved in the construction of the MULT, and it will likely be advantages to include more quads since the response might not be linear with respect to the quad currents over the range of interest (Fig. 4.10, black boxes). The obvious choice is the four large quads immediately upstream of the ring (Q022, Q023, Q024, Q025) as well as the two matching quads that feed beam into the M5 Final Focus (Q020, Q021). These six quads span about 20 m of beamline upstream of the muon storage ring. In order to determine the current ratios and relative signs of Q020–Q025 that define the MULT, one approach is to use an optics model such as *MAD-X* to construct the "response matrix" [72]

$$\begin{pmatrix} \Delta\beta_x \\ \Delta\alpha_x \\ \Delta\beta_y \\ \Delta\alpha_y \\ \vdots \end{pmatrix} = \underbrace{\begin{pmatrix} J_{11} & J_{12} & \cdots & J_{1N} \\ J_{21} & J_{22} & \cdots & J_{2N} \\ \vdots & \vdots & \ddots & \vdots \\ J_{M1} & J_{M2} & \cdots & J_{MN} \end{pmatrix}}_{\substack{\text{"Response Matrix"} \\ \text{(Jacobian)}}} \underbrace{\begin{pmatrix} \Delta K_1 \\ \Delta K_2 \\ \vdots \\ \Delta K_N \end{pmatrix}}_{\substack{\text{Quad} \\ \text{Perturbations}}}, \tag{4.14}$$

where $(\Delta K_1, \Delta K_2, \ldots, \Delta K_N)^T$ is the vector of quad-strength perturbations and the response matrix is the Jacobian (§3.3.1) in the Taylor expansion of the vector-valued function

$$\mathbf{f}(K_1, K_2, \ldots, K_N) = (\beta_x, \alpha_x, \beta_y, \alpha_y, \ldots)^T. \tag{4.15}$$

Once the response matrix has been constructed, Eq. (4.14) may then be inverted to solve for the change in quad strengths that generate a desired change to the beam parameters, for example, $J^{-1}(\Delta\beta_x = 1\,\text{m}, 0, 0, 0, \ldots)^T = \Delta\mathbf{K}$. A potential problem with this approach is it assumes the beam parameters change linearly with respect to the quad currents, which might not be true over the range of interest shown in Fig. 4.10 (black boxes). In order to guard against this possibility, a more global approach was taken, an example of which is shown in Fig. 4.11. The basic idea is to construct the function Eq. (4.15) instead of the perturbation Eq. (4.14), then switch to the local description once linearity has been verified and a sensible expansion point $\mathbf{x}_0 = (\beta_{x0}, \alpha_{x0}, \ldots)^T$ has been chosen. Figure 4.11 shows an example of

how the quad currents are indeed linear over the range of interest, so the local Jacobian description may be used. Continuing with the example of the α_x MULT, the relevant row of the Jacobian Eq. (4.14) may be written directly in terms of the quad currents since the focusing strength $[\Delta K] = \mathrm{m}^{-2}$ varies linearly with the current $[\Delta I] = \mathrm{A}$, leading to

$$\Delta\alpha_x = \frac{\partial\alpha_x}{\partial I_{\mathrm{Q020}}}\Delta I_{\mathrm{Q020}} + \frac{\partial\alpha_x}{\partial I_{\mathrm{Q021}}}\Delta I_{\mathrm{Q021}} + \cdots + \frac{\partial\alpha_x}{\partial I_{\mathrm{Q025}}}\Delta I_{\mathrm{Q025}}. \tag{4.16}$$

The final step is to use the chain rule from ordinary calculus to recast Eq. (4.16) in terms of one and only one quad current, for example,

$$\begin{aligned}
\Delta\alpha_x &= \frac{\partial\alpha_x}{\partial I_{\mathrm{Q020}}}\Delta I_{\mathrm{Q020}} + \frac{\partial\alpha_x}{\partial I_{\mathrm{Q021}}}\Delta I_{\mathrm{Q021}} + \cdots + \frac{\partial\alpha_x}{\partial I_{\mathrm{Q025}}}\Delta I_{\mathrm{Q025}} \\
&= \left(\frac{\partial\alpha_x}{\partial I_{\mathrm{Q020}}}\frac{\partial I_{\mathrm{Q020}}}{\partial I_{\mathrm{Q025}}} + \frac{\partial\alpha_x}{\partial I_{\mathrm{Q021}}}\frac{\partial I_{\mathrm{Q021}}}{\partial I_{\mathrm{Q025}}} + \cdots + \frac{\partial\alpha_x}{\partial I_{\mathrm{Q025}}}(1)\right)\Delta I_{\mathrm{Q025}} \\
&= \underbrace{\begin{pmatrix} \partial\alpha_x/\partial I_{\mathrm{Q020}} \\ \partial\alpha_x/\partial I_{\mathrm{Q021}} \\ \vdots \\ \partial\alpha_x/\partial I_{\mathrm{Q025}} \end{pmatrix}^T}_{\substack{\text{Row of} \\ \text{Jacobian}}} \underbrace{\begin{pmatrix} \partial I_{\mathrm{Q020}}/\partial I_{\mathrm{Q025}} \\ \partial I_{\mathrm{Q021}}/\partial I_{\mathrm{Q025}} \\ \vdots \\ 1 \end{pmatrix}}_{\substack{\text{MULT} \\ \text{Coefficients}}} \underbrace{\Delta I_{\mathrm{Q025}}}_{\substack{\text{MULT Seed} \\ \text{Current}}},
\end{aligned} \tag{4.17}$$

where the MULT has been arbitrarily defined in terms of the current of Q025 since this quad is nearest the ring and tends to have the biggest effect on muon capture efficiency. The MULT coefficients, i.e. the weights and relative signs of quad currents, are calculated using Eq. (4.17) together with the slopes shown in Fig. 4.11(D),

$$\boxed{w_{\mathrm{Q}} \equiv \frac{\partial I_{\mathrm{Q}}}{\partial I_{\mathrm{Q025}}} = \frac{\partial I_{\mathrm{Q}}/\partial N_{\mathrm{sim}}}{\partial I_{\mathrm{Q025}}/\partial N_{\mathrm{sim}}}, \qquad \mathrm{Q} \in \{\mathrm{Q020}, \mathrm{Q021}, \ldots, \mathrm{Q025}\}}\,. \tag{4.18}$$

The procedure outlined above was developed independently by the author and has been used to construct eight total MULTs in the M5 Final Focus, *viz.* one for each of the four canonical directions $\{\hat{\beta}_x, \hat{\alpha}_x, \hat{\beta}_y, \hat{\alpha}_y\}$ plus another four $\{\hat{x}_\perp, \hat{x}_\parallel, \hat{y}_\perp, \hat{y}_\parallel\}$ for each of the directions "perpendicular" and "parallel" to the red ridges of optimal beam-focusing parameters shown in Fig. 4.10. Each of the eight MULTs was entered into ACNET, as shown in Fig. 4.12, and an

example optimization of the horizontal beam focusing into the g–2 ring is shown in Fig. 4.13. Implementation of the above procedure has led to a means of rapidly and unambiguously optimizing the horizontal and vertical focusing of the injected beam into the muon $g-2$ storage ring.

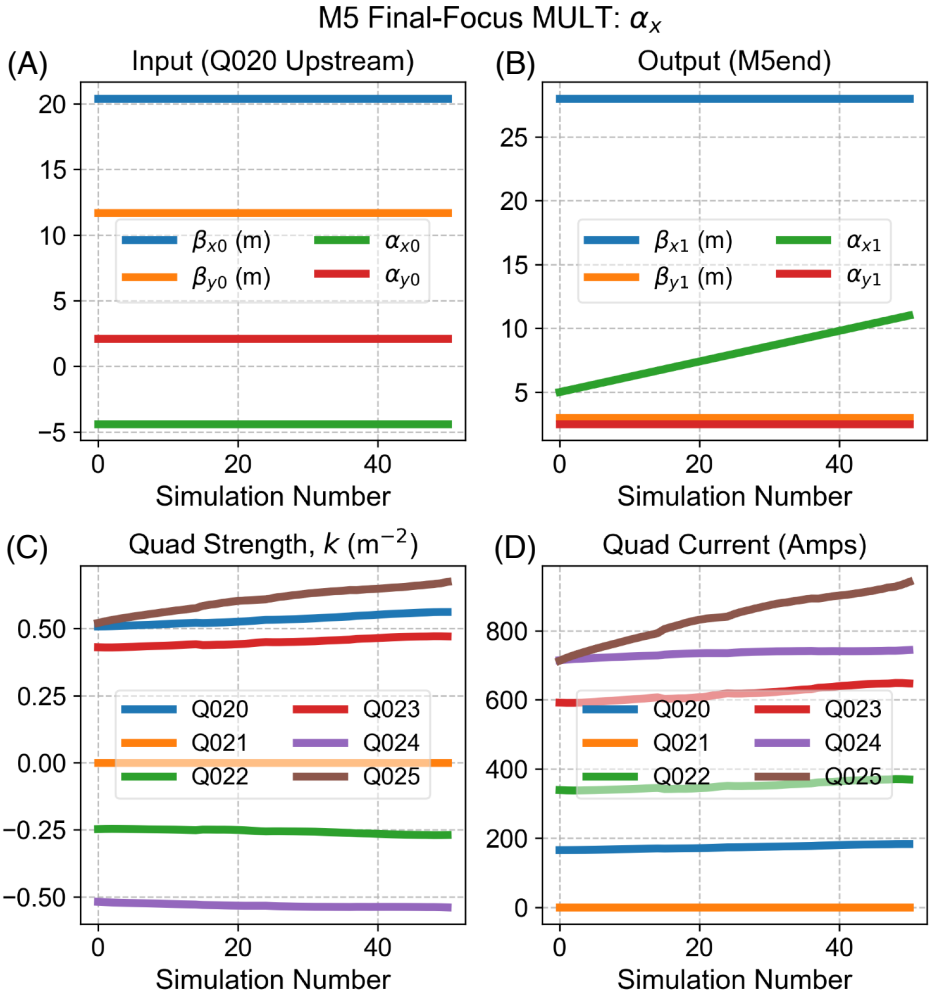

Figure 4.11: *Example procedure for constructing a "multiknob" (MULT) in the M5 Final Focus. This particular MULT uses Q020–Q025 to isolate the Courant-Snyder parameter* α_x *30* cm *upstream of the muon storage ring, which allows for the horizontal beam focusing to be varied while keeping the beam size and vertical focusing fixed. (A) The inputs to all MAD-X simulations are the measured beam parameters at Q020 shown in Fig. 4.8. (B) The desired effect is to vary only* α_x *(green line) over a range that encompasses the red ridge of optimal beam focusing shown in Fig. 4.10 while keeping* $\{\beta_x, \alpha_y, \beta_y\}$ *constant. (C) Quadrupole strengths and (D) quadrupole currents needed to achieve the beam parameters shown in (B). The MULT coefficients are defined using the ratios of slopes shown in (D), for example,* $w_Q \equiv \partial I_{\mathrm{Q}}/\partial I_{\mathrm{Q025}} = (\partial I_{\mathrm{Q}}/\partial N_{\mathrm{sim}})\,/\,(\partial I_{\mathrm{Q025}}/\partial N_{\mathrm{sim}})$ *as per Eq. (4.18).*

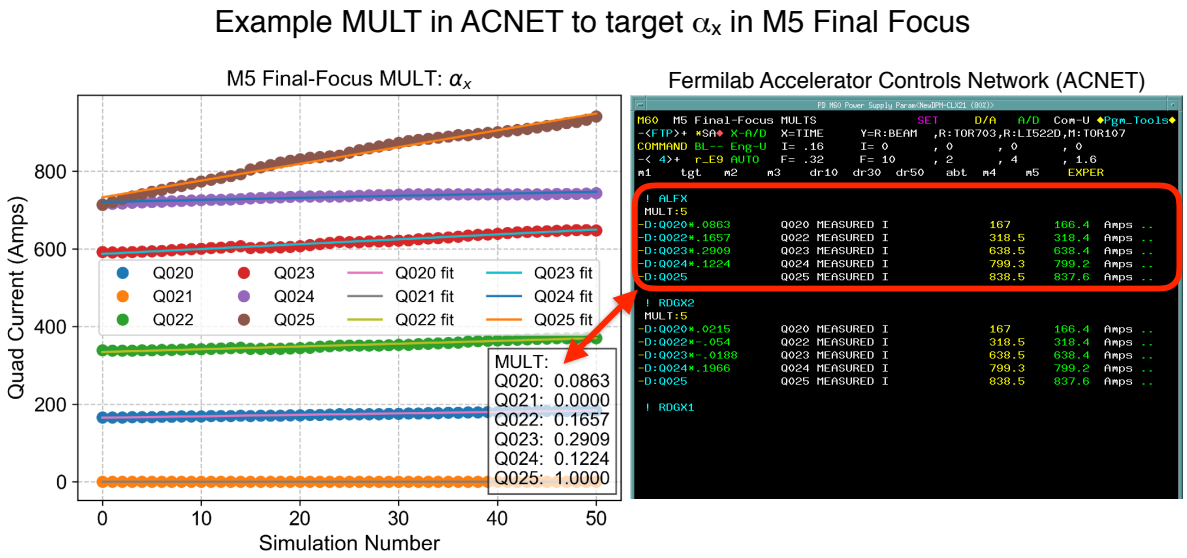

Figure 4.12: *Example quadrupole MULT used to isolate the Courant-Snyder parameter α_x 30 cm upstream of the muon storage ring. The left subplot shows the linear fits to the quad currents of Fig. 4.11(D) that are used to define the MULT coefficients, $w_Q \equiv \partial I_Q/\partial I_{Q025} = (\partial I_Q/\partial N_{sim})\,/\,(\partial I_{Q025}/\partial N_{sim})$ as per Eq. (4.18). Here, Q025 has been chosen as the MULT seed current since this horizontally focusing quadrupole is closest to the ring and it tends to have the biggest impact on focusing the beam through the narrow inflector channel 18(W) × 56(H) mm^2. The right subplot shows an example of how MULTs are entered into the Accelerator Controls Network (*ACNET*), which is used to control actual magnet currents. Eight MULTs were created in total to target the directions $\left\{\{\hat{\beta}_x, \hat{\alpha}_x, \hat{\beta}_y, \hat{\alpha}_y\}, \{\hat{x}_\perp, \hat{x}_\parallel, \hat{y}_\perp, \hat{y}_\parallel\}\right\}$, as discussed in the text. An example beam-focusing optimization performed using MULTs is shown in Fig. 4.13.*

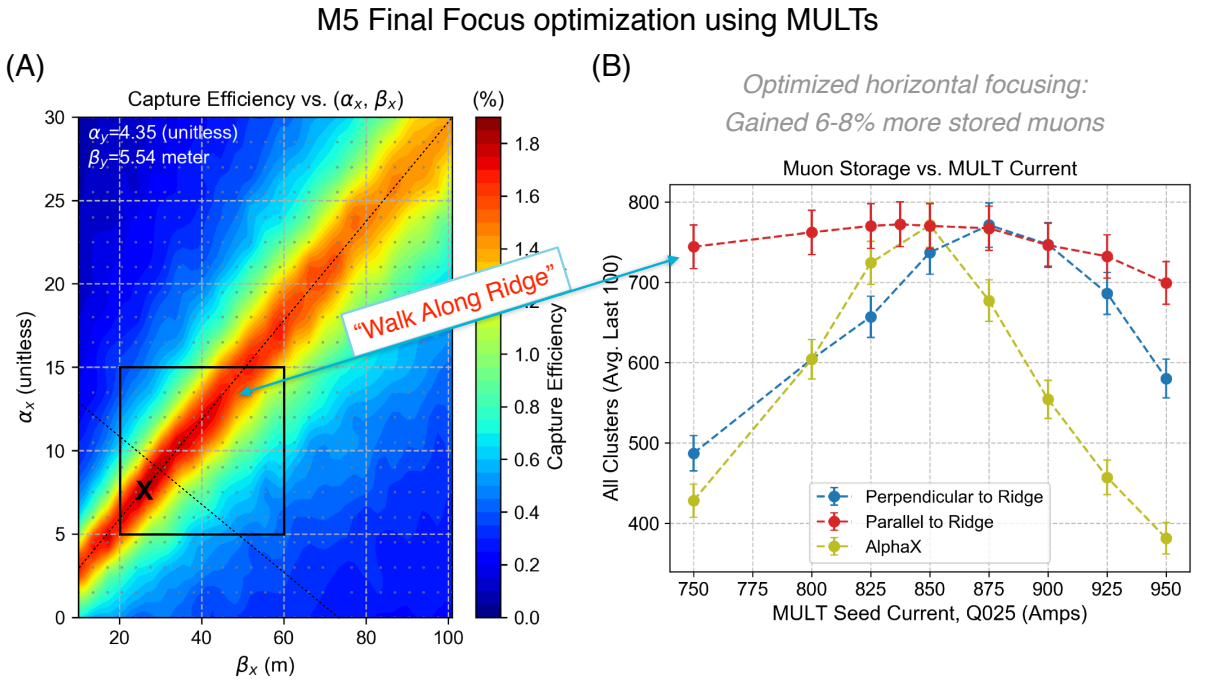

Figure 4.13: *Example results for beam-focusing optimization using horizontal quad MULTs in the M5 Final Focus. (A) The underlying contour plot comes from gm2ringsim, while the black "X" marks are the measured beam parameters at Q020 propagated to just upstream of the muon g−2 storage ring to connect with simulation. (B) Experimental results showing how various MULTs were used to explore the space of* $\{\beta_x, \alpha_x\}$ *and optimize horizontal beam focusing into the muon storage ring. Here, the horizontal axis is the MULT seed current (Q025) which controls the currents of all other quads as per Fig. 4.12 (right). First, the MULT that moves* (β_x, α_x) *perpendicular to the red ridge of optimal beam focusing was used to climb on top of the ridge as quickly as possible (B, blue). Next, the MULT that moves* (β_x, α_x) *parallel to the ridge was used to traverse the ridge until muon capture was optimized (B, red). Finally, the MULT that moves* (β_x, α_x) *along the canonical* $\hat{\alpha}_x$ *direction was used to make sure the beam parameters hadn't "fallen off the ridge," and that muon capture was still optimal (B, gold). The net effect was a 6-8% gain in muon storage over the course of the study.*

4.4 Inflector Misalignment vs. Suboptimal Kickers

Even after the beam steering and focusing optimizations discussed in the previous sections had been performed, the experiment was still fraught with problems: the number of stored muons per fill was only about 20% of the design value, the small amount of stored beam preferred a higher orbit radius (i.e. higher momentum) by $\Delta x \approx 10$–$15\,\text{mm}$ (i.e. $\Delta p/p_0 \approx 0.125$–$0.185\%$ at QHV $= 20.2\,\text{kV}$), the radial coherent-betatron-oscillation (CBO) amplitude was large ($\sim$10 mm), the radial CBO lifetime was long ($\sim$260 µs), the muon capture efficiency seemed to increase without bound as the kicker strength was increased, and inflector seemed to prefer +40 A higher current than BNL's operational value of 2740 A. To make matters worse, a cryopump vacuum accident on 15 Feb 2018 damaged the inner and outer electrodes of Q1-short and the experiment would be off for an unknown amount of downtime as repairs were being made [74]. In order to explain the injection inefficiencies and poor stored-beam quality mentioned above, there was a growing sentiment within the collaboration that the inflector must be misaligned and the downtime for the Q1-short repair should be used to rotate the inflector [75]. The arguments for rotating the inflector are summarized in Fig. 4.14.

Inflector Misalignment

Rotating the inflector is a serious operation that involves removing one of the twelve vacuum chambers in addition to several other components in the muon $g-2$ storage ring.[7] To make matters worse, the exact procedure for rotating the inflector was unknown,[8] something might break or become misaligned in the process, and it wasn't clear there was a problem with the inflector rotation to begin with – the operation might actually make the problem worse. As a result, a small team of experts was formed in order to help guide the decision-making process, and the simulation tools discussed in Chapter 3 were called upon to help assess whether any potential gains in the amount and/or quality of the stored muon beam were worth the risk of performing inflector surgery. Here, *gm2ringsim* was in a unique position given the simulation's detailed model of the inflector, quads, kickers, collimators, materials, fields, particle distributions, and injection overall – qualities not found in other simulations.

[7] Five calorimeters must also be removed, along with 4 multiplexors, 1 collimator, 1 vacuum manifold, 1 quad extension, 1 N2 letup, 1 trolley cable, etc. [74].

[8] Blueprints of the inflector region from BNL didn't match as-builts, for example.

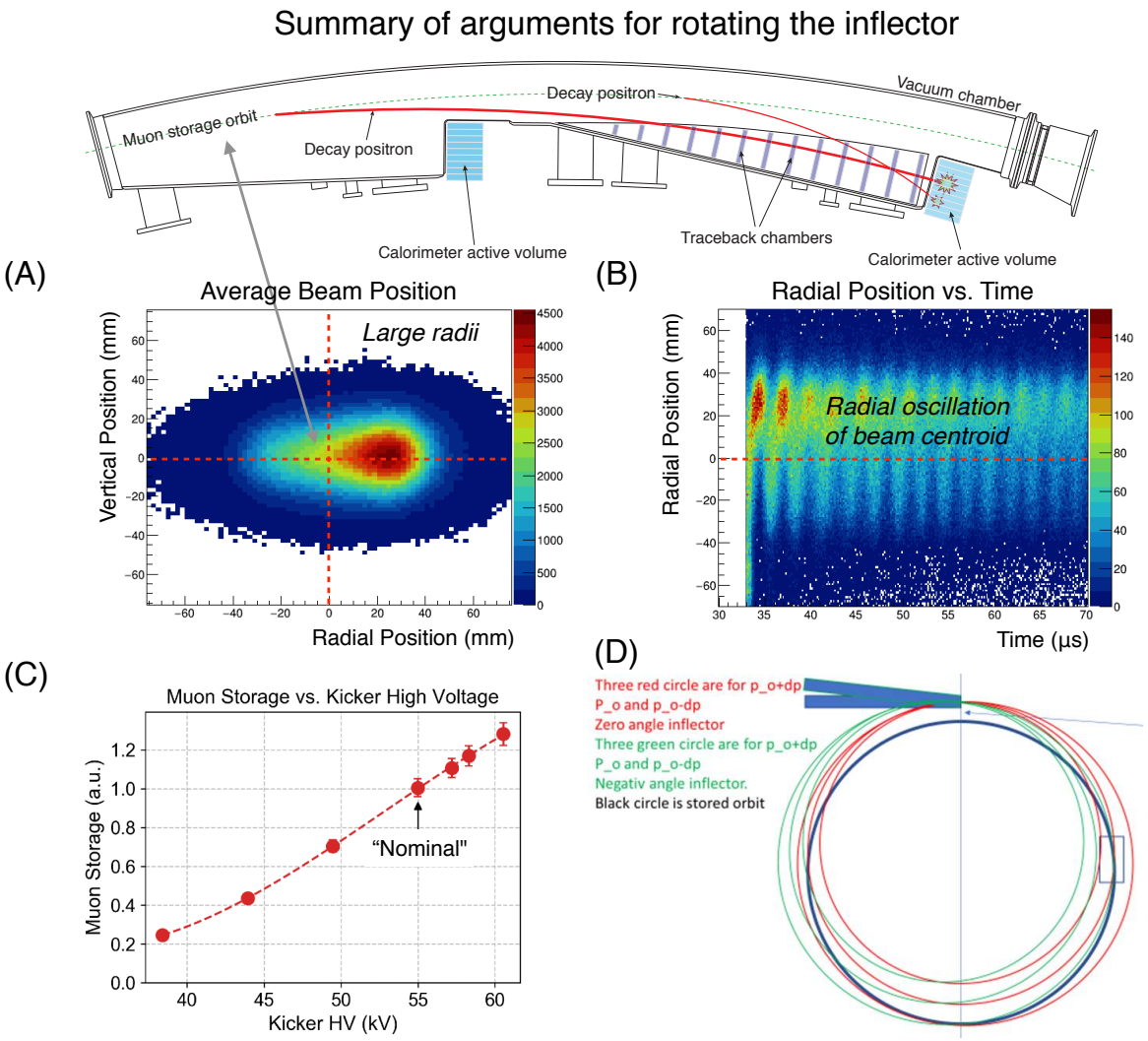

Figure 4.14: *Summary of arguments for rotating the inflector in early 2018. (A) Tracker data indicating the stored muon beam prefers a higher orbit radius than designed and (B) has a large radial coherent-betatron-oscillation amplitude. (C) As the kicker voltage is increased above the nominal setting (∼55 kV), the amount of stored beam seems to increase indefinitely. (D) Cartoon from M. Popovic to C. Polly [74] explaining how an inward-pointing inflector would cause the beam to cross the design orbit upstream of the nominal 90° location where the kickers are located (green circles vs. black box), thus rendering the kickers less effective. In the eyes of some, the case for rotating the inflector was simple: "The inflector rotation was the only knob left unturned."*

In order to help address whether the inflector should be rotated, several different inflector rotations were investigated using *gm2ringsim*, $\Delta x'_{\text{inf}} \in \{-6, -4, \ldots, +6\}$ mrad. Here, tools developed for the design of the new inflector (§3.4.5) were used to expedite the optimization process: the *JacobianGun* was used in tandem with virtual tracking planes and a custom merit function to minimize (1) the average distance of the injection reference trajectory from the centerline of the inflector beam channel, (2) the curvature of the trajectory in the inflector beam channel, and (3) the distance of the trajectory from the centerline of the backleg yoke hole at the entrance of the storage ring for a trajectory that exits the inflector with $(x, x') \approx (77\,\text{mm}, 0\,\text{mrad})$. An example of this stage of the optimization process is shown in Fig. 4.15 for $\Delta x'_{\text{inf}} = -2\,\text{mrad}$, which is the nominal inflector rotation installed at MC-1.[9] The output of this stage of the optimization process is a sensible starting point for more serious simulations.

Next, armed with a reasonable starting configuration for each inflector rotation, a 3D scan using *gm2ringsim* and *TheBeamGun* was performed around each "hot spot" like the one shown in Fig. 4.15 in an attempt to bracket the global optimum. An example scan along with a description of the scan parameters is shown in Table 4.2. This optimization step was performed for each inflector rotation, with the final results being summarized in Fig. 4.16. The results indicate an inflector rotation of $\Delta x'_{\text{inf}} = -2\,\text{mrad}$ is already optimal (Fig. 4.16(A)), which suggests that changing the inflector rotation in early 2018 would have likely been a mistake. This result is also consistent with Brookhaven's observation of a $\sim$10 % gain in muon storage when the inflector was rotated from $\Delta x'_{\text{inf}} = 0\,\text{mrad} \Rightarrow -2\,\text{mrad}$, i.e. it's present configuration at MC-1.

[9] Some authors define this inflector rotation to be "inward-pointing," i.e. the axis of the inflector beam channel is pointed slightly radially inward with respect to the line parallel to the tangent of the ring at the injection point.

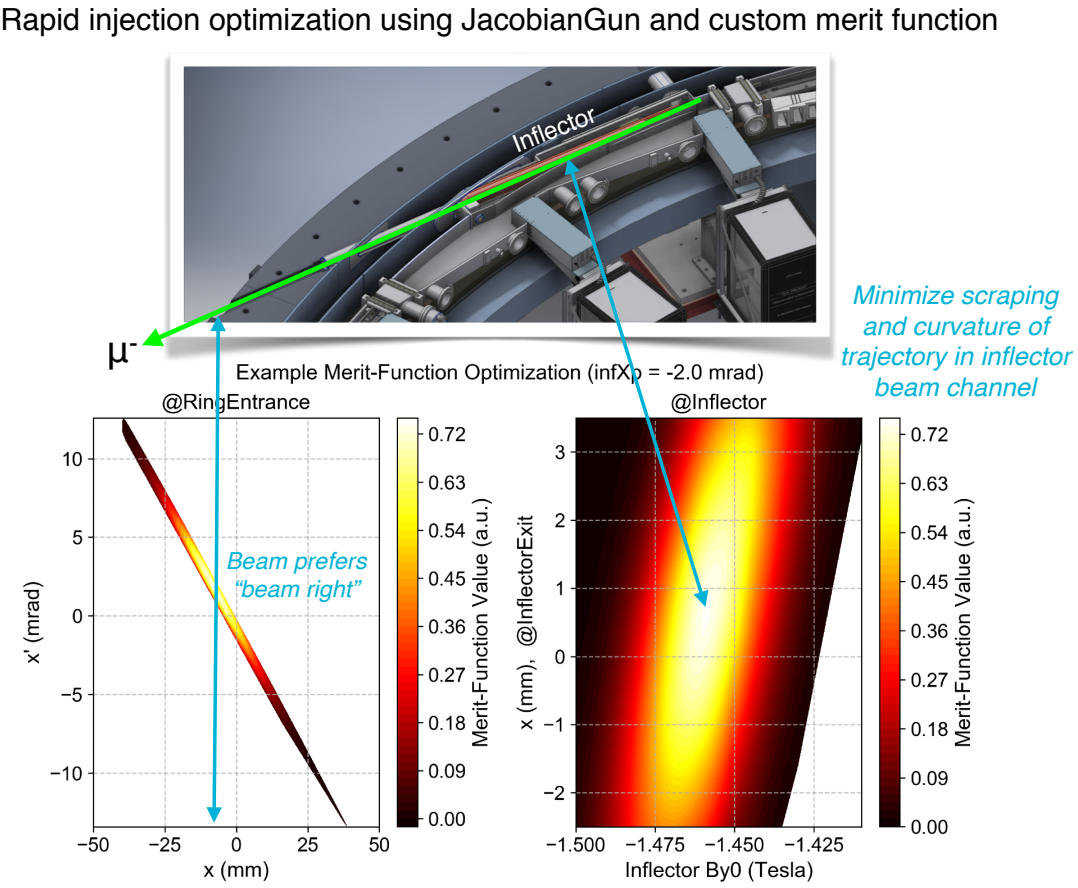

Figure 4.15: *In order to quickly establish an injection reference trajectory for each of the horizontal inflector rotations considered, the JacobianGun was used in conjunction with a custom merit function to minimize the offset and curvature in the inflector beam channel (lower right) while demanding the injection trajectory fall within the backleg yoke hole at the entrance of the storage ring (lower left). The optimization proceeds by shooting μ^- upstream from the inflector exit (top) and the optimization results are assumed to be valid for μ^+ proceeding downstream due to CPT symmetry. The results shown above are for the inflector rotation presently used by the experiment: $\Delta x'_{\text{inf}} = -2\,\text{mrad}$. The optimization predicts "beam right" at the entrance of the storage ring relative to the centerline of the backleg hole, which is consistent with observations, and an inflector magnetic field value of $-1.460\,\text{T}$ which is consistent with the design value of $(-1.5\,\text{T}/2850\,\text{A}) \Rightarrow -1.463\,\text{T}$ for a nominal inflector operating current of $2780\,\text{A}$ at MC-1.*

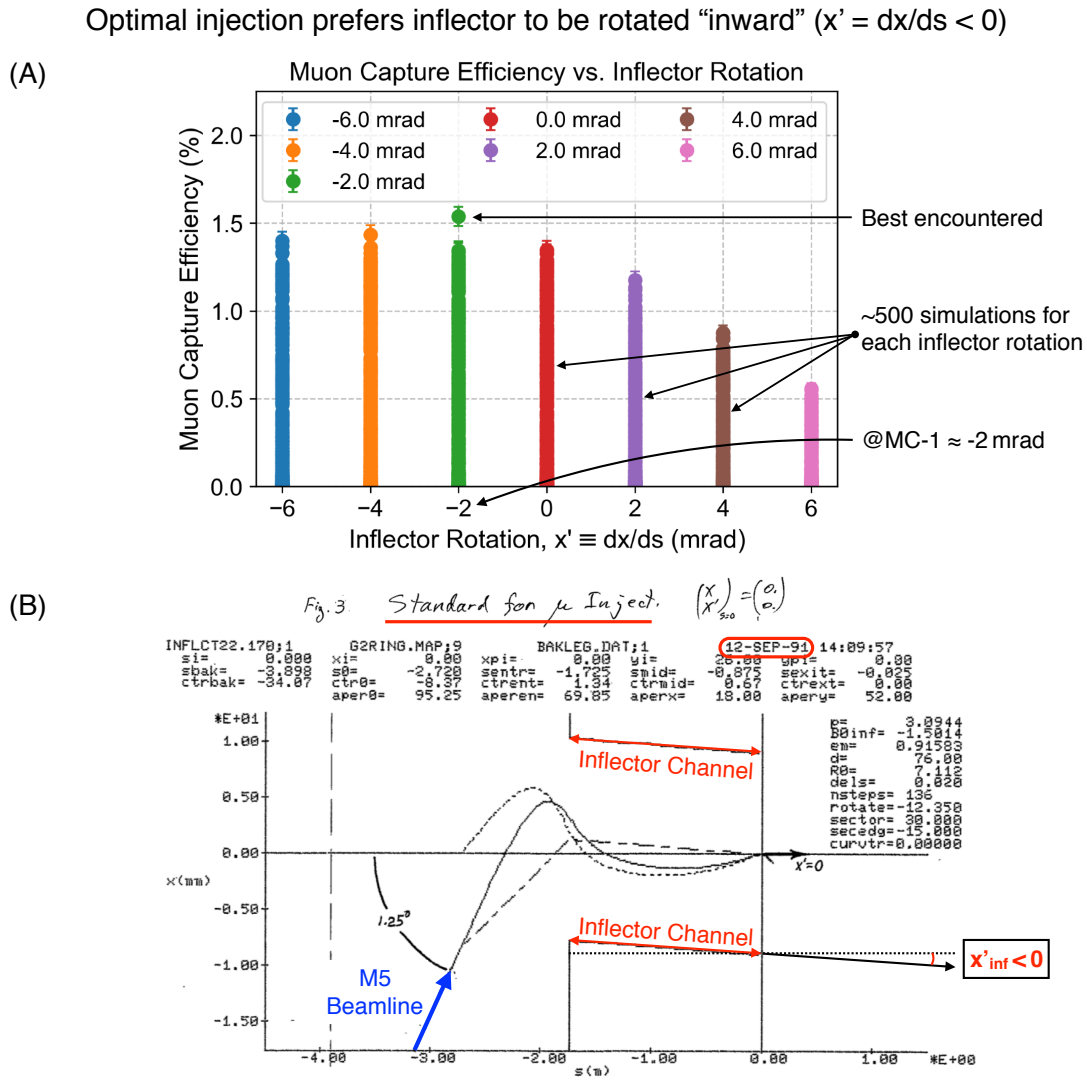

Figure 4.16: *(A) Results from gm2ringsim showing muon capture efficiency vs. inflector rotation. Approximately 500 different configurations were simulated for each inflector rotation* $\Delta x'_{\text{inf}} \in \{-6, -4, \ldots, +6\}$ mrad *after the injection reference trajectory had been optimized (Fig. 4.15). The optimal inflector rotation occurs at* $\Delta x'_{\text{inf}} = -2$ mrad*, which is exactly the inflector rotation presently installed at MC-1 [75]. E821 observed a gain of* $\sim$10 % *in changing the inflector rotation from* $\Delta x'_{\text{inf}} = 0$ mrad *(red) to* $\Delta x'_{\text{inf}} = -2$ mrad *(green), which is also consistent with the above results. (B) E821 design trajectory [76], clearly marked “Standard for μ Inject.,” indicating the default inflector rotation for muon injection should have* $\Delta x'_{\text{inf}} < 0$ mrad*. Bottom line: Rotating the inflector in early 2018 very likely would have been a mistake.*

Inflector-Emergency Scan-Parameters Example (*gm2ringsim*)

Scan Parameter	Description	Unit	Min	Max	Step	Total
x_0	Backleg injection offset	mm	-20	5	5	6
x_0'	Backleg injection angle	mrad	-3	7	1	11
B_{y0}	Inflector magnetic field	T	-1.49	-1.43	0.01	7
						462

Table 4.2: *Example 3D scan performed using gm2ringsim for* $\Delta x'_{\text{inf}} = -2\,\text{mrad}$ *in an attempt to bracket the candidate global optimum shown in Fig. 4.15. Approximately 500 simulations were performed for each inflector rotation at this stage of the optimization process.*

Suboptimal Kickers

It's hard to argue with experimental results like those shown in Fig. 4.4 that the trajectory of the injected beam through the inflector and into the storage ring wasn't optimized, or somehow *couldn't* be optimized, by the M5 Final Focus for any range of realistic inflector currents encountered in the experiment (2700 A to 2800 A). The kickers also play a critical role in injection, however, the kickers were not adjusted in Fig. 4.4 since the kicker timing had been optimized separately beforehand and the kicker strength was already "maxed out" at (or slightly above) the nominal voltage of "55 kV," as shown in Fig. 4.14(C). This suggested to the author that the kickers were acting as a downstream constraint that was throttling injection, ultimately leading to poor stored-beam quality and a suboptimal injection efficiency. More intuition at the time came from an introductory result in accelerator physics,

$$\underbrace{\begin{pmatrix} x \\ x' \\ \delta \end{pmatrix}}_{\text{Kickers}} \approx \underbrace{\begin{pmatrix} \cos(\sqrt{1-n}\theta) & \frac{\rho_0}{\sqrt{1-n}}\sin(\sqrt{1-n}\theta) & \frac{\rho_0}{1-n}(1-\cos(\sqrt{1-n}\theta)) \\ -\frac{\sqrt{1-n}}{\rho_0}\sin(\sqrt{1-n}\theta) & \cos(\sqrt{1-n}\theta) & \frac{1}{\sqrt{1-n}}\sin(\sqrt{1-n}\theta) \\ 0 & 0 & 1 \end{pmatrix}}_{\text{Transport beam } \sim 90^\circ \text{ downstream from inflector exit to kickers}} \underbrace{\begin{pmatrix} x \\ x' \\ \delta \end{pmatrix}}_{\substack{\text{Inflector} \\ \text{exit}}}, \tag{4.19}$$

where $Q_x = \sqrt{1-n}$ is the horizontal tune and $\theta \approx 90^\circ$ is the ring azimuthal angle of the kickers downstream from the inflector exit.The importance of Eq. (4.19) is that the required

kick is the negative of the second row, leading to

$$\begin{aligned}\Delta x'_{\text{kick}} &\approx +\frac{x_{\text{inf}}}{\rho_0} - M_{22}x'_{\text{inf}} - \delta \\ &\equiv \textcircled{1} + \textcircled{2} + \textcircled{3}.\end{aligned} \tag{4.20}$$

Thus, if the kickers cannot supply the nominal required kick $\textcircled{1} = 77\,\text{mm}/7112\,\text{mm} = 10.8\,\text{mrad}$ (where $\textcircled{2} = \textcircled{3} = 0$), then the terms $\textcircled{1} + \textcircled{2} + \textcircled{3}$ will be shifted away from their nominal values in order to compensate for what the kickers cannot do. Each of the three terms in Eq. (4.20) is interesting in its own right and worth slightly more discussion:

1. From the first term $\textcircled{1}$ in Eq. (4.20), it can be seen that decreasing the horizontal (radial) beam position at the inflector exit, x_{inf}, decreases the nominal required kick. A meaningful distance scale is set by the horizontal width of the inflector beam channel, $\Delta x_{\text{inf}} = \mathcal{O}(\pm 9\,\text{mm}/2)$, leading to a kick reduction of $\Delta x_{\text{inf}}/\rho_0 = \mathcal{O}(-4.5\,\text{mm}/7112\,\text{mm}) = \mathcal{O}(-0.6\,\text{mrad})$. The sign and magnitude of this term are an additional reason the injected beam prefers to be slightly more toward the "beam right" (e.g. Fig. 3.12) than if the kickers could perform the nominal task. The beam can only be shifted by a few millimeters, however, before significant losses are incurred due to scraping in the narrow horizontal inflector beam channel ($|\Delta x_{\text{inf}}| \leq 9\,\text{mm}$).

2. The second term $\textcircled{2}$ in Eq. (4.20) is approximately zero since $M_{22} = \cos(Q_x 90°) \approx 0$ and the angle of the beam exiting the inflector is at most of order $\Delta x'_{\text{inf}} = \mathcal{O}(\pm 4.5\,\text{mm}/1700\,\text{mm}) = \mathcal{O}(\pm 2.6\,\text{mrad})$, where $L_{\text{inf}} = 1700\,\text{mm}$ and $\Delta x_{\text{inf}} = \pm 4.5\,\text{mm}$ is the representative length scale mentioned above. Regardless of the sign of M_{22}, the magnitude of $\textcircled{2}$ is at most $|M_{22}x'_{\text{inf}}| = \mathcal{O}(0.1 \times 2.6\,\text{mrad})) = \mathcal{O}(0.26\,\text{mrad})$, which is the smallest of the three terms in Eq. (4.20).

3. It's easy to see $\textcircled{3}$ is the dominant term in Eq. (4.20) as follows: As was mentioned above, the average radius of the stored muon beam was observed to be too large by $\Delta x \approx 10$–$15\,\text{mm}$ (Fig. 4.14), corresponding to $\delta = 0.00125$–$0.00185 = 1.25$–$1.85\,\text{mrad}$, where δ has the same units as kick angle. Thus, of the three terms in Eq. (4.20), $\textcircled{3}$ is the most effective way to compensate for suboptimal kickers, leading to a higher stored-muon beam momentum overall, as observed in Fig. 4.14.

The arguments presented above made it clear to the author the kickers were dominating the properties of the injected/stored muon beam, not the inflector or M5 Final Focus. Nevertheless, confusion remained in the collaboration since it was believed the kicker-pulse measurement of $\|B_{\text{kick}}^{(\text{peak})}\| \simeq 250(25)\,\text{G}$ [77] was correct. Detailed simulations were needed in order to help understand and verify the cause of why the amount and quality of the stored muon beam was so unexpectedly poor.

Part of the injection-optimization process for both simulation and reality involves determining the kicker strength and timing at which the number of muons captured in the storage ring is maximized. Additionally, it is desirable to minimize the horizontal coherent-betatron-oscillation (CBO) amplitude, which might occur due to weak kickers or ringing kicker tails. The E989 kicker pulses were measured *in situ* by Keshavarzi *et al.* in late 2017 [77], as shown in Fig. 4.17(A). In early 2018, it was believed each of the three kickers each had a peak magnetic field of magnitude ∼250(25) G. The measured kicker pulses have been incorporated into *gm2ringsim*, where the user can adjust the magnetic-field strength and the pulse timing separately for all three kickers. The example shown in Fig. 4.17(B) has each kicker set to $B_{y0}^{(\text{kick})} = -225\,\text{G}$ at the center of the muon storage region, which was believed to be the actual experimental value at the time. Here, the kick has been applied to the nominal injection reference trajectory, which exits the inflector with phase-space coordinates $\mathbf{x} = (x, x', y, y', t, \delta \equiv \Delta p/p_0) = (77\,\text{mm}, 0, 0, 0, 0, 0)$.[10] Much intuition can be gained from this simple example, Fig. 4.17, since the reference trajectory represents the beam centroid, i.e. "the core of the storable beam." A striking feature of Fig. 4.17(B) is the large horizontal betatron oscillations ($A_{\text{CBO}x} \sim 30\,\text{mm}$) observed at early times due to the ringing kicker tails. It is clear that many muons would be lost on the first few turns for this kicker setting since much of the beam would scrape against the collimators ($r = 45\,\text{mm}$), kicker electrodes ($r \simeq 45\,\text{mm}$), and quad electrodes ($x = 50\,\text{mm}$). However, the trajectory ultimately settles down to an oscillation with amplitude $A_{\text{CBO}x} \lesssim 5\,\text{mm}$. This simple result is a big hint that maximizing muon capture efficiency and minimizing horizontal CBO amplitude are in fundamental conflict with one another for the E989 kicker pulses, as will be shown below.

The convolution of the kicker pulses against the injected beam pulse is what ultimately determines the amount and quality of the stored beam. Realistic beam pulses as measured by

[10] The kick has also been timed to minimize CBO, as will be discussed below.

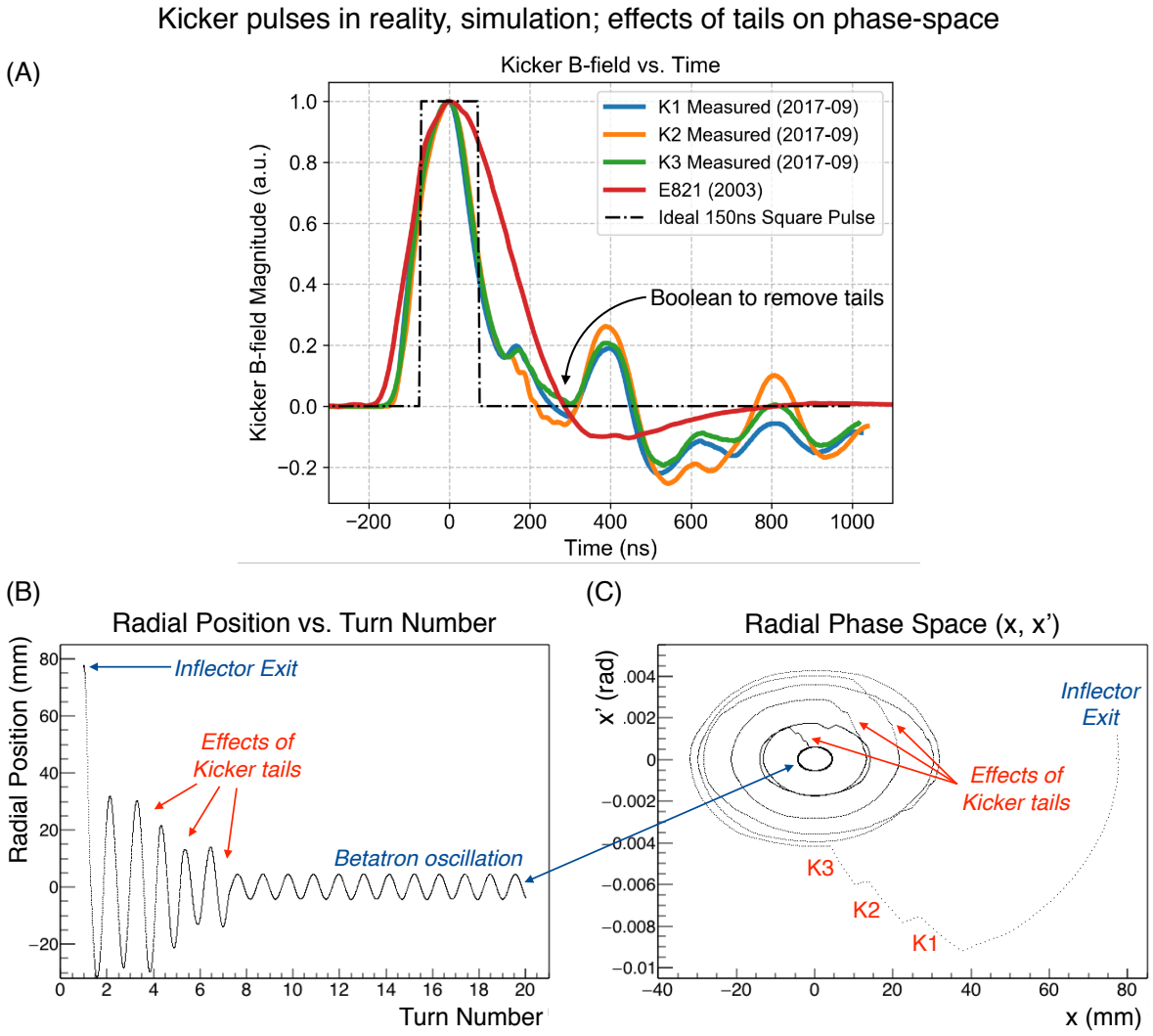

Figure 4.17: *Example effects of kicker tails on real space and phase space. (A) Measured kicker pulses [77] input into gm2ringsim (K1, K2, K3). Also shown are the E821 pulse (red line) and the ideal* 150 ns *square pulse (dashed black line) for reference. All pulses have been normalized to a peak height of* 1.0 *so they may easily be rescaled at simulation runtime. Similarly, the peak time of all pulses has been shifted to zero so the pulse timing may easily be changed at simulation runtime. (B) Example effect of the kicker tails on the radial position* $x \equiv R - R_0$ *of the design trajectory, which exits the inflector at* $(x, x') = (77\,\text{mm}, 0\,\text{mrad})$. *This trajectory is meant to represent the centroid of the beam, i.e. the core of the storable beam. (C) Phase-space picture of (B). The effect of the kicker tails on the first several turns is very clear, yet the trajectory ultimately settles down to within* 5 mm *of the design orbit.*

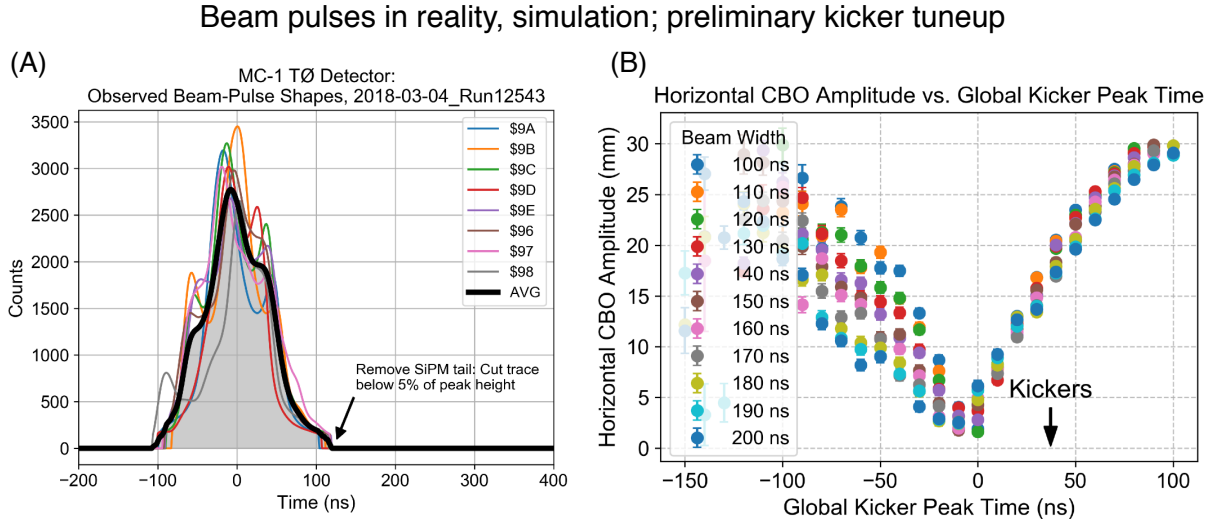

Figure 4.18: *(A) Measured beam pulses entering the muon $g-2$ storage ring as seen by the TØ detector. The weighted average of the pulse shapes (black) has been incorporated into gm2ringsim, where the user has the ability to control the beam width via* FHICL *parameter. (B) Kicker-timing scan for a variety of beam widths. Here, the beam is a transverse δ-function and the momentum is exactly the design momentum $p_0 = 3.094\,\mathrm{GeV}/c$, while the bunch length and kicker timing are being varied. The kicker strengths are fixed at $B_{y0}^{(\mathrm{kick})} = -225\,\mathrm{G}$, which were believed to be near to the experimental value in early 2018. The kickers are located 90° downstream of the inflector exit, i.e. $T_c/4 = 150\,\mathrm{ns}/4 = 37.5\,\mathrm{ns}$, as indicated by the black arrow on the plot. Thus the kickers prefer to be fired early in order to minimize horizontal CBO, which is the effects of the waveform tails shown in Fig. 4.17.*

the TØ detector have also been incorporated into *gm2ringsim*, as shown in Fig. 4.18(A). Once the optimal kicker timing in simulations had been initially located, Fig. 4.18(B), more serious (but computationally expensive) simulations were performed as shown in Fig. 4.19. Here, the main conclusion is that not only the timing but also the tails of the kicker waveforms have an adverse effect on muon storage and horizontal CBO amplitude: Removing the tail of the E989 Blumlein kicker pulse would increase the amount of stored beam by $\Delta f_{\text{store}} \approx \mathcal{O}(+60\%)$ while reducing the horizontal CBO amplitude by $\Delta A_{\text{CBO}x} = \mathcal{O}(-10\,\text{mm})$ toward the ideal value of 0 mm.

Although the timing of the kicker pulse is very important, another critical piece of the muon-injection puzzle is the kicker strength. Realistic kicker-strength studies were also performed with *gm2ringsim*, this time at a variety of inflector currents (since the inflector is a dipole whose current changes the outgoing angle of the injected beam), as shown in Fig. 4.20. The optimal inflector current was found to be $B_{y0}^{(\text{inf})} = 1.46\,\text{T}$ in *gm2ringsim*, in good agreement with Ref. [35] and the actual E989 run setting of 2780 A.[11] These simulations were the first in E989 to predict the kickers were significantly under-kicking the beam, and in Mar/Apr 2018, it was discovered a factor of two error had been made in the magnetometer measurements (so that the kick was only half of the reported value 250(25) G [77]) and the kicker high-voltage was incorrectly calibrated (another reason the kick was lower than expected). The amount of stored beam skyrocketed when the kicker high voltages were set closer to their actual nominal values of 55 kV, as shown in Fig. 4.21. Shortly thereafter, in late Apr 2018, a maximum rate of $\sim$580 e^+/fill was achieved, up from $\sim$225 e^+/fill before it was realized the kickers were the problem. This was an important milestone for the E989 collaboration since >50% of the design value had been achieved. At this point, the author left Fermilab to write his thesis having contributed in a significant way to one of the biggest challenges faced by the collaboration to date. Upgrades in the summer of 2018 will help get the experiment even closer to its design goal of $\sim$1050 e^+/fill, where much of the remaining $\sim$45% inefficiency is thought to be due to minor compounding inefficiencies across multiple subsystems, for example, $(85\%)^{4\text{ systems}} = 52\%^{\text{overall}}$.

[11] Ref. [35] lists 1.5 T/2850 A, so the nominal run setting in E989 is $B_{y0}^{(\text{inf})} = 2780\,\text{A}(1.5\,\text{T}/2850\,\text{A}) = 1.46\,\text{T}$ since the inflector magnetic field varies linearly with the current, which is the value predicted by *gm2ringsim*, as shown in Fig. 4.20.

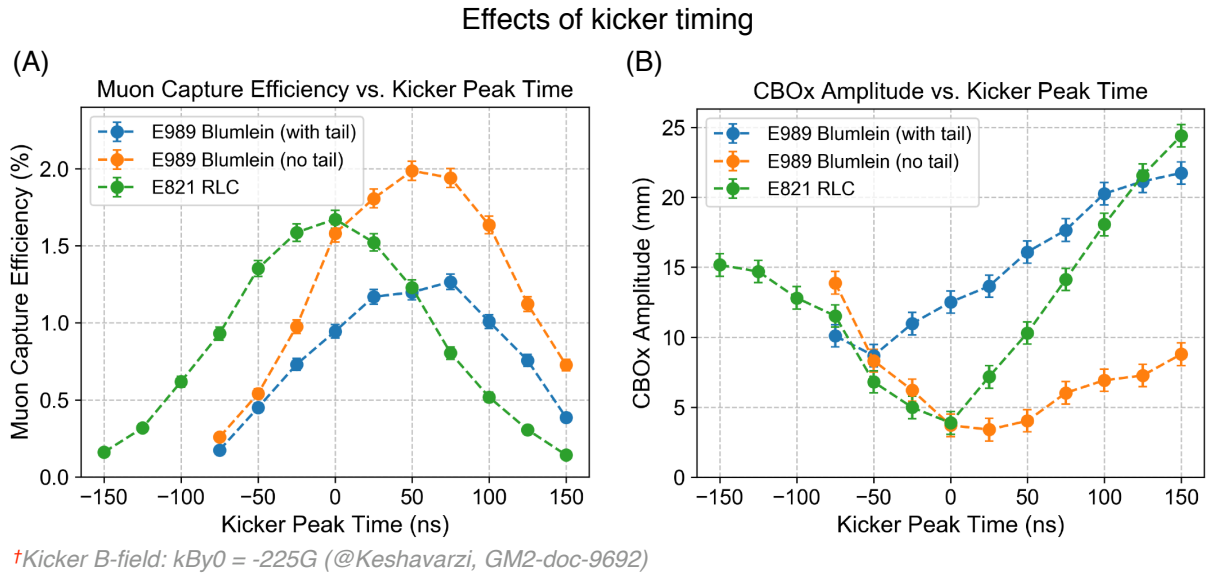

Figure 4.19: *Realistic simulation of the effects of kicker timing and waveform tails performed using gm2ringsim. (A) The timing of the kicker waveforms shown in Fig. 4.17(A) is investigated using the measured beam pulse shown in Fig. 4.18(A) together with a realistic phase-space distribution from G4beamline. The term "with tail" (blue) and "no tail" (orange) refer to a boolean flag in the simulation that allows the kicker tails to be removed at the first zero crossing in the kicker waveform after the peak. The kicker tails of the E989 Blumlein circuit clearly have an adverse effect on muon capture efficiency and horizontal CBO amplitude. Results for the measured E821 kicker pulse [78] are shown in green. The optimal timing is different for the E821 LCR pulse compared to the E989 Blumlein pulse due to the wider main peak of the E821 pulse, which "double kicks" the beam more significantly on subsequent turns after the first turn. Note also the timing at which capture efficiency is maximized does not change in the E989 pulses when the tails are removed, indicating the main peak is responsible for storing beam on the first turn. (B) Removing the E989 kicker tails also significantly reduces the horizontal CBO amplitude (blue → orange). The E821 results (green) are again shown for reference. The maximum muon capture efficiency and minimum CBO amplitude occur at the same kicker timing for the E821 pulse (green, $t_{\text{kick}} \approx 0\,\text{ns}$). Unfortunately, however, the maximum muon capture efficiency and minimum CBO amplitude do not occur at the same kicker timing for the E989 pulses due to the long, ringing kicker tails (Fig. 4.17).*

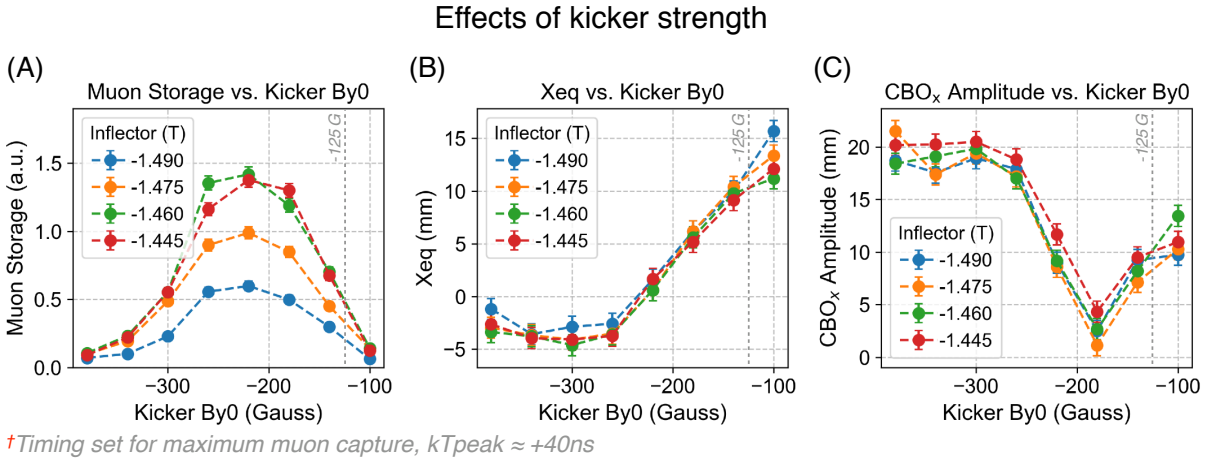

Figure 4.20: *Effects of E989 kicker strength on stored-muon amount and quality according to gm2ringsim. Here, the E989 Blumlein kicker pulse is investigated for a variety of inflector currents. The thin vertical dashed grey line at* 125 G *is close to the actual value of the kickers in prior to Apr 2018 [79]. (A) Muon capture efficiency vs. kicker strength and inflector current. (B) Beam average radial offset vs. kicker strength. (C) Horizontal CBO amplitude vs. kicker strength. The simulations shown above were the only ones in the E989 collaboration that were able to reproduce the trends observed in the data. These results were presented at IPAC18 [80].*

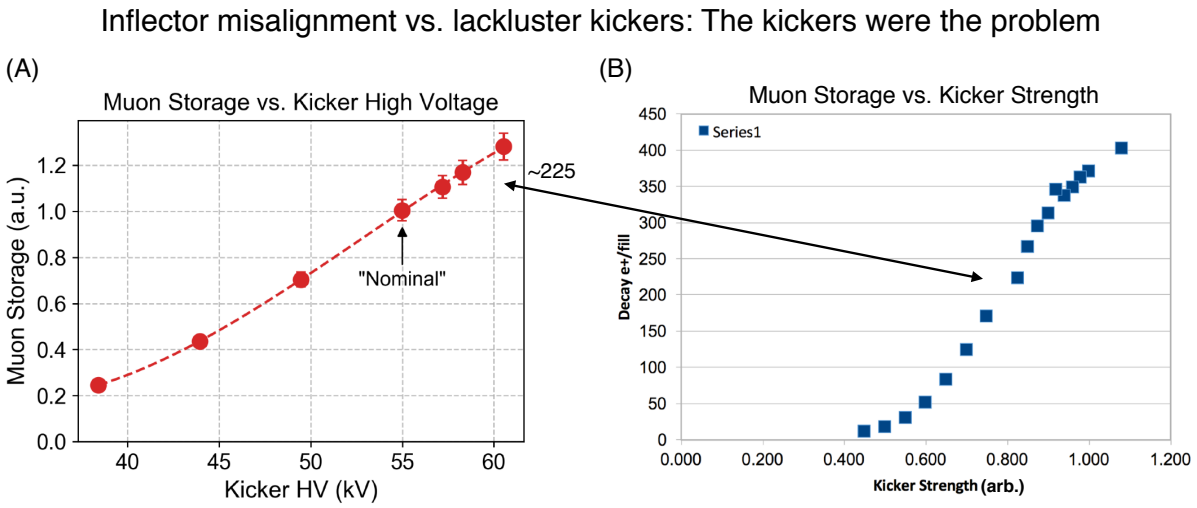

Figure 4.21: *Inflector misalignment vs. suboptimal kickers: The kickers were the problem. (A) Muon storage for a kick of* $\|B_{y0}^{(\mathrm{peak})}\| \simeq 125\,\mathrm{G}$*, corresponding to a nominal voltage of "*$55\,\mathrm{kV}$*." (B) Muon storage increases dramatically when the kickers are set closer to their actual design value of* $55\,\mathrm{kV}$*.*

Chapter 5

CONCLUSION

The Fermilab muon g–2 experiment (E989) completed its first data-collecting run (Run 1) in July 2018 in which approximately twice the entire BNL E821 dataset (1997–2001) was recorded in just 4 months of runtime, as shown in Fig. 5.1. These data are being analyzed presently, with a BNL-level result to be published within one year. The author of this thesis has made several significant contributions that ensure E989 will reach its physics goal of measuring a_μ to 140 parts-per-billion (ppb) precision in a timely manner and with the required statistics through various efforts associated with the optimization/maximization of muon injection efficiency, capture fraction, and stored-beam quality, as was discussed in the body of this thesis. Examples include, but are not limited to, the design of the Q1-outer electrode and supports (§3.4.1); the design of the kicker electrodes (§3.4.2) and kicker circuit (§4.4); the design of the new asymmetric beam collimators (§3.4.3); the design of the inflector beam-monitoring system (§3.4.4); the design of the new superconducting inflector magnet (§3.4.5); and the design, development, and implementation of various simulation tools and ACL/ACNET beam-tuning programs that allow for the rapid optimization/maximization of muon capture efficiency in the $g-2$ storage ring as a function of M5-Final-Focus magnet settings (Chapter 4). In the summer of 2018, the experiment is rebuilding and upgrading the kickers in order to achieve higher voltage, and hence, more stored muons with a smaller horizontal coherent betatron oscillation, as was discussed in (§4.4). The experiment is also making hardware upgrades this summer that will enable the electrostatic quadrupoles to operate more stably at higher voltages, which will also increase the overall rate of data collection. Another significant upgrade is new ionization-cooling wedges in M5/DR which will downshift the high-momentum tail of the injected muon bunch into the narrow momentum acceptance of the muon $g-2$ storage ring, which will also increase muon flux and data-collection rate. The new inflector is ready to be installed when time and resources are available. With these upgrades, the experiment is on track to record approximately 10X BNL statistics in fiscal year 2019 (FY19) during Run 2, followed by a publication, with

an additional ∼10X BNL statistics being recorded in FY20 during Run 3, also followed by a publication. In this way, E989 will achieve its nominal goal of recording ∼20X the entire BNL dataset that is required to measure a_μ to 140 parts-per-billion (ppb) precision. The author of this thesis is extremely grateful and pleased to report he will continue to work closely with the muon $g-2$ experiment, the Muon Campus, and Fermilab Accelerator Division as a post-doc with Professor Mike Syphers at NIU/Fermilab.

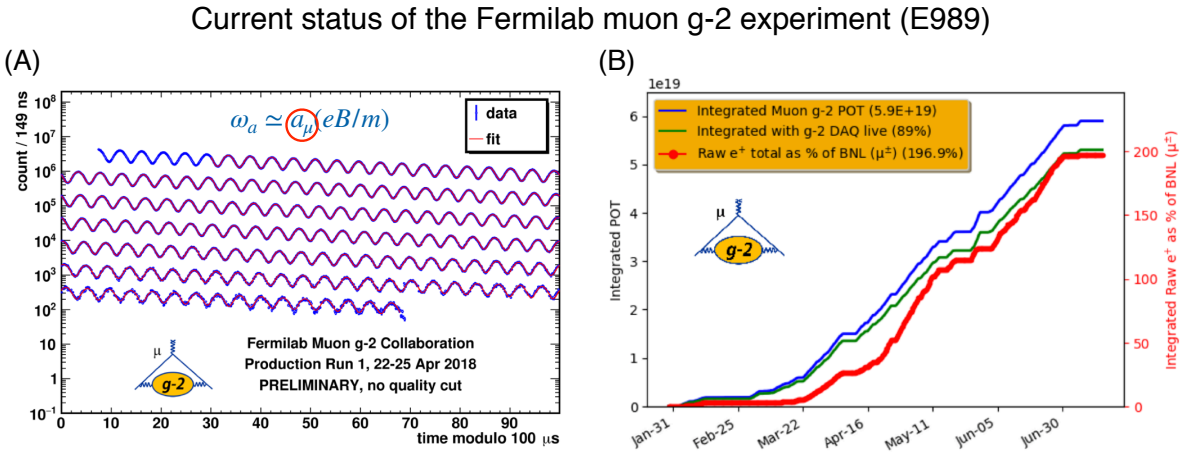

Figure 5.1: *Current status of the Fermilab muon $g-2$ experiment, E989 (August 2018). (A) Representative decay-positron signal observed during Run 1. These data are used to extract the anomalous precession angular frequency, ω_a, which is used together with data from the ring magnetic field and stored-muon-beam distribution in order to precisely determine a_μ (§2.2.7). (B) Integrated protons on target (POT) and integrated decay-positron counts vs. time during Run 1. The author left Fermilab in very late April 2018 to write his thesis, when the decay-e^+ rate was the highest the experiment had ever achieved, ∼580 e^+/fill.*

BIBLIOGRAPHY

[1] E. N. Parker, "The origin of magnetic fields," *Astrophys. J.*, vol. 160, p. 383, May 1970.

[2] W. Panofsky and M. Phillips, *Classical Electricity and Magnetism*. Dover, 2 ed., 2005.

[3] D. J. Griffiths, *Introduction to Electrodynamics*. Pearson, 4 ed., 2013.

[4] J. D. Jackson, *Classical electrodynamics*. John Wiley and Sons, Inc., 1999.

[5] A. Landé, "Über den anomalen Zeemaneffekt," *Z. Physik*, vol. 5, p. 231, 1921.

[6] G. Uhlenbeck and S. Goudsmit, "Zuschriften Und Vorläufige Mitteilungen," *Naturwissenschaften*, vol. 13, no. 47, p. 953, 1925.

[7] E. D. Commins, "Electron spin and its history," *Annual Review of Nuclear and Particle Science*, vol. 62, no. 1, pp. 133–157, 2012.

[8] L. H. Thomas, "The motion of the spinning electron," *Nature*, vol. 117, p. 514, Apr 1926.

[9] W. Pauli, "Zur Quantenmechanik des magnetischen Elektrons," *Zeitschrift fur Physik*, vol. 43, pp. 601–623, Sept. 1927.

[10] P. A. M. Dirac, "The Quantum Theory of the Electron," *Proceedings of the Royal Society of London Series A*, vol. 117, pp. 610–624, Feb. 1928.

[11] F. Schwabl, *Advanced Quantum Mechanics*. Springer, 2005.

[12] C. D. Anderson, "The positive electron," *Phys. Rev.*, vol. 43, pp. 491–494, Mar 1933.

[13] P. A. M. Dirac, "The quantum theory of the emission and absorption of radiation," *Proc. R. Soc. Lond. A*, vol. 114, p. 243, 1927.

[14] P. Kusch and H. M. Foley, "Precision Measurement of the Ratio of the Atomic 'g Values' in the ${}^2P_{\frac{3}{2}}$ and ${}^2P_{\frac{1}{2}}$ States of Gallium," *Phys. Rev.*, vol. 72, pp. 1256–1257, Dec 1947.

[15] P. Kusch and H. M. Foley, "The magnetic moment of the electron," *Phys. Rev.*, vol. 74, pp. 250–263, Aug 1948.

[16] T. Aoyama, M. Hayakawa, T. Kinoshita, and M. Nio, "Tenth-order qed contribution to the electron $g-2$ and an improved value of the fine structure constant," *Phys. Rev. Lett.*, vol. 109, p. 111807, Sep 2012.

[17] M. Tanabashi and others (Particle Data Group), "The Review of Particle Physics," *Phys. Rev. D*, vol. 98, p. 030001, 2018.

[18] F. Jegerlehner, "Muon $g-2$ Theory: the Hadronic Part," *arXiv:1705.00263 [hep-ph]*, 2017.

[19] A. Nyffeler, "Hadronic light-by-light scattering in the muon $g-2$," *arXiv:1710.09742 [hep-ph]*, 2017.

[20] F. Jegerlehner, "The Muon $g-2$ in Progress," *Acta Phys. Polon.*, vol. B49, p. 1157, 2018.

[21] A. Keshavarzi, D. Nomura, and T. Teubner, "Muon $g-2$ and $\alpha(M_Z^2)$: A new data-based analysis," *Phys. Rev. D*, vol. 97, p. 114025, Jun 2018.

[22] G. W. Bennett *et al.*, "Final report of the E821 muon anomalous magnetic moment measurement at BNL," *Phys. Rev. D*, vol. 73, p. 072003, Apr 2006.

[23] A. Czarnecki and W. J. Marciano, "Muon anomalous magnetic moment: A harbinger for "new physics"," *Phys. Rev. D*, vol. 64, p. 013014, Jun 2001.

[24] J. R. Batley *et al.*, "Search for the dark photon in π^0 decays," *Phys. Lett. B*, vol. 746, p. 178, 2015.

[25] V. Bargmann, L. Michel, and V. L. Telegdi, "Precession of the polarization of particles moving in a homogeneous electromagnetic field," *Phys. Rev. Lett.*, vol. 2, pp. 435–436, May 1959.

[26] J. Grange *et al.*, "Muon (g-2) Technical Design Report," 2015.

[27] H. Wiedemann, *Particle Accelerator Physics*. Berlin: Springer-Verlag, 3 ed., 2007.

[28] D. Stratakis, M. E. Convery, C. Johnstone, J. Johnstone, J. P. Morgan, D. Still, J. D. Crnkovic, V. Tishchenko, W. M. Morse, and M. J. Syphers, "Accelerator performance analysis of the fermilab muon campus," *Phys. Rev. Accel. Beams*, vol. 20, p. 111003, Nov 2017.

[29] M. Conte and W. W. MacKay, *An Introduction to the Physics of Particle Accelerators, 2nd ed.* 27 Warren St, Suite 401, Hackensack, NJ 07601: World Scientific, 2008.

[30] D. Stratakis, "400,000 Particles at the End of M5." GM2-doc-4461, Oct 2016.

[31] G. T. Danby *et al.*, "The Brookhaven muon storage ring magnet," *Nuclear Instruments and Methods in Physics Research Section A: Accelerators, Spectrometers, Detectors and Associated Equipment*, vol. 457, no. 1, pp. 151 – 174, 2001.

[32] W. Liu, M. G. Boshier, S. Dhawan, O. van Dyck, P. Egan, X. Fei, M. Grosse Perdekamp, V. W. Hughes, M. Janousch, K. Jungmann, D. Kawall, F. G. Mariam, C. Pillai, R. Prigl, G. zu Putlitz, I. Reinhard, W. Schwarz, P. A. Thompson, and K. A. Woodle, "High Precision Measurements of the Ground State Hyperfine Structure Interval of Muonium and of the Muon Magnetic Moment," *Phys. Rev. Lett.*, vol. 82, pp. 711–714, Jan 1999.

[33] F. Krienen, D. Loomba, and W. Meng, "The truncated double cosine theta superconducting septum magnet," *Nucl. Instrum. Meth.*, vol. A283, pp. 5–12, 1989.

[34] Y. Makida *et al.*, "Development of an ASTROMAG test coil with aluminum stabilized superconductor," *IEEE Transactions on Magnetics*, vol. 27, pp. 1944–1947, March 1991.

[35] A. Yamamoto *et al.*, "The superconducting inflector for the BNL $g-2$ experiment," *Nuclear Instruments and Methods in Physics Research Section A: Accelerators, Spectrometers, Detectors and Associated Equipment*, vol. 491, no. 1, pp. 23 – 40, 2002.

[36] E. Courant and H. Snyder, "Theory of the alternating-gradient synchrotron," *Annals of Physics*, vol. 3, no. 1, pp. 1 – 48, 1958.

[37] L. Alonzi, A. Anastasi, R. Bjorkquist, D. Cauz, G. Cantatore, S. Dabagov, G. D. Sciascio, R. D. Stefano, R. Fatemi, C. Ferrari, A. Fienberg, A. Fioretti, A. Frankenthal, C. Gabbanini, L. Gibbons, K. Giovanetti, S. Goadhouse, W. Gohn, T. Gorringe, D. Hampai, D. Hertzog, M. Iacovacci, P. Kammel, M. Karuza, J. Kaspar, B. Kiburg, L. Li, F. Marignetti, S. Mastroianni, D. Moricciani, G. Pauletta, D. Peterson, D. Počanić, L. Santi, M. Smith, D. Sweigart, V. Tishchenko, T. V. Wechel, G. Venanzoni, K. Wall, P. Winter, and K. Yai, "The calorimeter system of the new muon $g-2$ experiment at Fermilab," *Nuclear Instruments and Methods in Physics Research Section A: Accelerators, Spectrometers, Detectors and Associated Equipment*, vol. 824, pp. 718 – 720, 2016. Frontier Detectors for Frontier Physics: Proceedings of the 13th Pisa Meeting on Advanced Detectors.

[38] E. J. Konopinski, "The experimental clarification of the laws of beta-radioactivity," *Annual Review of Nuclear Science*, vol. 9, no. 1, pp. 99–158, 1959.

[39] P. J. Mohr, D. B. Newell, and B. N. Taylor, "CODATA recommended values of the fundamental physical constants: 2014," *Rev. Mod. Phys.*, vol. 88, p. 035009, Sep 2016.

[40] Fermi National Accelerator Laboratory, "Computing for neutrino and muon physics." http://computing.fnal.gov/neutrino-muon-physics-computing/, Jul 2018.

[41] S. Agostinelli *et al.*, "Geant4—a simulation toolkit," *Nuclear Instruments and Methods in Physics Research Section A: Accelerators, Spectrometers, Detectors and Associated Equipment*, vol. 506, no. 3, pp. 250 – 303, 2003.

[42] J. Allison *et al.*, "Geant4 developments and applications," *IEEE Transactions on Nuclear Science*, vol. 53, pp. 270–278, Feb 2006.

[43] J. Allison *et al.*, "Recent developments in Geant4," *Nuclear Instruments and Methods in Physics Research Section A: Accelerators, Spectrometers, Detectors and Associated Equipment*, vol. 835, no. Supplement C, pp. 186 – 225, 2016.

[44] C. Green, J. Kowalkowski, M. Paterno, M. Fischler, L. Garren, and Q. Lu, "The Art Framework," *J. Phys. Conf. Ser.*, vol. 396, p. 022020, 2012.

[45] A. Lyon, "Art + Geant4 = ArtG4." GM2-doc-1241-v1, Feb 2014.

[46] Fermi National Accelerator Laboratory, "The Fermilab Hierarchical Configuration Language (FHiCL)." https://cdcvs.fnal.gov/redmine/projects/fhicl/wiki, 2018.

[47] C. M. Poole, I. Cornelius, J. V. Trapp, and C. M. Langton, "A CAD Interface for GEANT4," 2011.

[48] VCGLib, "The Visualization and Computer Graphics Library," Jul 2018.

[49] B. Kiburg, "Storage ring fringe field." GM2-doc-2736-v2, Apr 2015.

[50] N. S. Froemming, "Muon gas gun." GM2-doc-411-v1, Jul 2012.

[51] A. Fienberg, "Detector position and CBO phase." GM2-doc-2793-v2, Jan 2017.

[52] Y. K. Semertzidis *et al.*, "The Brookhaven muon $(g-2)$ storage ring high voltage quadrupoles," *Nucl. Instrum. Meth. A*, vol. 503, p. 458, 2003.

[53] T. Stuttard, "Pitch correction." GM2-doc-4468-v1, Oct 2016.

[54] D. Rubin, "Injection into the muon ring." GM2-doc-2243-v2, Oct 2014.

[55] G. Guennebaud, B. Jacob, *et al.*, "Eigen v3." http://eigen.tuxfamily.org.

[56] D. Meeker *et al.*, "Finite element method magnetics." http://www.femm.info/wiki/HomePage, 2013.

[57] N. S. Froemming, "Scattering through Q1-outer." GM2-doc-567, Nov 2012.

[58] N. S. Froemming, "Simulations of beam losses in Q1-outer." GM2-doc-634, Dec 2012.

[59] N. S. Froemming, "Effect of quad configurations on muon capture efficiency." GM2-doc-3304, Nov 2015.

[60] N. S. Froemming, "Storage-ring simulations and muon guns." GM2-doc-3328, Nov 2015.

[61] H. Nguyen, "Q1 outer mylar progress." GM2-doc-4598, Dec 2016.

[62] N. S. Froemming, "Collimator study and simulation updates." GM2-doc-2361-v1, Nov 2014.

[63] Muon $g-2$ E989 Collaboration, "Conceptual Design Report." GM2-doc-1033-v1, May 2013.

[64] D. Rubin, "Beam dyamics." GM2-doc-915-v1, Apr 2013.

[65] W. Morse *et al.*, "E989 Note20: Collimator." GM2-doc-2212-v1, Sep 2014.

[66] D. Stratakis, "The wedge proposal." GM2-doc-11124-v2, Mar 2018.

[67] N. S. Froemming and P. Kammel, "BOE for Inflector Beam Monitoring System." GM2-doc-2722-v11, Mar 2015.

[68] P. Eckert *et al.*, "Characterisation studies of silicon photomultipliers," *Nucl. Instrum. Methods Phys. Res. A*, vol. 620, p. 217, 2010.

[69] I. Rech, A. Ingargiola, R. Spinelli, I. Labanca, S. Marangoni, M. Ghioni, and S. Cova, "Optical crosstalk in single photon avalanche diode arrays: a new complete model," *Opt. Express*, vol. 16, p. 8381, 2008.

[70] J. B. Birks, *The Theory and Practice of Scintillation Counting*, vol. 27 of *International Series of Monographs in Electronics and Instrumentation*. Pergamon, 1964.

[71] J. B. Birks, "Scintillations from Organic Crystals: Specific Fluorescence and Relative Response to Different Radiations," *Proc. Phys. Soc.*, vol. A64, pp. 874–877, 1951.

[72] M. G. Minty and F. Zimmermann, *Measurement and Control of Charged Particle Beams*. Berlin: Springer-Verlag, 2003.

[73] J. Morgan *et al.*, "M4 and M5 line magnet names, currents and lattice." GM2-doc-1568-v21, Feb 2018.

[74] C. Polly, "Discussion points about Q1 repair and inflector angle." GM2-doc-10490-v2, Feb 2018.

[75] D. W. Hertzog and C. Polly, "The case for rotating the Inflector." GM2-doc-10541, Feb 2018.

[76] H. Brown and G. Bunce, "Inflector adjustments for pion injection." E821-note-90, Sep 1991.

[77] A. Keshavarzi, "Measurement of the kicker pulse of the muon $g-2$ experiment (E989) using a Faraday magnetometer." GM2-doc-9692, Mar 2018.

[78] E. Efstathiadis *et al.*, "A fast non-ferric kicker for the muon $(g-2)$ experiment," *Nuclear Instruments and Methods in Physics Research Section A: Accelerators, Spectrometers, Detectors and Associated Equipment*, vol. 496, no. 1, pp. 8 – 25, 2003.

[79] C. Stoughton, "Kicker Futures—March 2018." GM2-doc-11139-v1, Mar 2018.

[80] A. P. Schreckenberger *et al.*, "New fast kicker results from the muon $g-2$ E-989 experiment at Fermilab," in *IPAC*, Apr 2018.

[81] D. A. Edwards and M. J. Syphers, *An Introduction to the Physics of High Energy Accelerators*. Wiley, 1992.

[82] J. Schwinger, "Quantum Electrodynamics. III. The Electromagnetic Properties of the Electron—Radiative Corrections to Scattering," *Phys. Rev.*, vol. 76, pp. 790–817, Sep 1949.

[83] J. Schwinger, "Quantum Electrodynamics. II. Vacuum Polarization and Self-Energy," *Phys. Rev.*, vol. 75, pp. 651–679, Feb 1949.

[84] J. Schwinger, "Quantum Electrodynamics. I. A Covariant Formulation," *Phys. Rev.*, vol. 74, pp. 1439–1461, Nov 1948.

[85] J. Schwinger, "On Quantum-Electrodynamics and the Magnetic Moment of the Electron," *Phys. Rev.*, vol. 73, pp. 416–417, Feb 1948.

[86] E. Rutherford, "The scattering of α and β particles by matter and the structure of the atom," *The London, Edinburgh, and Dublin Philosophical Magazine and Journal of Science*, vol. 21, no. 125, pp. 669–688, 1911.

[87] J. J. Thomson, "Cathode Rays," *The London, Edinburgh, and Dublin Philosophical Magazine and Journal of Science*, vol. 44, no. 269, pp. 293–316, 1897.

[88] J. Ahrens, G. Berk, and C. Law, *ParaView: An End-User Tool for Large Data Visualization, Visualization Handbook*. Elsevier, 2005.

[89] L. Welty-Rieger, "Timing Tests for CadMesh." GM2-doc-3366-v2, Dec 2015.

[90] S. Borsanyi, Z. Fodor, C. Hoelbling, T. Kawanai, S. Krieg, L. Lellouch, R. Malak, K. Miura, K. K. Szabo, C. Torrero, and B. C. Toth, "Hadronic vacuum polarization contribution to the anomalous magnetic moments of leptons from first principles," *Phys. Rev. Lett.*, vol. 121, p. 022002, Jul 2018.

[91] T. Blum, P. A. Boyle, V. Gülpers, T. Izubuchi, L. Jin, C. Jung, A. Jüttner, C. Lehner, A. Portelli, and J. T. Tsang, "Calculation of the hadronic vacuum polarization contribution to the muon anomalous magnetic moment," *Phys. Rev. Lett.*, vol. 121, p. 022003, Jul 2018.

[92] L. Welty-Rieger, "Muon $g-2$ Computing Review: CADMesh Geometries." https://indico.fnal.gov/event/13276/, Nov 2016.

[93] P. Kammel and B. MacCoy, "IBMS Manual." GM2-doc-9221, Nov 2017.

[94] M. Syphers, "E989 Note 146: Ionization Cooler for g-2 Muons." GM2-doc-12020-v1, May 2018.

[95] N. S. Froemming, "Collimator study update." GM2-doc-2417-v1, Dec 2014.

[96] D. Flay, "Storage ring magnet design and the uniform field." GM2-doc-10896, March 2018.

[97] G. R. Price, "Extension of covariance selection in mathematics," *Ann. Hum. Genet., Lond.*, vol. 35, p. 485, 1972.

[98] J. W. Brown and R. V. Churchill, *Complex variables and applications*. New York, NY: McGraw-Hill, 7 ed., 2004.

[99] D. Griffiths, *Introduction to Elementary Particles*. Wiley, 2 ed., 2008.

[100] R. Prigl, U. Haeberlen, K. Jungmann, G. zu Putlitz, and P. von Walter, "A high precision magnetometer based on pulsed NMR," *Nuclear Instruments and Methods in Physics Research Section A: Accelerators, Spectrometers, Detectors and Associated Equipment*, vol. 374, no. 1, pp. 118 – 126, 1996.

[101] C. Patrignani *et al.*, "Review of Particle Physics," *Chin. Phys.*, vol. C40, no. 10, p. 100001, 2016.

Appendix A

BASIC CONCEPTS IN ACCELERATOR PHYSICS, BEAM DYNAMICS, AND PHASE SPACE

Accelerator physics is a subject entirely unto itself that is almost never taught at undergraduate or graduate institutions. This chapter is a loose collection of basic concepts and derivations in accelerator physics, beam dynamics, and phase space that may aid the reader in understanding some of the formulas presented in the main body of this thesis. The chapter starts with a reminder of multipole expansions for electromagnetic potentials and fields for single-particle beam dynamics, then shifts more toward ensemble beam properties and transverse phase-space. The curious reader is encouraged to consult References [27, 29, 81], for example, for more details on the wonderful subject of accelerator physics.

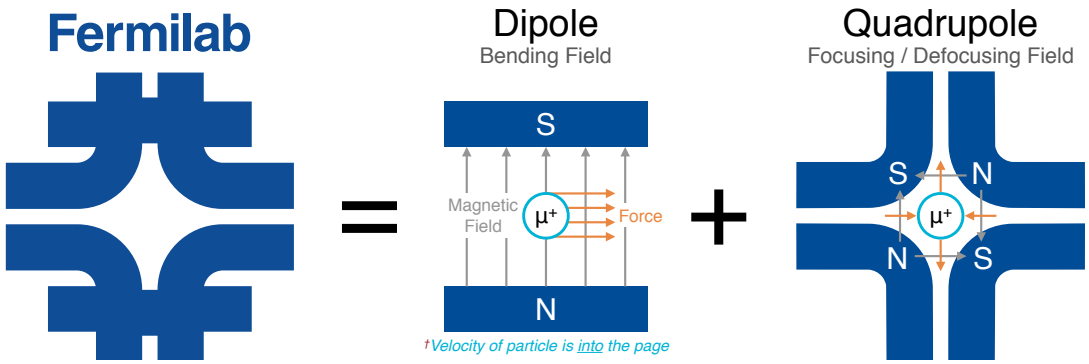

Figure A.1: *Fermilab's logo: magnetic fields used to steer (dipole) and focus (quadrupole) beams of charged particles like the* $p \to \pi^+ \to \mu^+$ *used in the Fermilab Muon g–2 Experiment E989. The sign convention for the velocity is that of Fermilab Acceleration Division: into the page, as if you were "riding along with the beam."*

A.1 Beamline Electromagnetic Fields, Especially Those in the Muon $g-2$ Experiment

In this section, a brief review of multipole expansions of electromagnetic potentials and fields is given, with an eye toward the EM fields encountered at the Fermilab Accelerator complex and in the muon $g-2$ experiment. Simple examples are shown in Fig. A.1 and Fig. 3.13. The force on a point charge q in an electromagnetic field is given by the Lorentz force,

$$\mathbf{F} = \frac{d\mathbf{p}}{dt} = q\left(\mathbf{E} + \mathbf{v} \times \mathbf{B}\right), \tag{A.1}$$

where $\mathbf{F}$ is the force, $\mathbf{p}$ is the mechanical momentum, $\mathbf{v}$ is the velocity, and $\{\mathbf{E}, \mathbf{B}\}$ are the electromagnetic fields. The field vectors $\{\mathbf{E}, \mathbf{B}\}$ obey Maxwell's Equations, which, for a classical point-particle in vacuum are

$$\begin{aligned} \boldsymbol{\nabla} \cdot \mathbf{B} &= 0, & \boldsymbol{\nabla} \times \mathbf{E} + \frac{\partial \mathbf{B}}{\partial t} &= 0, \\ \boldsymbol{\nabla} \cdot \mathbf{E} &= \frac{\rho}{\epsilon_0}, & \boldsymbol{\nabla} \times \mathbf{B} - \frac{1}{c^2}\frac{\partial \mathbf{E}}{\partial t} &= \mu_0 \mathbf{j}, \end{aligned} \tag{A.2}$$

where ρ and $\mathbf{j}$ are the electric charge and current densities, respectively, and $c^2 = 1/\epsilon_0\mu_0$ is the relationship between the speed of light c, the electric permittivity ϵ_0, and the magnetic permeability μ_0 of vacuum. Most of the fields of interest in the muon $g-2$ experiment are static and in a source-free region, i.e. $j^\mu \equiv (c\rho, \mathbf{j}) = 0$. For source-free electrostatics, in which the currents $\{\rho, \mathbf{j}\}$ vanish and the fields are independent of time, Maxwell's equations (A.2) reduce to

$$\begin{aligned} \boldsymbol{\nabla} \times \mathbf{E} = 0, \quad \boldsymbol{\nabla} \cdot \mathbf{E} = 0, \quad &\Rightarrow \quad \mathbf{E} = -\boldsymbol{\nabla}\phi_e, \\ \boldsymbol{\nabla} \times \mathbf{B} = 0, \quad \boldsymbol{\nabla} \cdot \mathbf{B} = 0, \quad &\Rightarrow \quad \mathbf{B} = -\boldsymbol{\nabla}\phi_m, \end{aligned} \tag{A.3}$$

where $\phi_{\{e,m\}}$ are the electric and magnetic scalar potentials and

$$\boldsymbol{\nabla} \cdot \{\mathbf{E}, \mathbf{B}\} = -\nabla^2 \phi_{\{e,m\}} = 0 \tag{A.4}$$

is Laplace's equation in 3 dimensions.

A convenient set of coordinates to use in the muon storage ring is cylindrical coordinates,

for which the Laplacian (A.4) is

$$-\nabla^2 A^\mu = -\left[\frac{1}{\rho}\frac{\partial}{\partial\rho}\left(\rho\frac{\partial}{\partial\rho}\right) + \frac{\partial^2}{\partial z^2} + \frac{1}{\rho^2}\frac{\partial^2}{\partial\phi^2}\right] A^\mu = 0, \tag{A.5}$$

where $A^\mu = (V/c, \mathbf{A})$ is the four-potential. A common approximation made in the muon $g-2$ experiment is A^μ is independent of the azimuthal angle ϕ, for example, in the "uniform quad" approximation in which the vertically focusing electric quads are assumed to cover 360° of ring azimuth. Additionally, in the limit the radius tends to infinity, $\rho \to \infty$, the curvature vanishes, and the Laplacian (A.5) reduces to

$$-\nabla^2 f = -\left[\frac{\partial^2}{\partial x^2} + \frac{\partial^2}{\partial y^2}\right] f = 0, \tag{A.6}$$

where $x \equiv \rho - \rho_0$ is the local radial direction outward from the design radius ρ_0 and $y \equiv z$ is the vertical direction redefined for convenience. A remarkable feature of Eq. (A.6) is that functions satisfying $(\partial_x^2 + \partial_y^2) f = 0$ may be written in terms of a single complex variable $z = x + iy$, and even more amazing, that *both* the real *and* the imaginary parts of the complex function $f(z)$ *separately* satisfy Laplace's equation in 2D. These facts are capitalized upon so ubiquitously in the muon $g-2$ experiment and in accelerator physics that they warrant further discussion.

Firstly, any analytic function of a complex variable $z = x + iy$ can be written as a sum of real and imaginary parts,

$$f(z) = u(x, y) + iv(x, y). \tag{A.7}$$

If the derivative of $f(z)$ is to exist, then the limit

$$\frac{df}{dz} \equiv \lim_{\Delta z \to 0} \frac{f(z_0 + \Delta z) - f(z_0)}{\Delta z} = \lim_{\Delta z \to 0} \frac{\Delta f}{\Delta z} = \lim_{\substack{\Delta x \to 0 \\ \Delta y \to 0}} \frac{\Delta u + i\Delta v}{\Delta x + i\Delta y} \tag{A.8}$$

must be independent of the path taken to $\Delta z \equiv (z - z_0) \to 0$ in the complex plane. By first setting $\Delta y = 0$ in the above equation first, followed by letting $\Delta x \to 0$, then repeating the process with the order reversed (i.e. setting $\Delta x = 0$ first followed by letting $\Delta y \to 0$), two

equations are obtained:

$$\begin{aligned} \text{Method 1:} \qquad & \frac{df}{dz} = \lim_{\substack{\Delta x\to 0\\ \Delta y=0}} \frac{\Delta u + i\Delta v}{\Delta x} = \partial_x u + i\partial_x v \\ \text{Method 2:} \qquad & \frac{df}{dz}, = \lim_{\substack{\Delta x=0\\ \Delta y\to 0}} \frac{\Delta u + i\Delta v}{i\Delta y} = \partial_y v - i\partial_y u. \end{aligned} \tag{A.9}$$

Therefore, if the derivative df/dz is to exist, the two approaches above must be equal, leading to

$$\partial_x u + i\partial_x v = \partial_y v - i\partial_y u. \tag{A.10}$$

Equating the real and the imaginary parts of the last expression gives the celebrated *Cauchy-Riemann Equations,*

$$\boxed{\partial_x u = \partial_y v, \quad \partial_y u = -\partial_x v}\,. \tag{A.11}$$

The Cauchy-Riemann equations, Eq. (A.11), are deeply connected to the transverse electromagnetic fields encountered by the beam, Eq. (A.6), as can be seen by trivially deriving two copies of the Laplacian,

$$\begin{aligned} \partial_x^2 u = \partial_x\partial_y v = \partial_y\partial_x v = -\partial_y^2 u \qquad &\Rightarrow \qquad (\partial_x^2 + \partial_y^2)u = \nabla^2 u = 0, \\ \partial_y^2 v = \partial_y\partial_x u = \partial_x\partial_y u = -\partial_x^2 v \qquad &\Rightarrow \qquad (\partial_x^2 + \partial_y^2)v = \nabla^2 v = 0, \end{aligned} \tag{A.12}$$

where the Cauchy-Riemann equations Eq. (A.11) have been used (and the fact that partial derivatives commute in flat spacetime) in order to write two copies of the Laplacian, one for each of the real and the imaginary parts of $f(z) = u(x,y) + iv(x,y)$.

Having successfully made the connection between the complex plane and a convenient representation of EM potentials used in the $g-2$ experiment, the potential may be expanded in a Laurent-Weierstrass series [98]

$$f(z) = \sum_{n=-\infty}^{\infty} c_n (z - z_0)^n, \tag{A.13}$$

where

$$c_n = \frac{1}{2\pi i} \oint \frac{f(z)\, dz}{(z - z_0)^{n+1}} \qquad (n = 0, \pm 1, \pm 2, \ldots). \tag{A.14}$$

Moreover, since the multipole expansions used in the $g-2$ experiment place the origin of

the coordinate system at the center of the muon storage region, the coefficients of all terms in which $(z - z_0)$ appears in the denominator are set to zero in order to prevent the series Eq. (A.13) from diverging to infinity.[1] Remembering that $z = x + iy = re^{i\theta}$, the relevant solution may also be expressed as

$$f(z) = \sum_{n=0}^{\infty} c_n (z - z_0)^n = \sum_{n=0}^{\infty} c_n r^n e^{in\theta}. \tag{A.15}$$

where the constant term c_0 is often ignored since the field is the derivative of the potential and the derivative of a constant is zero. Choosing a radius $r = r_0$ about which to carry out the expansion and remembering $e^{i\theta} = \cos\theta + i\sin\theta$, the above expression may be written as

$$V(r,\theta) = \mathrm{Re}\left\{\sum_{n=0}^{\infty} c_n \left(\frac{r}{r_0}\right)^n e^{in\theta}\right\} = \sum_{n=0}^{\infty}\left(\frac{r}{r_0}\right)^n [a_n \cos(n\theta) + b_n \sin(n\theta)] \tag{A.16}$$

where $f(z) = V(r,\theta) \in \mathbb{R}$ has been suggestively written for the electric or magnetic potential. Note the potential may also have been written as $V(x,y)$ instead of $V(r,\theta)$ since $z = x + iy = re^{i\theta}$. The 2D transverse field is then just the derivative of the potential Eq. (A.16).

A.2 Lattice Functions: "Beta" Functions, Phase Advance, and Dispersion

Accelerator physicists tend to use "beta functions," "phase advance," and "dispersion" to describe beamlines, e.g. the M4/M5 beamline shown in Fig. 2.7 that leads from the Delivery Ring to the muon $g-2$ storage ring. These variables and functions are likely unfamiliar to readers who have never dealt with accelerator physics before. The purpose of this section is to provide a quick introduction and key derivation that allows the reader to understand

Consider the following differential equation, known as Hill's Equation [27]:

$$\boxed{\frac{d^2x}{ds^2} + k(s)x = 0,} \qquad k(s)\begin{cases} > 0 & \text{(restoring force)}, \\ = 0 & \text{(no force, free space)}, \\ < 0 & \text{(diverging force)}. \end{cases} \tag{A.17}$$

Note the striking similarity to the harmonic oscillator, where the "spring constant" now

[1] This solution is also sometimes called the "interior solution."

depends on the longitudinal position in the beamline as parameterized by the distance s. The form of Eq. (A.17) suggest modifying the solutions of the familiar simple harmonic oscillator so the amplitude and phase are functions of the beamline distance,

$$x(s) = A(s)\cos\psi(s) + B(s)\sin\psi(s). \tag{A.18}$$

Inserting Eq. (A.18) into Eq. (A.17) then gives

$$x'' + kx = \underbrace{\left[A'' - A\psi'^2 + kA\right]}_{=0} c_\psi - \underbrace{\left[2A'\psi' + A\psi''\right]}_{=0} s_\psi = 0 \tag{A.19}$$

where each term in square brackets must separately vanish in order for $x'' + kx = 0$ to be true for all s, leading to

$$A'' + A(\psi')^2 + kA = 0 \tag{A.20a}$$

$$2A'\psi' + A\psi'' = 0. \tag{A.20b}$$

Notice a better choice would have been $A(s) = \sqrt{\beta(s)}$ since then Eq. (A.20b) could have been written as a total derivative,

$$2A'\psi' + A\psi'' = 2\left(\frac{\beta'}{2\sqrt{\beta}}\right)\psi' + \sqrt{\beta}\psi'' = \frac{1}{\sqrt{\beta}}\left(\beta\psi'\right)' = 0 \tag{A.21}$$

Integrating the last expression on the right of the above equation then defines the *betatron phase advance,*

$$\left(\beta\psi'\right)' = 0 \quad \rightarrow \quad \beta\psi' = \text{const.} \equiv 1 \quad \rightarrow \quad \boxed{\psi(s) = \psi(s_0) + \int_{s_0}^{s} \frac{dz}{\beta(z)}}. \tag{A.22}$$

The important point is that if the amplitude function $A(s) = \sqrt{\beta(s)}$ is known, the phase advance may be calculated using Eq. (A.22), which in turn may be used to build single-particle solutions using Eq. (A.18), which in turn may be used to describe the entire ensemble of particles. The connection to the ensemble beam properties is the phase-space ellipse shown

in Fig. A.2, where

$$\epsilon = \gamma x^2 + 2\alpha x x' + \beta x'^2 \tag{A.23}$$

describes the shape and orientation of the ellipse (discussed in more detail in the next section).

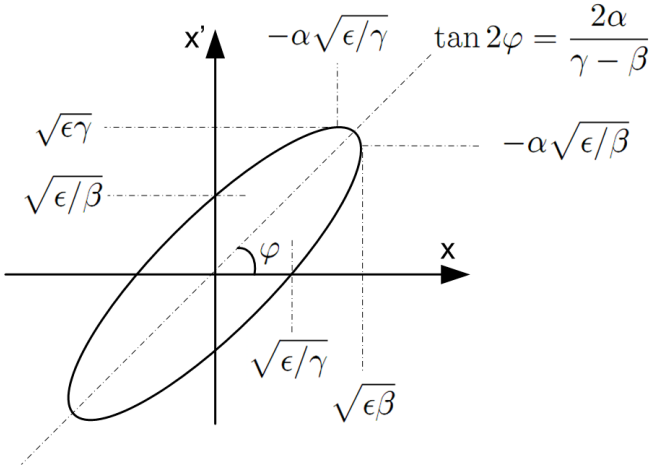

Figure A.2: *Example phase-space ellipse and connection to beam parameters.*

A.3 Evolution of Beam Parameters Downstream

For a 2×2 phase-space transformation matrix

$$\begin{pmatrix} x \\ x' \end{pmatrix} = \underbrace{\begin{pmatrix} C & S \\ C' & S' \end{pmatrix}}_{\mathcal{M}} \begin{pmatrix} x_0 \\ x'_0 \end{pmatrix}, \tag{A.24}$$

the Courant-Snyder invariant

$$\epsilon = \gamma x^2 + 2\alpha x x' + \beta x'^2 \tag{A.25}$$

may be used to prove

$$\boxed{\begin{pmatrix} \beta \\ \alpha \\ \gamma \end{pmatrix} = \begin{pmatrix} C^2 & -2CS & S^2 \\ -CC' & (C'S + CS') & -SS' \\ C'^2 & -2C'S' & S'^2 \end{pmatrix} \begin{pmatrix} \beta_0 \\ \alpha_0 \\ \gamma_0 \end{pmatrix}}, \tag{A.26}$$

where $C(s)$ and $S(s)$ are the cosine- and sine-like solutions to Hill's differential equation discussed above, s is the beamline distance, $(\beta_0, \alpha_0, \gamma_0)^T$ are the initial Twiss parameters, and $(\beta, \alpha, \gamma)^T$ are the final Twiss parameters at the downstream location in the beamline. The proof is simple: The inverse of Eq. (A.24) is

$$\begin{pmatrix} x_0 \\ x_0' \end{pmatrix} = \underbrace{\begin{pmatrix} S' & -S \\ -C' & C \end{pmatrix}}_{\mathcal{M}^{-1}} \begin{pmatrix} x \\ x' \end{pmatrix} = \begin{pmatrix} S'x - Sx' \\ -C'x + Cx' \end{pmatrix}, \tag{A.27}$$

where the determinant $\|\mathcal{M}\| = 1$ is the statement that the area of the phase-space ellipse is conserved, i.e. magnetic fields do no work. Plugging Eq. (A.27) into Eq. (A.25) and demanding equality at the upstream and downstream locations gives

$$\begin{aligned} \epsilon =& \gamma x^2 + 2\alpha x x' + \beta x'^2 \\ =& \gamma_0 x_0^2 + 2\alpha_0 x_0 x_0' + \beta_0 x_0'^2 \\ =& \gamma_0 \left(S'x - Sx'\right)^2 + 2\alpha \left(S'x - Sx'\right)\left(-C'x + Cx'\right) + \beta \left(-C'x + Cx'\right)^2 \\ =& \underbrace{\left(\beta_0 C^2 - 2\alpha_0 CS + \gamma_0 S^2\right)}_{=\beta} x'^2 \\ &+ 2\underbrace{\left(-\beta_0 CC' + \alpha_0\left(C'S + CS'\right) - \gamma_0 SS'\right)}_{=\alpha} xx' \\ &+ \underbrace{\left(\beta_0 C'^2 - 2\alpha_0 C'S' + \gamma_0 S'^2\right)}_{=\gamma} x^2 \end{aligned} \tag{A.28}$$

Equating the coefficients and writing in matrix form gives Eq. (A.26), thus completing the proof. The main utility of this result is that a matrix that transforms a single-particle phase-space vector downstream may be recast as describing the transformation of the ensemble beam properties downstream.

A.4 Optimal Phase Advance for FODOs in the Muon $g-2$ Experiment

In the muon $g-2$ experiment, 8 GeV kinetic-energy protons impinge on a target to create pions which in turn decay to muons as the beam is transported ∼2.5 km downstream to the experiment. It is important to understand how the beam is transported over such a large distance in a way that does not degrade the beam quality and captures as many muons

from pion decay as possible. The following discussion of transporting charged particle beams over large distances applies not only to the muon $g-2$ experiment but also to many other accelerator-based physics experiments in the past, present, and future. Typically a motif known as a "FODO," which consists of a periodic arrangement of alternating focusing (F) quadrupoles and defocusing (D) quadrupoles with open space (O) in between, is used to focus the beam alternately in the two transverse directions. This arrangement prevents the beam from diverging out of the beam pipe and allows the beam to be transported over large distances. The logic of a FODO is built up below, and some basic characteristic are derived in order to connect with the beamlines in the muon $g-2$ experiment. The thin-lens approximation is used throughout this section for mathematical and conceptual clarity.

The field of a quadrupole is focusing in one transverse direction and defocusing in the other. In the thin-lens approximation, the matrix for a horizontally focusing quadrupole that transforms the phase-space vector $(x, x', y, y')^T$ is

$$\mathcal{M}_{\text{thin-lens}} = \begin{pmatrix} 1 & 0 & 0 & 0 \\ -\frac{1}{f} & 1 & 0 & 0 \\ 0 & 0 & 1 & 0 \\ 0 & 0 & +\frac{1}{f} & 1 \end{pmatrix} = \begin{pmatrix} \mathcal{M}_x & 0 \\ 0 & \mathcal{M}_y \end{pmatrix}, \tag{A.29}$$

where the longitudinal subspace has been ignored for clarity. A collection of quadrupoles can be arranged to be net-focusing in both transverse directions provided the focusing strengths are chosen appropriately. Consider, for example, the case of two quadrupoles separated by a distance L. In the thin-lens approximation, the total transformation matrix for such a quad doublet is

$$\mathcal{M}_{\text{doublet}} = \begin{pmatrix} 1 & 0 \\ -\frac{1}{f_2} & 1 \end{pmatrix} \begin{pmatrix} 1 & L \\ 0 & 1 \end{pmatrix} \begin{pmatrix} 1 & 0 \\ -\frac{1}{f_1} & 1 \end{pmatrix} = \begin{pmatrix} 1 - \frac{L}{f_1} & L \\ -\frac{1}{f^\star} & 1 - \frac{L}{f_2} \end{pmatrix}, \tag{A.30}$$

where

$$\frac{1}{f^\star} = \frac{1}{f_1} + \frac{1}{f_2} - \frac{L}{f_1 f_2} \tag{A.31}$$

is the combined focal length and the other transverse is implied from Eq. (A.29). A particular solution is $f_2 = -f_1$, which gives $f^\star = f_1^2/L > 0$. The important observation is that a combination of a focusing quadrupole and defocusing quadrupole has been made net focusing

in both transverse directions. Such a setup is useful for the focusing of charged particle beams in general.[2]

The simple quadrupole doublet discussed above may be concatenated ad infinitum to form a lattice that transports charged particle beams over great distances like those in the Fermilab muon $g-2$ experiment. First, let us form a mirror-symmetric quad triplet by concatenating two doublets, one of which is reversed longitudinally. If the transport matrix for the upstream half is symbolically represented as

$$\mathcal{M} = \begin{pmatrix} a & b \\ c & d \end{pmatrix}, \tag{A.32}$$

then the transformation matrix for the mirror-symmetric downstream half is

$$\mathcal{M}_{\text{mirror}} = \begin{pmatrix} d & b \\ c & a \end{pmatrix}, \tag{A.33}$$

and the total transformation matrix is

$$\mathcal{M}_{\text{tot}} = \mathcal{M}_{\text{mirror}}\mathcal{M} = \begin{pmatrix} ad+bc & 2bd \\ 2ac & ad+bc \end{pmatrix}. \tag{A.34}$$

Using this general result together with Eq. (A.30) gives the total transformation matrix for a symmetric quad triplet,

$$\mathcal{M}_{\text{triplet}} = \begin{pmatrix} 1-2\frac{L^2}{f^2} & 2L\left(1+\frac{L}{f}\right) \\ -2\left(1-\frac{L}{f}\right)\frac{L}{f^2} & 1-2\frac{L^2}{f^2} \end{pmatrix}. \tag{A.35}$$

The formation of a FODO from a triplet amounts to enforcing periodic boundary conditions at the upstream and downstream ends of the quad triplet. The constraints are $\beta = \beta_0$ and its derivative $\alpha \equiv -\frac{1}{2}\partial_s\beta = 0 = \alpha_0$ are continuous. Using Eq. (A.26) to determine the downstream evolution of the Twiss parameters calculated from Eq. (A.35) and enforcing

[2]The above analysis using thick-lens quads gives similar results.

periodicity gives

$$\beta = \left(1 - 2\frac{L^2}{f^2}\right)^2 \beta + 4L^2 \left(1 + \frac{L}{f}\right)^2 \frac{1}{\beta}, \tag{A.36}$$

where the Courant-Snyder invariant $\beta\gamma - \alpha^2 = 1$ has been used to solve for $\gamma = 1/\beta$ when $\alpha = 0$. The solutions for the horizontal (x) and vertical (y) directions at the start of the lattice are

$$\beta_x = \beta^+ = L\frac{\kappa(\kappa+1)}{\sqrt{\kappa^2-1}}, \qquad \beta_y = \beta^- = L\frac{\kappa(\kappa-1)}{\sqrt{\kappa^2-1}}, \qquad \kappa \equiv \frac{f}{L} > 1, \tag{A.37}$$

where $\beta_x = \beta^+$ is the larger of the two solutions at the center of the horizontally focusing quadrupole, and $\kappa \equiv f/L > 1$ is a FODO parameter. Note that letting $f \to -f$ in the above analysis gives the symmetric quad triplet in which the horizontally and vertically focusing quads are interchanged longitudinally, which amounts to exchanging $\beta_x \leftrightarrow \beta_y$ in the results. The phase advance is then trivially calculated since the periodicity constraints ($\beta = \beta_0, \alpha = \alpha_0 = 0$) cause the total transformation matrix to reduce to

$$\begin{pmatrix} \sqrt{\frac{\beta}{\beta_0}}\left(\cos\mu + \alpha_0 \sin\mu\right) & \sqrt{\beta\beta_0}\sin\mu \\ \frac{\alpha_0-\alpha}{\sqrt{\beta\beta_0}}\cos\mu - \frac{1+\alpha\alpha_0}{\sqrt{\beta\beta_0}}\sin\mu & \frac{\beta_0}{\beta}\left(\cos\mu - \alpha\sin\mu\right) \end{pmatrix} \quad \Rightarrow \quad \begin{pmatrix} \cos\mu & \beta\sin\mu \\ -\frac{1}{\beta}\sin\mu & \cos\mu \end{pmatrix} \tag{A.38}$$

where μ is the betatron phase advance through one period of the FODO. Equating the above matrix to Eq. (A.35) gives the FODO phase advance,

$$\cos\mu = 1 - 2\frac{L^2}{f^2} = \frac{\kappa^2-2}{\kappa^2}, \qquad \sin\left(\frac{\mu}{2}\right) = \frac{1}{\kappa}. \tag{A.39}$$

The requirement $\kappa \equiv f/L > 1$ means the focal length of half a quadrupole in a FODO must be greater than the distance L between adjacent quadrupoles for stability reasons. In the limits $\kappa \to 1$ and $\kappa \to \infty$ Eq. (A.37) tends to infinity, so a minimum is expected somewhere in the range $\kappa \in (1, \infty)$. The choice of κ which minimizes β in the middle of the horizontally focusing quadrupole corresponds to the smallest physically realizable beam size that may be transported by the FODO, namely

$$\frac{\partial\beta_x}{\partial\kappa} = \kappa^2 - \kappa - 1 = 0 \qquad \Rightarrow \qquad \kappa = \tfrac{1}{2} + \sqrt{\tfrac{1}{4}+1} = 1.618, \tag{A.40}$$

where the positive root has been taken since $\kappa = f/L > 1$. This solution is indeed a minimum since the concavity $\partial_\kappa^2 \beta = 2\kappa - 1\big|_{\kappa=1.618} = 2.236$ is greater than zero. Using this result together with Eq. (A.39) gives the optimal phase advance per FODO cell as $\mu = 76.345°$.

The muon $g-2$ experiment is designed to have a "round beam," i.e. $\epsilon_y = \epsilon_x = \epsilon$, where $\sigma_{x,y}^2 = \epsilon\beta_{x,y}$ is the beam width.[3] The above analysis may be improved further by noting the overall transverse beam width will be minimized when

$$\sigma_r^2 = \sigma_x^2 + \sigma_y^2 = \epsilon\,(\beta_x + \beta_y) \tag{A.41}$$

is minimized, where r is the beam transverse radius (ideally much less than the beam-pipe radius, which is assumed to be circular in cross section), and $\beta_{x,y}$ are again taken at the center of the focusing quadrupole as per Eq. (A.37). Performing similar steps as above, the smallest beam size transported by the FODO occurs when

$$\frac{\partial(\beta_x + \beta_y)}{\partial\kappa} = 0 \qquad \Rightarrow \qquad \kappa_{\rm opt} = \frac{f}{L} = \sqrt{2}, \tag{A.42}$$

Thus the FODO phase advance that minimizes the beam size in the muon $g-2$ experiment is found by inserting $\kappa_{\rm opt} = \sqrt{2}$ into Eq. (A.39) giving

$$\boxed{\Delta\mu_{\rm opt} = 90°}\,. \tag{A.43}$$

The optimal values of β are found by inserting $\kappa_{\rm opt} = \sqrt{2}$ into Eq. (A.37) giving

$$\beta_{\rm opt}^{\pm} = L\left(2 \pm \sqrt{2}\right). \tag{A.44}$$

Since the $\sigma_r^2 = \epsilon(\beta_x + \beta_y) = \epsilon(\beta_{\rm opt}^+ + \beta_{\rm opt}^-) = \epsilon(4L)$, the maximum emittance transported by the FODO is

$$\epsilon_{\rm max} = \frac{r^2}{4L}, \tag{A.45}$$

where r is the beam radius and L is the half-length of the FODO cell.

A realistic example of the above analysis is the M3 beamline in the muon g–2 experiment.

[3]The FODOs in the muon $g-2$ experiment are designed to be free of dispersion, so the relation describing the beam width $\sigma^2 = \epsilon\beta + (\eta\delta)^2$ reduces to $\sigma^2 = \epsilon\beta$.

This section of beamline is immediately downstream of the production target used to create pions. M3 contains a FODO section with 90° phase advance per cell [Eq. (A.43)] in order to minimize the transverse beam size, which in turn maximizes the number of muons captured from pion decay as the beam is transported downstream. Since this FODO section of M3 has a half-cell length $L = 5.50\,\text{m}$ and the design emittance is $40\,\mu\text{m}$, the beam-pipe radius must be larger than [Eq. (A.45)]

$$r = \sqrt{4\epsilon L} = 3.0\,\text{cm}. \tag{A.46}$$

A.5 Derivation of the Muon Storage-Ring Acceptance

The phase-space ellipse that defines the horizontal ring acceptance may be calculated from Eq. (3.18),

$$\begin{pmatrix} x(\theta) \\ x'(\theta) \\ \delta \end{pmatrix} = \begin{pmatrix} \cos(Q_x\theta) & \frac{\rho_0}{Q_x}\sin(Q_x\theta) & \frac{\rho_0}{Q_x^2}(1-\cos(Q_x\theta)) \\ -\frac{Q_x}{\rho_0}\sin(Q_x\theta) & \cos(Q_x\theta) & \frac{1}{Q_x}\sin(Q_x\theta) \\ 0 & 0 & 1 \end{pmatrix} \begin{pmatrix} 45\,\text{mm} \\ 0 \\ \delta \end{pmatrix}, \tag{A.47}$$

where $\theta = s/\rho_0$ is the ring angle, $Q_x \approx \sqrt{1-n}$ is the betatron tune, $x_0 = r_0 = 45\,\text{mm}$ is the inner edge of the circular collimator. A similar expression holds for the (y, y') subspace using Eq. (3.19). These phase-space ellipses are shown in Fig. A.3. Additionally, the circular collimators enforce the constraint $x^2 + y^2 < r_0^2$.

A.6 Material Effects: Multiple Coulomb Scattering and Energy Loss

Multiple Coulomb Scattering

When a charged particle travels through a material, the particle undergoes many small-angle deflections arising predominantly from Coulomb interactions with nuclei. The resulting scattering angle is approximately Gaussian in nature, where

$$\theta_0 = \theta_{\text{plane}}^{\text{rms}} = \frac{13.6\,\text{MeV}}{\beta cp} z\sqrt{\frac{x}{X_0}}\left[1 + 0.038\ln\left(\frac{x}{X_0}\right)\right] \tag{A.48}$$

is the RMS change in angle for the transverse phase-space coordinates (x', y'), $\{\beta, c, p\}$ take on their usual meaning in relativistic kinematics, z is the charge of the incident particle, and

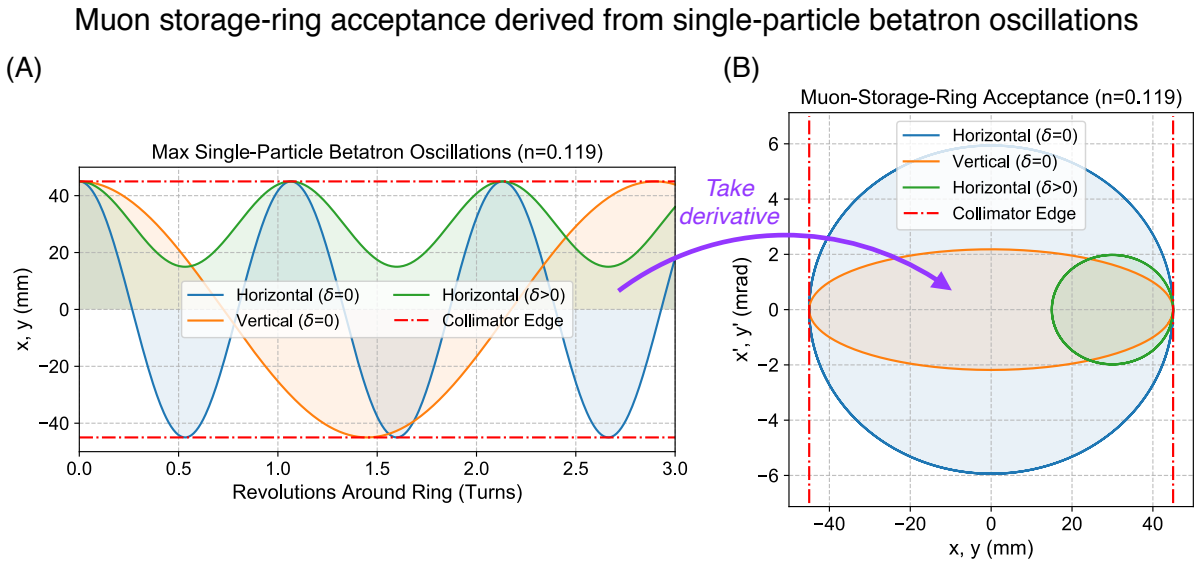

Figure A.3: *Muon storage-ring acceptance derived from single-particle betatron oscillations. (A) At a quadrupole high voltage of* 20.2 kV *(*$n = 0.119$*), the horizontal betatron oscillation (blue) has a period of* $T_x = \sqrt{1-n} \approx 1.1$ *turns, while the vertical oscillation (orange) has a period of* $T_y = 1/\sqrt{n} \approx 2.9$ *turns. Higher-momentum particles (green) have larger orbit radii,* $\rho = \rho_0 + x$*. Stored muons are contained within the inner edges of the circular collimator aperture described by the equation* $x^2 + y^2 < r_0^2 = (45\,\text{mm})^2$ *(dotted red lines). (B) The muon storage ring acceptance is found by taking the derivative of (A) with respect to the downstream distance* $s \equiv \rho_0\theta$ *and plotting* $\{(x, x'), (y, y')\}$ *as functions of the parameter* s*. All stored particles must have transverse phase-space coordinates* (x, x', y, y') *entirely within these ellipses in addition to* $x^2 + y^2 < r_0^2$*. The maximum storage occurs when* x'_{max} *and* y'_{max} *are equal, corresponding to a quad high voltage of* ∼85 kV.

x/X_0 is the thickness of the material in radiation lengths [101]. For a 1-cm thick material with $\theta_0 \sim 1\,\text{mrad}$, for example, the change to displacement is of order $\Delta x \sim L\theta_0 = 10\,\mu\text{m}$, i.e. the change to transverse displacement is typically ignored. The net scattering angle is intimately connected to phase space, the absolute transverse momentum acceptance of the $g-2$ storage ring, and the material budget of the beamline overall. As was discussed above, the transverse momentum acceptance of the $g-2$ storage ring is only

$$y'_{max} = \frac{r_0}{R_0}\sqrt{n} = \frac{45\,\text{mm}}{7112\,\text{mm}}\sqrt{0.119} = 2.2\,\text{mrad} \tag{A.49}$$

for a quadrupole high voltage of 20.2 kV, which is on par with the scattering angle given by Eq. (A.48) for common HEP materials $\sim$1 cm thick. Thus, small scattering angles play an important role in the muon capture efficiency of the $g-2$ storage ring overall, as shown in Fig. A.4.

Energy Loss: Average vs. Most Probable

The average energy loss by moderately relativistic ($0.1 \lesssim \beta\gamma \lesssim 1000$) charged heavy particles is well described by the Bethe Equation,

$$\left\langle -\frac{dE}{dx} \right\rangle = Kz^2 \frac{Z}{A}\frac{1}{\beta^2}\left[\frac{1}{2}\log\left(\frac{2m_e c^2\beta^2\gamma^2 W_{\text{max}}}{I^2}\right) - \beta^2 - \frac{\delta(\beta\gamma)}{2}\right] \tag{A.50}$$

where $K = 4\pi N_A r_e^2 m_e c^2$ is related to the classical electron density in the material, z is the charge of the incident particle, Z is the charge of the nucleus of the material, A is the mass number of the material, etc. Notice that, at low energies the $(1/\beta^2)$ prefactor tends to infinity, while at higher energies $1/\beta^2 \to 0$ and $\log(\beta\gamma)$ rises monotonically until the critical energy, at which Bremsstrahlung and pair production begin to dominate energy loss. The Particle Data Group gives an interesting, strongly worded caveat about the use of the Bethe Eq. (A.50) for practical material calculations involving energy loss [101],

> *Few concepts in high-energy physics are as misused as $\langle dE/dx \rangle$. The main problem is that the mean is weighted by very rare events with large single-collision energy deposits. Even with samples of hundreds of events a dependable value for the mean energy loss cannot be obtained. Far better and more easily measured is the most probable energy loss, discussed [below]. The most probable energy*

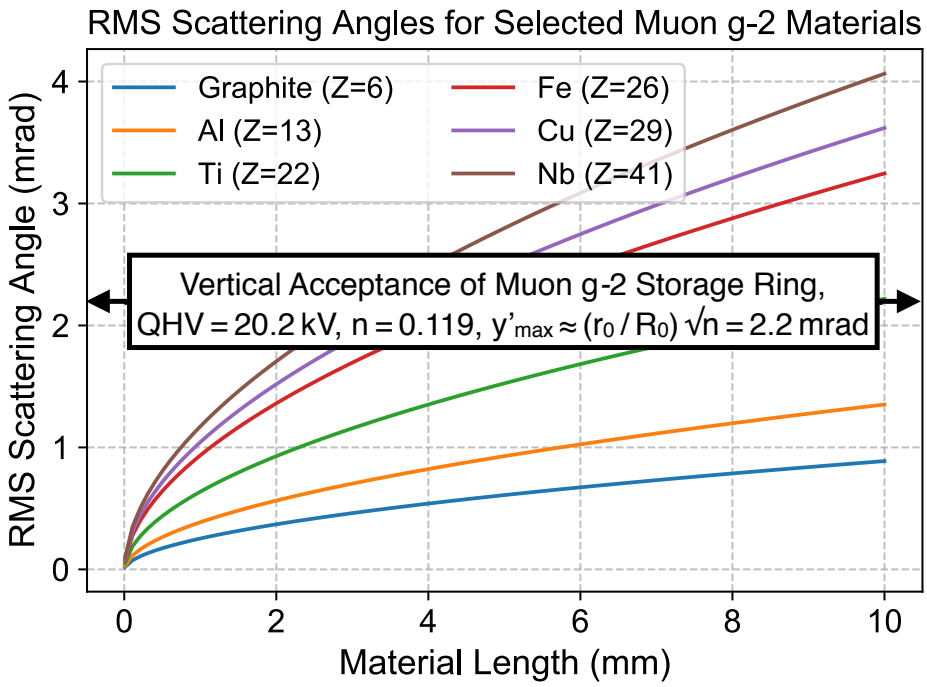

Figure A.4: *RMS scattering angles for common materials and thicknesses in the muon $g-2$ experiment. The data are reinterpreted as beamline material budget using the vertical acceptance of the g–2 storage ring, $y'_{max} = (r_0/R_0)\sqrt{n} \approx 2.2\,\mathrm{mrad}$, which dominates injection compared to $x'_{max} = (r_0/R_0)\sqrt{1-n} \approx 5.9\,\mathrm{mrad}$ at a quadrupole voltage of $20.2\,\mathrm{kV}$ ($n = 0.119$). This is why muon storage goes approximately as $\sqrt{\mathrm{QHV}} \propto \sqrt{n}$.*

loss in a detector is considerably below the mean given by the Bethe equation[, Eq. (A.50)].

As the PDG advises, it is much better to use the highly skewed Landau-Vavilov distribution where the most probable energy loss is given by

$$\Delta_p = \xi \left[\ln \left(\frac{2mc^2\beta^2\gamma^2}{I} \right) + \ln \frac{\xi}{I} + j - \beta^2 - \delta(\beta\gamma) \right]. \tag{A.51}$$